Plasma Physics Reports, Vol. 30, No. 12, 2004, pp. 1006–1011. Translated from Fizika Plazmy, Vol. 30, No. 12, 2004, pp. 1082–1087.

ISOTOPE SEPARATION

Calculation of the Ion Distribution Function over Transverse Velocities under ICR Heating Conditions and Separation Parameters of a Collector of Heated Ions

A. I. Karchevskiĭ† and E. P. Potanin

Institute of Molecular Physics, Russian Research Centre Kurchatov Institute, pl. Kurchatova 1, Moscow, 123182 Russia

Received January 8, 2004; in final form, March 17, 2004

Abstract—The ion distribution function over transverse velocities and the ion heating efficiency (which is defined as the fraction η of ions heated above a certain energy W_{min}) are calculated in the context of a plasma method for isotope separation on the basis of ion cyclotron resonance heating. The ion distribution function over longitudinal velocities is assumed to be linear in the range of low velocities. It is shown that, when the ions are heated to high energies, the averaged ion distribution function over transverse velocities becomes highly nonequilibrium and has two peaks. Results are presented from calculations of the ion heating efficiency η for W_{min} = 40 eV and for different values of the parameter p that characterizes the ratio of the wavelength λ of the antenna electric field to the length L of the heating region. The relative roles of the time-of-flight and the Doppler broadening are analyzed, and the separation parameters of a collector of heated ions are estimated. © *2004 MAIK "Nauka/Interperiodica".*

1. INTRODUCTION

The ion cyclotron resonance (ICR) method for isotope separation is based on the selective cyclotron resonance heating of the ions of a target isotope in mutually perpendicular alternating electric and constant magnetic fields [1–7]. Stable isotopes are now separated in two ways: by the electromagnetic method [8] or with the help of cascade gas centrifuges [9]. The centrifuges, however, are capable of separating isotopes of only those elements that form gaseous compounds with sufficiently high vapor pressures at room temperature. The electromagnetic method is well developed but is used to separate out only relatively small amounts of the target isotope. The plasma method is based on selective cyclotron resonance heating of the ions of the target isotope. In the separation of isotopes of metal elements in medium-scale industry, the plasma method seems to have some advantages over the electromagnetic method because it is essentially free of restrictions on the intensities of the ion fluxes. At present, the technological aspects of the ICR method are being developed.

2. CALCULATION OF THE ION DISTRIBUTION FUNCTION OVER TRANSVERSE VELOCITIES

Important elements of an ICR separator are a plasma source that produces ion fluxes with a certain spread over transverse and longitudinal velocities and an RF antenna that generates electromagnetic fields in the ICR heating region. When the plasma passes through the ICR heating region, the ion distribution over transverse velocities changes appreciably. In some ICR devices (see, e.g., [4]), use is made of inductive antennas in the form of multiphase cylindrical helices—the so-called helical (or spiral) antennas. For a four-phase antenna in which the ac current in each subsequent phase is shifted by $\pi/2$, the alternating electric field within the cylindrical heating region can be represented as a circularly polarized wave that runs in the positive direction along the z axis and whose polarization vector rotates with an angular velocity ω,

$$E_x = E\cos(\omega t - Kz - \varphi), \quad (1)$$

$$E_y = -E\sin(\omega t - Kz - \varphi), \quad (2)$$

where $K = \frac{2\pi}{\lambda}$ is the wavenumber, E is the electric field amplitude, and φ is the initial phase. In this approximation (which can be regarded as linear), the alternating components of the wave magnetic field are ignored. Nonlinear effects were taken into account by Laz'ko [10] by deriving the integrals of motion and by Panov and Timofeev [11] by applying the theory of adiabatic invariants. Note that, if the inverse effect of the motion of plasma particles on the vacuum antenna field is ignored (which corresponds to the case of relatively low plasma densities), then Eqs. (1) and (2) satisfactorily describe the heating electric field in the plasma at radii of $r \le R/2$, where R is the antenna radius [12].

In Cartesian coordinates, the equations of motion of singly charged ions of mass m and charge e in a wave electric field that is described by Eqs. (1) and (2) and

† Deceased.

1063-780X/04/3012-1006$26.00 © 2004 MAIK "Nauka/Interperiodica"

rotates in the direction of ion gyration in a longitudinal magnetic field B_z can be written as

$$m\frac{dV_x}{dt} = eE\cos(\omega t - KV_z t) + eV_y B_z, \quad (3)$$

$$m\frac{dV_y}{dt} = -eE\sin(\omega t - KV_z t) - eV_x B_z, \quad (4)$$

where V_x and V_y are the transverse components of the velocity of the ions and V_z is their longitudinal velocity. We introduce the absolute value of the transverse ion velocity $V_\perp = \sqrt{V_x^2 + V_x^2}$. Our objective here is to consider the ICR heating of an ion flux with certain initial distributions over longitudinal and transverse velocities and to determine the ion distribution function over transverse velocities at the exit from the heating region of finite length L. We assume that, at the entrance to the ICR heating region, the ion distribution function over transverse velocities is Maxwellian,

$$f_{\perp 0}(V_\perp) = \left(\frac{m}{2\pi k T_{0\perp}}\right)\exp\left(-\frac{m}{2kT_{0\perp}}(V_x^2 + V_y^2)\right), \quad (5)$$

where $T_{0\perp}$ is the initial transverse ion temperature.

As a first step, we use the expression that was obtained by Ustinov [12] for the transverse ion distribution function at the exit from the heating region for the case of a beam of ions with the same longitudinal velocity V_z:

$$f_\perp(V_\perp) = \left(\frac{m}{2\pi k T_{0\perp}}\right)\exp\left(-\frac{m}{2kT_{0\perp}}(V_\perp^2 + V_0^2)\right) I_0\left(\frac{mV_0V_\perp}{kT_{0\perp}}\right), \quad (6)$$

where k is Boltzmann's constant and I_0 is the zero-order modified Bessel function. For a heating regime in which the transverse energy of the ions is much higher than their initial thermal energy, the quantity V_0 is given by the formula

$$V_0 \cong \frac{2E\omega_0}{B_z(\omega - KV_z - \omega_0)}\sin\left((\omega - KV_z - \omega_0)\frac{L}{2V_z}\right),$$

where ω_0 is the ion gyrofrequency. Distribution function (6) is normalized to unity and depends on both the longitudinal velocity V_z of the ion beam and the heating field frequency ω. At the entrance to the heating region, an actual beam is a superposition of individual beams, each having its own longitudinal velocity V_z. We denote the distribution function over longitudinal velocities by $f_z(V_z)$ in order to represent the total ion distribution function as a product of two functions,

$$f(V_\perp, V_z) = f_\perp(V_\perp) f_z(V_z). \quad (7)$$

Let us investigate the heating of the ions described by a model non-Maxwellian longitudinal distribution function $f_z(V_z)$. We assume that this model distribution function depends linearly on the ion velocity in the low-velocity range and decreases exponentially at high ion velocities,

$$f_z(V_z) = \frac{mV_z}{kT_z}\exp\left(-\frac{mV_z^2}{2kT_z}\right), \quad V_z > 0, \quad (8)$$

where T_z is the effective longitudinal ion temperature. We also assume that this function does not change over the entire length of the heating region. We introduce the parameter $p = \frac{\lambda}{L}$, which is equal to the ratio of the wavelength λ to the length L of the heating region. For a fixed length L of the heating region, the variation of the parameter p corresponds to the variation of the wavelength λ and, accordingly, of the wavenumber K, whereas, for a fixed wavelength λ, the variation of the parameter p corresponds to the variation of the length of the heating region. We define the distribution function averaged over longitudinal velocities to be

$$F(y) = \bar{f}(y)/\left(\frac{m}{2kT_{0\perp}}\right)^{1/2} = 4\int_0^\infty \exp(-(y^2 + y_0^2 + x^2) I_0(2yy_0) xy\,dx, \quad (9)$$

where we have introduced the notation

$$y = \frac{V_\perp}{(2kT_{\perp 0}/m)^{1/2}}, \quad x = \frac{V_z}{(2kT_z/m)^{1/2}},$$

$$n_L = \left(\frac{2kT_z}{m}\right)^{1/2}\frac{2}{L\omega_0}, \quad n_E = \frac{2E}{B_z\left(\frac{2kT_{\perp 0}}{m}\right)^{1/2}},$$

$$y_0 = \frac{n_E\sin\left((\Omega - \pi n_L x/p - 1)\frac{1}{n_L x}\right)}{(\Omega - \pi n_L x/p - 1)}, \quad \Omega = \frac{\omega}{\omega_0}.$$

All the simulations were carried out for a model binary mixture of isotopes with mass numbers of 6 and 7. We introduce the dimensionless parameter n, which characterizes the detuning of the antenna field frequency from the ion gyrofrequency: $n = \frac{2\delta\omega}{KV_{z0}}$, where $\delta\omega = \omega - \omega_0$ and $V_{z0} = \left(\frac{\pi k T_z}{2m}\right)^{1/2}$ is the mean longitudinal ion velocity.

The value $n = 2$ of the frequency detuning parameter n so defined corresponds to the precise tuning of the mean longitudinal ion velocity to a value at which the heating efficiency is maximum. The condition under which the tuning of the longitudinal velocity V_z of an ion to the resonant value is sufficiently precise can be

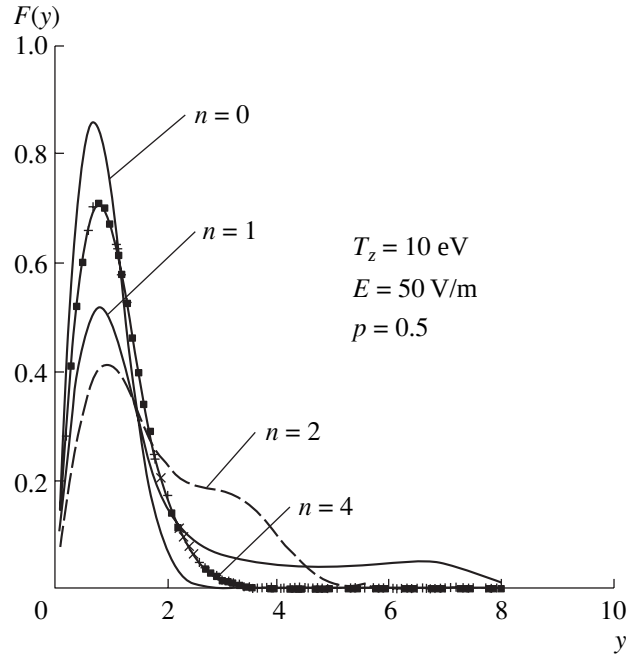

Fig. 1. Distribution function of the heated ions over transverse velocities for $p = 0.5$ and for different values of the parameter n.

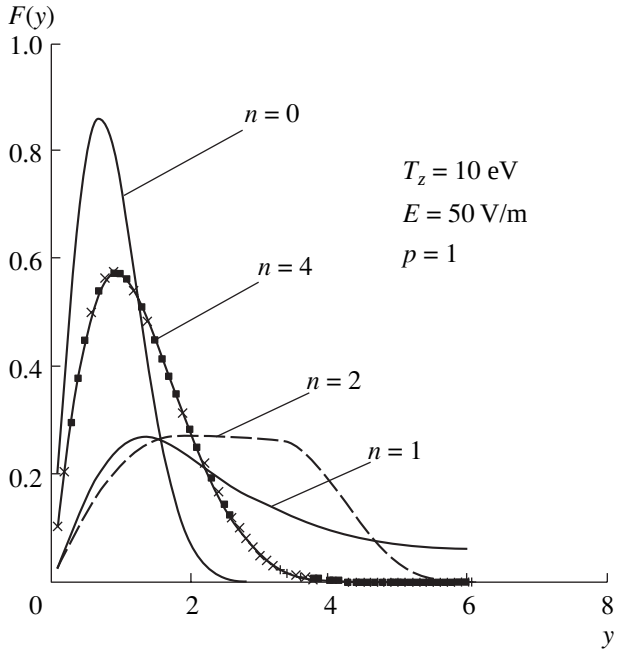

Fig. 2. Distribution function of the heated ions over transverse velocities for $p = 1.0$ and for different values of the parameter n.

written as $|\omega - \omega_0 - KV_z| \ll \dfrac{2\pi V_z}{L}$, which, in the notation adopted here, reduces to the inequality $|n - 2| \ll 2p$. For $n = 0$ and $n = 4$, this inequality fails to hold, which corresponds to a substantial frequency detuning from resonance. For $n = 2$, this inequality is satisfied with finite values of the parameter p.

The distribution functions $F(y)$ of the ions of an isotope with a mass number of 6 are shown in Figs. 1–3, which illustrate the results of calculations carried out for an alternating electric field with an amplitude of $E = 50$ V/m, a longitudinal ion temperature of $T_z = 10$ eV, and a heating region of length $L = 0.8$ m and for different values of the parameters p and n. The values $n = 0$ and $n = 4$ correspond to a substantial frequency detuning from resonance. In this case, an increase in the parameter p indicates a decrease in the wavenumber K. Figure 4 shows the ion distribution functions $F(y)$ calculated for different amplitudes E of the heating field in the case of precise tuning of the mean longitudinal ion velocity to resonance ($\omega - \omega_0 = KV_{z0}$, $n = 2$) at $T_z = 10$ eV, $T_{\perp 0} = 5$ eV, and $p = 1$ (which corresponds to a one-wavelength antenna). Curve *1* was obtained for a zero heating field ($E = 0$) and corresponds to a Maxwellian distribution function. Curves *2*, *3*, and *4* were computed for heating fields with the amplitudes $E = 50$, 100, and 200 V/m, respectively. We note that the spectrum of the transverse ion energies is fairly broad and that the distribution of the ions heated to high energies has two peaks. The results calculated for a strong heating electric field are somewhat incorrect because they were obtained in the linear approximation. From formulas (7), (8), and (9), we can derive the following expression for the ion heating efficiency η, which is defined as the relative fraction of ions heated above a certain given energy $W_{\min}$:

$$\eta = 4\int_0^\infty dx \int_{y_1}^\infty xy \exp(-(y^2 + y_0^2 + x^2)) I_0(2yy_0)\, dy, \quad (10)$$

where $\left(y_1 = \sqrt{\dfrac{W_{\min}}{kT_{0\perp}}}\right)$.

Figure 5 illustrates the results of calculating the ion heating efficiency η for $W_{\min} = 40$ eV and for different values of the parameter p, which characterizes the ratio of the wavelength λ of the antenna electric field to the length L of the heating region and, thereby, the relative roles of the time-of-flight broadening and Doppler broadening. Since the calculations were carried out for a fixed length of the heating region, $L = 0.8$ m, variations in the parameter p corresponded to variations in the wavenumber K.

For large values of the parameter p (i.e., for large λ values and small K values), the time-of-flight broadening predominates over the Doppler broadening and vice versa for small p values. For $p = 5$, the width of the heating efficiency profile is determined by the time-of-flight broadening. The dashed curve in Fig. 5 was calculated for $p = 5$ with allowance for the dependence of the electric field amplitude on the wavenumber by means of the

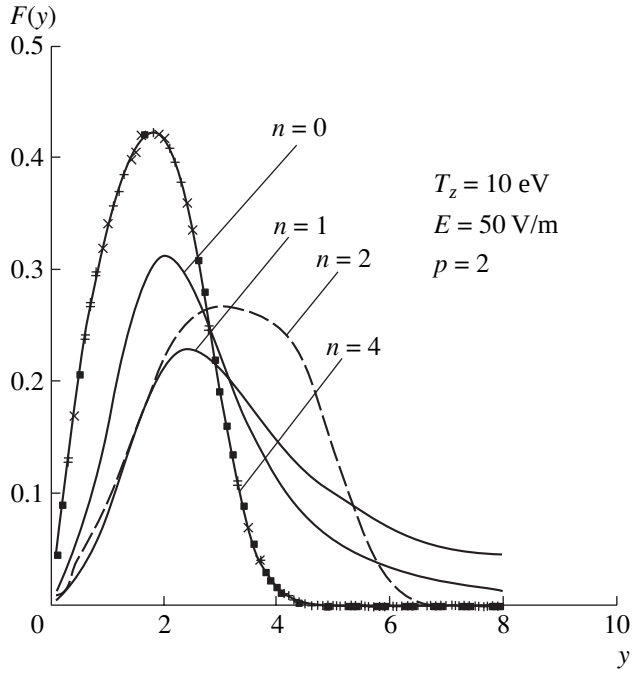

Fig. 3. Distribution function of the heated ions over transverse velocities for $p = 2.0$ and for different values of the parameter n.

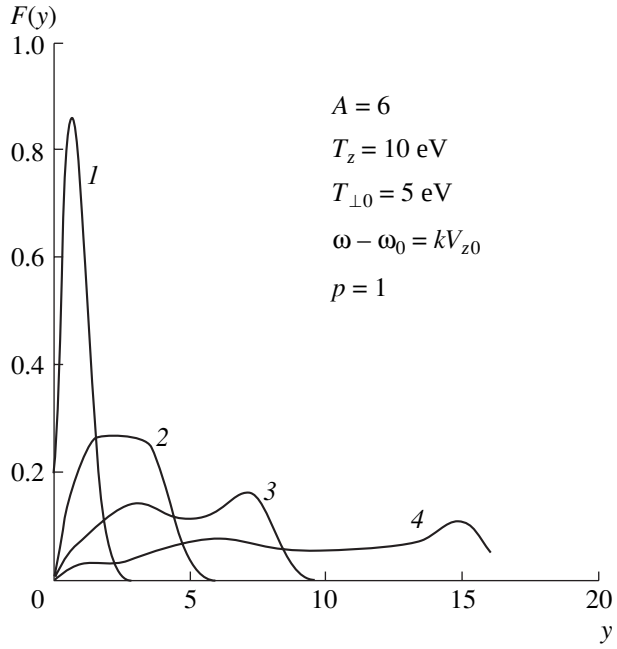

Fig. 4. Ion distribution function over transverse velocities for different amplitudes of the heating electric field: $E =$ (*1*) 0, (*2*) 50, (*3*) 100, and (*4*) 200 V/m.

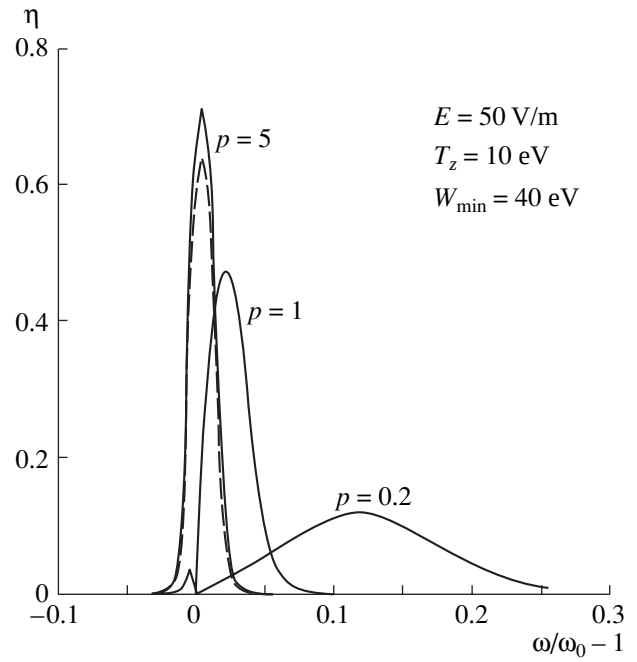

Fig. 5. Dependence of the ion heating efficiency η on the frequency detuning $\omega/\omega_0 - 1$ for $E = 50$ V/m, $n = 2$, and different values of the parameter p.

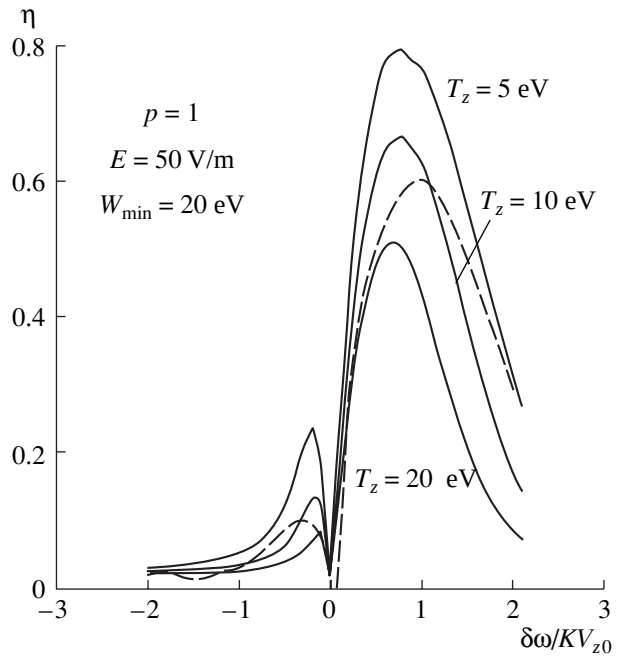

Fig. 6. Dependence of the ion heating efficiency η on the dimensionless detuning $\delta\omega/KV_{z0}$ for $p = 1$, $n = 2$, and different longitudinal temperatures.

approximations used in [12]. Figure 6 illustrates the dependence of the heating efficiency η on the dimensionless detuning of the heating field frequency from the ion gyrofrequency, $\delta\omega/KV_{z0}$, for a one-wavelength antenna ($p = 1$), for $E = 50$ V/m and $W_{min} = 20$ eV, and for different longitudinal ion temperatures. The dashed

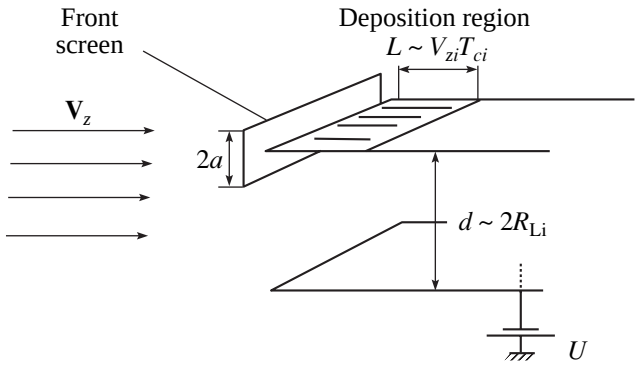

Fig. 7. Element of the scheme of a collector of heated ions. The optimum distance d between the plates is about two gyroradii of the heated ions. The notation is as follows: L is the length of the deposition region, T_{ci} is the period of ion gyration, and V_{zi} is the longitudinal ion velocity.

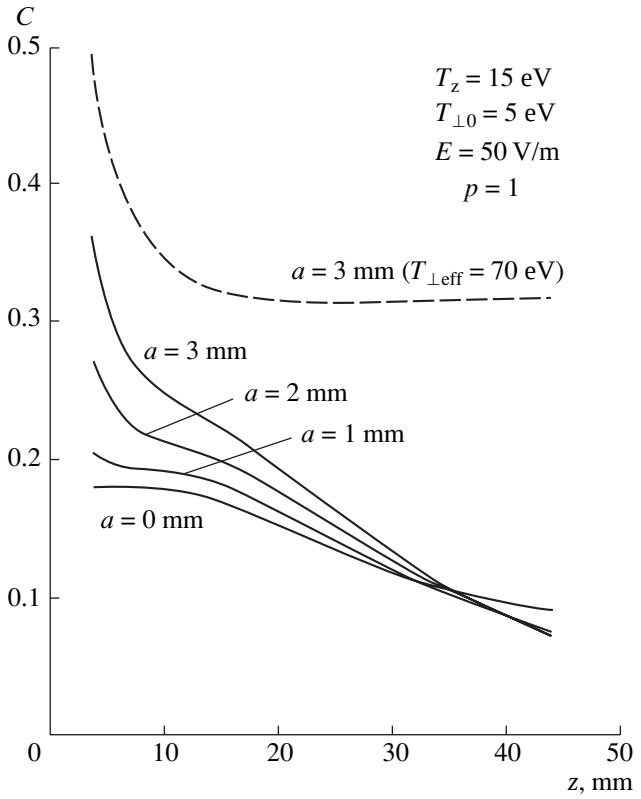

Fig. 8. Dependence of the concentration C of the lighter isotope of mass number 6 on the longitudinal coordinate Z for different half-heights a of the front screen. The dashed curve illustrates the results of model calculations for $\delta\omega = KV_{z0}$.

curve shows the relevant result obtained in [12] for an electric field amplitude of $E \approx 50$ V/m and for a longitudinal ion temperature of $T_z = 10$ eV.

3. SEPARATION PARAMETERS OF A COLLECTOR OF HEATED IONS

The heated ions of the target isotope are usually separated out by a collector in the form of equidistant ion-collecting plates oriented parallel to the plasma flow. As a result, the heated target ions, which gyrate over large Larmor orbits, are primarily deposited on the collector plates. The plates are protected from the plasma flow by the front screens. An element of a collector that includes two neighboring plates is demonstrated in Fig. 7 (the screen protecting the lower plate is not shown).

In order to estimate the separation properties of the collector, it is necessary to calculate the fluxes of ions of different species on the collector plate. The density of the transverse ion flux onto an element of the collector plate surface is expressed in terms of distribution function (7) as follows:

$$dj = fV_y dV_x dV_y dV_z. \tag{11}$$

In this case, the flux density can be defined as

$$j = \int f\omega_0 V_\perp dV_\perp dV_z dy_0, \tag{12}$$

where y_0 is the transverse coordinate of the guiding center of an ion Larmor orbit in a plane in front of the collecting plate. Integration in formula (12) is carried out in accordance with the restrictions imposed on the velocities and coordinates of the ion guiding centers in front of the collector.

For a binary mixture of isotopes, the concentration C of the first ion species can be determined from the relationship

$$\frac{C}{1-C} = \frac{C_0}{1-C_0}\frac{j_1 n_{20}}{j_2 n_{10}}\sqrt{\frac{m_2}{m_1}}, \tag{13}$$

where C_0 is the initial concentration of the first ion species and n_{10} and n_{20} are, respectively, the number densities of the first and second ion species.

In our earlier papers [13, 14], formulas (11)–(13) were used to obtain similar estimates on the basis of model Maxwellian distribution functions over transverse velocities with different effective transverse temperatures. In the present study, the separation properties of the collector are calculated with allowance for a distribution function that is obtained based on solving the Boltzmann equation and takes into account the time-of-flight and Doppler broadening of the heating efficiency profile [15]. The calculations were carried out for an antenna field frequency detuned from the gyrofrequency of the ions of an isotope with a mass number of 6 by an amount equal to the Doppler broadening, $\delta\omega = \omega - \omega_0 = KV_{z0}$, where $V_{z0} = \left(\frac{\pi k T_z}{2m}\right)^{1/2}$ is the mean longitudinal ion velocity.

Figure 8 illustrates the results of calculating the profile of the concentration C of the lighter isotope ions over the length of a collector plate in an operating mode with no applied repulsive potential. The calculations were carried out for $p = 1$ and for different heights of the front screen ($a = 0$, 1, 2, and 3 mm). The remaining parameter values were as follows: the initial transverse ion temperature was $T_{\perp 0} = 5$ eV, the longitudinal ion temperature was $T_z = 15$ eV, the heating field amplitude was $E = 50$ V/m, and the magnetic induction was $B = 0.25$ T. The dashed curve in the figure shows the profile $C(z)$ for a model Maxwellian distribution function with the effective temperature determined from the following relationship for the mean transverse ion energy:

$$\langle E_\perp \rangle = 4kT_{\perp 0}\int_0^\infty\int_0^\infty I_0(2yy_0) \times \exp(-(x^2 + y^2 + y_0^2))y^3 x\,dy\,dx.$$

It can be seen that the concentration calculated from a model Maxwellian distribution differs markedly from those obtained using actual nonequilibrium ion distributions over transverse velocities. The unrealistically high separating ability of the separator in the first case is associated with the fact that the fraction of strongly heated ions implied by a model Maxwellian distribution function over transverse velocities considerably exceeds that calculated for actual conditions.

ACKNOWLEDGMENTS

We are grateful to V.G. Pashkovskiĭ for his help in carrying out our numerical simulations.

REFERENCES

1. G. A. Askar'yan, V. A. Namiot, and A. A. Rukhadze, Pis'ma Zh. Tekh. Fiz. **1**, 820 (1975) [Sov. Tech. Phys. Lett. **1**, 356 (1975)].
2. J. M. Dawson, H. C. Kim, D. Arnush, *et al.*, Phys. Rev. Lett. **37**, 1547 (1976).
3. Yu. A. Muromkin, Itogi Nauki Tekh., Ser. Fizika Plazmy **12**, 83 (1991).
4. A. I. Karchevskiĭ, V. S. Laz'ko, Yu. A. Muromkin, *et al.*, Fiz. Plazmy **19**, 411 (1993) [Plasma Phys. Rep. **19**, 214 (1993)].
5. A. C. La Fontaine and P. Louvet, in *Compte rendu des Journees sur les Isotopes Stables* (Centre dè Études de Saclay, Saclay, 1993), p. 332.
6. M. I. Belavin, A. B. Zvonkov, and A. V. Timofeev, RF Patent No. 1742900, July 5, 1993.
7. V. I. Volosov, I. A. Kotel'nikov, and S. G. Kuz'min, Fiz. Plazmy **24**, 517 (1998) [Plasma Phys. Rep. **24**, 474 (1998)].
8. V. G. Bondarenko and R. N. Kuz'min, in *Isotopes: Their Properties, Production, and Applications*, Ed. by V. Yu. Baranov (IzdAT, Moscow, 2000).
9. E. I. Abbakumov, V. A. Bazhenov, Yu. V. Verbin, *et al.*, At. Energ. **67** (4), 255 (1989).
10. V. S. Laz'ko, Fiz. Plazmy **20**, 523 (1994) [Plasma Phys. Rep. **20**, 470 (1994)].
11. D. A. Panov and A. V. Timofeev, Fiz. Plazmy **21**, 1092 (1995) [Plasma Phys. Rep. **21**, 1031 (1995)].
12. A. L. Ustinov, Preprint No. 5354/6 (Kurchatov Institute of Atomic Energy, Moscow, 1991).
13. A. I. Karchevskiĭ and E. P. Potanin, Fiz. Plazmy **21**, 416 (1995) [Plasma Phys. Rep. **21**, 394 (1995)].
14. A. I. Karchevskiĭ and E. P. Potanin, Fiz. Plazmy **22**, 1146 (1996) [Plasma Phys. Rep. **22**, 1044 (1996)].
15. A. I. Karchevskiĭ and E. P. Potanin, in *Proceedings of the 6th All-Russia Conference on Physicochemical Processes During the Selection of Atoms and Molecules* (TsNIIATOMINFORM, Moscow, 2001).

Translated by G.V. Shepekina

Plasma Physics Reports, Vol. 30, No. 12, 2004, pp. 1012–1027. Translated from Fizika Plazmy, Vol. 30, No. 12, 2004, pp. 1088–1104.

LOW-TEMPERATURE PLASMA

Structure of the Surface Streamers of an AC Barrier Corona in Argon

Yu. S. Akishev, G. I. Aponin, V. B. Karal'nik, A. E. Monich, and N. I. Trushkin

Troitsk Institute for Innovation and Fusion Research, Troitsk, Moscow oblast, 142190 Russia

Received December 19, 2003; in final form, April 16, 2004

Abstract—Results are presented from experimental studies of the structure of an ac surface discharge excited by a metal needle over a plane dielectric surface. A barrier corona discharge was ignited in atmospheric-pressure argon at frequencies of the applied sinusoidal voltage from 50 Hz to 30 kHz. In experiments, the area of a dielectric covered with the discharge plasma increased with applied voltage. The discharge structure in diffuse and streamer modes was recorded using a digital camera and a high-speed image tube operating in a frame mode. It is found that, in the positive and negative half-periods of the applied voltage, the structure of the surface discharge is substantially different. The statistical characteristics of the branching surface streamers in the positive and negative half-periods are determined as functions of the voltage frequency. The most intense lines in the emission spectrum of the barrier corona are determined for both half-periods. The correlation between the dynamics of the emission intensity and the dynamics of the discharge current and voltage is investigated.

1. INTRODUCTION

The so-called "slipping" discharge, i.e., a high-current surface discharge propagating perpendicular to an elongated electrode over a plane dielectric surface, has long been known [1]. A schematic of a device for igniting slipping discharges is shown in Fig. 1. In fact, this is a plane variable capacitor in which the surface area of the grounded plate is much larger than surface area of the plate (strip) to which a high-voltage pulse is applied. After the voltage is applied, gas breakdown occurs near the metal strip; this gives rise to an ionization wave propagating over the dielectric surface and covering it with a thin layer of highly conducting plasma (a plasma sheet). If the amplitude of the high-voltage pulse is kept constant, the discharge current through the dielectric is provided by the displacement current caused by an increase in the capacitance of the distributed capacitor, one of whose plates is the plasma sheet. In such a situation, the slipping surface discharge lasts until the plasma occupies the entire area of the grounded plate. If the voltage increases over time, then the discharge current can continue to flow after the plasma has occupied this area.

As a rule, the energy deposited at the plasma–dielectric interface in a pulsed high-current slipping discharge is fairly high; this makes it impossible to use this type of surface discharge when operating with thermally unstable dielectric materials. In this study, we are dealing with a low-current ac surface discharge excited by a point electrode (needle) located above a dielectric surface. Such a discharge is characterized by a low current density (lower than 10 mA/cm^2) and low specific power deposited in the dielectric (lower than 10 W/cm^2).

Low-current atmospheric-pressure surface discharges, as well as low-current volume discharges (i.e., steady-state and pulsed corona discharges [2–5]), can operate in a diffuse and/or streamer mode in different gases at various electrode configurations over a wide range of discharge currents and voltages. These are classical barrier discharges [6]; short-time surface partial discharges [7], which operate over a dielectric surface after a unipolar voltage pulse of any polarity is applied; and an ac barrier corona [8]. It is of great scientific and practical interest to study the conditions under which the low-current surface discharge operates in a diffuse or a streamer mode, as well as to determine the discharge structure in both of these modes.

It should be taken into account that conditions for the propagation of the surface streamers depend substantially on whether a unipolar voltage pulse or an ac

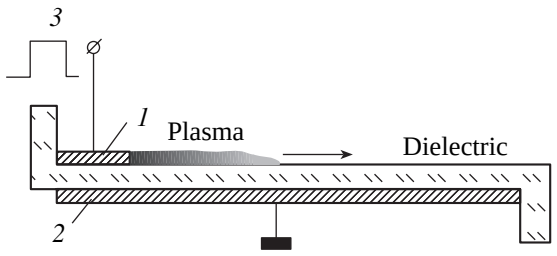

Fig. 1. Scheme illustrating the ignition of a high-current pulsed slipping discharge: (*1*) high-voltage electrode, (*2*) grounded electrode, and (*3*) high-voltage pulse.

1063-780X/04/3012-1012$26.00 © 2004 MAIK "Nauka/Interperiodica"

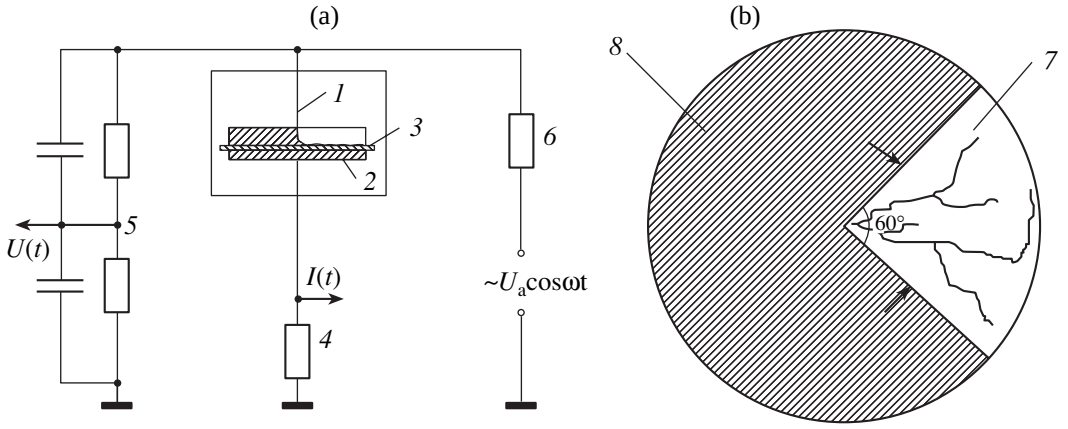

Fig. 2. (a) Electric circuit of the experimental device for studying a barrier corona in atmospheric-pressure argon: (*1*) needle, (*2*) plane electrode, (*3*) dielectric barrier (polymer film), (*4*) low-inductance current shunt, (*5*) voltage divider, (*6*) ballast resistance, (*7*) surface streamers, and (*8*) dielectric screen; (b) top view of the electrode system for igniting a limited surface discharge.

voltage is applied to the discharge gap and whether high voltage is applied to a point or to an elongated electrode. In the case of a unipolar voltage pulse, the streamers propagate along an uncharged dielectric surface, whereas in the case of ac voltage, the streamers propagate along a dielectric surface charged during the previous half-period of the applied voltage.

When operating with a long rod (or strip) electrode, a large number of closely spaced streamers can propagate from it in parallel to one another (see [9]). In this case, streamer branching can be suppressed. When using a needle (point) electrode placed above a dielectric surface, the branching of the surface streamers can be more pronounced (see, e.g., [8]).

In this study, which is a continuation of [7], we investigate the emission dynamics and spatiotemporal structure of an ac barrier corona in argon in a diffuse and a streamer modes in the needle-to-plane geometry. In contrast to conventional corona discharges, the metal plate in a barrier corona is covered with dielectric, which is an obstacle for a dc current.

2. EXPERIMENTAL SETUP

A schematic of the experimental setup is shown in Fig. 2. The experiments were performed with a cylindrical organic-glass discharge cell with an inner diameter of 200 mm and a height of 100 mm. A point-to-plane electrode system mounted inside the cell consisted of a 120-mm-diameter copper disc with rounded edges and a stainless-steel point electrode (needle) with a parabolically shaped end and a tip radius of 50 μm. The plane electrode was entirely covered with polyethylene, Teflon, or Mylar films or with dielectric plates. The film thickness was varied from 15 to 80 μm, the thickness of the dielectric plates was up to 1 mm. Generally, the distance between the point tip and the dielectric film (plate) was 0.5–1 mm.

In some experiments, a thick dielectric disk from which a 60° sector was cut out was glued to the dielectric film. The needle was shifted outward from the vertex of the sector by 5 mm along its bisectrix. The disk thickness slightly exceeded the distance between the needle tip and the film; the area available for the surface discharge was therefore limited by this sector. Such a reduction in the discharge area allowed us to improve spatial resolution when recording surface streamers with the help of an image tube. A 100-mm-diameter viewing window was mounted in the upper flange of the cell (above the discharge) to perform optical measurements.

A sinusoidal voltage was supplied to the needle trough the ballast resistance R = 300 kΩ. The voltage frequency was varied from 50 Hz to 30 kHz, and the voltage amplitude was up to 4.5 kV. The waveform and amplitude of the discharge voltage were recorded using a balanced *RC* voltage divider and a Tektronics TDS-520 and an S8-17 storage oscilloscopes. The signals from a low-inductive current shunt with a resistance of R_{sh} = 50 Ω were also supplied to these oscilloscopes. When measuring the current averaged over a half-period, the shunt was replaced with an arrow microammeter connected in series to the discharge gap through a diode that passed the current in either positive or negative half-periods. To prevent the microammeter from mechanical damages, it was set in parallel to a capacitor that passed the high-frequency component of the current.

In our experiments, we used high-purity argon (with a certified purity of 99.99%). All of the experiments were performed at a pressure slightly exceeding atmospheric pressure (P = 770 torr). Before each experiment, the discharge cell was pumped out to a pressure of $P = 10^{-3}$ torr and then filled with a working gas at a required pressure. To maintain the certified purity of argon, the experiments were carried out in a continuous gas-flow regime at a low gas flow rate.

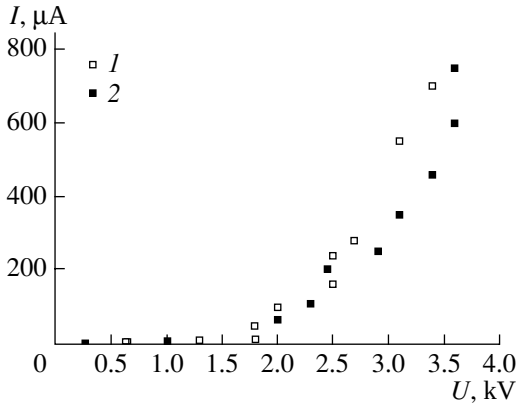

Fig. 3. The average current of a sector-limited barrier corona vs. voltage amplitude in (*1*) positive and (*2*) negative half-periods of the applied voltage (f = 1 kHz).

The structure of the surface streamers of a barrier corona was studied using an image tube operating in a frame mode. The frame exposure time was varied from 1 to 20 μs. The special electronic scheme enabled triggering the image tube during any discharge phase of interest. The image of the surface discharge was projected onto the image-tube photocathode with a 1 : 5 demagnification. The photographs of the discharge with a larger exposure time were taken using an Olympus E-100RS digital camera and a Zenit photographic camera.

The emission spectra of the surface streamers in argon were recorded using an MUM-2 monochromator with a 1200 groove/mm diffraction grating and an FEU-100 photomultiplier (with an operating wavelength range of 170–830 nm and a maximum sensitivity at $\lambda \sim 420$ nm) installed at the output of the monochromator. The surface discharge segments (20×0.5 mm^2 in size) from the three different discharge regions—the region around the needle, the middle part of the discharge at the distance of 25 mm from the needle, and the discharge periphery at the distance of 45 mm from the needle—were projected onto the entrance slit of the monochromator with a 1 : 2 demagnification. The photomultiplier signal was recorded in parallel with the discharge current.

3. EXPERIMENTAL RESULTS

3.1. Discharge Dynamics

The dependence of the discharge current I on the applied voltage U is called the current–voltage (I–V) characteristic of a discharge. In an ac barrier discharge, the current averaged over the oscillation period is close to zero; therefore, it is reasonable to introduce an I–V characteristic that relates the current averaged over a half-period $\langle I \rangle = \frac{2}{T}\int_0^{T/2} I(t)dt$ to the amplitude of the applied voltage U.

In the case of an ac surface discharge excited by a point electrode placed above a dielectric surface, the average current is determined by the capacitance of a distributed plasma capacitor formed by the discharge during one half-period of the applied voltage. It was shown in [7] that the area occupied by the plasma on the dielectric surface increases with the voltage amplitude. Hence, the current averaged over a half-period should be an increasing function of this amplitude. This is illustrated in Fig. 3, which shows the time-averaged I–V characteristics of a barrier corona in positive and negative half-periods of the applied voltage.

It is interesting that the above defined I–V characteristic of an ac barrier corona can be approximated by the same algebraic expression as the I–V characteristic of a conventional dc corona discharge [9], namely, $\langle I \rangle \cong kU(U - U_0)$, where $\langle I \rangle$ is the corona current averaged over a half-period, U is the amplitude of the applied voltage, and U_0 is the corona ignition (or extinction) voltage. In our case, the dimensional coefficient k is equal to $k = 0.11f$ (μA s)/kV^2, where f is the frequency of the applied voltage. Discovering the physical reasons for such a similarity between the ac barrier corona and the dc corona is beyond the scope of the present study.

In an ac barrier corona, the discharge structure on the dielectric surface varies continuously over time. Moreover, the details of this structure are functions of the voltage frequency and amplitude, as well as of the thickness and permittivity of the dielectric coating. However, it has been shown experimentally that, together with a chaotic behavior, the surface structure also exhibits regular features that are retained as the discharge parameters vary.

It was found that three ranges of the voltage amplitude U (all other factors being the same) corresponding to three characteristic discharge regimes can be distinguished. The first (low-voltage) range, $U_0 < U < U_1$, corresponds to the formation of a diffuse round spot on the dielectric surface. In the second range, $U_1 < U < U_2$, the discharge on the dielectric surface takes the shape of a rosette. In the third range, $U_2 < U < U_3$, all the discharge region is occupied by surface streamers. Here, U_1 and U_2 are certain boundary values of the voltage amplitude and U_3 is the voltage corresponding to the transition of the barrier corona into a spark mode, i.e., to the appearance of bright sparks on the dielectric surface. Within each of these ranges, the surface discharge in argon has a pronounced characteristic structure that correlates with the waveform of the discharge current.

Figure 4 shows a series of photographs and waveforms illustrating the aforesaid using, as an example, a surface discharge excited by a point electrode above a 1-mm-thick organic-glass plate. The figure demonstrates how (a) the discharge structure averaged over many discharge periods (i.e., the structure on the dielectric surface that is seen with the naked eye), (b) the current and voltage waveforms, and (c, d) the instantaneous discharge structures taken by an image

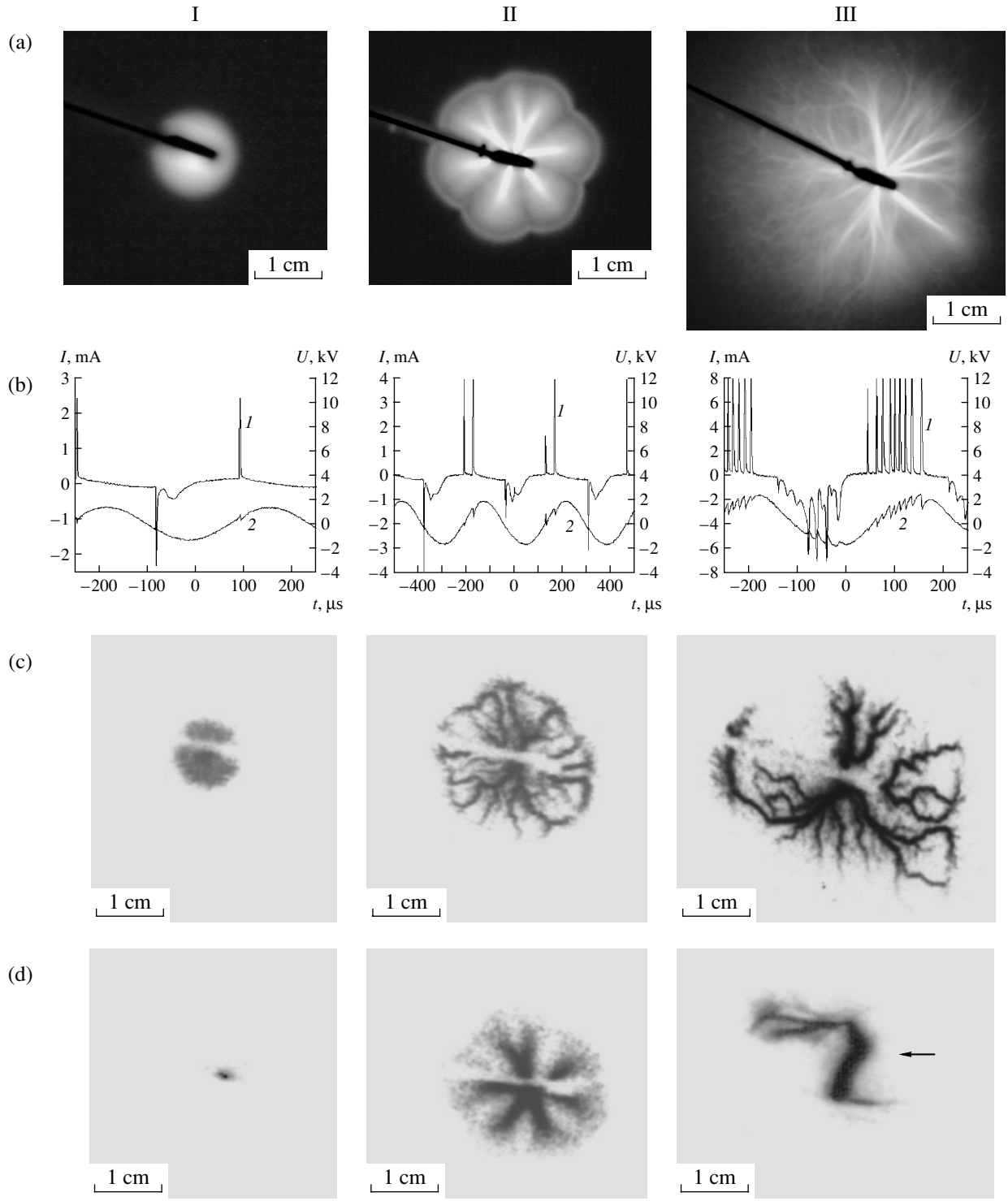

Fig. 4. Photographs (top view) and waveforms of the discharge current and voltage illustrating the evolution of a barrier corona discharge with increasing voltage amplitude. The dielectric barrier is an organic-glass plate of thickness $d = 1$ mm. The frequency of the applied voltage is $f = 3$ kHz. The center of each photograph corresponds to the discharge axis (the position of the needle). (a) The time-averaged structure of a surface barrier corona discharge recorded with a digital camera (positive images). The black strip at the centers of the photographs is the shadow of the point electrode holder. (b) The current (curves *1*) and voltage (curves *2*) waveforms corresponding to the three regimes of a barrier corona discharge. (c) Electron-optical photographs of a barrier corona discharge in a positive half-period (negative images). The exposure times are $\tau = 20$ (I, II) and 10 (III) μs. The white strip at the centers of the photographs is the shadow of the point electrode holder. (d) Electron-optical photographs of a barrier corona discharge in a negative half-period (negative images). The arrow in Fig. 4d(III) indicates the plasma strip that has developed from the rosette's spoke. The exposure time is $\tau = 20$ μs.

tube with a short exposure time in the positive and negative half-periods of the applied voltage vary with increasing U.

3.1.1. Range I: $U_0 < U < U_1$. In this voltage range, the surface discharge on the dielectric surface is seen with the naked eye as a round diffuse spot with a diameter of no more that 1 cm (Fig. 4a(I)). However, photographs taken with the image tube show that the time evolution of the discharge is more complicated. Information about this evolution can be derived from comparing current waveforms with electron-optical images of the discharge at different instants within the positive and negative half-periods of the barrier corona.

It was found that, during a positive half-period, the round diffuse plasma spot exists over a very short time (no longer than 5 μs) after the appearance of a spike in the current waveform in the stage when the voltage increases (see Figs. 4b(I), 4c(I)). Neither before nor after this short time interval was any emission of the surface discharge observed. Thus, during the current spike, the negative charge accumulated on the dielectric surface in the preceding negative half-period is neutralized and a positive charge of the same magnitude is accumulated on the dielectric surface.

During the current spike, a generation zone arises near the positively charged point electrode. This zone persists throughout the entire current spike and allows the electron current to flow through the entire discharge surface.

Quite another behavior is observed in the negative half-periods. The generation zone near the point electrode (the cathode sheath of a negative corona) also arises during the current spike. However, during the negative half-period, the generation zone persists almost over the entire stage in which the voltage increases (i.e., over about 150 μs). In such a situation, the positive charge accumulated on the dielectric surface in the preceding positive half-period is neutralized and a negative charge of the same magnitude is accumulated on the surface at a much slower rate. Accordingly, the conduction current is much lower than in the positive half-periods. In the negative half-periods, the maximum value of the slowly varying conduction current increases with the voltage amplitude and frequency. Since the density of the current flowing through the surface plasma is lower than that in the positive half-periods, the emission intensity is also lower. Indeed, electron-optical images taken in the negative half-periods demonstrate the presence of a bright cathode glow near the point electrode during the entire stage in which the voltage increases (over ≈150 μs). Simultaneously, a faint diffuse glowing spot appears on the dielectric surface (Fig. 4d(I)]) and then expands up to the size of the plasma spot observed in the positive half-periods.

3.1.2. Range II: $U_1 < U < U_2$. As the amplitude of the applied voltage reaches the first boundary value U_1, the discharge passes into the second regime. In this regime, the discharge area becomes much larger than in the first regime and the discharge structure that is seen with the naked eye takes the shape of a stable and spatially symmetric rosette with quite a sharp boundary (Fig. 4a(II)).

Both the diffuse (the rosette petals) and contracted (spoke) forms of a discharge can be seen on the dielectric surface. The spoke length increases with the amplitude of the applied voltage, whereas the number of spokes is a function of the voltage frequency and the thickness and permittivity of the dielectric coating. The lower the frequency, the narrower the $[U_1, U_2]$ interval (up to its complete disappearance). For example, at a frequency of $f = 400$ Hz, regime II does not occur and the discharge passes directly into regime III.

A comparison of the current waveforms with electron-optical images reveal a more complicated picture of the discharge dynamics than is seen with the naked eye. The number of current spikes in the positive half-periods increases (up to two or three spikes). Each of these spikes corresponds to corona ignition and the formation of a short-lived (with a lifetime of no more than 5 μs) generation zone near the positively charged point electrode. In this stage, many streamers begin to propagate simultaneously from the point electrode (Fig. 4c(II)) not going beyond the rosette petals. After reaching the periphery of the rosette, the streamers suddenly change their propagation direction and begin to move along the rosette's boundary. This is why the rosette's boundary in time-integrated photographs is so sharp. That streamers are not able to penetrate beyond the rosette's boundary is most likely related to the conservation (in both half-periods) of the discharge area on which the surface charge accumulated in the preceding half-period is neutralized and a new charge of opposite sign appears.

The number of primary streamers (i.e., those that started from the point electrode and have not yet undergone branching) is seemingly no larger than the number of the rosette's petals. It can be seen in electron-optical photographs that the space between the positive streamers is filled with a diffuse plasma. An analysis of the current waveforms and electron-optical images show that, during the positive half-period, the surface discharge is glowing for only about 5 μs after each current spike. Over the rest of the time, the conduction current is very low and, accordingly, the discharge glow is almost absent.

In the negative half-periods, there is only one current spike corresponding to the origin of the cathode sheath near the point electrode. In this case, as in regime I, the cathode sheath persists during the entire stage in which the voltage increases. One of the electron-optical photographs of a surface discharge taken in regime II is shown in Fig. 4d(II). One can see that the discharge structure is more symmetrical but is also more blurred, compared to that in the positive half-periods. The spokes and diffuse rosette petals are more pro-

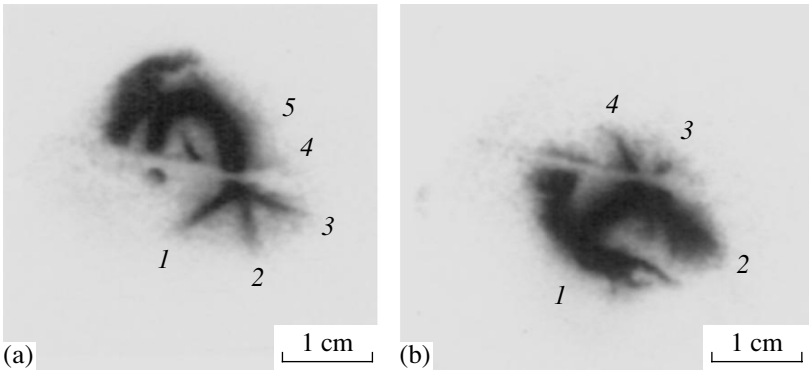

Fig. 5. Electron-optical photographs of a surface discharge at the instant corresponding to the transition from the rosette to the streamer phase. The exposure time is $\tau = 20$ μs. The frequency of the applied voltage is $f = 3$ kHz. Each photograph is a superposition of the discharge images taken over 17 μs before and 3 μs after the current spike (including the spike itself). The rosette spokes corresponding to the first 17 μs and the plasma strips corresponding to the last 3 μs are seen. The center of each photograph corresponds to the discharge axis (the position of the needle). The white strip at the centers of the photographs is the shadow of the point electrode holder. (a) The formation of one plasma strip from spoke no. 5 and (b) the formation of two plasma strips from spoke nos. 1 and 2.

nounced. By the end of the negative half-period, the rosette grows to its maximum size.

3.1.3. Range III: $U_2 < U < U_3$. When the barrier corona switches to regime III, the regular structure on the dielectric surface disappears. The time-averaged picture of a discharge that is seen with the naked eye is shown in Fig. 4a(III). It can be seen that the surface discharge consists of a large number of streamers of different size and a diffuse plasma that occupies the space between the streamers.

In regime III, the number of current spikes within a positive half-period increases greatly and, most important, current spikes also appear during negative half-periods (Fig. 4b(III)). At a fixed amplitude and frequency of the applied voltage, the number of current spikes in positive and negative half-periods is not constant and varies from half-period to half-period, especially for negative half-periods. The average number of spikes in both positive and negative half-periods increases with the amplitude of the applied voltage. Generally, the number of spikes in a positive half-period is larger than in a negative one.

It can be seen from electron-optical photographs that any current spike in a positive half-period corresponds to the emergence from the point electrode of a bunch of streamers surrounded by a diffuse plasma. The streamer bunch is asymmetric and consists of a few large primary streamers that branch out into a lot of side streamers. The shape of the streamer bunch is not repeated from spike to spike; however, on the whole, the streamers and the diffuse plasma cover all of the area on which the charge was accumulated during the preceding negative half-period. Between the current spikes, the conduction current and the surface discharge glow are almost absent.

The electron-optical photographs and current waveforms indicate that, in negative half-periods, both the surface discharge glow and the conduction current persist during the entire stage in which the voltage increases. A specific feature of regime III is the appearance of sharp current spikes during these half-periods. Each current spike is accompanied by the emergence from the point electrode of one (sometimes two) wide (with a visible width of about 3 mm) bright 2- to 3-cm-long plasma strip near the end of which one can see a bunch of more narrow streamers (Fig. 4d(III)). The bright plasma strip and the streamers are surrounded by a faintly glowing diffuse plasma. The propagation direction of the plasma strip along the surface and the streamer configuration are not the same from spike to spike; however, on the whole, the streamer and the diffuse plasma cover all the area on which the positive charge was accumulated during the preceding positive half-period.

In regime III, current spikes in negative half-periods arise not immediately after the initial pulse corresponding to the ignition of a negative corona (i.e., the formation of a cathode sheath at the point electrode). It can be seen from the current waveforms in Fig. 4b(III) that the large current spike (with an amplitude of about 100–200 mA) is preceded by two to three small spikes.

One can see from electron-optical images of the discharge that the current spike is preceded by the aforementioned rosette structure. One (sometimes two) of the rosette's spokes transform into a bright plasma strip. Such behavior can be seen in Fig. 5, which presents two images of the surface discharge taken with an exposure time of 20 μs. Each image is a superposition of the discharge images taken during 17 μs before and 3 μs after the current spike (including the spike itself). The center of each photograph corresponds to the discharge axis, i.e., to the position of the point electrode. The rosette

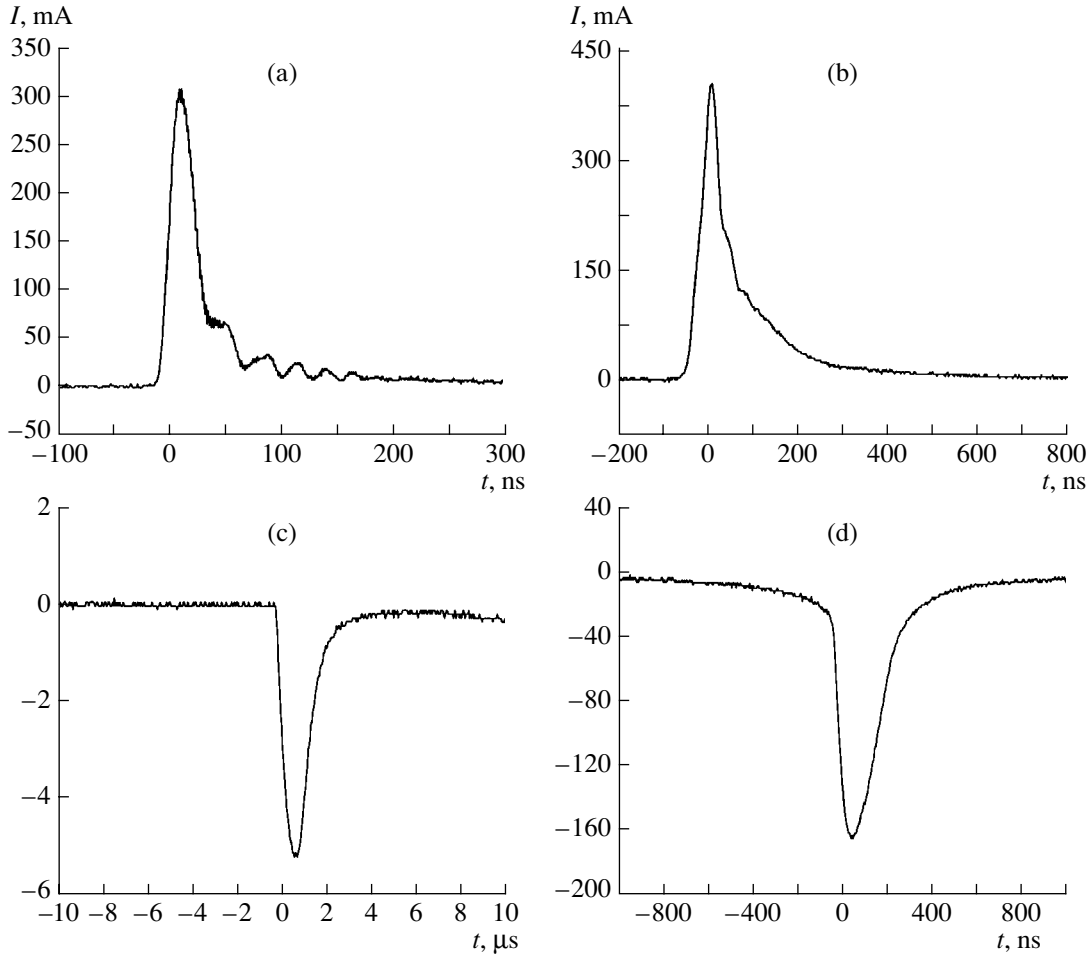

Fig. 6. Nanosecond-scale waveforms of the current spikes of a barrier corona in a positive and a negative half-periods of the applied voltage (f = 3 kHz). The dielectric barrier is a 100-μm Mylar film. (a) The first current spike in a positive half-period (regime II), (b) the fourth current spike in a positive half-period (regime II), (c) the first current spike in a negative half-period (regime II), and (d) an example of a current spike in a negative half-period (regime III).

spokes and the diffuse plasma surrounding them are seen in both images. One can see that, in Fig. 5a, a bright plasma strip is formed from the upper spoke, whereas Fig. 5b shows two bright strips formed from two lower spokes.

Nanosecond-scale waveforms of the current spikes in both half-periods are presented in Fig. 6. The structure of the first current spike in a positive half-period is shown in Fig. 6a. The spike amplitude is 300 mA, and the rise time (at a level of 10 to 90% of the spike amplitude) is 12 ns. At the trailing edge of the spike, the current rapidly (over 125 ns) decreases from 300 mA to 10 mA and then slowly (over 5–10 μs) decreases to a quasi-steady level of 0.1 mA. The shapes of the subsequent spikes is qualitatively the same, but their amplitudes and the full widths at half-maximum (FWHM) are somewhat larger. Thus, Fig. 6b presents the waveform of the fourth spike. Its amplitude is 400 mA and the rise time is 40 ns. The time during which the current decreases from 400 mA to 10 mA is 300 ns, while the time during which the current decreases slowly from 10 to 0.1 mA is 5–10 μs.

The waveforms of the current spikes in a negative half-period are shown in Figs. 6c and 6d. The amplitude of the first spike is as low as 5 mA (Fig. 6c), which is much lower than that in the positive half-period; however, its rise time (600 ns) and the time during which the current decreases from 5 to 1 mA (2 μs) are much longer than those in the positive half-period. The time during which the current slowly decreases to a level of 0.1 mA (about 5 μs) is approximately the same as in the positive half-period.

The amplitudes of the negative current spikes in regime III (Fig. 6d) are much higher (160 mA) than that of the initial current pulse corresponding to the ignition of a negative corona, whereas their rise and fall times (140 and 300 μs, respectively) are shorter as compared to those of the initial current pulse. The characteristic time during which the current decreases slowly from

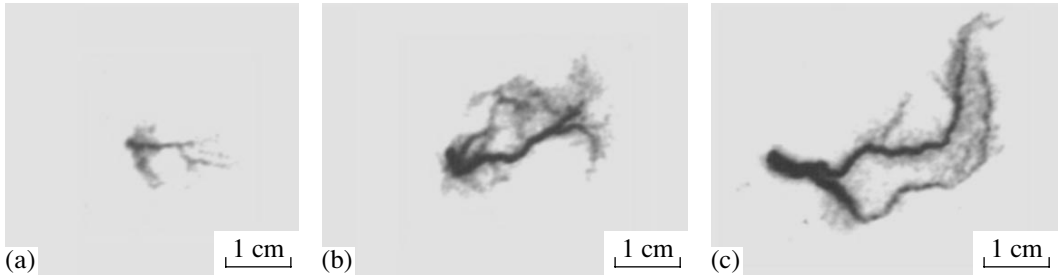

Fig. 7. Electron-optical photographs of a sector-limited barrier corona in argon in a positive half-period of the applied voltage. The voltage frequency and amplitude are f = 1 kHz and U_a = 3.5 kV, respectively. The exposure time is τ = 20 μs. The discharge images are formed by the (a) first, (b) fifth, and (c) tenth current spikes.

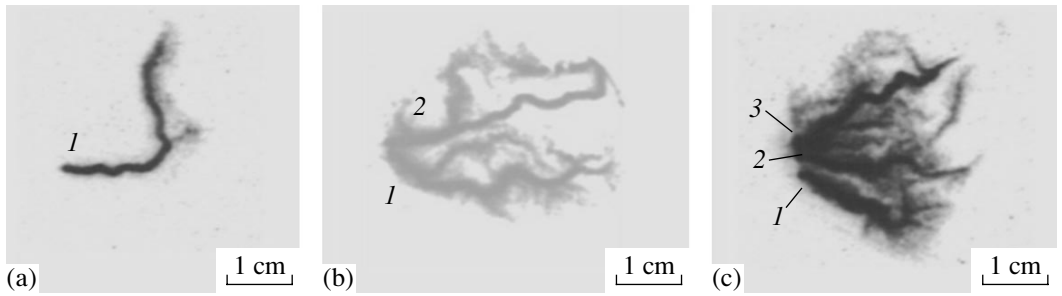

Fig. 8. Electron-optical photographs of a sector-limited barrier corona in argon in a positive half-period of the applied voltage. The voltage frequency and amplitude are f = 3 kHz and U_a = 3 kV, respectively. The exposure time is τ = (a, b) 10 and (c) 20 μs. The number N of the streamers formed in the discharge during these exposure times is N = (a) 1, (b) 2, and (c) 3. The numerals indicate the sequence numbers of the streamers.

10 to 0.1 mA is approximately the same for all the spikes and amounts to 5–10 μs.

The limitation of the area accessible for a surface discharge by a sector lead to certain qualitative changes in the discharge structure. Let us illustrate this using the structure of a limited surface discharge operating in the streamer mode as an example. In these experiments, we used a thinner dielectric barrier (a 100-μm-thick Mylar film).

An analysis of the current waveforms of a limited surface discharge shows that the main parameters of the current spikes in both half-periods are nearly the same as those in an unlimited discharge. The amplitude of the current spikes varies in the range 0.2–0.6 A, and their FWHM is about 100–300 ns, whereas their rise time is approximately five to ten times shorter than in an unlimited discharge. At the trailing edge, the current drops to 8–15 mA over 100–300 ns and then slowly (over 5–10 μs) decreases to a quasi-steady level.

Figure 7 presents electron-optical photographs of a limited barrier corona in a positive half-period. The exposure time of each photograph is 20 μs. The time intervals during which each electron-optical photographs were taken contained only one current spike; i.e., each photograph shows a discharge image formed by a single current spike, namely, by the first (Fig. 7a), fifth (Fig. 7b), or tenth (Fig. 7c) spike.

One can see that, like in an unlimited discharge, the surface streamer is surrounded on all sides by a diffuse glow that occurs both near and far from the streamer. The glow intensity and the streamer length, as well as the area occupied by the diffuse glow around the streamers, increase with the voltage. The absence of traces produced by the streamers and by the diffuse plasma in preceding current spikes indicates that the glow time of the surface streamers and the diffuse plasma is rather short, no longer than 10 μs, which is in good agreement with the fall time of the current spikes.

Figure 8 presents another series of electron-optical photographs taken in a positive half-period (approximately in the middle of the spike train) of a sector-limited discharge. Each photograph shows a discharge image formed by the different number of current spikes: (a) a single (sixth) spike, (b) two consecutive (sixth and seventh) spikes, and (c) three consecutive (sixth, seventh, and eighth) spikes.

It can be seen from Figs. 7 and 8 that, in a limited discharge (in contrast to an unlimited one), each current

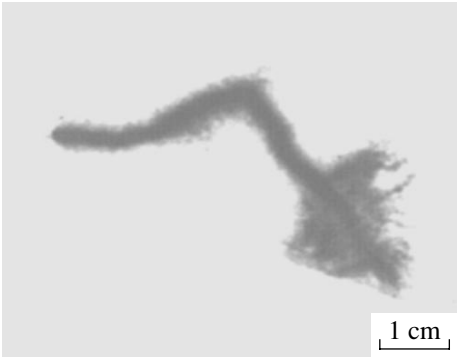

Fig. 9. Electron-optical photograph of a sector-limited barrier corona in argon in a negative half-period of the applied voltage (streamer mode). The voltage frequency and amplitude are $f = 3$ kHz and $U_a = 3$ kV, respectively. The exposure time is $\tau = 20$ μs. The discharge image is formed by the fifth current spike.

spike corresponds to a single primary streamer, which then propagates along a twisted trajectory along the surface and undergoes branching. Each subsequent streamer propagates along its own trajectory rather than along the trajectory of the preceding streamer. It was also found that positive streamers did not follow the trajectories of negative streamers.

Figure 9 shows an electron-optical photograph of a limited barrier corona in a negative half-period at a frequency of $f = 3$ kHz. The glow intensity of the negative streamers is appreciably higher than that of the positive ones. For this reason, the photographs of the negative streamers were taken with a smaller aperture of the image-tube objective. The exposure time was 20 μs. The photograph shows the image of the surface discharge formed by the fifth current spike. One can see a wide bright streamer (which resembles a plasma strip in an unlimited discharge) with a large-area diffuse glow around the streamer head and a lot of thin streamers emerging from the head in different directions. Note that such behavior in some respects resembles the propagation of a leader, in front of which a fan of streamers also arises. The diffuse glow is less pronounced far from the negative streamer, although special experiments reveal its existence. The absence of the traces of the negative streamers formed during the preceding current spike also indicates that their glow time is rather short (shorter than the time interval between two consecutive spikes), which agrees with the fact that the current decay time is no longer than 10 μs.

The length of the negative streamers increases with the voltage; however, they are generally shorter than the positive streamers. In argon, the length of the surface streamers can exceed 10 cm, whereas their trajectory can be quite intricate, which leads to amazing effects. Electron-optical photographs of the streamers propagating from a point electrode show that, as the streamer propagates and branches, it can not only to move away from the point electrode (which seems to be quite reasonable) but also to approach it when moving along a curved trajectory. Such behavior has never been observed for volume and surface streamers propagating perpendicularly to a long rod electrode.

An analysis of the electron-optical photographs shows that the diffuse plasma that exists together with the streamers is nonuniformly distributed over the dielectric surface: it is concentrated within individual domains, in which the distribution of the glow intensity is also nonuniform. Beaded structures in which the streamers alternated with diffuse plasma regions were often observed (see, e.g., Fig. 8b). In such structures, either several diffuse plasma regions were connected by streamers or, vice versa, a streamer was broken with diffuse plasma regions. Such a structure can also be interpreted as an irregular surface contraction of the diffuse plasma.

3.2. Statistical Characteristics of the Surface Streamers

Statistical characteristics of surface streamers (such as the mean free path of a streamer from one branch point to the next, the dependence of this mean free path on the sequence number of the branch point and the frequency of the applied voltage, the average number of branch points in a single streamer that started from the point electrode, and the average number of branchings per branch point) are of great interest. To determine these characteristics, we processed many electron-optical images of limited discharges similar to those shown in Figs. 7–9.

Figure 10 shows the normalized distributions of the positive and negative surface streamers, $F(i) = N_i/N_\Sigma$, over the number i of their branch points at different frequencies of the applied voltage (here, N_Σ is the total number of the recorded streamers that started from the point electrode and N_i is the number of the streamers that underwent i branchings).

One can see that the branching parameters are approximately the same (to within the statistical error) for negative and positive streamers and depend only slightly on the voltage frequency. The average number of branch points in an initial streamer is small: from 0.8 to 1.35 (i.e., approximately one branch point per streamer). The fraction of streamers that undergo more than three (from four to six) branchings is very low ($\leq 1\%$).

Figure 11 shows the dependences of the streamer mean free path between two consecutive branch points on the frequency of the applied voltage in (a) positive and (b) negative half-periods. Here, l_{01}, l_{12}, and l_{23} stand for the streamer mean free paths between the point electrode and the first branch point, between the first and the second branch points, and between the second and the third branch points, respectively. In other words, the

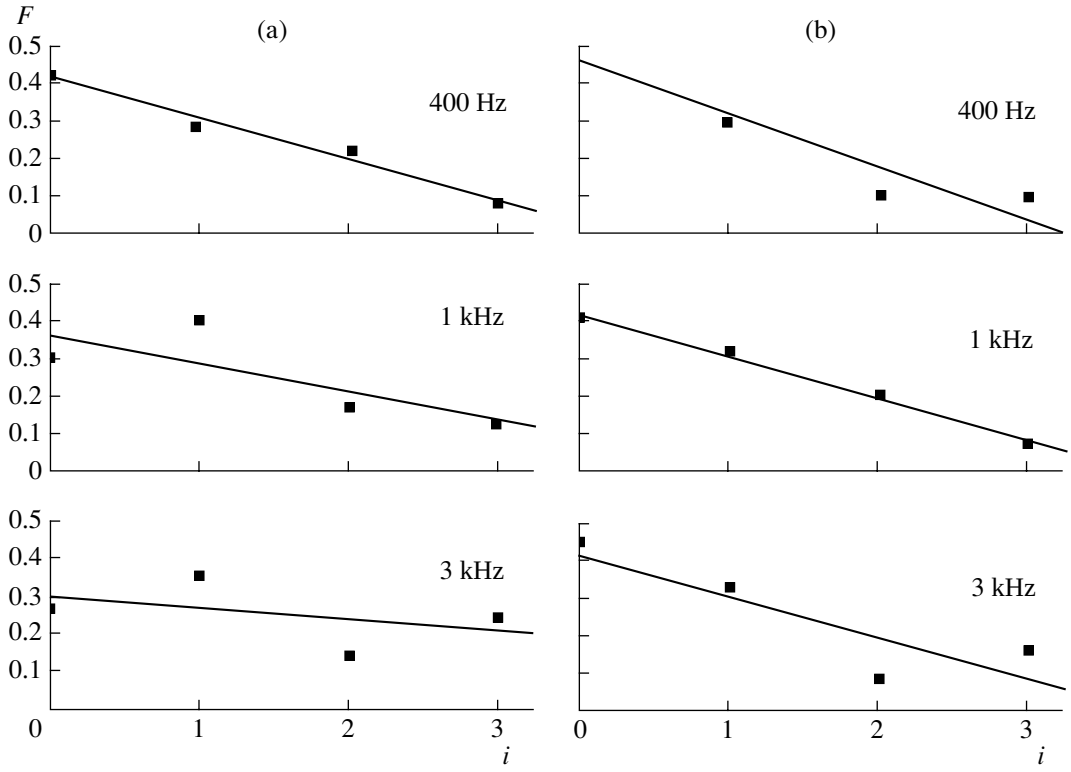

Fig. 10. Normalized distribution $F = N_i/N_\Sigma$ of the (a) positive and (b) negative surface streamers in argon over the number i of their branch points for different frequencies of the applied voltage. Here, N_Σ is the total number of the recorded streamers that started from the point electrode and N_i is the number of the streamers that underwent i branchings. The voltage amplitude is U_a = 3.5 kV.

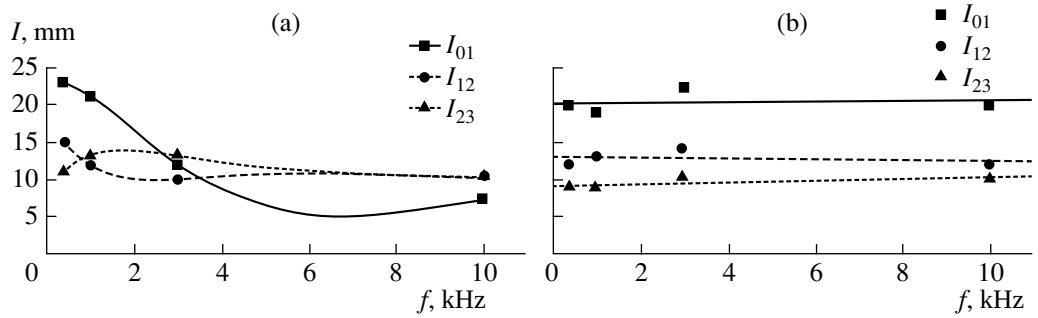

Fig. 11. The mean free path of a surface streamer between two consecutive branch points vs. voltage frequency f in a sector-limited barrier corona in (a) positive and (b) negative half-periods. The voltage amplitude is U_a = 3.5 kV. Here, l_{01}, l_{12}, and l_{23} stand for the streamers of different generations.

figure shows the distribution of the mean free paths of the streamers of different generations.

We can see that, in both half-periods, the streamers of the first generation have the longest mean free path (about 2 cm) and, at frequencies lower than 3 kHz, are approximately twice as long as the streamers of the second and third generations ($l_{01} \cong 2l_{12}$ and $l_{01} \cong 2l_{23}$). In negative half-periods, such a ratio between the streamer lengths was observed at all the frequencies under study (up to 10 kHz).

To within statistical scatter, the lengths of the second- and third-generation streamers are the same ($l_{12} \cong l_{23} \approx 1$ cm) in both half-periods and are almost independent of the frequency. In positive half-periods, at frequencies higher than 3 kHz, the length of the first-generation streamers becomes equal (to within the same

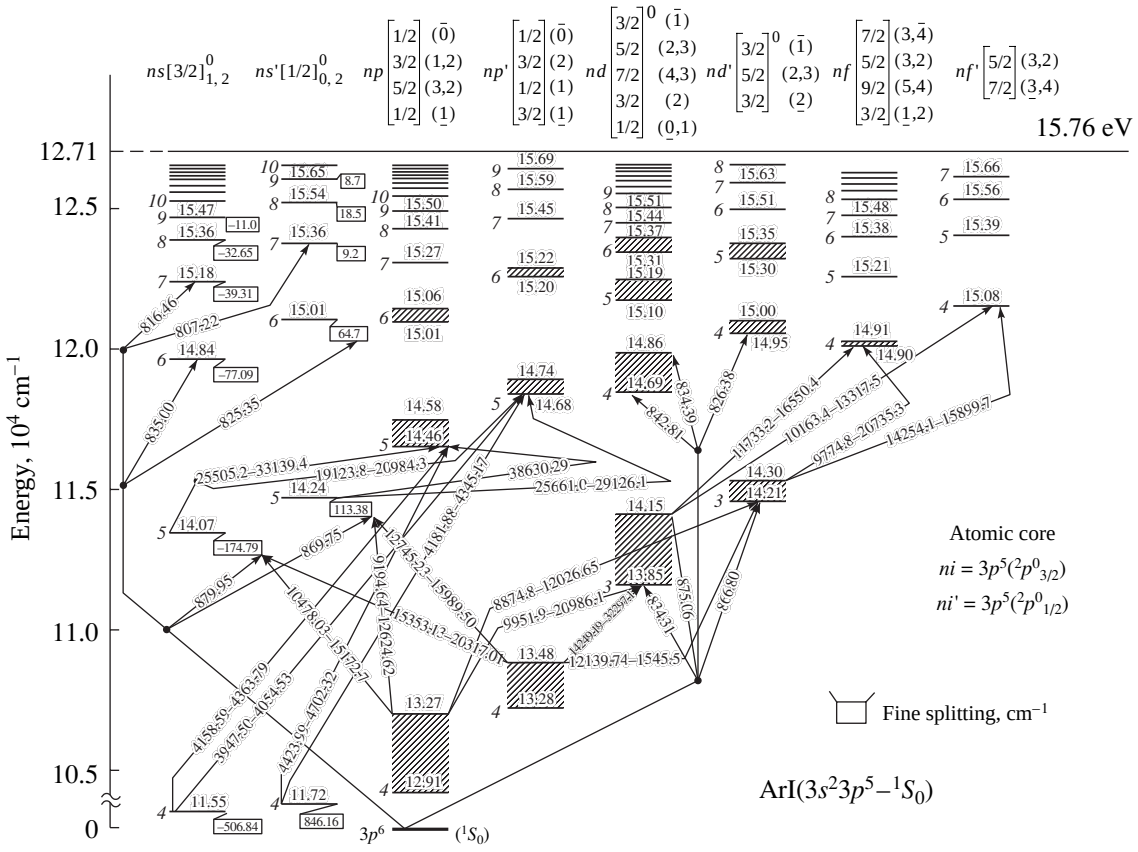

Fig. 12. Diagram of the energy levels, the emission spectra, and the oscillator strengths of different transitions for an argon atom [10].

accuracy) to the lengths of the second- and third-generation streamers.

In most of the branch points, a streamer splits into two daughter streamers. The fraction of the branch points in which three daughter streamers are formed does not exceed 5%. The angle α between the daughter streamers varies in a wide range from 10° to 110°.

Thus, we can conclude that the visual difference between positive and negative half-periods is mainly related to the different number of streamers in these half-periods rather than to the different properties of branching: in positive half-periods, each current spike corresponds to a new streamer, whereas in negative half-periods, there is typically only one streamer which then undergoes branching.

3.3. Emission Spectrum of a Barrier Corona in Argon

Spectroscopic studies can provide important data on the parameters of the diffuse and streamer plasmas. An analysis of the emission spectrum from a sector-limited barrier corona in the visible and UV spectral regions shows that the plasma of a surface discharge in argon is an efficient source of emission in various argon atomic lines. In atmospheric-pressure argon, intense VUV emission of argon dimers at $\lambda \approx 110$ and 126 nm is also feasible; however, in our experiments, such emission was not recorded.

The most intense emission is concentrated in the red wing of the spectrum in the Ar atomic lines with λ = 810.4 and 811.5 nm, corresponding to the $4P \longrightarrow 4S$ transitions [10] (see Fig. 12). There are also many atomic lines with an appreciable emission intensity in the blue–green spectral region (λ = 350–500 nm). Here, the most intense lines are those with wavelengths of λ = 416.4 and 426.6 nm (the $4P \longrightarrow 4S$ transitions). Their emission intensities in negative half-periods are approximately twice as high as those in positive half-periods.

In a barrier corona, there is also fairly intense emission from Ar^+ atomic ions. Here, the most intense lines are those with wavelengths of λ = 480.6, 484.8, and 488.0 nm (the $4P \longrightarrow 4S$ transitions). Their emission intensities are approximately equal to one another. As in the case of argon atomic emission, the intensities of the ion lines in negative half-periods are nearly twice as high as those in positive periods and are almost inde-

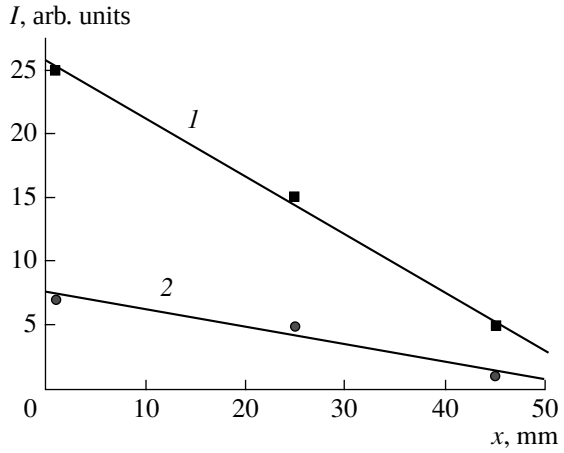

Fig. 13. Time-averaged intensity of the (*1*) 426.6-nm and (*2*) 488.0-nm line emission from a sector-limited barrier corona in argon vs. distance from the discharge axis. The voltage frequency and amplitude are f = 400 Hz and U_a = 3.5 kV, respectively.

pendent of the frequency of the applied voltage. The emission intensities of all the lines under study (both atomic and ionic) normalized to the intensity of the 416.4-nm line (the $5P \longrightarrow 4S$ transition) are

$$I_{416.4} : I_{426.6} : I_{565.1} : I_{310.0} : I_{810.4} : I_{811.5} : I_{480.6} : I_{484.8} : I_{488.0}$$
$$= 1 : 0.7 : 0.1 : 4 : 1.5 : 4 : 0.18 : 0.15 : 0.21.$$

We compared our results with the table data on the emission intensities of different lines [11]. It turned out that the intensity of the 565-nm line (the $5D \longrightarrow 4P$ transition) in a barrier corona is very low, approximately five times lower than the intensity of the 426.6-nm line, although the table [11] shows that their intensities are nearly the same. In contrast, the rather weak (according to [11]) 310-nm line (the $8F \longrightarrow 4S$ transition) turned out to be quite intense under conditions of a barrier corona. (Note that, in [11], the data on the emission intensities of the atomic and ionic lines from discharges excited in a Geissler tube are presented.)

Our experiments showed that the time-averaged emission intensities I_λ of all the spectral lines under study monotonically decreased with distance from the point electrode. As an illustration, Fig. 13 shows the dependences of the emission intensities I_λ at λ = (*1*) 426.6 and (*2*) 488.0 nm on the distance r from the point electrode in negative half-periods. It can be seen that, in spite of the axial geometry of a surface discharge, the averaged intensity I_λ is not proportional to $1/r$.

The time evolution of the emission intensity in different lines from different regions of a discharge is also of great interest. Figure 14 presents waveforms of the barrier corona current during a negative half-period together with the time behavior of the intensity of the 416.4-nm line emitted from a region located a distance of 25 mm from the point electrode. Since the trajectories of negative streamers in different current spikes were close to one another, the observational zone (20 mm in size) covered all possible trajectories of the negative streamers within the discharge region under study. Thus, all streamers definitely passed through the observational zone.

One can see (Fig. 14a) that the first emission pulse in the observational zone occurred at the instant corresponding to the fourth current spike. The number of the current spikes after which the first emission pulse occurs is a function of the voltage frequency and amplitude. Such a delayed emission agrees with electron-optical photographs, which show that the length of a negative streamer increases in a stepwise manner from spike to spike. From this time delay (of about 50 μs), we can estimate the average velocity of the stepwise propagation of a negative streamer as $V_{st} \cong 2 \times 10^4$ cm/s,

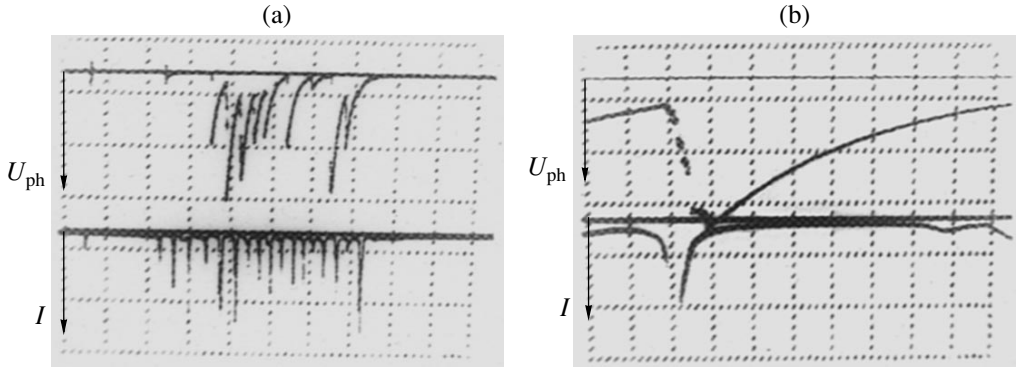

Fig. 14. Waveforms of the current I and the emission signal U_{ph} (λ = 416.4 nm) in a negative half-period of a sector-limited barrier corona in argon. The emission was recorded from a region located a distance of 25 mm from the point electrode. The voltage frequency and amplitude are f = 400 Hz and U_a = 3.5 kV, respectively. The current scale is 20 mA/division, the voltage scale is 5 mV/division, and the time scale is (a) 50 and (b) 2 μs/division.

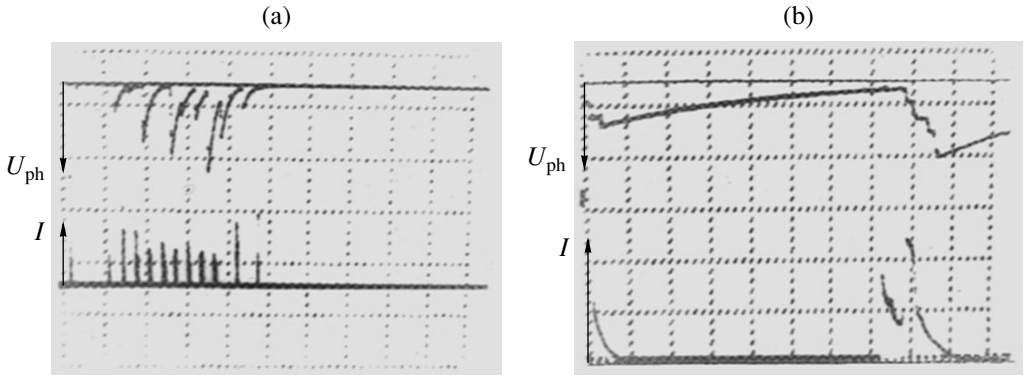

Fig. 15. Waveforms of the current I and the emission signal U_{ph} (λ = 416.4 nm) in a positive half-period of a sector-limited barrier corona in argon. The emission was recorded from a region located a distance of 25 mm from the point electrode. The voltage frequency and amplitude are f = 400 Hz and U_a = 3.5 kV, respectively. The current scale is (a) 100 and (b) 20 mA/division, the voltage scale is 5 mV/division, and the time scale is (a) 50 and (b) 2 μs/division.

although the actual propagation velocity of a negative streamer is much higher ($V_- \cong 10^8$ cm/s), because, in each current spike, the streamer starts from the point electrode.

The number of emission pulses recorded at a great distance from the point electrode turns out to be lower than the number of the current spikes. However, in the immediate vicinity of the point electrode, the numbers of the emission pulses and current spikes are equal to one another. Hence, some streamers corresponding to low-amplitude current spikes do not reach the observational zone.

In the case of positive streamers (Fig. 15a), the time delay between the first current spike and the arrival of the first streamer to the observational zone is almost absent; i.e., each current spike corresponds to its own fast streamer propagating with a velocity of $V_+ \cong 2 \times 10^8$ cm/s (which is about twice as high as that of a negative streamer) over a large distance from the point electrode. In positive half-periods, the number of the emission pulses recorded at a large distance from the point electrode is also less than the number of the current spikes, but for another reason.

As was noted above, positive streamers do not follow the same trajectory: they are more or less uniformly distributed over the dielectric surface. On the other hand, the observational zone covered only a fraction (about one-half) of all the possible trajectories of the positive streamers. Most likely, this is the reason why the number of the current spikes was not equal to the number of the emission pulses.

Another amazing feature of the surface streamers was found in experiments on studying their emission dynamics. It was found (see Figs. 14b and 15b) that the maximum intensity of the streamer emission (both in positive and negative half-periods) was reached much later than the maximum of the current spike corresponding to this streamer; i.e., the emission intensity of the streamer kept increasing after the streamer current had already passed its maximum and rapidly decreased. The corresponding time delay was about 2 μs, whereas the FWHM of the current spike was about 0.1–0.2 μs. Note that we also observed the long-term (lasting over 10–20 μs) afterglow of the positive and negative streamers.

4. DISCUSSION

The evolution of the slowly varying current of a diffuse barrier corona in negative half-periods (regime I) can be described using the experimental fact that the radius r of the area occupied by the diffuse plasma of a surface discharge increases linearly with the applied voltage $U(t) = U_a \sin\omega t$: $r = a(U - U_0)$, where a is a dimensional proportionality coefficient (e.g., for f = 1 kHz, we have a = 2.2 cm/kV) and U_0 is the corona ignition voltage. The capacitance of the barrier covered with the diffuse plasma is $C = c_1 \pi a^2 (U - U_0)^2$, where c_1 is the specific (per unit area) barrier capacitance, and the charge accumulated on the barrier is $q = CU$. Hence, the discharge current, which is equal to the time derivative of the charge, is

$$I(t) = \pi a^2 c_1 U_a^3 \omega \cos\omega t \left(\sin\omega t - \frac{U_0}{U_a}\right)\left(3\sin\omega t - \frac{U_0}{U_a}\right). \quad (1)$$

Current waveform (1) is close to the one experimentally observed; moreover, this expression provides a qualitatively correct description of the parametric dependences of the quasi-steady current of a diffuse surface discharge on the amplitude and frequency of the applied voltage.

In a streamer regime, the area occupied by the streamers on the dielectric surface and the streamer lifetime are too small for the streamers to carry the total

current of the barrier corona. Hence, the current in the streamer regime can be closed as follows: first, the streamer rapidly propagates along the surface and the high potential of the point electrode spreads over the entire streamer length; a nearly planar ionization wave then propagates slowly from the streamer side surface and covers a large area on the dielectric surface, thus allowing the main corona current to flow through the corona.

The propagation of the ionization wave, which leaves a diffuse plasma behind its front, can be regarded as the propagation of a charging wave along the dielectric surface. This leads to the charging of a progressively increasing barrier capacitance through the distributed plasma resistance. This process is analogous to the charging of an infinite sequence of discrete *RC* cells in which the capacitance of any subsequent cell begins to be charged only when the capacitance of the previous cell has already been charged to a certain threshold voltage U^*. The presence of such a threshold voltage makes the propagation of the ionization wave substantially different from the propagation of an ordinary charging wave along a chain of distributed or discrete *RC* cells. This is related to the existence of a critical electric field (or a reduced electric field E/N) that must be present at the front of the ionization wave for it could propagate.

The propagation time of such a wave is limited, on the one hand, by the plasma decay time and, on the other, by the plasma lifetime in the streamer from which the plane ionization wave propagates. The characteristic time between current spikes is 10–30 μs. It is known [12] that, in atmospheric-pressure argon, the most abundant ions are the molecular Ar_2^+ ions. The coefficient of dissociative recombination of these ions is about 10^{-7} cm^3/s. One can readily estimate that, within the above time interval, the plasma density holds at a fairly high level of no lower than 3×10^{11} cm^{-3}.

Let us consider a simple model that does not claim to quantitatively describe the experimental results but provides a reasonable qualitative picture of the phenomenon observed. We assume that a uniform plasma sheet with a thickness δ and time-independent conductivity σ is formed behind the front of a plane ionization wave. In this case, the specific resistance of the plasma sheet per unit width, R_0, increases linearly with the sheet length x:

$$R_0(x) = \frac{x}{\delta\sigma}. \tag{2}$$

The capacitance (per unit width) C_0 of a barrier region of length Δx in front of the ionization wave is $C_0 = c_1\Delta x$, where $c_1 = \varepsilon_0\varepsilon/d$ is the specific (per unit area) capacitance of a barrier with a permittivity ε and thickness d. After the ionization wave travels the distance Δx, this barrier region is charged to the threshold voltage U^* over a time that is determined by the RC product:

$$\Delta t = \tau(x)\ln\frac{U}{U-U^*}, \tag{3}$$

where $\tau(x) = \frac{c_1}{\delta\sigma}x\Delta x$ and $U \equiv U(t)$ is the discharge voltage. It follows from this that the velocity V of the ionization wave is

$$V(x) = \frac{\Delta x}{\Delta t} = \frac{\delta\sigma}{c_1\ln\dfrac{U}{U-U^*}}\frac{1}{x}. \tag{4}$$

According to expression (4), the plane ionization wave decelerates as it propagates away from the side surface of the streamer. The deceleration rate is determined by the parameters of the plasma sheet and dielectric barrier: the higher the plasma conductivity, the larger the plasma sheet thickness, and the lower the specific barrier capacitance, the higher the wave propagation velocity. The wave velocity also depends on the overvoltage U/U^*. For high overvoltages ($U/U^* \gg 1$), the wave velocity is proportional to the overvoltage value.

The current related to the propagation of the plane ionization wave along the barrier surface is

$$I(t) = c_1\int_{x_0}^{x_f}\frac{\partial U_b(x,t)}{\partial t}dx, \tag{5}$$

where $U_b(x, t)$ is the voltage at the barrier under the plasma sheet at a distance x from streamer at the instant t, x_0 is the streamer radius, and x_f is the coordinate of the wave front at the time t. The relation between x_f, x_0, and t can be obtained from expression (4)

$$x_f^2 = x_0^2 + \frac{2\delta\sigma}{c_1\ln\dfrac{U}{U-U^*}}t. \tag{6}$$

Let us assume that the electric field E in the plasma sheet is uniform and depends only on time. The formulas for the field $E(t)$ and voltage $U_b(x, t)$ can then be derived from the voltage balance at the points $x_f(t)$ and x_0:

$$E(t)x_f(t) = U - U^*, \tag{7}$$

$$U_b(x, t) = U - E(t)x. \tag{8}$$

After substituting the expression $U_b(x, t) = U - \frac{U-U^*}{x_f(t)}x$ into formula (5), we obtain

$$I(t) = c_1\frac{\partial}{\partial t}\left[U(\sqrt{x_0^2 + at} - x_0) - \frac{U-U^*}{2}\frac{at}{\sqrt{x_0^2 + at}}\right], \tag{9}$$

where $a = \dfrac{2\delta\sigma}{c_1 \ln\dfrac{U}{U - U^*}}$.

The applied voltage changes only slightly during the propagation of the plane ionization wave between two consecutive current spikes; hence, the voltage U in can be considered constant when differentiating expression (9) over time. We thus obtain

$$I(t) = \frac{c_1 a}{2\sqrt{x_0^2 + at}}\left[U - \frac{U - U^*}{2}\frac{2x_0^2 + at}{x_0^2 + at}\right]. \quad (10)$$

At the time corresponding to a sharp decrease in the current after the fast propagation of the surface streamer is complete, the current is $I_0 = \dfrac{c_1 a}{2}\dfrac{U^*}{x_0} = \dfrac{\delta\sigma}{x_0 \ln\dfrac{U}{U - U^*}} \cong \dfrac{\delta\sigma U}{x_0} \cong 10$ mA. As the ionization wave propagates far away from the streamer, the current decreases over time as $(\sqrt{t})^{-1}$:

$$I(t) = \frac{c_1\sqrt{a}}{\sqrt{t}}\frac{U + U^*}{4} \cong \sqrt{\frac{2c_1\delta\sigma}{t}}\sqrt{\frac{U}{U^*}}\frac{U + U^*}{4}. \quad (11)$$

Thus, the above simple model accounts for the slow (over 5–10 μs) decay of the discharge current after the fast streamer propagation. The expressions obtained can be used to estimate the energy deposited in a surface streamer. This allows one to discover the reasons for an increase in the streamer glow intensity in the stage when the current decreases. Note that a similar phenomenon (namely, an increase in the streamer glow intensity after the current has already passed its maximum corresponding to the bridging of the interelectrode gap) was also observed in the case of volume streamers [13].

The above model can also be used to estimate the specific energy deposition required for the surface contraction of the diffuse plasma. Note that the presence of a diffuse plasma around streamers does not allow one to directly use the fractal approach [14] when describing the structure (in particular, the branching characteristics) of surface streamers.

The reasons why diffuse regime I of a barrier corona transforms into streamer regime II are related to the ionization instability of the cathode and anode sheaths near the point electrode during the corresponding voltage half-periods. Indeed, as we showed earlier in [15], there are critical currents for transforming the cathode and anode sheaths into prearc spots that induce the streamer formation. The current needed for the formation of an anode spot is appreciably lower than that required for the formation of a cathode spot. This seems to be one reason why an increase in the amplitude of the ac voltage applied to a barrier corona leads first to the formation of streamers in positive half-periods and then in negative ones.

5. CONCLUSIONS

(i) In a barrier corona, the conduction current is carried along the dielectric surface both by streamers and by a diffuse plasma.

(ii) The time evolution of the quasi-steady current correlates with the behavior of the diffuse plasma. The current amplitude in negative half-periods is higher than in positive ones and increases with increasing amplitude and frequency of the applied voltage.

(iii) In the streamer mode of a sector-limited discharge, each current spike corresponds to an individual surface streamer propagating along its own trajectory. In an unlimited discharge, one current spike can be related to several surface streamers.

(iv) Generally, the emission intensity and visible diameter of the negative streamers are higher than those of the positive streamers.

(v) The duration of the emission pulses from both positive and negative surface streamers significantly exceeds the duration of the corresponding current spikes, the maximum of the emission intensity being delayed with respect to the discharge current maximum.

(vi) The degree of branching of the surface streamers is relatively low: up to 50% of the streamers propagate without branching.

ACKNOWLEDGMENTS

We are grateful to M.E. Grushin for his help in performing the experiments. This study was supported in part by the Russian Foundation for Basic Research (project no. 03-02-17239) and the RF Presidential Program for Support of Leading Scientific Schools (project no. NSh-794.2003.2).

REFERENCES

1. *High-Speed Physics*, Ed. by K. Vollrath and G. Thomer (Springer-Verlag, New York, 1967; Mir, Moscow, 1971), Vol. 1.
2. L. B. Loeb, *Electrical Coronas* (Univ. of California Press, Berkeley, 1965), p. 760.
3. Yu. Akishev, V. Karalnik, and N. Trushkin, Proc. SPIE **4460**, 26 (2002).
4. É. M. Bazelyan, V. A. Goncharov, and A. Yu. Goryunov, Izv. AN SSSR, Ser. Énerg. Transp., No. 2, 154 (1985).
5. E. M. van Veldhuizen and W. R. Rutgers, J. Phys. D **35**, 2169 (2002).
6. B. Eliasson, M. Hirth, and U. Kogelschatz, J. Phys. D **20**, 1421 (1987).
7. C. Heuser and G. Pietsch, in *Proceedings of VI International Conference on Gas Discharges and Their Applications, Edinburg, 1980*, p. 98.

8. Yu. S. Akishev, A. V. Dem'yanov, V. B. Karal'nik, *et al.*, Fiz. Plazmy **29**, 90 (2003) [Plasma Phys. Rep. **29**, 82 (2003)].

9. A. B. Saveliev and G. J. Pietsch, in *Proceedings of the International Symposium on High-Pressure Low-Temperature Plasma Chemistry, Tartu, 2002*, Vol. 2, p. 229.

10. A. A. Radtsig and B. M. Smirnov, *Reference Data on Atoms, Molecules, and Ions* (Atomizdat, Moscow, 1980; Springer-Verlag, Berlin, 1985).

11. A. R Striganov and N. S. Sventitskii, *Tables of Spectral Lines of Neutral and Ionized Atoms* (Atomizdat, Moscow, 1966; Plenum Press, New York, 1968).

12. B. M. Smirnov, *Negative Ions* (Atomizdat, Moscow, 1978; McGraw-Hill, New York, 1982).

13. Yu. S. Akishev, G. I. Aponin, V. B. Karal'nik, *et al.*, Fiz. Plazmy **30**, 1044 (2004) [Plasma Phys. Rep. **30**, 779 (2004)].

14. L. Niemeyer, L. Pietronero, and H. J. Wiesmann, Phys. Rev. Lett. **52**, 1033 (1984).

15. Yu. S. Akishev, A. P. Napartovich, V. V. Ponomarenko, and N. I. Trushkin, Zh. Tekh. Fiz. **55**, 655 (1985) [Sov. Phys. Tech. Phys. **30**, 388 (1985)].

Translated by N.N. Ustinovskiĭ

Plasma Physics Reports, Vol. 30, No. 12, 2004, pp. 1028–1042. Translated from Fizika Plazmy, Vol. 30, No. 12, 2004, pp. 1105–1120.

LOW-TEMPERATURE PLASMA

Study of the Oxidation of Alkanes in Their Mixtures with Oxygen and Air under the Action of a Pulsed Volume Nanosecond Discharge

N. B. Anikin, S. M. Starikovskaia, and A. Yu. Starikovskii

Moscow Institute for Physics and Technology, Institutskiĭ proezd 9, Dolgoprudnyĭ, Moscow oblast, 141700 Russia

Received February 25, 2004; in final form, April 24, 2004

Abstract—The slow oxidation of alkanes (from methane to hexane) in their stoichiometric mixtures with oxygen or air under the action of nanosecond pulsed discharges was investigated. The discharges were excited in a tube of diameter 5 cm and length of 20 cm by 25-ns voltage pulses with an amplitude of 10 kV and a repetition rate of 40 Hz. The initial pressure in the mixture was varied in the range 0.76–10.1 torr. The current, the electric field strength, and the power deposited in a discharge were measured with a nanosecond time resolution. In time-resolved and time-integrated measurements, the intensities of the following bands were determined: CO_2^+ ($B^2\Sigma \longrightarrow X^2\Pi$, $\delta v = 0$), CH($A^2\Delta$, $v' = 0 \longrightarrow X^2\Pi$, $v'' = 0$), OH($A^2\Sigma$, $v' = 0 \longrightarrow X^2\Pi$, $v'' = 0$), CO($B^1\Sigma$, $v' = 0 \longrightarrow A^1\Pi$, $v'' = 2$), NO($A^2\Sigma \longrightarrow X^2\Pi$, $\delta v = 3$), N_2($C^3\Pi$, $v' = 1 \longrightarrow B^3\Pi$, $v'' = 7$), N_2($B^3\Pi$, $v' = 6 \longrightarrow A^3\Sigma$, $v'' = 3$), and N_2^+ ($B^2\Sigma$, $v' = 0 \longrightarrow X^2\Sigma$, $v'' = 2$). The methane concentration was measured from the absorption of He–Ne laser radiation. Based on the results of optical measurements, the times of the complete oxidation of hydrocarbons were determined. © *2004 MAIK "Nauka/Interperiodica".*

1. INTRODUCTION

Plasmochemical studies cover a wide range of problems—from creating chemical lasers and ozonizer to processing liquid and solid wastes. Two large areas of application can be distinguished: those in which plasma is used to heat reacting mixtures [1, 2] and those in which excited and charged particles play an important role [1, 3, 4]. It is clear that the basic parameter determining the efficiency of plasma sources in the second area of application is how far the plasma state is from equilibrium. This parameter can be defined as the ratio of the energy deposited in all the internal degrees of freedom of a gas to the energy deposited in translational and rotational degrees of freedom. The reactivity of a gas mixture with a high value of this ratio is many orders of magnitude higher than that of a plasma in an equilibrium state, provided that the total energies are the same. From the standpoint of the chemical activity of a gas mixture, the most advantageous types of discharge are those in which energy is more efficiently deposited in the higher energy degrees of freedom. For many plasmochemical applications (e.g., for the plasma processing of surfaces and ignition of combustible mixtures in engines), an important requirement is that the plasma be highly homogenous.

Therefore, it is of considerable interest to develop generators of a strongly nonequilibrium plasma that would be capable of operating at gas pressures close to atmospheric and would be characterized by the high efficiency and high plasma homogeneity. In recent decades, results demonstrating the high efficiency of a nanosecond pulsed power supply have been obtained. Its high efficiency is due to the high reduced electric field in a discharge and due to the high spatial homogeneity and low gas temperature of the plasma produced. A discharge in the form of a fast ionization wave (FIW) [5–7] can be an efficient source of a strongly nonequilibrium plasma.

FIW discharges are usually excited in long tubes or at high overvoltages (the return stroke in lightning is a natural example of an FIW). The characteristic growth time of the ionization wave ranges from several nanoseconds to several tens of nanoseconds. The propagation velocity of an FIW can be as high as two-thirds of the speed of light [8]. FIW discharges are characterized by their high plasma homogeneity, their high reproducibility (in the regime of a repetitive discharge), the high degree to which the plasma is far from equilibrium, and the relatively low gas temperature. This type of discharge has been produced in large volumes (up to 40 l) under laboratory conditions [9]. An FIW discharge is highly efficient and can be excited at pressures close to atmospheric. In the experiments in [10], where the amplitude of the voltage pulse at the high-voltage electrode reached 100–160 kV, almost uniform FIWs were produced in combustible mixtures at high translational temperatures and gas densities corresponding to pressures of several hundred torr. In [8], FIWs were excited in a 4-mm-diameter 47-cm-long tube filled with air at a pressure of 500 torr or with helium at atmospheric pressure, the voltage-pulse amplitude being 250 kV. A characteristic feature of an FIW is its low sensitivity to the

1063-780X/04/3012-1028$26.00 © 2004 MAIK "Nauka/Interperiodica"

electronegative property of a gas. Thus, FIWs have been excited in SF_6 at a pressure of 400 torr and a voltage of 125 kV [11]. A maximum efficiency of 95% was achieved in experiments with repetitive discharges at a voltage amplitude of 16 kV [12, 13]. The energy deposited in a discharge is typically about 70% of the initial energy in the electric pulse. In experiments in nitrogen, hydrogen, and air, the field strength measured at the FIW front at a voltage amplitude of 15 kV exceeded the threshold for generating runaway electrons [14]; in this case, 50% of the deposited energy was spent on ionization and the excitation of oscillations [7]. Hence, an FIW is a highly efficient source of nonequilibrium low-temperature spatially uniform plasma.

The interest in igniting combustible mixtures by a uniform nonequilibrium plasma is motivated to a large extent by the possibility of using this type of ignition in the jet engines of hypersonic aircraft. In this case, a necessary condition for applying FIW-induced ignition is high plasma homogeneity and high mixture density corresponding to pressures of several tens of torr to several hundred torr. The efficiency of such ignition was demonstrated in [10, 15]. It was shown that the ignition threshold for methane–air mixtures was reduced by 600 K at a rather low energy deposition (corresponding to a temperature below 100 K) in the discharge. The experiments were carried out in a single-pulse mode behind the reflected shock wave; this circumstance substantially limited the possibility of studying the discharge kinetics in those experiments.

The kinetics of chemical reactions in hydrocarbon–air fuel mixtures is fairly intricate. A typical kinetic scheme adequately describing the self-ignition of a heptane–air mixture contains about 550 components and involves 5000 reactions [16]. The oxidation kinetics in a gas discharge is also significantly complicated by the influence of ions, electronically excited molecules, and radicals. In the present paper, we describe the results from experimental studies of the oxidation kinetics of alkanes under the action of a high-voltage repetitive nanosecond discharge.

2. EXPERIMENTAL SETUP

Figure 1 shows a block diagram of the experimental setup. The discharge was excited in a quartz tube by negative voltage pulses with an amplitude of 11 kV, a full width at half-maximum (FWHM) of 25 ns, a rise time of 5 ns, and a repetition rate of 40 Hz. The voltage pulses, generated by a high-voltage source, were fed to the discharge device through an RK-50-11-11 rf cable of length 20 m. The discharge cell was a quartz tube with an inner diameter of 47 mm and outer diameter of 50 mm. The braided screen of the cable was connected to the low-voltage electrode (anode) of the discharge cell by eight 12-mm-diameter brass rods that were parallel to the cell and were arranged equidistantly along a circle 140 mm in diameter. The high-voltage electrode (cathode) was a duralumin cone with a cone angle of 60°. The distance between the anode and the cathode was 200 mm. The pressure in the mixture in the course of oxidation was monitored by an MD × 4S mechanotron.

The system for the electric diagnostics of the discharge consisted of a capacitive gauge that could be displaced along the discharge cell and a return-current shunt mounted in the break of the screen of the high-voltage cable. The distance from the current shunt to the discharge cell was chosen such that the current pulses applied to the discharge cell and those reflected from it were separated in time.

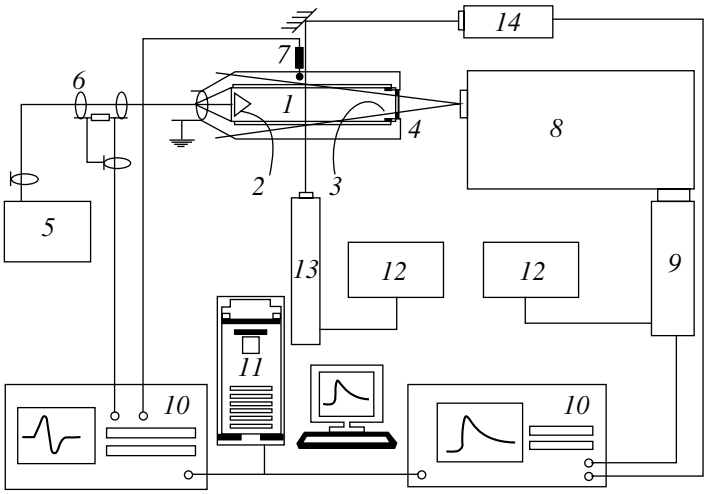

Fig. 1. Schematic of the experimental setup: (*1*) discharge cell, (*2*, *3*) electrodes, (*4*) CaF_2 optical window, (*5*) high-voltage generator, (*6*) current shunt, (*7*) capacitive gauge, (*8*) monochromator, (*9*) FEU-100 photomultiplier, (*10*) S9-8 and TDS-380 oscilloscopes, (*11*) PC, (*12*) power supply units, (*13*) He–Ne laser (λ = 3.3922 μm, and (*14*) Pb–Se photoresistor.

Table 1. Mixtures under study

Hydrocarbon	CH_4	C_2H_6	C_3H_8	C_4H_{10}	C_5H_{12}	C_6H_{14}
Mixture with O_2	33.3%	22.2%	16.6%	13.3%	11.1%	9.5%
Mixture with air	11.11%	–	–	–	3.03%	2.56%

In all of the mixtures under study, we performed both time-integrated and time-resolved measurements of the emission intensity of various molecular bands (the passband of the signal line was 150 MHz). The discharge emission was output through a 30-mm-diameter CaF_2 window in the low-voltage ring electrode. The emission intensity was measured with an MDR-23 monochromator (with a 1200-groove/mm grating and a linear dispersion of 1.2 nm/mm) and an FEU-100 photomultiplier (with a signal rise time of no more than 3 ns and a spectral sensitivity range of 200–800 nm). The power supply circuit and the signal cables of the photomultiplier were additionally screened so that the noise amplitude did not exceed 15 mV. The entrance slit of the monochromator was located 13 cm from the optical window; this allowed us to collect emission from almost the entire volume of the discharge cell.

The measurements were performed over 128 pulses; at a repetition rate of 40 Hz, this corresponded to a time interval of 3.2 s. Except for the potential distribution along the discharge gap, the time-resolved measurements were performed near the instant at which the discharge was switched on and after the complete oxidation of hydrocarbons. The spatiotemporal evolution of the potential along the discharge cell was measured only after oxidation.

In addition, the absorption of He–Ne laser radiation at a wavelength of 3.3922 μm was measured in methane-containing mixtures.

Time-resolved signals were recorded by a Tektronix TDS-380 oscilloscope with a passband of 400 MHz, and time-integrated measurements were performed with the help of an S9-8 oscilloscope with a time base of 100, 200, or 400 s.

We studied the oxidation of hydrocarbons under the action of nanosecond pulsed discharges in stoichiometric mixtures of alkanes (from methane to hexane) with oxygen and stoichiometric mixtures of methane, pentane, and hexane with air in the pressure range of 0.76–10.06 torr with a step of 0.76 torr. The percentage of hydrocarbons in the mixtures under study is listed in Table 1.

Mixtures of heavy hydrocarbons were prepared at a partial pressure below the saturation vapor pressure at room temperature. Hydrocarbons were injected into an evacuated 20-l glass vessel. The mass of the injected hydrocarbon was 20% lower than the mass of saturated vapor in the vessel volume at room temperature. By monitoring the pressure in the vessel (as the hydrocarbon evaporates and is heated to room temperature, the pressure increases and reaches its steady-state value), we could determine the hydrocarbon concentration in the vessel. The vessel was then filled with oxygen up to the pressure corresponding to a stoichiometric mixture. The gases inside the vessel were mixed for two days. In the experiments with hydrocarbon–air mixtures, nitrogen was added to a hydrocarbon–oxygen mixture.

3. MEASUREMENT TECHNIQUES

3.1. Measurements of the Current, Electric Field Strength, and Deposited Energy

The electric potential $V_i(t)$ along the discharge cell was measured by the capacitive gauge, which was positioned successively at distances of x_i = 0.0, 3.6, 7.2, 10.8, 14.4, and 18.0 cm from the edge of the conical electrode.

The current $J_0(t)$ through the high-voltage electrode was measured by the return-current shunt using the conventional measurement procedure [17]. Figure 2a shows a typical waveform of the shunt current. The first ("incident") current pulse is that supplied from the generator. This pulse is partially reflected from the discharge cell and 100 ns later returns into the cable cross section at which the current shunt is located; this is the second ("reflected") pulse recorded by the current shunt. The pulse then returns to the generator and, reflecting from it, returns to the shunt and again to the discharge cell; i.e., the process of propagation of the current pulses is repeated over time. Therefore, the current shunt records pairs of pulses; each pair consists of the incident and reflected pulse, the time interval between them being 200 ns. The energy deposited in the discharge gap in one pulse is equal to the difference between the energies of the incident and reflected pulses. From the charge continuity equation at the high-voltage electrode (with allowance for the fact that the reflected pulse is of opposite sign), we find the current through the discharge cell:

$$J_0(t) = J(t) + J(t + 2\Delta t), \quad (1)$$

where $J = J(t)$ is the current in the incident pulse, $J = J(t + 2\Delta t)$ is the current in the reflected pulse (Fig. 2), and Δt is the time it takes for an electric pulse to travel the distance from the shunt to the high-voltage electrode. It should be noted that the shunt measurements allow us to determine not only the current through the high-voltage electrode, but also its potential U_0 (Fig. 2b). The potential of the high-voltage electrode is

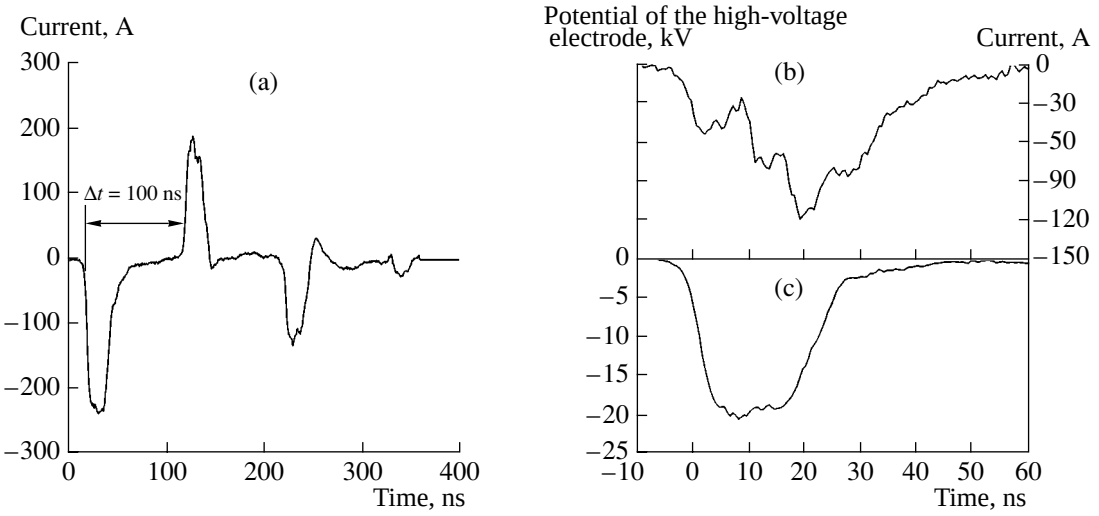

Fig. 2. Discharge characteristics measured by the current shunt: (a) waveform of the current in the cable, (b) current through the electrode, and (c) potential of the high-voltage electrode. The initial pressure of the CH_4–air mixture is 1.51 torr.

proportional to the difference between the currents the incident and reflected pulses:

$$U_0(t) = R[J(t) - J(t + 2\Delta t)], \tag{2}$$

where $R = 50\ \Omega$ is wave impedance of the supply cable.

To determine the electric field strength and the current in different cross sections along the discharge cell, we used telegraph equations in which both the capacitance and inductance of the discharge cell were taken into account. The capacitance (per unit length) of the discharge cell ($C = 5.2$ nF/cm) was calculated assuming that an excessive charge was accumulated near the cell wall. Assuming that the current density is constant over the cross section, the linear inductance of the discharge cell was found to be $L = 2.8$ nH/cm. The resistance was assumed to be variable over space and time.

The telegraph equations have the form

$$\frac{\partial V}{\partial x} + RJ = -L\frac{\partial J}{\partial t}, \qquad \frac{\partial J}{\partial x} = -C\frac{\partial V}{\partial t}, \tag{3}$$

where $J(x, t)$ is the current, $V(x, t)$ is the potential, and $R(x, t)$ is the resistance per unit length in the cross section x at a time t.

Assuming that the longitudinal component of the electric field is equal to $E_l(x, t) = J(x, t)R(x, t)$ (hereinafter, this component is denoted as E), we obtain

$$\frac{\partial V}{\partial x} + E = -L\frac{\partial J}{\partial t}, \qquad \frac{\partial J}{\partial x} = -C\frac{\partial V}{\partial t}. \tag{4}$$

Since the measurements were performed with a discrete set of points, we approximate $V_i(t)$ and $J_i(t)$ in the intervals (x_i, x_{i+1}) by linear functions of x:

$$V = V_i(t) + \frac{x - x_i}{x_{i+1} - x_i}(V_{i+1}(t) - V_i(t)), \qquad J = J_i(t) + \frac{x - x_i}{x_{i+1} - x_i}(J_{i+1}(t) - J_i(t)). \tag{5}$$

In finite differences with respect to x, the second equation of set (3) can be represented as

$$\frac{J_{i+1}(t) - J_i(t)}{x_{i+1} - x_i} = -C\frac{\partial V}{\partial t}. \tag{6}$$

The right-hand side of this equation depends on x, whereas the left-had side does not. To solve this equation, we average the right-hand side of Eq. (6) over the interval (x_i, x_{i+1}):

$$J_{i+1} = J_i - \frac{C(x_{i+1} - x_i)}{2}\frac{\partial}{\partial t}(V_i + V_{i+1}). \tag{7}$$

As a result, we find that the current in the cross section with the coordinate x_{i+1} is equal to

$$J_{i+1} = J_0 - \sum_{k=0}^{i}\frac{C(x_{k+1} - x_k)}{2}\frac{\partial}{\partial t}(V_k + V_{k+1}). \tag{8}$$

To find the electric field strength, we average Eq. (1) over the interval (x_i, x_{i+1}):

$$\frac{E_{i+1}(t) + E_i(t)}{2} = -\frac{V_{i+1}(t) - V_i(t)}{x_{i+1} - x_i} - \frac{L}{2}\frac{\partial}{\partial t}(J_i(t) + J_{i+1}). \tag{9}$$

Thus, we have recalculated the measured electric current through the high-voltage electrode and the measured potentials in different cross sections of the discharge cell to the electric field strengths and currents in these cross sections with allowance for the capacitance and inductance of the discharge cell.

The obtained values of $E(x, t)$ and $J(x, t)$ were used to calculate the spatiotemporal evolution of the specific power $W(x, t) = E(x, t)J(x, t)/S$ deposited in the gas.

It should be noted that the approximations used in the above calculations do not allow one to adequately describe the evolution of the field at the front of the ionization wave [18], because the radial fields and currents were ignored and the spatial sensitivity function of the capacitive gauge was approximated by a delta function. However, behind the front and further, after the ionization wave has bridged the gap, the above assumptions are well justified [18]. The approximation of the spatial sensitivity function by a delta function also does not allow one to calculate the electric field near the cathode. Note that, under our experimental conditions at pressures $p > 3$ torr (corresponding to the maximum deposited energy), most of the energy is deposited in the gas in later stages of the discharge in which the value of the cathode voltage drop is of minor importance. Hence, the technique used in our study allows us to find the distribution of the electric field within the time interval that is most important from the standpoint of gas excitation.

3.2. Emission Spectroscopy: Experimental Study of the Optical Characteristics of a Discharge

Under our experimental conditions, a few thousand pulses are required to completely oxidize alkanes (this takes from several tens of seconds to several hundred seconds); hence, the time-integrated signal from the photomultiplier provides information about the dynamics of hydrocarbon oxidation. A capacitor connected in parallel with the oscilloscope input was used as an integrating element. The integration time constant $\tau = CR_0 = 2.5$ s was determined by the capacitor's capacitance C and the oscilloscope internal resistance R_0. Since the photomultiplier is a current source, Ohm's law for the measuring circuit has the form

$$\frac{U}{R_0} + \frac{dq}{dt} = J. \tag{10}$$

Therefore, we have

$$U + \tau\frac{dU}{dt} = R_0 J, \tag{11}$$

where U is the voltage at the oscilloscope, q is the capacitor charge, and J is the photomultiplier current.

The characteristic duration of the discharge emission is much shorter than the integration time; hence, we may assume that, during a discharge, the capacitor only accumulates an electric charge and, between pulses, it discharges through the oscilloscope. The lifetime of the states under study (<10 μs) is much shorter than the time interval between pulses, $1/f \approx 25$ ms. Therefore, the residual current of the preceding pulses can be ignored and the pulse current can be written as

$$J(\delta t) = \frac{IAkN_0'}{\tau_l}\exp\left(-\frac{\delta t}{\tau_l^{\text{eff}}}\right), \tag{12}$$

where I is the emission intensity at a given wavelength λ, $A = A(\lambda)$ is the sensitivity of the monochromator–photomultiplier optical system, N_0' is the density of unexcited molecules from which the emitting state is produced, k is the time-integrated excitation constant of the emitting state, τ_l is the radiative time of the transition, τ_l^{eff} is the effective lifetime of the emitting state, and δt is the time counted from the last pulse. The effective lifetime of the emitting state accounts for the radiative and collisional deexcitation:

$$\tau_l^{\text{eff}} = \frac{1}{1/\tau_l + N_0\sum_i^M \alpha_i k_i^q}, \tag{13}$$

where M is the number of stable components in the mixture, α_i is the fraction of the ith component, k_i^q is the constant for the deexcitation by the ith component, and N_0 is the total density of the molecules of the stable components.

For a slowly reacting mixture (i.e., for a mixture whose composition changes over a time that is much longer than the integration time), the excitation rate k and the effective lifetime τ_l^{eff} of the emitting state vary only slightly from pulse to pulse.

The initial voltage at the capacitor is equal to the final voltage produced by the previous pulse; therefore, Eq. (11) should be solved over the $(n + 1)$th time interval with the initial condition $U_{n+1}(0) = U_n(n/f)$:

$$U_{n+1} + \tau_0\frac{dU_{n+1}}{dt} = \frac{AR_0kN_0'}{\tau_l}\exp\left[-\frac{t}{\tau_l^{\text{eff}}}\right], \tag{14}$$

where τ_0 is the characteristic time over which the photomultiplier signal reaches its steady-state value. If the characteristic time during which the mixture composition changes is longer than τ_0, then the solution to Eq. (14) is a slowly varying function $\langle U\rangle(t)$, which is superimposed by oscillations with a frequency f and amplitude $\delta U(t)$:

$$\langle U\rangle \approx \frac{AR_0k(t)N_0'(t)f}{1 + \tau_l N_0\sum_i^M \alpha_i(t)k_i^q}, \tag{15}$$

$$\delta U \approx \frac{\langle U\rangle}{2\tau_0 f}. \tag{16}$$

Table 2. Spectral transitions monitored in all of the mixtures

λ, nm	δλ, nm	Measured band	Background band system
518.6	2.8	Angstrom band of CO, CO ($B^1\Sigma$, $v' = 0 \longrightarrow A^1\Pi$, $v'' = 2$)	–
430	3	CH ($A^2\Delta$, $v' = 0 \longrightarrow X^2\Pi$, $v'' = 0$)	CO_2^+ ($A^2\Pi \longrightarrow X^2\Pi$), the first negative and second positive systems of nitrogen
307.8	3.4	OH ($A^2\Sigma$, $v' = 0 \longrightarrow X^2\Pi$, $v'' = 0$)	CO_2^+ ($A^2\Pi \longrightarrow X^2\Pi$), the second positive system of nitrogen
290	2.8	CO_2^+ ($B^2\Sigma \longrightarrow X^2\Pi$, $\delta v = 0$)[1]	OH($A^2\Sigma \longrightarrow X^2\Pi$)

Note: 1. The group of transitions accompanied by a change in the vibrational quantum number by the same value of n is denoted as $\delta v = n$.

Table 3. Spectral transitions monitored in mixtures with air

λ, nm	δλ, nm	Measured band system	Background band system
258.2	3.7	γ-system of NO, NO ($A^2\Sigma \longrightarrow X^2\Pi$, $\delta v = 3$)	–
490	3.7	N_2 ($C^3\Pi$, $v' = 1 \longrightarrow B^3\Pi$, $v'' = 7$)	CO_2^+ ($A^2\Pi \longrightarrow X^2\Pi$)
669.6	3.7	N_2 ($B^3\Pi$, $v' = 6 \longrightarrow A^3\Sigma$, $v'' = 3$)	CO_2^+ ($A^2\Pi \longrightarrow X^2\Pi$)
469.2	3.3	N_2^+ ($B^2\Sigma$, $v' = 0 \longrightarrow X^2\Sigma$, $v'' = 2$)	CO_2^+ ($A^2\Pi \longrightarrow X^2\Pi$)

Each discharge is accompanied by a burst in the emission signal, which relaxes over a characteristic time τ_0. The signals from successive pulses are accumulated to form the integral signal.

Hence, the measured integral optical characteristics provide information about the composition of the reacting mixture. In our case, $f\tau_0 \approx 100$ and the amplitude of oscillations was nearly 3% of the signal amplitude. In processing the signal from the oscilloscope, it was averaged over the discharge repetition period; this allowed us to eliminate these oscillations.

The emission intensity was monitored for a number of transitions; in this case, some bands may be partially overlapped. Table 2 lists the transitions that were monitored in all of the mixtures under study. Table 3 lists the transitions that were additionally monitored in mixtures of hydrocarbons with air. We note that the emission intensity for the transitions given in Table 3 is so high that the emission from the background bands can be ignored.

To identify the emission from substantially overlapped bands, we performed time-resolved measurements of the emission intensities at given wavelengths near the instant at which the discharge was switched on and after the complete oxidation of hydrocarbons (when the photomultiplier signal had already reached its steady-state value). The time-resolved measurements also allowed us to calculate the deexcitation constants in the initial and reacted mixtures. Taking deexcitation into account made it possible to find the populations of the states in a discharge.

3.3. Absorption Spectroscopy: Measurements of the Methane Concentration

The methane concentration was measured by the laser absorption technique. Radiation of an LGN-118 He–Ne laser (λ = 3.3922 μm), whose wavelength coincides with that of the vibrational–vibrational transition of an asymmetric vibrational mode of the CH_3 group, was passed through the discharge cell perpendicularly to its axis and fell onto a Pb–Se photoresistor with the spectral sensitivity range of 2–4 μm. During the filling of the cell with a mixture, the signal from the pressure gauge and the photomultiplier signal were fed to the oscilloscope. From the known composition of the mixture and from the measured dependence of the signal amplitude on the pressure $I(p)$, we found the dependence $I([CH_4])$, which was then used as a calibration curve in processing the experimental data. The concentrations of hydrocarbons in other mixtures were not measured because of their small absorption coefficient at a wavelength of 3.3922 μm.

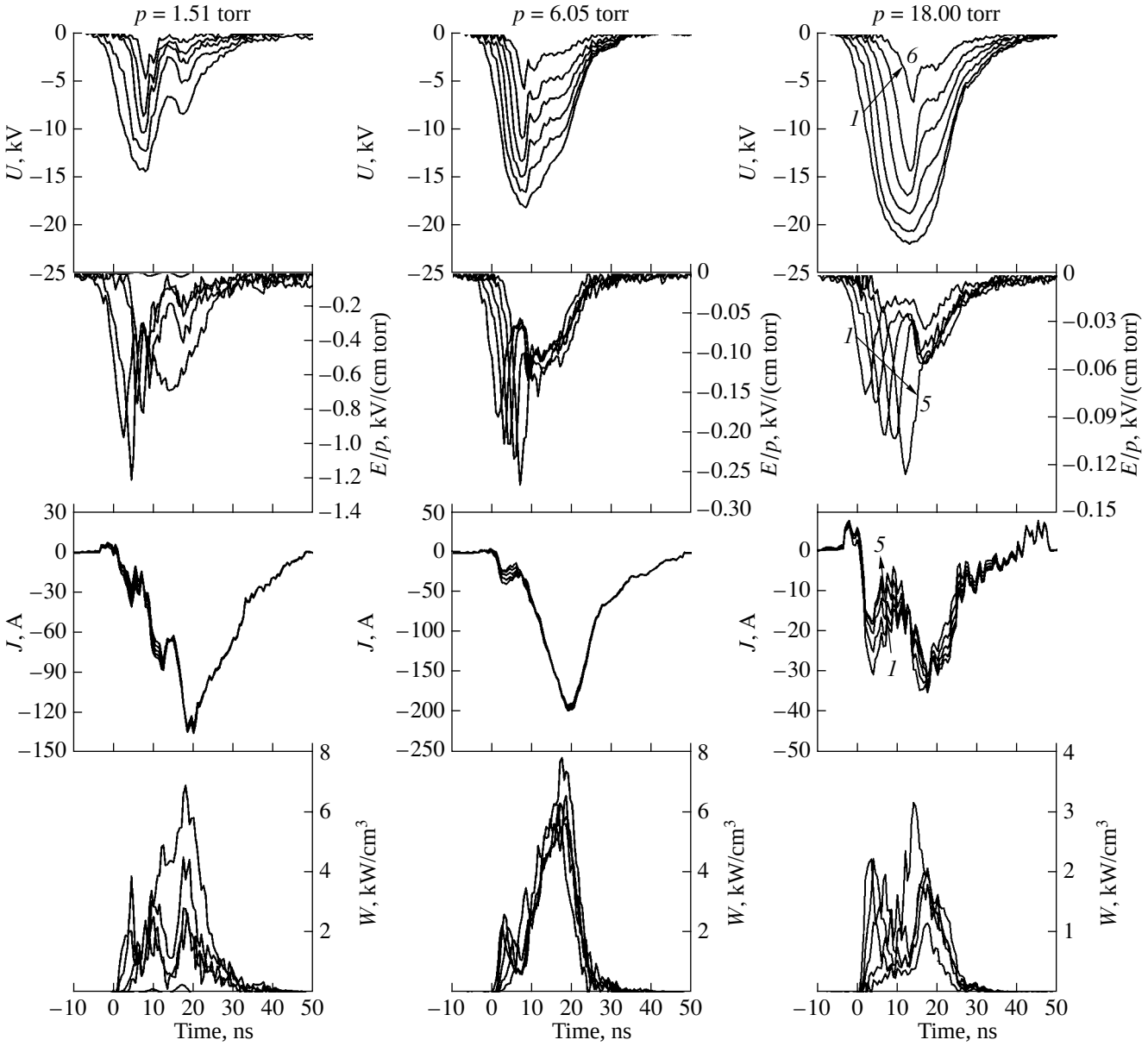

Fig. 3. Electrodynamic characteristics of the discharge during the first high-voltage pulse at pressures of 1.51, 6.05, and 18 torr. The distributions of the electric potential in the cross sections x = 0.0, 3.6, 7.2, 10.8, 14.4, and 18 cm are presented. The distribution of the reduced electric field $E(t)/p$, the current $J(t)$, and the specific power deposition $W(t)$ are averaged over the spatial intervals 0.0–3.6, 3.6–7.2, 7.2–10.8, 10.8–14.4, and 14.4–18.0 cm. The arrows show the numbering order of the curves when passing from the first to the sixth cross section for the voltage and from the first to the fifth interval for the other quantities. The mixture is the oxidation products of CH_4 in a methane–air stoichiometric mixture.

4. RESULTS AND DISCUSSION

4.1. Electrodynamic Characteristics of a Discharge

Figure 3 shows the waveforms of the potential, electric field strength, current, and specific power deposition in different cross sections of a discharge cell filled with a methane–air mixture. The measurements were performed with the capacitive gauge and the current shunt. In order to give an idea of the electrodynamic characteristics of a discharge at higher pressures, the results of measurements at a pressure of 18 torr are also presented in the figure.

Let us consider the effect of the capacitance and inductance of the discharge cell. It follows from Eq. (1) that

$$E = -\frac{\partial V}{\partial x} - L\frac{\partial J}{\partial t}.$$

Taking the inductance into account is necessary at low electric fields and fast variations in the current. It can be seen from Fig. 3 that low electric fields at fast current

variations occur at the trailing edge of the high-voltage pulse. In Fig. 3 at a pressure of 6.05 torr, this corresponds to $t > 25$ ns. Thus, at $t = 25$ ns, the current growth rate is 20 A/ns, and the inductive addition to the electric field is 60 V/cm (or 10 V/(cm torr)), which is comparable to the field strength itself. At the same time, the power deposited in the gap at $t > 25$ ns is rather low. In this figure, we also clearly see the influence of the capacitance of the discharge cell at $t < 10$ ns. The propagation of the ionization wave is caused by the charging of the capacitance of the discharge cell; as a result, the current decreases as the wave propagates from the high-voltage to the low-voltage electrode. In later stages, the influence of the capacitance is insignificant.

On the whole, the electrodynamical picture of a discharge in a relatively short discharge cell is fairly intricate and differs substantially from that in long tubes whose length exceeds the diameter by one order of magnitude or more [18]. In our experiments, the typical propagation velocity of the ionization wave was 2–3 cm/ns and the typical propagation time along the discharge cell was 7–15 ns, which was shorter than the pulse duration. As a result, a short-circuit regime took place under our conditions (note that such a regime was not observed in [18]). In this regime, the electric field strength and the current were constant along the discharge chamber and varied relatively slowly with time. For example, at a pressure of $p = 6.05$ torr, this phase began at $t = 10$ ns.

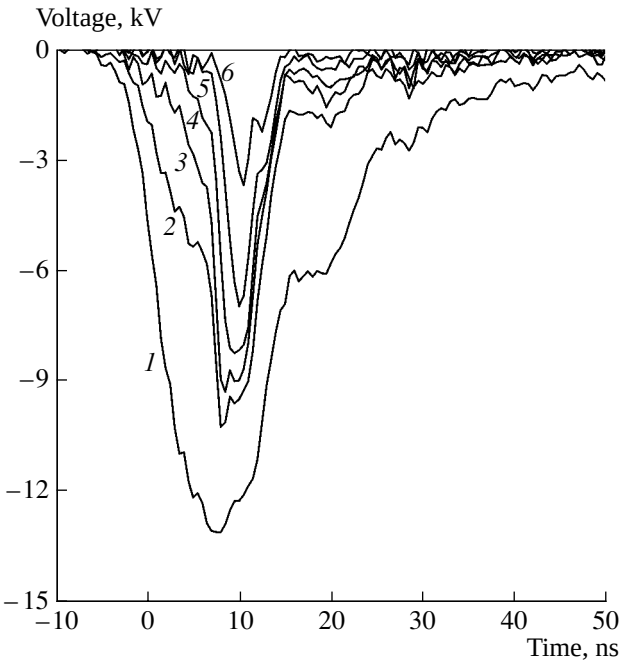

Fig. 4. Distribution of the electric potential during the first high-voltage pulse at a pressure of 0.76 torr in the cross sections x = (*1*) 0.0, (*2*) 3.6, (*3*) 7.2, (*4*) 10.8, (*5*) 14.4, and (*6*) 18 cm. The mixture is the oxidation products of CH_4 in a methane–air stoichiometric mixture.

At a pressure of 0.76 torr, one can easily distinguish a low-current precursor—an ionization wave developing against the background of a large cathode voltage drop (see Fig. 4, $t < 8$ ns). The development of the precursor and the main ionization wave was studied in detail in [18, 19], where it was shown that the precursor appeared in the initial phase of the discharge. The development of the precursor is primarily caused by the polarization current near the cathode at a relatively low emission current. The increase in the electric field strength near the cathode leads to a sharp increase in the emission current. This, in turn, gives rise to the main ionization wave that propagates through the preionized gas at a velocity several times higher than the precursor velocity. After the main ionization wave runs down the precursor and merges with it, the wave velocity decreases to a value that is higher than the precursor velocity but is lower than the initial velocity of the main ionization wave. The start of the main ionization wave results in a neutralization of the positive charge near the cathode; as a result, the cathode voltage drop sharply decreases (in [18], the cathode voltage drop after the start of the main wave was below the level determined by the experimental errors).

In our experiments, two distinctive features were observed at a pressure of 0.76 torr: (i) the precursor had time to arrive at the anode before the start of the main wave, and (ii) the cathode voltage drop remained substantial throughout the entire discharge phase. The first feature is explained by the fact that the length of the discharge tube in our study was three times shorter than that in [18] ((20 and 60 cm, respectively). For this reason, at nearly the same delay time of the main wave and nearly the same propagation velocity of the precursor, the latter had time to reach the anode. In this case, the main wave propagated through a preionized gas with a velocity on the order 10^{10} cm/s and, as a result, crossed the discharge gap over nearly 2 ns. The second feature is also explained by the difference in the dimensions of the discharge tubes: in our experiments, the tube length was shorter and, moreover, the tube diameter was a factor of 2.5 larger than in [18]. At nearly the same electron density, the resistance of the discharge gap (with the exception of the cathode sheath) in our case was twenty times lower than in [18]. As a result, the voltage drop across the cathode sheath was much higher.

At low pressures ($p < 4$ torr), the ionization wave develops and bridges the gap against the background of the large cathode voltage drop. It should be noted that, in this case, the cathode voltage drop is much larger and the electric field strength in the cathode sheath is much higher (by several orders of magnitude) than those shown in the figures, because the FWHM of the sensitivity function of the capacitive gauge is on the order of the screen diameter [18].

The cathode sheath thickness can be estimated using the theory of a glow discharge. Under our experimental conditions, the parameters of the cathode sheath corre-

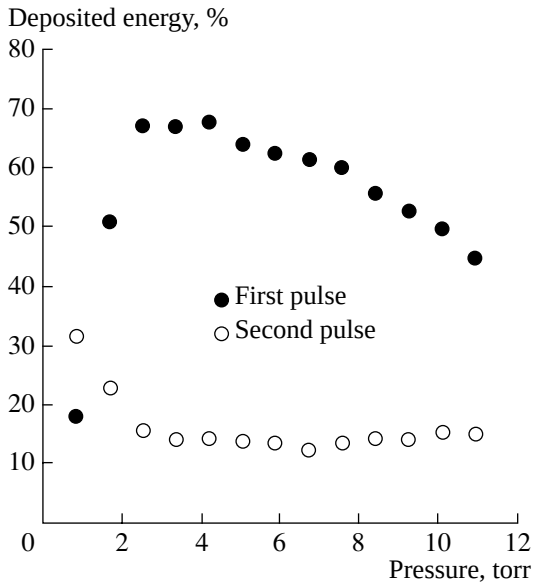

Fig. 5. Energy deposited in a discharge during the first two high-voltage pulses in a processed methane–air mixture as a function of the initial pressure in the mixture.

spond to the case of an abnormal glow discharge because the typical current density is from several units to several tens of A/cm^2, which is higher than the normal current density by three to four orders of magnitude. It follows from this (see [20]) that the reduced cathode sheath thickness is $pd \approx (pd)_n/e$, where d is the cathode sheath thickness, $(pd)_n$ is the normal reduced cathode sheath thickness, and e is the base of natural logarithms. For an aluminum cathode in air, we have $(pd)_n \approx 0.25$ torr cm [20]; hence, we obtain $pd \approx 0.09$ torr cm. At a pressure of $p = 0.76$ torr, we have $d \approx 1.2$ mm, whereas at a pressure of $p = 9.83$ torr, we have $d \approx 100$ μm.

Let us consider the results obtained at a pressure of $p = 1.51$ torr in more detail. In this case, the cathode sheath thickness is $d = 0.6$ mm. It can be seen from Fig. 3 that, at intermediate pressures ($p = 6.05$ torr), starting from $t = 10$ ns, a quasi-steady distribution of the electric field is established in the discharge gap. It follows from shunt measurements that, at this time, the voltage across the entire discharge gap is about 20 kV (see Fig. 2). The voltage drop across the discharge gap with the exception of the cathode sheath is about 10 kV (it can be seen from Fig. 3 that, at a distance of 3.6 cm from the cathode, the electric potential is –8 kV, and the electric field strength in the discharge gap is ~600 V/cm). Hence, the electric field strength in the cathode sheath is about (20000 – 10000)/0.06 V/cm = 1.7×10^5 V/cm. Such an electric field is sufficient for the vacuum breakdown of an aluminum cathode trained with pulsed discharges [21]. Over the subsequent 3 ns, the potential drop across the bulk of the discharge gap decreases to ~2 kV because of ionization. Over this time interval, the potential of the high-voltage electrode varies only slightly (decreases to 19 kV). As a result, the electric field in the cathode sheath increases to 2.8×10^5 V/cm and the field-emission current increases manyfold. This leads to the field-emission breakdown of the cathode sheath and the formation of a rebreakdown wave propagating with a velocity on the order of the speed of light. The rebreakdown wave redistributes the potential between the cathode sheath and the remaining part of the discharge gap. It can be seen from Fig. 4 that, at a pressure of 0.76 torr, two rebreakdown waves are generated at $t = 20$ and 27 ns. In the pressure range $p = 1.51$–3.02 torr, only one breakdown of the cathode sheath occurs during the high-voltage pulse. At higher voltages, no breakdowns of the cathode sheath are observed (Fig. 3).

The above considerations allow us to conclude that, at pressures below 3–4 torr, a substantial fraction of energy is deposited in the thin cathode sheath. Moreover, at low pressures, a substantial fraction of energy is deposited during the propagation of the ionization wave. However, even at a pressure of 3.02 torr, most of the energy is deposited in the discharge after bridging the gap. In this case, the energy deposited in the cathode sheath and that deposited in the gas during the propagation of the ionization wave comprise a small fraction of the total discharge energy. At pressures of 10 torr, the energy deposited after bridging the gap decreases with increasing pressure; however, even at a pressure of 18 torr, this energy is larger than that deposited during the propagation of the ionization wave.

As was shown above, a fraction of the high-voltage pulse is reflected from the discharge cell, returns to the generator, is reflected from it, and then comes again to the discharge cell. Under the action of such repeated pulses, the breakdown of the discharge gap occurs without the formation of an ionization wave. The cathode voltage drop in the second pulse is substantially lower (at pressures of higher than 0.76 torr, the cathode voltage drop was below the measurement error); therefore, the energy is deposited over the discharge cell more uniformly.

Figure 5 shows the ratios of the energies deposited during the first and second incident pulses to the energy of the first incident pulse as a function of the gas pressure. It can be seen that, at a pressure of 0.76 torr, the energy deposited during the second pulse is larger than that deposited during the first pulse. As the pressure increases, the energy deposited during the first pulse increases and reaches its maximum at a pressure of about 3.5 torr. The energy deposited during the second pulse decreases monotonically up to a pressure of 3.5 torr and then remains nearly constant. The energy fraction deposited during the third and subsequent pulses does not exceed 2%. Note that, at low pressures, the nonuniformity of energy deposition is partially compensated for by the relatively large energy deposited during the second pulse.

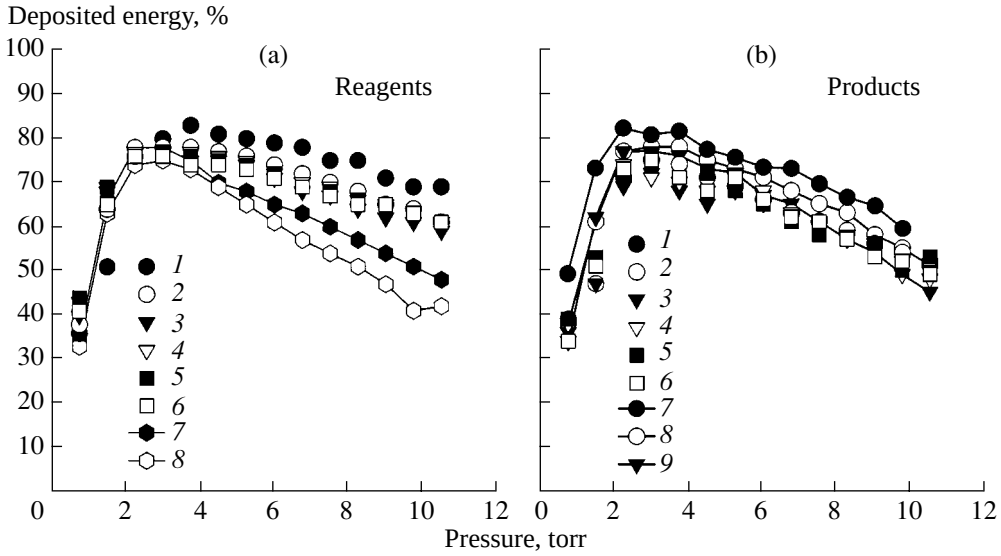

Fig. 6. Total energy deposited in a discharge during the first two high-voltage pulses as a function of the initial pressure (a) in the initial mixture: (*1*) $CH_4 : O_2$, (*2*) $C_2H_6 : O_2$, (*3*) $C_3H_8 : O_2$, (*4*) $C_4H_{10} : O_2$, (*5*) $C_5H_{12} : O_2$, (*6*) $C_6H_{14} : O_2$, (*7*) C_5H_{12} : air, and (*8*) C_6H_{14} : air and (b) in the mixture after the complete oxidation of hydrocarbons: (*1*) $CH_4 : O_2$, (*2*) $C_2H_6 : O_2$, (*3*) $C_3H_8 : O_2$, (*4*) $C_4H_{10} : O_2$, (*5*) $C_5H_{12} : O_2$, (*6*) $C_6H_{14} : O_2$, (*7*) CH_4 : air, (*8*) C_5H_{12} : air, and (*9*) C_6H_{14} : air.

Hence, over the pressure range under study (0.76–10.06 torr), most of the energy is deposited in the gas in the stage of bridging during either the first or the second high-voltage pulse. The nonuniformity of energy deposition caused by the presence of the cathode sheath can be ignored. In view of this, we could measure the electric field, the current, and the specific power deposition by using the current shunt only; this is very important in studying chemically reacting mixtures because, in such mixtures, changes in the chemical composition cause variations in the electrodynamic characteristics of a discharge. Measurements performed in processed mixtures of hydrocarbons (from ethane to hexane) with oxygen and air gave results similar to those described above.

Figure 6 shows the efficiency of energy deposition as a function of the gas pressure for all of the mixtures under study at the beginning of the oxidation process and after its completion. The total energy of the high-voltage pulse was 60 mJ. It can be seen from the figure that, at the beginning of the oxidation process, the energy deposited in mixtures with oxygen at pressures of $p > 3$ torr is larger than the energy deposited in mixtures with air. This difference increases with pressure and reaches 12% at $p = 10.06$ torr. In processed mixtures, the efficiency of energy deposition is almost the same for all of the mixtures under study; the presence or absence of nitrogen has little effect on the deposited energy. We note only that, in a methane–oxygen mixture, the deposited energy is somewhat larger than in other hydrocarbon–oxygen mixtures.

4.2. Kinetics of the Oxidation of Hydrocarbons in a Discharge

Figure 7 shows the emission spectrum of a discharge in pure methane and the afterglow spectrum of a processed methane–oxygen mixture. The emission spectrum of a discharge in pure methane consists mainly of the hydrogen continuum corresponding to the $H_2(a^3\Pi - b^3\Sigma)$ transition. The $CH(A^2\Delta \longrightarrow X^2\Pi)$ band corresponding to the $v' = 0 \longrightarrow v'' = 0$ transition is also clearly seen.

Most bands in the processed methane–oxygen mixture belong to the $CO_2^+(A^2\Pi)$ molecules. The emission bands of the $OH(A^2\Sigma \longrightarrow X^2\Pi)$ hydroxyl radical and the weak CO bands of the Angstrom system, $CO(B^1\Sigma \longrightarrow A^1\Pi)$), can also be clearly identified. It can be seen that the $CH(A^2\Delta \longrightarrow X^2\Pi)$ band in methane (Fig. 7a) is substantially overlapped by the $CO_2^+(A^2\Pi \longrightarrow X^2\Pi)$ band in the mixture (Fig. 7b). Therefore, to identify the spectral bands, it is necessary to take special measures in order to separate these bands in the early stage of processing the methane–oxygen mixture. The $OH(A^2\Sigma \longrightarrow X^2\Pi)$ emission band is also overlapped by the emission spectrum of CO_2^+. In hydrocarbon–air mixtures, numerous bands of the first negative and the first and second positive systems of nitrogen appear in the spectrum. These bands partially overlap the emission bands of CH, CO_2^+, and OH. In the Angstrom system of CO, at least one band at 518.6 nm is not overlapped by other bands. In all of the spectra, we observed weak lines of the hydrogen Balmer series. We did not measure the intensities of

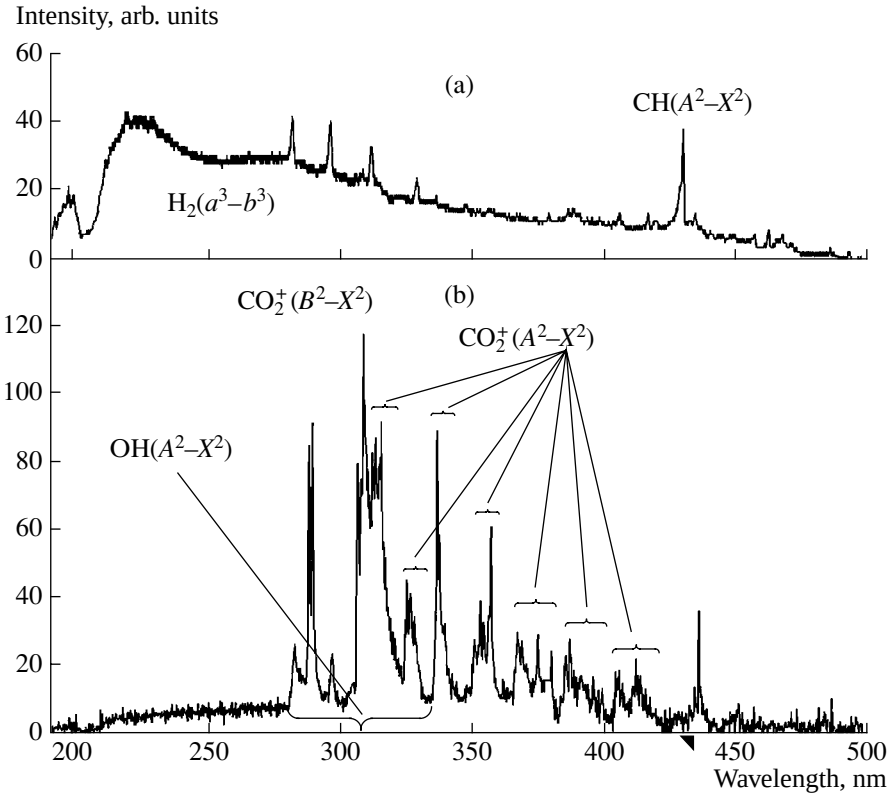

Fig. 7. Emission spectra from discharges in (a) pure methane and (b) a processed methane–oxygen mixture. The initial pressure is 4 torr.

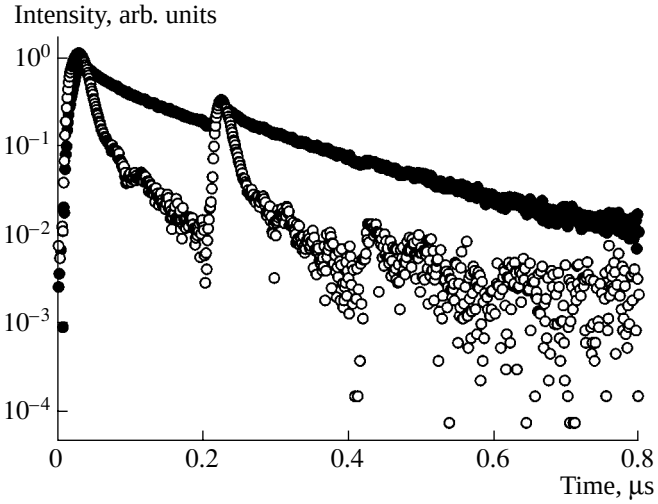

Fig. 8. Waveforms of the emission intensity at a wavelength of $\lambda = 430$ nm in the initial $CH_4 + O_2$ mixture and in the processed mixture. The initial pressure in the mixture is 3.78 torr. The closed circles correspond to the CH(A) + CO_2^+ (B) reagents, and the open circles correspond to the CO_2^+ (B) products.

these lines systematically because they were too weak and were present in both the initial and processed mixtures.

As was noted above, when the bands overlapped in a narrow spectral interval, they could be identified from measurements with a nanosecond time resolution. As an example, Fig. 8 shows the waveforms of the emission intensity at a wavelength of 430 nm in the initial and final stages of the mixture processing. Two excitation peaks corresponding to two high-voltage pulses are clearly seen. The decrease in the emission intensity in each pulse can be approximated with good accuracy by the sum of two exponential functions with different characteristic decay times. It is well known that the lifetime of the CO_2^+ ($A^2\Pi$) state ($\tau = 124$ ns, [22]) is several times shorter than that of the CH($A^2\Delta$) state ($\tau = 600$ ns, [23]). In this case, the exponential function with a longer decay time corresponds to the emission from the CH($A^2\Delta$) state, whereas the one with a shorter decay time corresponds to the emission from the CO_2^+ ($B^2\Sigma$) state. It can also be seen that the intensity of the emission corresponding to the CH($A^2\Delta \longrightarrow X^2\Pi$) transition decreases severalfold in the course of oxidation. In contrast, the intensity of the emission corresponding to the CO_2^+ ($A^2\Pi \longrightarrow X^2\Pi$) transition increases severalfold.

The lifetime and the deexcitation constant for the "fast" emission are the same as for the emission of CO_2^+ at a wavelength of 290 nm. For this reason, the time dependence of the emission intensity of CH($A^2\Delta \longrightarrow X^2\Pi$) can be obtained by subtracting the normalized waveform of the emission intensity at a wavelength of 290 nm from the waveform of the total emission intensity at a wavelength of 430 nm. The normalizing factor was chosen such that the time-resolved signal of the 290-nm emission coincided with the "fast" signal at a wavelength of 430 nm.

With time-resolved measurements, the wavelength interval for measuring the emission of the OH($A^2\Sigma$) radical could be chosen such that the background due to the second positive system of nitrogen and due to the band of the CO_2 ions could be ignored. The OH($A^2\Sigma \longrightarrow X^2\Pi$) emission corresponding to transitions from the $v' = 1$–3 vibrationally excited states was negligibly small against the background of the emission of the CO_2 ions at a wavelength of 290 nm.

The above bands were observed in all of the mixtures under study and served as indicators of the oxidation process under the action of a discharge.

Using the results from time-resolved measurements of the lifetimes and deexcitation constants of the excited states (this technique was described in detail in [24]), we determined the time-integrated (over the pulse duration) excitation rates of the emitting states. It should be noted that the deexcitation constants for the CO($B^1\Sigma$), CH($A^2\Delta$), and OH($A^2\Sigma$) states in the reagents are lower by 30–50% than those in the products (which is explained by the appearance of water). This means that, in order to determine variations in the density of the excited molecules in the course of oxidation, the measured waveforms of the emission intensity must be corrected with allowance for the deexcitation constants. Note that the constants for the deexcitation of the CO CO_2^+ ($B^2\Sigma$), CO_2^+ ($A^2\Pi$), and N_2^+ ($B^2\Sigma$) states by the reagents and by the products are almost the same.

In hydrocarbon–air mixtures, we determined the time-integrated (over the pulse duration) population rates of the upper states by using the data from time-resolved measurements of the emission from the $N_2(C^3\Pi, v' = 1 \longrightarrow B^3\Pi, v'' = 7)$, $N_2(B^3\Pi, v' = 6 \longrightarrow A^3\Sigma, v'' = 3)$, and $N_2^+(B^2\Sigma, v' = 0 \longrightarrow X^2\Sigma, v'' = 2)$ transitions near the instant at which the discharge was switched on and after the complete oxidation of hydrocarbons. It was found that, in both cases, the excitation rates for the states of molecular nitrogen differed by no more than 10%. The excitation rate for the $N_2^+(B^2\Sigma, v' = 0)$ state decreased by nearly 25% in the course of oxidation. In [24], it was found that, in a similar nanosecond discharge, the main mechanism for the population of the $N_2(C^3\Pi)$ and $N_2^+(B^2\Sigma)$ states was the electron-impact excitation of molecular nitrogen. Since the nitrogen concentration in a discharge varies only slightly, the time-integrated (over the pulse duration) rate constants for the population of the $N_2(C^3\Pi, v' = 1)$ and $N_2^+(B^2\Sigma, v' = 0)$ states vary by 10% and 25%, respectively. Note also that the $N_2(C^3\Pi, v' = 1)$ and $N_2^+(B^2\Sigma, v' = 0)$ states are populated during the discharge, whereas the $N_2(B^3\Pi, v' = 6)$ state is mainly populated in the discharge afterglow and its population rate correlates well with the emission from the $N_2(C^3\Pi, v' = 1 \longrightarrow B^3\Pi, v'' = 7)$ transition. It follows from this that the $N_2(B^3\Pi, v' = 6)$ state is mainly populated via the deexcitation of the $N_2(C^3\Pi)$ state.

The threshold energies for the electron-impact excitation of the $N_2(C^3\Pi, v' = 1)$ and $N_2^+(B^2\Sigma, v' = 0)$ states are ~11 and 19 eV, respectively. Since the threshold excitation energies for all of the states under consideration do not exceed 19 eV, we can assume that, when we pass from the products to the reagents, the excitation rate constants averaged over the high-voltage pulse vary by no more than 25% for all of the states under study. In addition, the lower the threshold excitation energy for a given state, the smaller the difference between the excitation constants.

Thus, the change in the mixture composition in the course of oxidation and the accompanying variations in the deexcitation and excitation rate constants lead to variations of no more than 50% in the time-integrated (over the pulse duration) emission intensity from any of the transitions under consideration. Therefore, from measurements of the time-integrated emission, we can only obtain a qualitative time dependence of the concentrations of the components from which the excited states are produced. At the same time, this has little effect on the characteristic oxidation time determined from the time-integrated emission from the CO($B^1\Sigma \longrightarrow A^1\Pi$), CO_2^+ ($B^2\Sigma \longrightarrow X^2\Pi$), OH($A^2\Sigma \longrightarrow X^2\Pi$), and CH($A^2\Delta \longrightarrow X^2\Pi$) transitions.

The time dependences of the integral emission intensity in methane-containing mixtures are well approximated by the function $\exp(-t/\tau(p))$ or our function $1 - \exp(-t/\tau(p))$ (see Fig. 9). Note that, in our experiment, we observed the complete oxidation of methane, as is seen from the curve $[CH_4](t)$ obtained from the absorption measurements of the IR radiation of the He–Ne laser. Figure 9 also shows the time behavior of the time-integrated emission of the CH($A^2\Delta \longrightarrow X^2\Pi$) radicals. It can be seen that, from the very beginning of the discharge, the time behavior of the emission intensity from the CH($A^2\Delta \longrightarrow X^2\Pi$) transition coincides (to within the measurement accuracy) with that of the methane concentration. For this reason, the emission from the CH($A^2\Delta \longrightarrow X^2\Pi$) transition can be considered a reliable indicator of the hydrocarbon concentration in a discharge.

In mixtures of hydrocarbons that are heavier than methane, the time dependences of the emission inten-

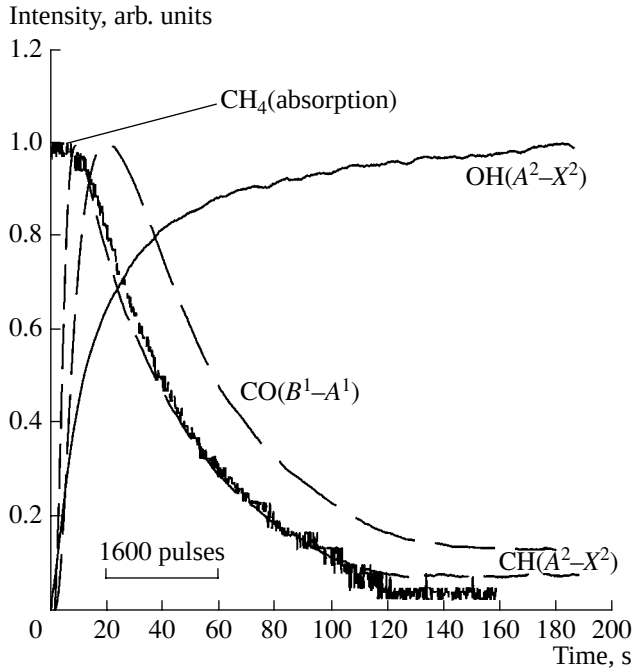

Fig. 9. Time evolution of the time-integrated (over the pulse duration) emission intensities from the CH($A^2\Delta \longrightarrow X^2\Pi$), CO($B^1\Sigma \longrightarrow A^1\Pi$), and OH($A^2\Sigma \longrightarrow X^2\Pi$) transitions and the methane concentration measured from the absorption of the 3.3922-μm laser radiation. The initial pressure of a $CH_4 + O_2$ mixture is 7.56 torr.

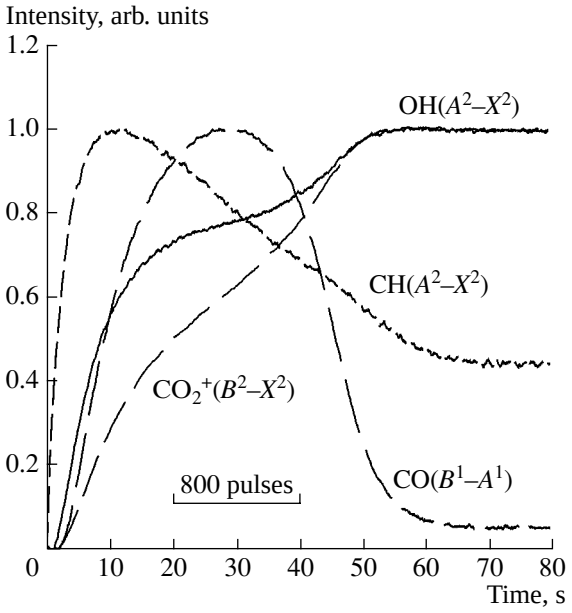

Fig. 10. Time evolution of the time-integrated (over the pulse duration) emission intensities from the CH($A^2\Delta \longrightarrow X^2\Pi$), CO($B^1\Sigma \longrightarrow A^1\Pi$), and CO_2^+ ($B^2\Sigma \longrightarrow X^2\Pi$) transitions. The initial pressure of a $C_2H_6 + O_2$ mixture is 7.56 torr.

sity are more complicated. This can be explained by the fact that a large amount of the intermediate components (probably of unsaturated hydrocarbons and CO) is accumulated in the initial phase of oxidation and during the subsequent oxidation of these components. Figure 10 shows an example of the time behavior of the time-integrated emission from a discharge in ethane at a pressure of 7.54 torr. It can be seen that the curves obtained for different emitting states differ substantially from one another.

Figure 11 shows the times of complete oxidation that were determined from different emission bands for mixtures of hydrocarbons (beginning from ethane) with oxygen. The time of complete oxidation was defined as the time over which the emission signals at wavelengths of 290 and 307.8 nm (which correspond to the CO_2^+ ($B^2\Sigma \longrightarrow X^2\Pi$) and OH($A^2\Sigma \longrightarrow X^2\Pi$) transitions) reached a level of $0.95I_\infty$ and the emission signals at wavelengths of 430 and 518.6 nm (which correspond to the CH($A^2\Delta \longrightarrow X^2\Pi$) and CO($B^1\Sigma \longrightarrow A^1\Pi$) transi-

Table 4. Times of complete oxidation of hydrocarbons τ_{ox}, determined from the CO ($B^1\Sigma \longrightarrow A^1\Pi$) emission band, as functions of the initial pressure in the mixture

Pressure, torr	0.76	1.51	2.27	3.02	3.78	4.54	5.29	6.05	6.80	7.56	8.32	9.07	9.83	10.06
τ_{ox}, s ($CH_4 + O_2$)	17	43	63	69	74	84	97	125	149	131	172	175	320	294
τ_{ox}, s ($C_2H_6 + O_2$)	28	27	24	26	30	36	44	51	61	67	80	87	110	131
τ_{ox}, s ($C_3H_8 + O_2$)	25	25	24	26	30	39	44	50	58	69	81	93	114	135
τ_{ox}, s ($C_4H_{10} + O_2$)	26	25	24	26	29	38	42	46	54	69	87	100	121	144
τ_{ox}, s ($C_5H_{12} + O_2$)	18	24	26	25	31	38	47	53	63	71	90	104	118	143
τ_{ox}, s ($C_6H_{14} + O_2$)	23	27	24	25	34	38	51	53	73	69	81	88	109	130
τ_{ox}, s (CH_4 + air)	26	18	19	24	22	29	33	34	44	46	47	56	73	–
τ_{ox}, s (C_5H_{12} + air)	34	16	14	14	16	18	19	20	20	25	33	34	37	45
τ_{ox}, s (C_6H_{14} + air)	45	13	17	17	17	14	20	22	22	22	28	27	33	35

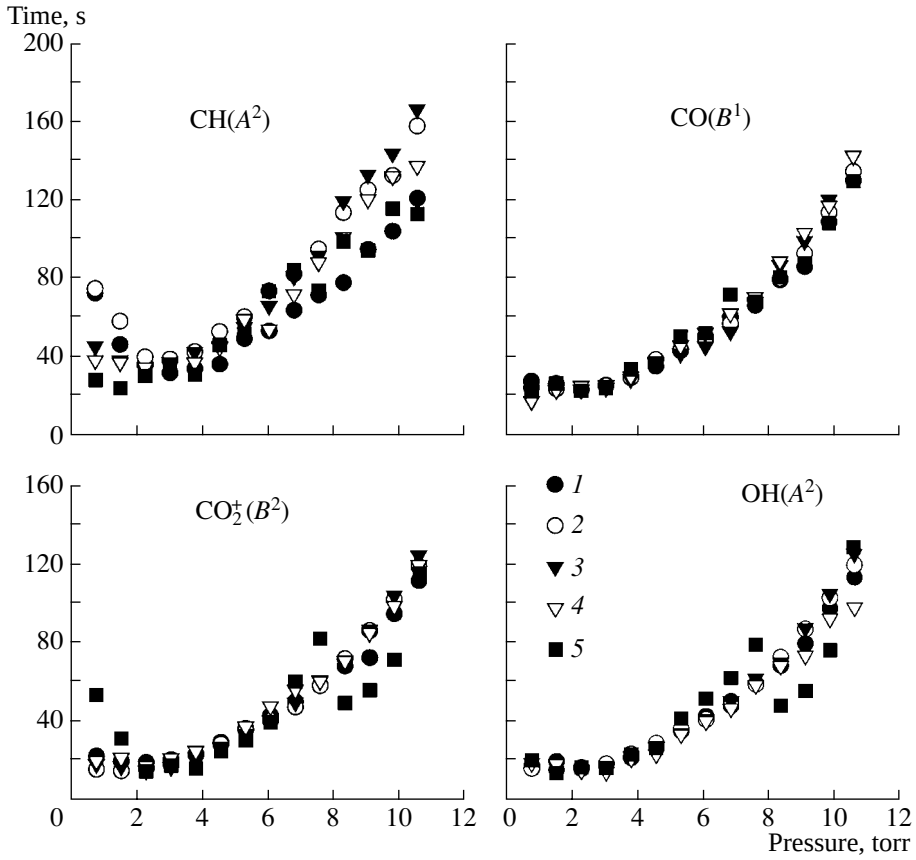

Fig. 11. Times of complete oxidation in hydrocarbon–oxygen mixtures, determined from the CH($A^2\Delta \longrightarrow X^2\Pi$), CO($B^1\Sigma \longrightarrow A^1\Pi$), $CO_2^+(B^2\Sigma \longrightarrow X^2\Pi)$, and OH($A^2\Sigma \longrightarrow X^2\Pi$) emission bands, as functions of the initial pressure in the mixture: (*1*) $C_2H_6 : O_2$, (*2*) $C_3H_8 : O_2$, (*3*) $C_4H_{10} : O_2$, (*4*) $C_5H_{12} : O_2$, and (*5*) $C_6H_{14} : O_2$.

tions) reached a level of $1.05I_\infty$. We note that the characteristic times that were determined for the same mixture from different emission bands differed markedly because the deexcitation and excitation of the products and reagents influence the emission from different components in different ways. However, the times determined from the same emission bands in different mixtures of hydrocarbons (beginning from ethane) with oxygen coincide well with one another. The scatter in the oxidation time was minimal when it was determined from the CO($B^1\Sigma \longrightarrow A^1\Pi$) emission band. Therefore, the time determined from this emission band was assumed to be the time of complete oxidation.

Figure 12 and Table 4 show the times of complete oxidation of hydrocarbons in all of the mixtures under study. It can be seen that the oxidation time of methane is always nearly twice as long as the oxidation times of other hydrocarbons both in mixtures with oxygen and in mixtures with air. For other hydrocarbons, the times coincide to within the experimental error. In hydrocarbon–air mixtures, the characteristic oxidation time of hydrocarbons, including methane, is a factor of 2 to 3 shorter than that in mixtures with oxygen. Taking into account that the total amount of hydrocarbons in their

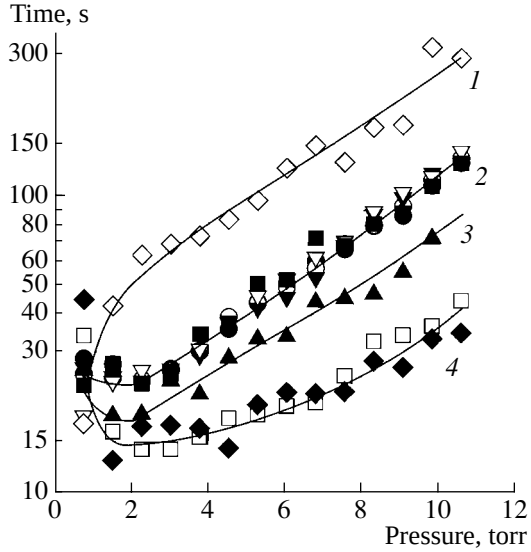

Fig. 12. Times of complete oxidation of hydrocarbons, determined from the CO($B^1\Sigma \longrightarrow A^1\Pi$) emission band, as functions of the initial pressure for different mixtures (see Tables 1 and 4): (*1*) $CH_4 + O_2$, (*2*) stoichiometric mixtures of hydrocarbons (from ethane to hexane) with oxygen, (*3*) CH_4 : air, and (*4*) stoichiometric mixtures of pentane and hexane with air.

mixtures with air is smaller at the same initial pressures, we can conclude that the oxidation rate in mixtures with air is almost half that in mixtures with oxygen.

Thus, mixtures of alkanes with oxygen or air at room temperature are completely oxidized under the action of pulsed discharges. The oxidation rate of all of the hydrocarbons under study (beginning from ethane) in their stoichiometric mixtures with oxygen or air is almost the same for all the hydrocarbons. Methane oxidizes at half the speed of any other hydrocarbon under consideration.

5. CONCLUSIONS

The kinetics of the slow oxidation of alkanes (from CH_4 to C_6H_{14}) in their stoichiometric mixtures with oxygen or air under the action of a repetitive FIW discharge was studied experimentally.

The development of a repetitive nanosecond discharge in a screened gap of moderate length has been described qualitatively. The uniformity of energy deposition in the discharge gap was studied experimentally. It was shown that, at a total pressure in the mixture below 3 torr, the discharge develops at the background of a large cathode voltage drop, which results in a nonuniform energy deposition. At pressures of $p > 3$ torr, most of the energy is deposited during the short-circuit stage of the discharge, when the cathode voltage drop is insignificant and the field strength is constant over the entire discharge gap; as a result, the energy deposition turns out to be fairly uniform.

It was shown that hydrocarbons are completely oxidized under the action of a nanosecond discharge at room temperature. For hydrocarbons heavier than methane, the times of complete oxidation are found to be the same at the same deposited energy and the same initial pressure in a stoichiometric mixture. Methane oxidizes at nearly half the speed of other hydrocarbons. The oxidation efficiency of hydrocarbons in their stoichiometric mixtures with oxygen is nearly twice as high as that in their mixtures with air.

ACKNOWLEDGMENTS

This work was supported in part by the Russian Foundation for Basic Research (project no. 02-03-33376), the RF Presidential Program for Support of Young Doctors of Science (grant no. MD-334.2003.02), the RF Ministry of Education (grant no. E02-3.2-97), the International Science and Technology Center (project no. ISTC-1440), the EOARD/CRDF (project no. PR0-1349-MO-02), and the Young Scientists Grant of the Joint Russian–American Basic Research and Development Foundation Program no. MO-011-0 (proposal no. Y1-C-11-09).

REFERENCES

1. L. S. Polak, A. A. Ovsyannikov, D. I. Slovetskiĭ, and F. B. Vurzel', *Theoretical and Applied Plasmochemistry* (Nauka, Moscow, 1975).
2. F. J. Zanner and L. A. Bertram, IEEE Trans. Plasma Sci. **11**, 32 (1983).
3. J. P. Boeuf, J. Phys. D **36**, 53 (2003).
4. Ch. Hollenstein, Plasma Phys. Controlled Fusion **42**, R93 (2000).
5. L. M. Vasilyak, S. V. Kostyuchenko, N. N. Kudryavtsev, and I. V. Filyugin, Usp. Fiz. Nauk **164**, 263 (1994) [Phys. Usp. **37**, 247 (1994)].
6. S. M. Starikovskaia, N. B. Anikin, S. V. Pancheshnyi, *et al.*, Plasma Sources Sci. Technol. **10**, 344 (2001).
7. N. B. Anikin, S. M. Starikovskaia, and A. Yu. Starikovskii, Fiz. Plazmy **26**, 647 (2000) [Plasma Phys. Rep. **26**, 606 (2000)].
8. É. I. Asinovskiĭ, L. M. Vasilyak, V. V. Markovets, and Yu. M. Tokunov, Dokl. Akad. Nauk SSSR **263**, 1364 (1982) [Sov. Phys. Dokl. **27**, 348 (1982)].
9. S. M. Starikovskaia, A. Yu. Starikovskii, and D. V. Zatsepin, J. Phys. D **31**, 1118 (1998).
10. S. A. Bozhenkov, S. M. Starikovskaia, and A. Yu. Starikovskii, Combust. Flame **133**, 133 (2003).
11. R. Kh. Amirov, É. I. Asinovskiĭ, and S. V. Kostyuchenko, Teplofiz. Vys. Temp. **29**, 671 (1991).
12. A. V. Krasnochub, Candidate's Dissertation (Moscow Institute for Physics and Technology, Moscow, 1998).
13. A. V. Krasnochub and L. M. Vasilyak, J. Phys. D **34**, 1678 (2001).
14. N. B. Anikin, S. V. Pancheshnyi, S. M. Starikovskaia, and A. Yu. Starikovskii, J. Phys. D **31**, 826 (1998).
15. L. M. Kof and A. Yu. Starikovskii, in *Proceedings of the 26th Symposium on Combustion, Napoli, 1996*, p. R.05-052.
16. H. J. Curran, P. Gaffuri, W. J. Pitz, and C. K. Westbrook, Combust. Flame **114**, 149 (1998).
17. É. I. Asinovskiĭ, L. M. Vasilyak, A. V. Kirillin, and V. V. Markovets, Teplofiz. Vys. Temp. **13**, 195 (1975).
18. N. B. Anikin, S. M. Starikovskaia, and A. Yu. Starikovskii, J. Phys. D **34**, 177 (2001).
19. N. B. Anikin, S. M. Starikovskaia, and A. Yu. Starikovskii, Teplofiz. Vys. Temp. **36**, 992 (1998).
20. Yu. P. Raizer, *Gas Discharge Physics* (Nauka, Moscow, 1987; Springer-Verlag, Berlin, 1991).
21. Yu. D. Korolev and G. A. Mesyats, *Field-Emission and Explosion Processes in Gas Discharges* (Nauka, Novosibirsk, 1982).
22. D. R. Farley and R. J. Cattolica, Chem. Phys. Lett. **274**, 445 (1997).
23. L. A. Kuznetsova, N. E. Kuz'menko, Yu. Ya. Kuzyakov, and Yu. A. Plastinin, *Probabilities of Optical Transitions in Diatomic Molecules* (Nauka, Moscow, 1980).
24. S. V. Pancheshnyi, S. M. Starikovskaia, and A. Yu. Starikovskii, J. Phys. D **32**, 1 (1999).

Translated by N.F. Larionova

Plasma Physics Reports, Vol. 30, No. 12, 2004, pp. 1043–1051. Translated from Fizika Plazmy, Vol. 30, No. 12, 2004, pp. 1121–1129.

LOW-TEMPERATURE PLASMA

Two-Dimensional Plasma Density Distributions in Low-Pressure Gas Discharges

E. V. Berlin, S. A. Dvinin, V. V. Mikheev, M. O. Omarov, and V. S. Sviridkina

Moscow State University, Vorob'evy gory, Moscow, 119899 Russia

Received November 27, 2003; in final form, March 22, 2004

Abstract—The plasma density distribution in a two-dimensional nonuniform positive column of a low-pressure gas discharge is studied in the hydrodynamic approximation with allowance for ion inertia. Exact solutions are derived for discharges in a rectangular and a cylindrical chamber. Asymptotic solutions near the coordinate origin and near the critical surface are considered. It is shown that, for potential plasma flows, the flow velocity component normal to the plasma boundary is equal to the ion acoustic velocity. The results obtained can be used to analyze the processes occurring in low-pressure plasmochemical reactors. *© 2004 MAIK "Nauka/Interperiodica".*

1. INTRODUCTION

Plasma sources operating at low pressures of plasma-producing gases have recently come into general use in aerospace engineering and microelectronics technologies. In such applications, the ion mean free path can be either longer or shorter than the characteristic dimensions of the system. In existing kinetic [1–5] and hydrodynamic [2, 6, 7] models of the positive column of a gas discharge, the plasma is assumed to be inhomogeneous in only one direction. However, in actual technological plasma sources in which the plasma flow to the wall should be uniform in order to ensure a constant rate of chemical processing, the transverse and longitudinal plasma dimensions are of the same order of magnitude. However, to the best of our knowledge, no attempts have been made to solve the relevant problem for a system in which the ion mean free path exceeds the plasma dimensions.

Moreover, in hydrodynamics, the problem of formulating the boundary conditions for a gas-discharge plasma remains unresolved. In the quasineutral approximation (i.e, when the Debye length is much less than the characteristic dimensions of the system), Bohm's criterion [8], which implies that the plasma flow velocity to the wall is equal to the ion acoustic velocity, is frequently used as a boundary condition for a one-dimensional plasma flow. A comprehensive review of the literature devoted to the analysis of the applicability conditions and formulation of Bohm's criterion in the hydrodynamic and kinetic approximations was given by Riemann [9]. In a two-dimensional plasma flow, the ion velocity can be directed at any angle to the boundary. It can be expected that, in most problems, the conditions for the sheath formation should be analogous to those for the generation of an oblique shock wave at low Mach numbers in hydrodynamics; i.e., the ion velocity component normal to the boundary should be equal to the local speed of sound [10–12]. In actuality, however, the problem is more complicated because, in a divergent nozzle, the shock wave either can be formed at flow velocities above the speed of sound or cannot be formed at all (a Laval nozzle). Therefore, this question also requires additional investigations.

2. FORMULATION OF THE PROBLEM

In this study, we will obtain a number of possible spatial distributions of the plasma density in the hydrodynamic approximation. Although the ions in the long-mean-free-path regime (which will be considered as a limiting one) should be described by a kinetic equation, it can be expected that the hydrodynamic approach will provide a qualitatively correct solution to the problem and a physically meaningful boundary condition. It can also be anticipated that the algorithm for constructing a hydrodynamic solution will serve as the basis to construct two-dimensional solutions to the ion kinetic equation. We denote the boundary surface of the plasma by S and start with the one-fluid hydrodynamic equations

$$\frac{\partial n}{\partial t} + \nabla \cdot (n\mathbf{V}) = n\nu_i, \tag{1}$$

$$\frac{\partial \mathbf{V}}{\partial t} + (\mathbf{V} \cdot \nabla)\mathbf{V} = -V_S^2 \frac{\nabla n}{n} - \nu_{in}\mathbf{V}. \tag{2}$$

Here, n is the plasma density (the positive column is assumed to be quasineutral), $\mathbf{V} = (u, v)$ is the hydrodynamic velocity of the plasma flow (where u and v are the x and y components of the velocity, respectively), $V_S = \sqrt{T_e/M}$ is the ion acoustic speed, the electron temperature T_e is expressed in energy units and is assumed to be constant, M is the mass of an ion, ν_{in} is the ion–neutral collision frequency, and ν_i is the ionization fre-

1063-780X/04/3012-1043$26.00 © 2004 MAIK "Nauka/Interperiodica"

quency. The ions are assumed to recombine at the critical surface S at which the one-to-one correspondence between coordinates and velocities breaks down.

We will solve the problem about the plasma flow in the same manner as in the standard hydrodynamics [10, 11], restricting the study to the class of steady-state two-dimensional potential flows.[1] It should be noted that Thomson's theorem fails to hold for our problem. Carrying out the same manipulations as in [12], we obtain the equations

$$\frac{d}{dt}\oint \mathbf{V}\cdot d\mathbf{l} = -\nu_{in}\iint(\nabla\times\mathbf{V})\cdot d\mathbf{S},$$

$$\frac{\partial}{\partial t}(\nabla\times\mathbf{V}) - \nabla\times(\mathbf{V}\times(\nabla\times\mathbf{V})) = -\nu_{in}(\nabla\times\mathbf{V}).$$

We thus see that, because of plasma friction with neutral particles (the neutral gas is assumed to be immobile), the vorticity decreases with time. An important point for our analysis is that, if the flow is potential at any time, then it will continue to remain potential.

The flow is assumed to be either planar ($\mu = 0$) or axisymmetric ($\mu = 1$; in this case, the coordinate y is the distance from the axis) and also symmetric about the coordinate origin. The electron density at the origin is maximum, and the ion velocity at the origin is assumed to be zero. Under these assumptions, Eqs. (1) and (2) reduce to[2]

$$v_x - u_y = 0, \tag{3}$$

$$\begin{aligned}(u^2 - V_S^2)u_x + uv(v_x + u_y) + (v^2 - V_S^2)v_y \\ = \frac{\mu}{y}V_S^2 v - \nu_i V_S^2 - \nu_{in}(u^2 + v^2).\end{aligned} \tag{4}$$

We introduce the velocity potential $\mathbf{V} = \nabla\varphi$ to write Eq. (4) as

$$\begin{aligned}(u^2 - V_S^2)\varphi_{xx} + 2uv\varphi_{xy} + (v^2 - V_S^2)\varphi_{yy} \\ = \frac{\mu}{y}V_S^2\varphi_y - \nu_i V_S^2 - \nu_{in}(\varphi_x^2 + \varphi_y^2).\end{aligned}$$

In terms of the velocity potential, the plasma density can easily be calculated from the equation

$$\nabla\frac{(\nabla\varphi)^2}{2} = -V_S^2\nabla\ln n - \nu_{in}\nabla\varphi.$$

Taking into account the fact that the velocity potential at the coordinate origin is zero and integrating this equation along the current lines yields

$$n = n_0\exp\left(-\frac{(\nabla\varphi)^2}{2V_S^2} - \frac{\nu_{in}}{V_S^2}\varphi\right), \tag{5}$$

where n_0 is the electron density at the spatial point at which the flow velocity is zero.

Applying the hodograph transformation [8, 9] to Eqs. (3) and (4), we obtain

$$x_v - y_u = 0, \tag{6}$$

$$\begin{aligned}(u^2 - V_S^2)y_v - uv(y_u + x_v) + (v^2 - V_S^2)x_u \\ = \left\{\frac{\mu}{y}V_S^2 v - \nu_{in}(u^2 + v^2) - \nu_i V_S^2\right\}\{x_u y_v - x_v y_u\}.\end{aligned} \tag{7}$$

In contrast to the case of classical hydrodynamics (without allowance for chemical processes), Eq. (7) is nonlinear not only for axisymmetric but also for planar flows. The boundary surface of a two-dimensional flow is a surface at which the one-to-one correspondence between coordinates and velocities breaks down, i.e., where the Jacobian vanishes,

$$\frac{\partial(x, y)}{\partial(u, v)} = x_u y_v - x_v y_u = 0. \tag{8}$$

Equations (6) and (7) can be further simplified by introducing the Legendre potentials in such a way as to make the final equation dimensionless:

$$\begin{aligned}U = u/V_S, \quad V = v/V_S, \quad x = \frac{V_S}{\nu_i}X = \frac{V_S}{\nu_i}\Phi_U(U, V), \\ y = \frac{V_S}{\nu_i}Y = \frac{V_S}{\nu_i}\Phi_V(U, V).\end{aligned} \tag{9}$$

As a result, Eq. (7) takes the form

$$\begin{aligned}(U^2 - 1)\Phi_{VV} - 2UV\Phi_{UV} + (V^2 - 1)\Phi_{UU} \\ = \left\{\frac{\mu}{\Phi_V}V - 1 - \zeta(U^2 + V^2)\right\}\{\Phi_{UU}\Phi_{VV} - \Phi_{UV}^2\},\end{aligned} \tag{10}$$

where we have introduced the notation $\zeta = \nu_{in}/\nu_i$, which will be used below.

Since the potential of the velocity field is related to the Legendre potentials by the relationship

$$\varphi = -\Phi + XU + YV = -\Phi + U\Phi_U + V\Phi_V, \tag{11}$$

the plasma density can be calculated from the formula

$$n = n_0\exp\left(-\frac{U^2 + V^2}{2} - \zeta(U\Phi_U + V\Phi_V - \Phi)\right). \tag{12}$$

The position of the boundary is determined by the equation

$$\Phi_{UU}\Phi_{VV} - \Phi_{UV}^2 = 0. \tag{13}$$

[1] We do not address here the problem of the flow stability.

[2] Here and below, the partial derivative of the function a with respect to the variable b is denoted by a_b, as is usually done in hydrodynamics.

It is sometimes more convenient to use the absolute value of the velocity, W, and the angle θ [12]:

$$U = W\cos\theta,\ \ V = W\sin\theta,\ \ X = \Phi_W\cos\theta - \frac{\sin\theta}{W}\Phi_\theta,$$
$$Y = \Phi_V\sin\theta + \frac{\cos\theta}{V}\Phi_\theta. \tag{14}$$

In these variables, Eq. (10) reads

$$(1-W^2)(\Phi_{\theta\theta} + W\Phi_W) + W^2\Phi_{WW}$$
$$= \{1+\zeta W^2\}\left\{\Phi_{WW}(W\Phi_W + \Phi_{\theta\theta}) - \left(\Phi_{W\theta} - \frac{\Phi_\theta}{W}\right)^2\right\}. \tag{15}$$

The cylindrical coordinates $R = \sqrt{X^2+Y^2}$ and Θ are given by the formulas

$$R = \sqrt{\Phi_W^2 + \Phi_\theta^2/W^2},$$
$$\Theta = \arctan\left\{\frac{\Phi_W\sin\theta + \frac{\cos\theta}{W}\Phi_\theta}{\Phi_W\cos\theta - \frac{\sin\theta}{W}\Phi_\theta}\right\}. \tag{16}$$

The flow is exactly radial at the points at which $\Phi_\theta = 0$, the angle between the flow velocity and the position vector being $\Theta - \theta = \arctan(\Phi_\theta/W\Phi_W)$. The boundary condition has the form

$$\frac{\partial(x,y)}{\partial(W,\theta)} = \Phi_{WW}(W\Phi_W + \Phi_{\theta\theta}) - \left(\Phi_{W\theta} - \frac{\Phi_\theta}{W}\right)^2 = 0, \tag{17}$$

and the plasma density is given by a formula analogous to formula (12):

$$n = n_0\exp\left(-\frac{W^2}{2} - \zeta(W\Phi_W - \Phi)\right). \tag{18}$$

3. GENERAL PROPERTIES OF THE SOLUTIONS: SOLUTION NEAR THE COORDINATE ORIGIN

Here, we consider a solution that is slightly inhomogeneous in the azimuthal direction:

$$\Phi = \Phi_0(W) + \delta\Phi(W,\theta), \tag{19}$$

where the axisymmetric solution $\Phi_0(W)$ to Eq. (15) can be calculated numerically or can be found in the form of a series, $\Phi_0(W) = \sum_{n=1}^{\infty} A_{0n}W^{2n}$, and the nonaxisymmetric component of the solution is

$$\delta\Phi(W) = \sum_{m=1}^{\infty}\{B_m^1(W)\sin(m\theta) + B_m^2(W)\cos(m\theta)\}. \tag{20}$$

In the vicinity of the coordinate origin, we can set $\delta\Phi(W) \ll \Phi(W)$. In this case, the equation for $\delta\Phi(W)$ takes the form

$$(1-W^2)(\delta\Phi_{\theta\theta} + W\delta\Phi_W) + W^2\delta\Phi_{WW}$$
$$= \{1+\zeta W^2\}[\Phi_{0WW}(W\delta\Phi_W + \delta\Phi_{\theta\theta}) + W\Phi_{0W}\delta\Phi_{WW}]. \tag{21}$$

We seek the asymptotic expressions for each of the terms in representation (20) in the form

$$B_m^{i,j}(W) = B_\alpha W^\alpha. \tag{22}$$

Substituting expressions (22) into Eq. (21) and taking into account the fact that the solution Φ_0 to Eq. (15) is independent of the azimuthal angle, we obtain the formula for the term with the minimum power α:

$$B_\alpha(1-2A_2)(\alpha^2 - m^2) = 0. \tag{23}$$

This formula yields the following asymptotic expression for nonaxisymmetric component (20) at $r \longrightarrow 0$:

$$\delta\Phi(W) = \sum_{m=1}^{\infty}\{\tilde{B}_{m0}^1 W^m\sin(m\theta) + \tilde{B}_{m0}^2 W^m\cos(m\theta)\}. \tag{24}$$

Since the divergence of the velocity field of the flow described by expression (24) is zero, the flow does not affect (in the linear approximation) the ionization balance and the distribution of the plasma density near the coordinate origin. The constants $\tilde{B}_{m0}^1$ and $\tilde{B}_{m0}^2$ can be chosen arbitrarily (in what follows, we will assume that they are prescribed). In fact, these constants should be defined so that the boundary of the flow described by Eqs. (6) and (7) coincides with the boundary of the chosen discharge region (e.g., of a rectangle); in this case, they are Fourier coefficients in the expansion of the corresponding functions in the azimuthal angle.

By virtue of representation (20) and expression (24), the solution to Eq. (15) can be sought in the form

$$\Phi = \sum_{n=1}^{\infty} A_{0n}W^{2n} + \sum_{m=1}^{\infty}\sum_{k=0}^{\infty} W^{m+2k}\{B_{mk}^{(1)}\sin(m\theta) + B_{mk}^{(2)}\cos(m\theta)\}. \tag{25}$$

The coefficients in representation (25) can be calculated by inserting it into Eq. (15) and collecting terms with the same azimuthal modes and the same powers of velocity. Since the resulting expressions are very involved, we do not write them out here. Taking into account the nonlinear coupling between the harmonics

will change the expressions for the coefficients A_{0n} of the main distribution.[3]

4. BEHAVIOR OF THE SOLUTION NEAR THE CRITICAL SURFACE

Here, we examine the general properties of the solution near the critical surface. We seek the solution in the form

$$\begin{aligned}\Phi(U, V) &= \Phi(U_{S0} + \delta U, V_{S0} + \delta V)\\ &= \Phi(U_{S0}, V_{S0}) + \sum_{m=2}^{\infty}\sum_{k=0}^{m} a_{m-k,k}\delta U^{m-k}\delta V^k,\end{aligned} \quad (26)$$

where (U_{S0}, V_{S0}) is a point at the critical surface. Since the coefficients a_{01} and a_{10} determine the position of the point $(X_{S0}(U_{S0}, V_{S0}), Y_{S0}(U_{S0}, V_{S0}))$ in the xy plane, they can be set at zero; this indicates that the coordinate origin is translated to this point. Equation (13) for the critical surface implies that the relationship $4a_{20}a_{02} - a_{11}^2 = 0$ is satisfied. We choose the coordinate system in such a way that the critical surface is crossed by moving only in the x direction; in this case, we have $a_{20} = a_{11} = 0$.

We restrict our analysis to polynomials of order less than four, which provides a fairly accurate description of the flow near the critical surface. In this case, we have

$$\begin{aligned}X &= (3a_{30}\delta U^2 + 2a_{21}\delta U\delta V + a_{12}\delta V^2)\\ &+ (4a_{40}\delta U^3 + 3a_{31}\delta U^2\delta V + 2a_{22}\delta U\delta V^2\\ &+ a_{13}\delta V^3) + \ldots,\end{aligned} \quad (27)$$

$$\begin{aligned}Y &= 2a_{02}\delta V + (a_{21}\delta U^2 + 2a_{12}\delta U\delta V + 3a_{03}\delta V^2)\\ &+ (a_{31}\delta U^3 + 2a_{22}\delta U^2\delta V + 3a_{13}\delta U\delta V^2\\ &+ 4a_{04}\delta V^3) + \ldots.\end{aligned} \quad (28)$$

The parametric formula for the coordinates of the critical surface near the point (U_{S0}, V_{S0}) can be obtained by expressing δV as a function of δU with the help of Eq. (13),

$$\begin{aligned}\Phi_{UU}\Phi_{VV} - \Phi_{UV}^2 &= 4\{3a_{02}a_{30}\delta U + a_{02}a_{21}\delta V\\ &+ (6a_{02}a_{40} + 3a_{30}a_{12} - a_{21}a_{21})\delta U^2\\ &+ (3a_{02}a_{31} + 9a_{30}a_{03} - a_{21}a_{12})\delta U\delta V\\ &+ (a_{02}a_{22} + 3a_{21}a_{03} - a_{12}a_{12})\delta V^2 + \ldots\}\\ &= A_{10}\delta U + A_{01}\delta V + A_{20}\delta U^2 + A_{11}\delta U\delta V\\ &+ A_{02}\delta V^2 + \ldots = 0\end{aligned} \quad (29)$$

and by substituting it into relationships (27) and (28). To second order in δU, we obtain $\delta V = -3a_{30}\delta U/a_{21}$ and, accordingly,

$$\begin{aligned}X &= 3(3a_{12}(a_{30}/a_{21})^2 - a_{30})\delta U^2 + \ldots,\\ Y &= -6a_{02}a_{30}\delta U/a_{21}\\ &+ (a_{21} - 6a_{12}a_{30}/a_{21} + 27a_{03}(a_{30}/a_{21})^2)\delta U^2 + \ldots.\end{aligned}$$

Hence, at the point in question, the normal to the critical surface is directed along the x axis.[4] The fact that the point (U_{S0}, V_{S0}) is a point of the critical surface imposes limitations on the plasma flow velocity at this surface. Substituting expansion (26) into Eq. (10) and equating the coefficients of the same powers of $\delta U^i\delta V^i$, we arrive at the following relationship for $i = j = 0$:

$$(1 - U_{S0}^2)a_{02} = 0. \quad (30)$$

Thus, at a regular point ($a_{02} \neq 0$), the flow velocity component that is normal to the wall and is equal to the ion acoustic velocity; in this case, the flow velocity component parallel to the boundary can be arbitrary. The coefficient a_{02} determines the characteristic dimension of the flow in the y direction. Hence, we have generalized the result obtained by Persson [7] for one-dimensional plasma flows to the case of an arbitrarily shaped smooth boundary of a two-dimensional region. With allowance for relationship (30), the coefficients in expansion (26) satisfy the equations

$$\begin{aligned}3a_{30}\{(V_{S0}^2 - 1) + 2a_{02}\} - 2a_{21}V_{S0} &= -2a_{02},\\ a_{21}\{(V_{S0}^2 - 1) + 2a_{02}\} - 2a_{12}V_{S0} &= 0,\end{aligned} \quad (31)$$

$$\begin{aligned}6a_{40}\{(V_{S0}^2 - 1) + 2a_{02}\} - 3a_{31}V_{S0}\\ = -a_{02} - 2a_{12} + 2a_{21}V_{S0} - 6a_{30}a_{12} + 2a_{21}^2,\\ 3a_{31}\{(V_{S0}^2 - 1) + 2a_{02}\} - 4a_{22}V_{S0}\\ = -6a_{03} + 2a_{21} + 2a_{12}V_{S0} - 6a_{30}V_{S0}\\ - 18a_{30}a_{03} + 2a_{21}a_{12},\\ a_{22}\{(V_{S0}^2 - 1) + 2a_{02}\} - 3a_{13}V_{S0}\\ = 2a_{12} - 4a_{21}V_{S0} - 6a_{21}a_{03} + 2a_{12}^2.\end{aligned} \quad (32)$$

The number of equations for the coefficients of the same powers $m = i + j$ of the terms of the series $a_{ij}U^iV^j$ is equal to $m - 2$; i.e., two coefficients (in our case, these

[3] Analogous results can be obtained using Eq. (10) and a power series expansion of the form

$$\Phi(U, V) = \sum_{m=1}^{\infty}\sum_{k=0}^{m} a_{m-k,k}U^{m-k}V^k.$$

[4] Since the point (U_{S0}, V_{S0}) is a regular point of the critical surface, at least one of the coefficients a_{21} and a_{30} is nonzero. If $a_{21} = 0$, then we obtain $\delta U = -a_{21}\delta V/3a_{30}$ and, accordingly,

$$X = (a_{12} - a_{21}^2/3a_{30})\delta V^2 + \ldots,$$

$$Y = 2a_{02}\delta V + (a_{21}^3/9a_{30}^2 - 2a_{12}a_{21}/3a_{30} + 3a_{03})\delta V^2 + \ldots,$$

which yields an analogous result.

are a_{0m} and $a_{1(m-1)}$) can be chosen arbitrarily. One of the coefficients describes the shape of the critical surface, and the other determines the characteristic spatial scale on which the flow parameters vary in the direction away from the boundary. The value of the second coefficient is in fact determined by the position and shape of the critical surface near the second boundary point in the given cross section of the plasma column. In particular, for the above expansion in polynomials of order less than four, we can specify the coefficients V_{S0}, a_{02}, a_{12}, a_{03}, a_{13}, and a_{04} independently. We now proceed to the construction of distributions that are important for practical applications.

5. DISCHARGE IN A LONG PLANAR CHAMBER

In the one-dimensional case ($\partial/\partial x \equiv 0$, $u \equiv 0$), Eq. (4) reduces to a much simpler form,

$$\left(1 + \zeta V^2 - \frac{\mu}{Y} V\right) Y_V = (1 - V^2), \qquad (33)$$

and describes the well-known density distribution [7], which, for $\mu = 0$, is integrable in terms of elementary functions:

$$Y(V, \zeta) = Y_P(V, \zeta) = \frac{1}{\sqrt{\zeta}}\left\{1 + \frac{1}{\zeta}\right\}\arctan(\sqrt{\zeta}V) - \frac{V}{\zeta}, \qquad (34)$$

$$\Phi_P(V, \zeta) = \int_0^V dV\left\{\frac{1}{\sqrt{\zeta}}\left\{1 + \frac{1}{\zeta}\right\}\arctan(\sqrt{\zeta}V) - \frac{V}{\zeta}\right\}, \qquad (35)$$

where the integration constant is set equal to zero because it is responsible only for a shift along the coordinate axis.[5]

At the point $V = 1$, we have $Y_V = 0$, which indicates that the solution does not have a unique continuation to the range of supersonic speeds. The physically meaningful portion of the distribution is the central portion lying near the point $Y = 0$ between the two extremes at which $Y_V \geq 0$; i.e., the position of the boundary (L) at which recombination occurs is determined by the condition $Y_V = 0$ (or $V_Y = \infty$). Solution (35) gives the relationships $\nu(L) = V_S$ and $L = \frac{V_S}{\nu_i}\left\{\frac{1}{\sqrt{\zeta}}\left\{1 + \frac{1}{\zeta}\right\}\arctan(\sqrt{\zeta}) - \frac{1}{\zeta}\right\}$. The former is Bohm's criterion, while the latter determines the ionization frequency in the discharge at a given position of the boundary.

[5] Integral (35) is easy to calculate; the results is

$$\Phi_P(V, \zeta) = \left\{1 + \frac{1}{\zeta}\right\}\left\{\frac{V}{\sqrt{\zeta}}\arctan(\sqrt{\zeta}V) - \frac{1}{2\zeta}\ln(1 + \zeta V^2)\right\} - \frac{V^2}{2\zeta}.$$

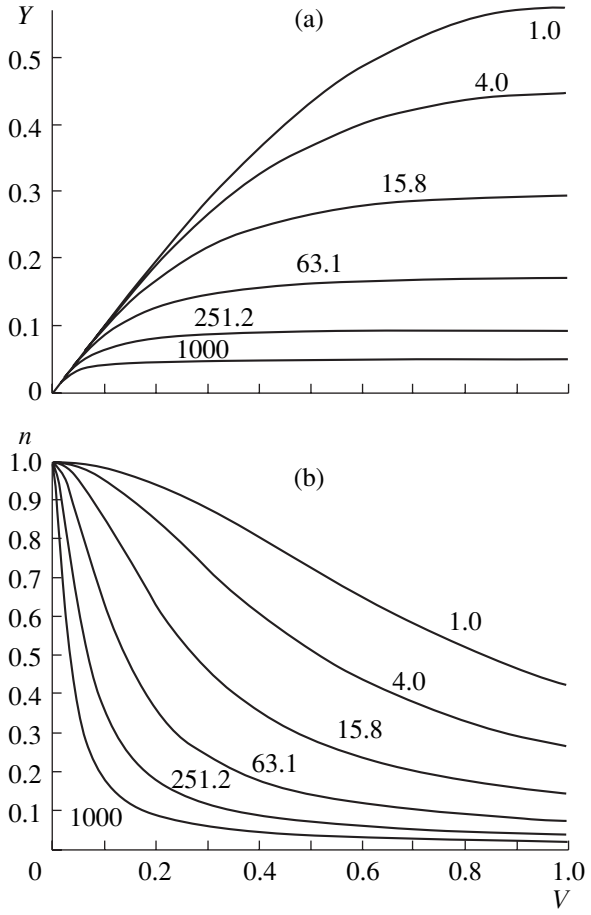

Fig. 1. (a) Coordinate Y and (b) the plasma density as functions of the velocity V for a positive discharge column in planar geometry. Numerals above the curves denote the values of the parameter ζ.

6. CYLINDRICALLY SYMMETRIC DISCHARGE

A cylindrically symmetric solution can be derived from Eq. (10) with $\mu = 1$ or from Eq. (13) with $\partial/\partial\theta \equiv 0$; in this case, it reduces to the equation

$$(1 - W^2)\Phi_W + W\Phi_{WW} = (1 + \zeta W^2)\Phi_{WW}\Phi_W. \qquad (36)$$

This equation cannot be integrated in terms of elementary functions. We denote the cylindrically symmetric solution by $\Phi_0(\zeta, V)$. The coordinate Y and the plasma density calculated from Eqs. (36) and (12) as functions of the velocity V in planar and cylindrical geometries are shown in Figs. 1 and 2, respectively.

The dependence of the boundary position (in dimensionless variables) on the parameter ζ is presented in Fig. 3. For comparison, this figure displays the results obtained for a positive discharge column not only in planar ($\mu = 0$) and cylindrical ($\mu = 1$) geometries but also in spherical ($\mu = 2$) geometry. As expected, when ion collisions play an equally important role, the boundary surface in a spherical discharge is farther

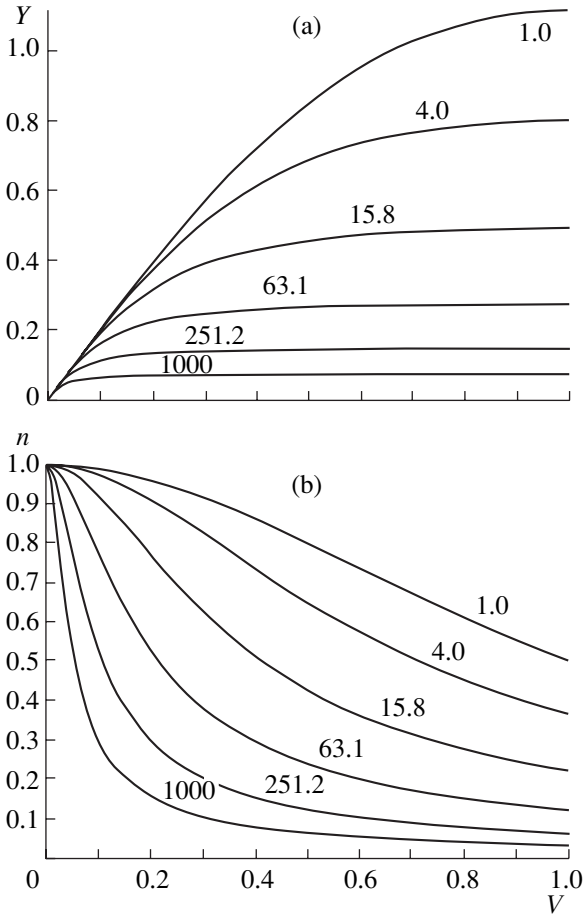

Fig. 2. (a) Coordinate Y and (b) the plasma density as functions of the velocity V for a positive discharge column in cylindrical geometry. Numerals above the curves denote the values of the parameter ζ.

from the coordinate origin than in a cylindrical discharge (and even more so in a planar discharge) because, in a spherical discharge, diffusive losses at the same distance are greater.

7. SIMPLE TWO-DIMENSIONAL FLOWS

We seek a solution to Eq. (10) in the form

$$\Phi = F(U) + G(V). \tag{37}$$

Inserting representation (37) into Eq. (10), we obtain

$$\frac{G_{VV}}{(1-V^2)} + \frac{F_{UU}}{(1-U^2)} = \left\{1 + \zeta(U^2+V^2) - \frac{\mu}{G_V}V\right\}\frac{F_{UU}}{(1-U^2)}\frac{G_{VV}}{(1-V^2)}. \tag{38}$$

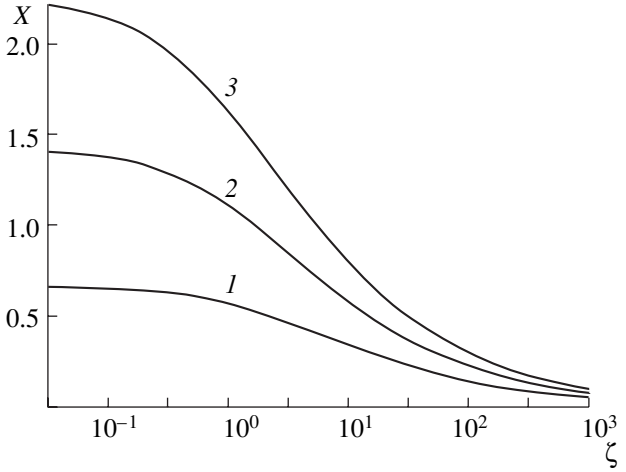

Fig. 3. Position of the boundary as a function of the parameter ζ in (*1*) planar, (*2*) cylindrical, and (*3*) spherical geometries.

We require that the following relationship be satisfied:

$$F_{UU} = \alpha^2\frac{(1-U^2)}{(1+\alpha^2\zeta U^2)}. \tag{39}$$

Substituting relationship (39) into Eq. (38) gives

$$\left\{\frac{\alpha^2-1}{\alpha^2} + \zeta V^2 - \frac{\mu}{G_V}V\right\}G_{VV} = (1-V^2). \tag{40}$$

In this case, the solution to Eq. (39) can be expressed in terms of solution (35):

$$F = \left\{1 + \frac{1}{\alpha^2\zeta}\right\} \times \left\{\frac{\alpha V}{\sqrt{\zeta}}\arctan(\alpha\sqrt{\zeta}V) - \frac{1}{2\zeta}\ln(1+\alpha^2\zeta V^2)\right\} - \frac{V^2}{2\zeta}.$$

Replacement of the variable $Y = G_V$ reduces Eq. (40) (with the corresponding change of notation for the coefficients) to Eq. (36), which has been analyzed above. The solution to this equation is very simply expressed in terms of the familiar solution to Eq. (36) (see Fig. 2b):

$$G(V) = \frac{\alpha^2}{\alpha^2-1}\Phi_0\left(V, \frac{\alpha^2\zeta}{\alpha^2-1}\right).$$

Hence, we have constructed plasma density distributions for both a rectangular and a cylindrical discharge chamber in two-dimensional geometries. This result is important for state-of-the-art technological devices. As expected, Bohm's criterion at a planar boundary is satisfied for the flow velocity component perpendicular to it.

We now consider a discharge in a cylindrical chamber with diameter r_0 and a height of $2L_0$ cm. The distribution of the plasma density in such a chamber can be determined as follows. For the solution obtained in this section, the position of the boundary is given by the equations

$$L_0 = \frac{V_S}{\nu_i}\alpha^2\Phi_{PU}\left(1, \frac{\alpha^2\nu_{in}}{\nu_i}\right),$$
$$R_0 = \frac{V_S}{\nu_i}\frac{\alpha^2}{\alpha^2-1}\Phi_{0V}\left(1, \frac{\alpha^2\nu_{in}}{(\alpha^2-1)\nu_i}\right), \quad (41)$$

where the ion–neutral collision frequency is determined by the neutral gas pressure. Equations (41) makes it possible to find the values of the coefficient α and ionization rate ν_i in the discharge in the same way as in the standard Schottky theory. Using the second of these equations, one can calculate the electron temperature, electric field strength, and other discharge parameters from known dependences [2]. The electron density distributions calculated for a planar discharge chamber are presented in Fig. 4a, and those calculated for a cylindrical chamber are given in Figs. 4b–4f.[6] Since, in all of our calculations, the ionization frequency was assumed to be spatially uniform, the calculated results are valid under the following condition for electron temperature equalization within the plasma volume: $\lambda_e/(2m/M)^{1/2} \gg L$, where λ_e is the electron mean free path; L is the characteristic spatial scale on which the parameters of the system vary; and m and M are the electron and ion masses, respectively. At low pressures, the ionization frequency can become spatially nonuniform because of the collisionless mechanisms for field absorption. To estimate the quantitative role of these mechanisms requires further investigation.

[6] It is also possible to obtain a solution for a three-dimensional rectangular discharge chamber of sizes L_X, L_Y, and L_Z. In this case, a three-dimensional analogue of Eq. (10) with $\mu = 0$ can be written as

$$(U^2-1)\frac{\partial(\Phi_V,\Phi_W)}{\partial(V,W)} + (V^2-1)\frac{\partial(\Phi_U,\Phi_W)}{\partial(U,W)}$$
$$+ (W^2-1)\frac{\partial(\Phi_U,\Phi_V)}{\partial(U,V)} - UV\left\{\frac{\partial(\Phi_U,\Phi_W)}{\partial(W,U)} + \frac{\partial(\Phi_W,\Phi_V)}{\partial(U,W)}\right\}$$
$$- UW\left\{\frac{\partial(\Phi_V,\Phi_W)}{\partial(U,V)} + \frac{\partial(\Phi_U,\Phi_V)}{\partial(V,W)}\right\}$$
$$- VW\left\{\frac{\partial(\Phi_W,\Phi_U)}{\partial(U,V)} + \frac{\partial(\Phi_U,\Phi_V)}{\partial(W,U)}\right\}$$
$$= -(1+\zeta(U^2+V^2+W^2))\frac{\partial(\Phi_U,\Phi_V,\Phi_W)}{\partial(U,V,W)},$$

where $W = V_z/V_S$. The solution to this equation can be sought in the form

$$\Phi = \alpha^2\Phi_P(U,\zeta^{(U)}) + \beta^2\Phi_P(V,\zeta^{(V)}) + \gamma^2\Phi_P(W,\zeta^{(W)}).$$

8. DISTINCTIVE FEATURES OF THE BEHAVIOR OF THE SOLUTION IN THE LONG-ION-MEAN-FREE-PATH REGIME

It is of interest to investigate the applicability of the equations derived above to the limit of small ζ values (which corresponds to a positive gas-discharge column in which the ions move freely toward the wall [1]). In this limit, the ions can in fact be described in terms of collisionless hydrodynamics; in this case, however, the ionizing electron collisions should be taken into account because only the fastest electrons are absorbed at the plasma boundary, while the remaining electrons are reflected from the potential barrier. Elastic electron collisions are unimportant because electrons are much lighter than ions and neutrals. The coordinate of the boundary of a positive discharge column is equal to $Y_G = 2/3$ in planar geometry, $Y_G = 1.427$ in cylindrical geometry, and $Y_G = 2.26$ in spherical geometry. A comparison of the one-dimensional hydrodynamic solution with the one-dimensional solution to the kinetic equation shows that the former overestimates the losses to the wall. Thus, in the kinetic approximation, we have $Y_G = 0.58$, 1.1, and 1.6 for a planar, a cylindrical, and a spherical plasma column, respectively (see, e.g., [1, 4]). This discrepancy is due to the fact that, in the collisionless approximation, Eq. (5) reduces to the Bernoulli integral

$$n = n_0\exp\left(-\frac{V^2}{2V_S^2}\right), \quad (42)$$

which relates the ion flow velocity to the electric potential difference between the point at which the measurements are performed and the point from which the current line originates (in our case, the coordinate origin). On the other hand, not all of the ions that reach a given point have been produced at the coordinate origin; consequently, the actual hydrodynamic flow velocity obtained from the kinetic equation is lower than that calculated from Bernoulli integral (42). In the hydrodynamic approximation, this effect could be taken into account by introducing the ion temperature, which, however, would depend on the properties of the flow along the entire streamline. Nevertheless, the fact that the flow velocity is lower than that calculated from formula (42) can be accounted for phenomenologically by introducing the effective ionization-related ion collision frequency. In particular, the one-dimensional solutions with $\zeta = 0.602$, 1.0, and 1.1 are close to the corresponding numerical solutions to the one-dimensional ion kinetic equation [4] for a planar, a cylindrical, and a spherical positive discharge column, respectively. An increase in ζ with increasing dimensionality of the problem is attributed to the fact that, in cylindrical and spherical geometries, the number of slow ions is larger than in planar geometry.

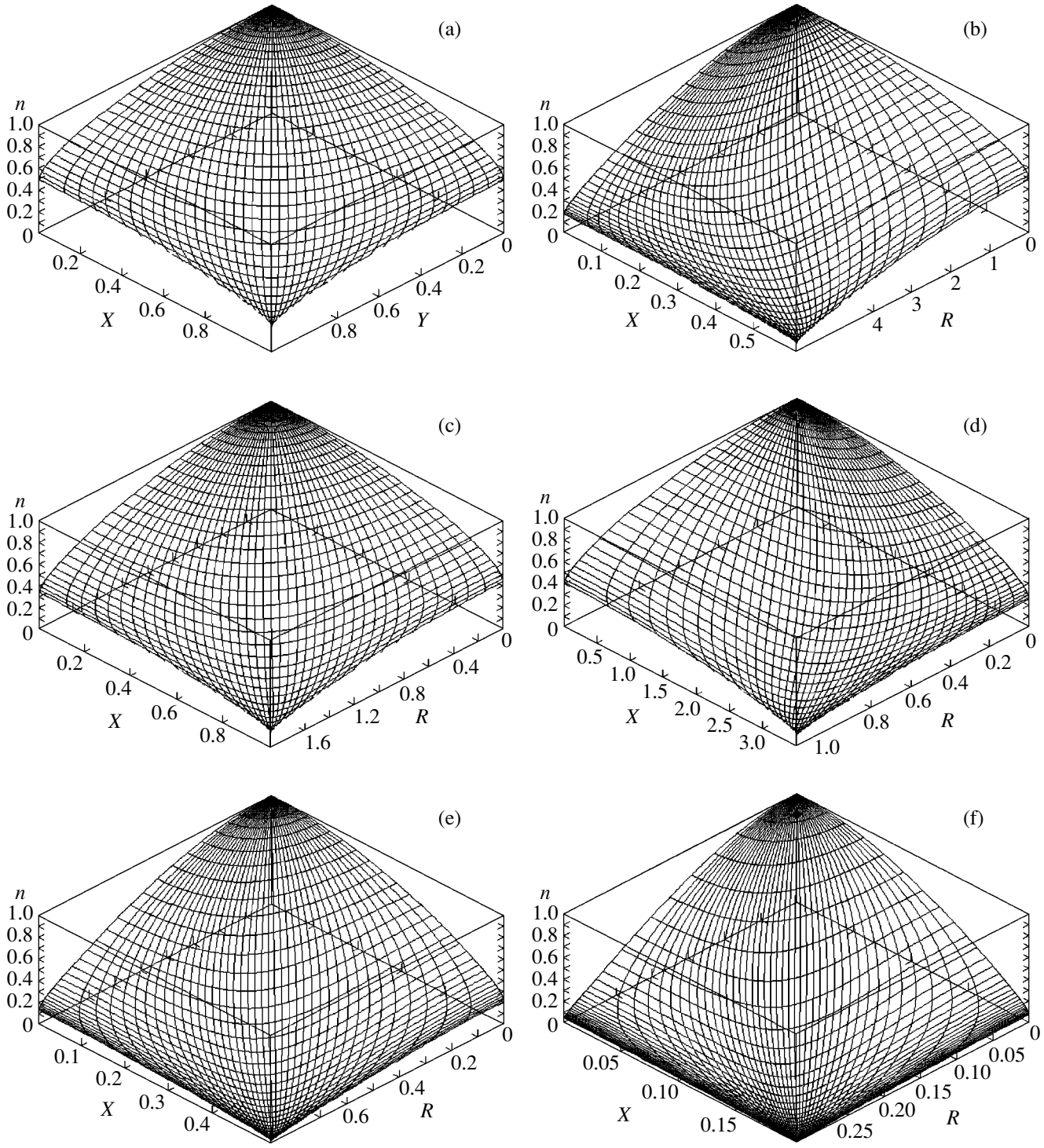

Fig. 4. Electron density distributions in discharges in (a) a planar and (b–f) a cylindrical chamber for ζ = (a) 0.6, (b–d) 1.1, (e) 10, and (f) 100 and α^2 = (a, c, e, f) 2.0 and (b, d) 1.1. The curves forming the surfaces are contours of constant velocity modulus W and constant velocity direction (or, equivalently, constant angle θ).

9. CONCLUSIONS

We have constructed spatial distributions of the plasma density and the velocity of the plasma flow to the wall in a positive column of a gas discharge in the diffusive regime with allowance for ion inertia for several different configurations of the plasma boundary. We have calculated the ionization frequency in the dis-

charge plasma as a function of the geometric parameters of the discharge. We have shown that, for potential flows, Bohm's criterion is satisfied for the flow velocity component normal to the plasma boundary. The total plasma velocity at the plasma boundary can exceed the ion acoustic velocity and can be equal to it only when the flow velocity vector is perpendicular to the boundary.

REFERENCES

1. I. Langmuir and L. Tonks, Phys. Rev. **34**, 876 (1929).
2. V. L. Granovskiĭ, *Electric Current in a Gas: Steady-State Current* (Nauka, Moscow, 1971).
3. B. M. Smirnov, *Physics of Weakly Ionized Gases* (Nauka, Moscow, 1978).
4. S. A. Dvinin, V. A. Dovzhenko, and A. A. Kuzovnikov, Fiz. Plazmy **25**, 957 (1999) [Plasma Phys. Rep. **25**, 882 (1999)].
5. S. A. Dvinin, V. A. Dovzhenko, and A. A. Kuzovnikov, Fiz. Plazmy **26**, 179 (2000) [Plasma Phys. Rep. **26**, 164 (2000)].
6. W. Schottky, Z. Phys. **25**, 635 (1924).
7. K. B. Persson, Phys. Fluids **5**, 1625 (1962).
8. D. Bohm, in *The Characteristics of Electrical Discharges in Magnetic Fields*, Ed. by A. Guthry and R. K. Wakerling (MacGraw-Hill, New York, 1949), Ch. 3, p. 77.
9. K.-U. Riemann, J. Phys. D **24**, 493 (1991).
10. L. V. Ovsyannikov, *Course of Basic Gas Gynamics* (Nauka, Moscow, 1981).
11. G. G. Chernyĭ, *Gas Dynamics* (Nauka, Moscow, 1988).
12. L. D. Landau and E. M. Lifshitz, *Fluid Mechanics* (Nauka, Moscow, 1986; Pergamon Press, Oxford, 1987).

Translated by O.E. Khadin

Plasma Physics Reports, Vol. 30, No. 12, 2004, pp. 1052–1060. Translated from Fizika Plazmy, Vol. 30, No. 12, 2004, pp. 1130–1138.

LOW-TEMPERATURE PLASMA

Experimental and Theoretical Studies of the Optical and Electrical Characteristics of a High-Pressure Pulsed Discharge in Argon

A. V. Dem'yanov* and D. Lo**

**Troitsk Institute for Innovation and Fusion Research, Troitsk, Moscow oblast, 142190 Russia*

***China University, Hong Kong, China*

Received March 17, 2004; in final form, April 6, 2004

Abstract—The optical and electrical characteristics of pulsed discharges in pure Ar at pressures of up to 7 atm, at which the discharge becomes unstable, are studied in a simple experimental device with automatic preionization. The gas temperature in the discharge is estimated from the width of the recorded emission spectrum. An analytical model of the vibrational relaxation of $Ar_2^*(v)$ is used to better determine the constants of the vibrational–translational relaxation of $Ar_2^*(v)$ molecules in their collisions with Ar atoms. The zero-dimensional numerical model of a pulsed discharge in Ar is modified. The experimental and calculated results are compared in detail. Good agreement is achieved between the measured and calculated time dependences of the electrode voltage and the intensity of spontaneous emission in the pressure range of 1–6 atm, as well as between the measured and calculated values of the gas temperature at pressures of 3–6 atm. Preliminary results from numerical studies of the possibility of achieving generation are discussed. © *2004 MAIK "Nauka/Interperiodica".*

1. INTRODUCTION

Progress in microelectronics is largely related to the development of fine-scale technologies, which require creating new efficient high-power sources of short-wavelength radiation. Such radiation is also needed in other applications, e.g., in medicine and chemistry. At present, the generation of coherent high-power radiation with the shortest wavelength has been achieved with Ar_2^* excimer molecules (for Ne_2^* excimer molecules, fluorescence has only been observed). In view of the fact that, for noble gas dimers, the cross section for stimulated emission is rather small ($\sim 10^{-17}$ cm^2) and, consequently, the gain is low, lasing is possible only at gas pressures of higher than 20 atm. So far, generation has been achieved only with pumping by a high-power electron beam [1, 2]. In this connection, pulsed electric discharges are more attractive because they can be excited in simpler and more compact devices. However, attempts to achieve generation in pulsed discharges have been unsuccessful, mainly because of discharge instabilities (whose growth rate increases with gas pressure). There are few studies on the possibility of achieving the lasing effect with Ar_2^* molecules in electric discharges [3, 4]. In [3], a system consisting of four successively arranged pairs of knife electrodes connected to the Blumlein line was used. The interelectrode distance in each pair was different and was chosen such that the intensity of the output spontaneous radiation was maximal. By comparing the intensity of spontaneous emission from one pair of the electrodes with that from four pairs, the authors of [3] estimated the small-signal gain (0.006 cm^{-1}) at a wavelength of 126 nm in pure Ar at pressures of 3.5 atm.

Based on recent experimental data [2, 3, 5–7], we modified the previous zero-dimensional model [8] for describing the kinetics of Ar_2^* excimer molecules excited by a fast electron beam or an electric discharge [9]. The model [9] adequately describes experimental data on the excitation by a high-power electron beam [2, 5, 6] and works satisfactorily in the case of excitation by a pulsed discharge [3]. Thus, the small-signal gain (minus absorption) predicted by the model is 0.002 cm^{-1}, which is about three times lower than the estimate obtained in [3]. A comparison with the results of [3] is difficult because of the rather complicated discharge geometry and complicated electric circuit of the power supply.

In [10], the numerical model of a pulsed discharge in Ar [9] was used to study the emission efficiency of Ar_2^* excimer molecules and the resulting gain in an active medium. It was shown that, under actual experimental conditions [3], the small-signal gain in a uniform discharge reaches 0.04 cm^{-1} at a pressure of 15 atm and room temperature, whereas it reaches 0.065 cm^{-1} at a pressure of 10 atm and an initial temperature of 170 K. The possibility of achieving such a

1063-780X/04/3012-1052$26.00 © 2004 MAIK "Nauka/Interperiodica"

high gain has recently been confirmed experimentally [4]. In that study, carried out in a device with plasma electrodes, the electron density and the small-signal gain (0.086 cm^{-1}) were measured in a discharge in pure Ar at a pressure of 15 atm.

In [10], the model was also tested at low electron-beam currents (low excitation powers), at which the efficiency of spontaneous emission was maximum.

This study continues investigations on the kinetics of Ar_2^* excimer molecules in a pulsed discharge. In contrast to [3, 4], we use an ordinary electrode system and a simple electric circuit with two *LC* elements; this substantially facilitates comparison between theory and experiment. The aim of our study was to verify and refine the model [9, 10] over a wide pressure range. The results obtained can be used to estimate the possibility of achieving generation with Ar_2^* excimer molecules.

2. EXPERIMENTAL SETUP AND ANALYSIS OF THE EXPERIMENTAL RESULTS

The experiments were carried out in pure Ar at room temperature. The experimental device is described in detail in [11]. Figure 1 shows the equivalent electric circuit and geometry of the discharge. 45-cm-long brass electrodes with an Ernst profile were arranged in a cylindrical chamber. The actual discharge length was l = 42 cm. To provide uniform energy deposition, 90 capacitors C_p were uniformly arranged along the electrodes on both sides of them. The charge accumulated in capacitors C_c was transferred to each of capacitors C_p through a spark gap. The UV radiation of spark discharges generated before the main discharge provided the uniform preionization of the discharge gap by the instant of breakdown. This is why such a discharge chamber design is usually referred to as an electric-discharge system with automatic preionization. In these experiments, the total capacitances of our TDK UHV-10A-50 capacitors were C_c = 52.1 nF and C_p = 45.5 nF. The interelectrode distance was d = 5 mm. The device operated reliably at gas pressures of up to 10 atm.

Time-integrated (over an observational time of 1 ms) emission spectra of Ar_2^* were measured with a VUV diode array detector, whereas the time evolution of the spontaneous emission was recorded with a photomultiplier and a digital oscilloscope.

The cavity consisted of two plane MgF_2 mirrors with reflection coefficients of 80% at a wavelength of 126 nm. Attempts to achieve generation were unsuccessful, apparently because of the low Q factor of the optical cavity. Unfortunately, higher quality mirrors were not available in these experiments. In our experiments, we measured the voltage at the laser head, the emission spectra, and the spontaneous emission intensity at pressures from 1 to 7 atm and charging voltages

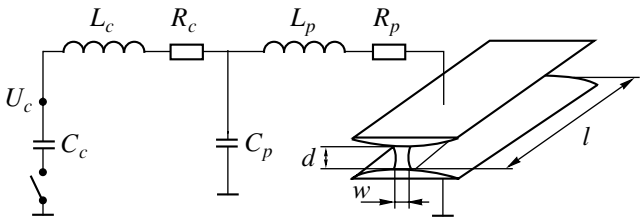

Fig. 1. Equivalent electric circuit and geometry of the discharge.

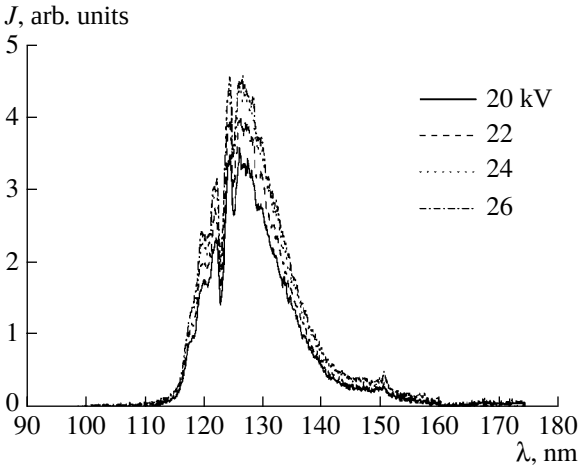

Fig. 2. Measured time-integrated emission spectra for P = 3 atm.

U_c from 10 to 34 kV. Up to pressures of 6 atm, the discharge was uniform, and instabilities were observed only at a pressure of 7 atm. To compare experimental and calculated results, we chose typical experimental data for pressures of P = 1, 3, and 6 atm. The width of the discharge was estimated from its glow and turned out to be w = 0.3 cm within the entire pressure range under study.

2.1. Emission Spectra

Figure 2 shows the emission spectra at a gas pressure of 3 atm and different charging voltages. The spectra at pressures of 1 and 6 atm are qualitatively the same. An analysis of the spectra measured at different pressures shows that, unlike in Xe [11], the intensity of the first continuum in Ar (λ = 107–115 nm) is low in comparison to the intensity of the second continuum (λ = 120–135 nm) over the pressure range under study (P = 1–6 atm). This indicates that the relaxation rate of the high vibrational levels of Ar_2^* (v) at these pressures is higher and the constants of the vibrational–transla-

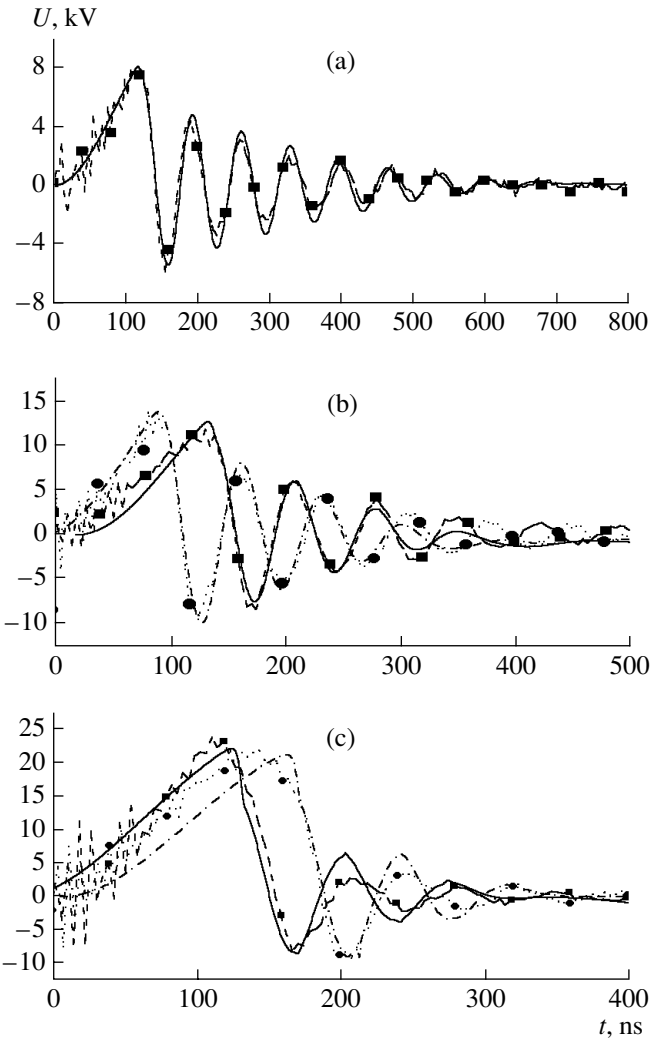

Fig. 3. Comparison of the experimental (lines with symbols) and calculated waveforms of the electrode voltage for P = (a) 1, (b) 3, and (c) 6 atm. For P = 1 atm, the charging voltage is U_c = 12 kV. For P = 3 atm, the charging voltages are U_c = 20 kV (the dashed line with squares for experiment and the solid line for calculations) and U_c = 28 kV (the dotted line with circles for experiment and the dashed-and-dotted line for calculations). For P = 6 atm, the charging voltages are U_c = 30 kV (the dashed line with squares for experiment and the solid line for calculations) and U_c = 34 kV (the dotted line with circles for experiment and the dashed-and-dotted line for calculations).

tional relaxation in Ar are much higher than those in Xe.

It is well known that the spectral width of the second continuum of the Ar_2^* excimer increases with temperature [12, 13]. Therefore, this dependence can be used to estimate the gas temperature. The experimental data on the full width at half maximum (FWHM) of the second continuum of Ar_2^*, $\Delta\lambda$, are available only for temperatures from 30 K ($\Delta\lambda$ = 7.2 nm) to 300 K ($\Delta\lambda$ = 8.7 nm) [12, 13]. In our experiments, the temperature was higher and, accordingly, the spectrum was wider: $\Delta\lambda$ = 15.0–15.7 nm at P = 1 atm, 13.6–14.6 nm at P = 3 atm, and 12.3–13.5 nm at P = 6 atm. To estimate the gas temperature, we used the analytical dependence of the width of the Ar_2^* emission spectrum on the temperature [13]. The values of the gas temperature were found to be T = 980–1070 K for P = 1 atm at charging voltages of U_c = 10–12 kV; T = 800 and 930 K for P = 3 atm at U_c = 20 and 28 kV, respectively; and T = 790 and 650 K for P = 6 atm at U_c = 30 and 34 kV, respectively. These data will be used below (see Section 4.1) to determine the discharge area more correctly.

2.2. Discharge Characteristics

Figure 3 shows waveforms of the electrode voltage at gas pressures of P = 1, 3, and 6 atm and different charging voltages (for comparison, the results of calculations that will be discussed in detail in Section 4 are also presented). A comparison of the measured waveforms of the electrode voltage at P = 3 and 6 atm and different charging voltages shows that, at P = 3 atm, the electrode voltage increases at a progressively higher rate as the charging voltage increases. Such behavior can be considered "normal," because the charging current of capacitor C_p increases with increasing charging voltage. Similar behavior was also observed at lower pressures. At P = 6 atm, the situation is the opposite (see Fig. 3c). As the charging voltage increases from 30 to 34 kV, capacitor C_p is charged more slowly. Such a dependence may occur if the capacitor's capacitance decreases with increasing charging voltage. This effect was taken into account in [14] when simulating an electric-discharge ArF excimer laser: the capacitance of the forming line in the equivalent electric circuit was reduced in order to achieve better agreement between the measured and calculated waveforms of the electrode voltage. In the present paper, we also take into account the dependence of the capacitance on the charging voltage (see Section 3 for details).

Note that, at P = 6 atm, the charging voltage of U_c = 26 kV is insufficient for the efficient breakdown of the interelectrode gap. At the same time, the intensity of spontaneous emission at U_c = 26 kV and P = 6 atm is only slightly lower than at higher charging voltages and much higher discharge powers. This confirms the conclusion of [10] that the efficiency of spontaneous emission is maximum at low discharge powers, when the electron density is relatively low and, accordingly, the quenching rate of the Ar_2^* excimer by electrons is low.

The measured waveforms of spontaneous emission will be considered in Section 4.

3. THEORETICAL MODEL

The zero-dimensional model was discussed in detail in [9, 10]. Here, we only present a brief description of it. In this model, the reduced electric field E/N (where E is the electric field strength and N is the neutral particle density) or the intensity of the source of secondary electrons (when the discharge is excited by an electron beam) is used as an input parameter when solving the quasi-steady Boltzmann equation in the two-term approximation. The model takes into account electron–ion recombination and elastic and inelastic energy losses of electrons in their collisions with atoms and molecules in the ground and excited states. Account is also taken of electron–electron and superelastic collisions. The rate constants of direct processes are determined from the calculated electron energy distribution function and the cross sections for the corresponding processes, and the rate constants of inverse processes are found from the principle of detailed balance. The rate constants of the processes with the participation of electrons are used to determine the densities of the plasma components and photons from the balance equations that are solved simultaneously with the equations for the gas temperature and the electric circuit. The electron density and mobility, which are found by solving the Boltzmann equation, are used to calculate the plasma conductivity, which is then used to find the currents and voltages in the electric circuit and, accordingly, E/N.

As compared to the model proposed previously in [8], the model of [9, 10] also incorporates gas heating and the vibrational relaxation of the low levels of the Ar_2^* ($^1\Sigma$) and Ar_2^* ($^3\Sigma$) states. This is necessary to correctly determine the gain factor of the active medium as the gas temperature varies.

In this paper, the model is modified as follows:

(i) The equivalent electric circuit is modified (Fig. 1). The electric circuit equations are supplemented with terms describing the dependence of the capacitor's capacitance on the voltage.

(ii) The model incorporates equations describing generation of radiation and the corresponding parameters of the optical cavity.

(iii) The processes of vibrational–translational (VT) relaxation of the high vibrational levels of Ar_2^*, the spontaneous emission from these levels, and their deexcitation by electrons are included in order to describe more correctly the time dependences of the output radiation at high excitation powers and to study the intensity ratio between the second and the first continua of Ar_2^*.

(iv) The model allows for time variations in the discharge area in order to model the contraction effect.

As in [9, 10], the parameters of the equivalent electric circuit (the resistances and inductances) were chosen so as to achieve the best agreement with the experimental results for P = 1–6 atm. These parameters were chosen to be L_c = 140 nH, L_p = 2.6 nH, R_c = 0.4 Ω, and R_p = 0.

Let us consider the basic modifications in more detail.

3.1. Dependence of the Capacitance on the Applied Voltage

As was noted above (see also Fig. 3c), at P = 6 atm, the growth rate of the voltage at capacitor C_p decreases as the applied voltage increases. Such "atypical" behavior is possible if the capacitor's capacitance decreases with increasing applied voltage. According to the TDK certificate data, the capacitance of the UHV-10A-50 capacitors decreases by ~10% as the dc voltage increases to 50 kV. We suppose that the decrease in the capacitance may be even greater for a pulsed voltage. In our calculations, we used the dependence $C(V/U_0)/C_0 = 1/(1 + 2^m/(m-1)*(V/U_0)^m)$ with m = 5 [14]. To study the influence of this effect in more detail, we also performed calculations with m = 10 and 15. The increase in m leads to a more rapid decrease in the capacitance with increasing applied voltage (see Fig. 4a). Figure 4b shows the dependence of the relative charge of the capacitor on the applied voltage. It can be seen that, as the voltage increases, the charge first increases, reaches its maximum at $V = U_0/2$, and then decreases. The best agreement between the waveforms of the calculated and measured voltages (see Fig. 3) was achieved for U_0 = 60 kV. In this case, the time dependences of the discharge voltage were affected only slightly by the parameter m, which determines the rate at which the capacitance decreases with increasing applied voltage (calculations were performed for m = 5, 10, and 15). Thus, at voltages above $U_0/2$ (in our case, 30 kV), the capacitor charge decreases because of a decrease in the capacitance. However, the same capacitor charge can also be at a lower voltage. The descending segment of the voltage dependence of the capacitor charge corresponds to an unstable state. When the switch is closed, the voltage at capacitor C_c decreases sharply to a value corresponding to the ascending segment of the dependence. Thus, for an initial voltage of 34 kV, the voltage at capacitor C_c after closing the switch will be 24.6, 22.8, and 21.6 kV for m = 5, 10, and 15, respectively. The results of calculations for U_c = 34 and 24.5 with m = 5 are very close to one another. Clearly, it makes no sense to increase the initial voltage above the value at which the capacitor charge begins to decrease. Therefore, in designing an actual device, it is necessary to take into account that the capacitor's capacitance may depend on the pulse voltage. In our experiments, this effect was observed only at P = 6 atm and was negligibly small at P = 1 and 3 atm.

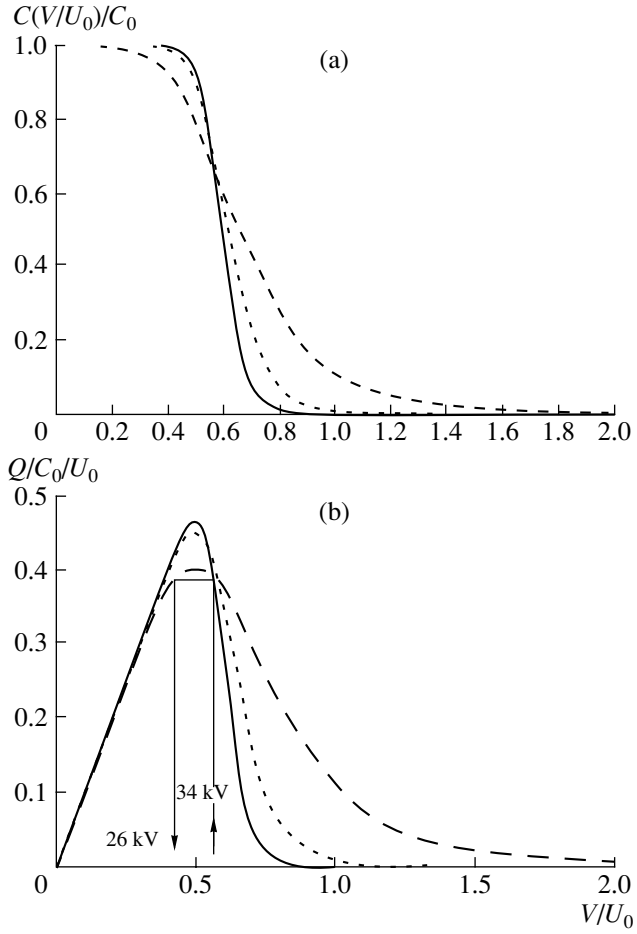

Fig. 4. (a) Relative capacitance $C(V/U_0)/C_0$ and (b) relative charge $Q/(C_0U_0)$ as functions of the relative charging voltage V/U_0. The dashed, dotted, and solid lines show the calculated results for m = 5, 10, and 15, respectively.

3.2. Vibrational Relaxation of $Ar_2^*(v)$

In experiments carried out at pressures in the range 1–6 atm, the intensity of the first continuum (the emission from the higher lying $Ar_2^*(v)$ vibrational states with wavelengths of 107–115 nm) was very low, compared to the intensity of the second continuum (the emission from the low $Ar_2^*(v)$ vibrational states with wavelengths of 120–135 nm). At the same time, one can estimate the VT relaxation constants of the vibrational states of excimer molecules from the pressure dependence of the intensity ratio between the second and the first continua. For example, in [11], the constant of VT relaxation of the $Xe_2^*(v)$ vibrational states in collisions with He atoms was determined. In [12], the pressure dependence of the intensity ratio between the second and the first continua of Ar_2^* was measured during the supersonic expansion of a gas at pressures

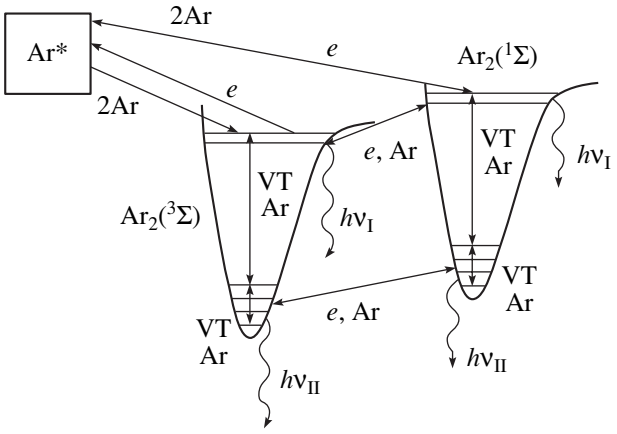

Fig. 5. Diagram illustrating the processes of the excitation, mixing, and vibrational relaxation of the triplet and singlet states of Ar_2^*. Heavy lines show the main processes.

below 40 torr. The authors of [12] also proposed a theoretical model for calculating the populations of the $Ar_2^*(v)$ vibrational states and the intensity ratio between the second and the first continua. To estimate the constants of VT relaxation of the $Ar_2^*(v)$ vibrational states in collisions with Ar atoms, the authors of [12] used theoretical estimates. Unfortunately, the model proposed in that paper failed to explain the saturation of the intensity ratio of spontaneous emission at higher pressures.

Here, we propose a simple model of vibrational relaxation and emission that can explain the dependence observed in [12]. Figure 5 illustrates the kinetic model used in our calculations. In contrast to [12], we assume that not only the emission from the $^3\Sigma$ term but also the emission from the high vibrational levels of the $^1\Sigma$ term contribute to the first continuum. At the same time, the emission from the low vibrational levels of the $^3\Sigma$ term is predominant in the second continuum, because, at pressures of $P < 40$ torr [12], vibrational relaxation is slow in comparison to the radiative deexcitation of the high vibrational levels of the $^1\Sigma$ term. The ratio between the excitation rates of the high vibrational levels of the $^1\Sigma$ and $^3\Sigma$ terms is equal to the ratio of the constants of the three-body processes

$$\begin{aligned} &Ar^* + Ar + Ar \longrightarrow Ar_2(^1\Sigma) + Ar, \\ &K = 1.5 \times 10^{-33}\ cm^6/s\ \ [15], \end{aligned} \tag{1}$$

$$\begin{aligned} &Ar^* + Ar + Ar \longrightarrow Ar_2(^3\Sigma) + Ar, \\ &K = 1.3 \times 10^{-32}\ cm^6/s\ \ [15], \end{aligned} \tag{2}$$

and is equal to ~0.12.

We assume that the reaction of single-quantum relaxation

$$Ar_2^*(v) + Ar \longrightarrow Ar_2^*(v-1) + Ar, \ K_{VT} \qquad (3)$$

is predominant. For the VT relaxation constants K_{VT}, we use the anharmonic oscillator approximation $K_{VT} = K_{10} v \exp(\delta_{VT}(v-1))$ [16]. The parameters K_{10} and δ_{VT} are chosen so that to provide the best agreement with the experimental data. We also assume that, in processes (1) and (2), excimer molecules are formed at the 25th vibrational level. Taking into account the observational spectral ranges for the second and first continua in [12] (124–130 and 108–110 nm, respectively), we assume that the emission from the 19th to 25th levels contributes to the first continuum, whereas the emission from the zeroth to fourth levels contributes to the second continuum. The best agreement was achieved for $\delta_{VT} = 0.15$ and $K_{10} = 7.8 \times 10^{-13}$ cm^3/s. Figure 6 compares the calculated and measured [12] pressure dependences of the intensity ratio between the second and the first continua. The calculated dependence from [12] is also shown in Fig. 6. Note that it follows from the data on the $^3\Sigma$ term of Ar_2^*, the data on the Ar_2^*–Ar interaction [12], and the estimates in [16] that $\delta_{VT} = 0.2$–0.28.

In our numerical model, which takes into account the refined data on the VT relaxation of $Ar_2^*(v)$ in collisions with Ar atoms, the vibrational kinetics of the $Ar_2(^3\Sigma)$ and $Ar_2(^1\Sigma)$ terms is described by the following processes:

$$Ar_2(^3\Sigma, h) + e, Ar \longleftrightarrow Ar_2(^1\Sigma, h) + e, Ar, \qquad (4)$$

$$Ar_2(^3\Sigma, l) + e, Ar \longleftrightarrow Ar_2(^1\Sigma, l) + e, Ar, \qquad (5)$$

$$Ar_2(^3\Sigma, h) + Ar \longleftrightarrow Ar_2(^3\Sigma, l) + Ar, \quad 2.7 \times 10^{-10} \text{ cm}^3/\text{s}, \qquad (6)$$

$$Ar_2(^1\Sigma, h) + Ar \longleftrightarrow Ar_2(^1\Sigma, l) + Ar, \quad 2.7 \times 10^{-10} \text{ cm}^3/\text{s}, \qquad (7)$$

$$Ar_2(^3\Sigma, l) + Ar \longleftrightarrow Ar_2(^3\Sigma, v = 0) + Ar, \quad 7.8 \times 10^{-13} \text{ cm}^3/\text{s}, \qquad (8)$$

$$Ar_2(^1\Sigma, l) + Ar \longleftrightarrow Ar_2(^1\Sigma, v = 0) + Ar, \quad 7.8 \times 10^{-13} \text{ cm}^3/\text{s}, \qquad (9)$$

$$Ar_2(^3\Sigma, h) \longrightarrow 2Ar + h\nu_I, \quad 4.8 \times 10^6 \text{ s}^{-1}, \qquad (10)$$

$$Ar_2(^3\Sigma, l) \longrightarrow 2Ar + h\nu_{II}, \quad 3.4 \times 10^5 \text{ s}^{-1}, \qquad (11)$$

$$Ar_2(^1\Sigma, h) \longrightarrow 2Ar + h\nu_I, \quad 3.7 \times 10^9 \text{ s}^{-1}, \qquad (12)$$

$$Ar_2(^1\Sigma, l) \longrightarrow 2Ar + h\nu_{II}, \quad 2.6 \times 10^8 \text{ s}^{-1}. \qquad (13)$$

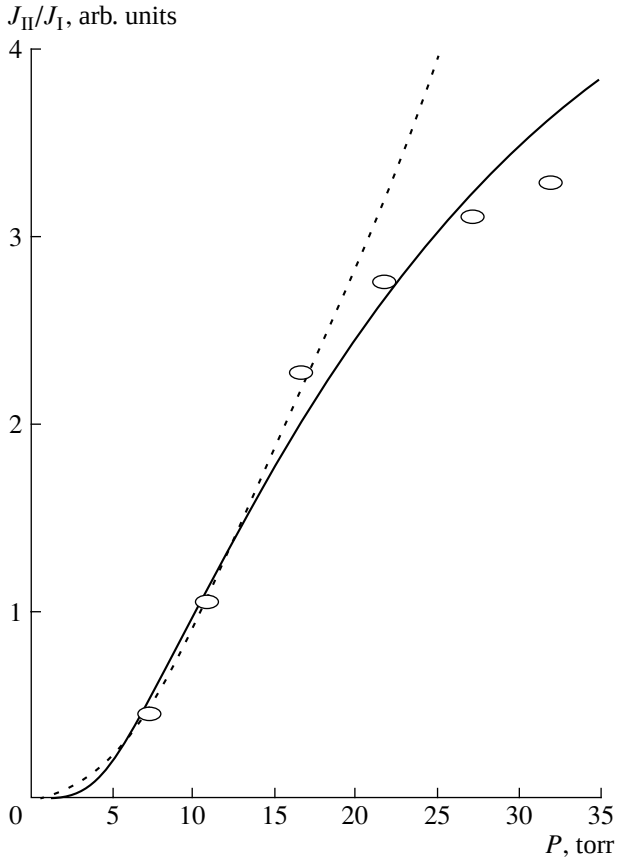

Fig. 6. Pressure dependence of the intensity ratio between the second and the first continua of Ar_2^*. The solid line show the results of the present study, the dashed line corresponds to the model of [12], and the symbols show the experimental results of [12].

Here, by the $Ar_2(^{3,1}\Sigma, h)$ and $Ar_2(^{3,1}\Sigma, l)$, we mean the total populations of the high (v = 20–30) and low (v = 0–4) vibrational levels, respectively, of the $Ar_2(^3\Sigma)$ and $Ar_2(^1\Sigma)$ terms. The constants of direct processes (4) and (5) are presented in [9, 10], whereas the constants of inverse processes (4)–(9) are calculated from the principle of detailed balance with allowance for gas heating.

Note that the refined data on VT relaxation do not affect the agreement between the calculated and experimental results of our previous studies, because, at high pressures [9, 10], a Boltzmann distribution that depends on the gas temperature only is established for the populations of the low vibrational levels. However, even at P = 1 atm, the results can be affected by the finite rate of the VT relaxation of the low $Ar_2^*(v)$ vibrational states in collisions with Ar atoms.

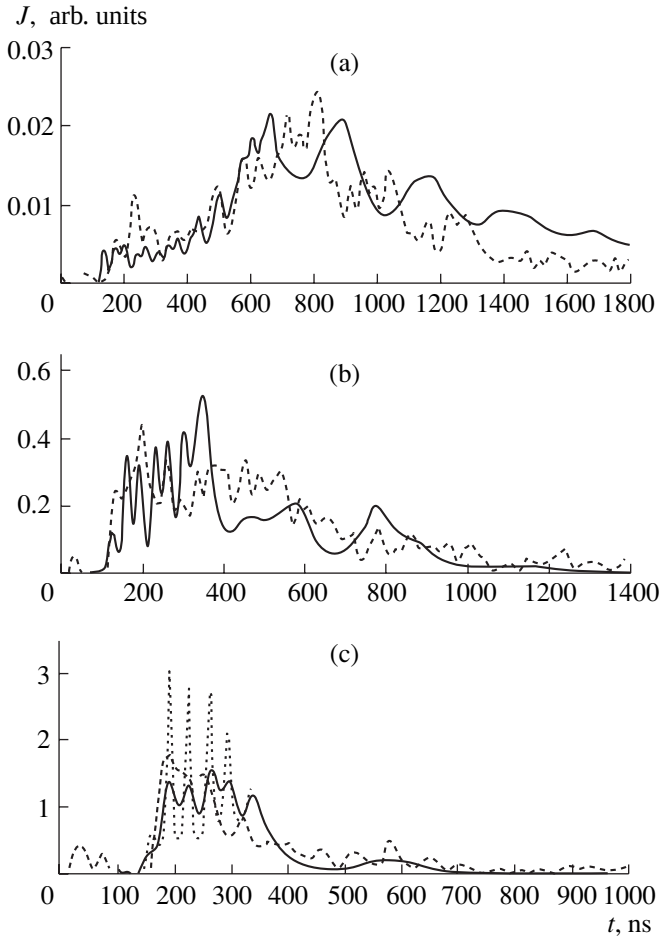

Fig. 7. Comparison of the experimental (dashed lines) and calculated (solid lines) waveforms of the spontaneous emission intensity for (a) $P = 1$ atm and $U_c = 12$ kV, (b) $P = 3$ atm and $U_c = 20$ kV, and (c) $P = 6$ atm and $U_c = 30$ kV. In plot (c), the dashed and solid lines correspond to calculations without and with allowance for the instrument function of the photomultiplier, respectively.

4. COMPARISON TO THE EXPERIMENTAL DATA

The choice of the equivalent electric circuit and its parameters, as well as the inclusion of the dependence of the capacitor's capacitance on the applied voltage in our model, made it possible to achieve good agreement between the measured and calculated waveforms of the electrode voltage (Fig. 2) over the range of pressures and voltages under study. The calculations show that the waveforms of the voltage depend only slightly on the discharge area, whereas the waveforms of the intensity of spontaneous emission vary significantly. Under our experimental conditions, the dominant process is the dissociation of Ar_2^* in the high vibrational states in collisions with electrons [9, 10]. At the same time, the electron density is determined by the discharge current and discharge area. The discharge current is specified by the electric circuit and the charging voltage. Therefore, the electron density depends mainly on the discharge area. It is well known [14, 17] that the width of the current channel decreases during a discharge due to contraction. The contraction rate is determined, first of all, by the electrode profile and also by the preionization inhomogeneity and the dependence of the ionization rate on E/N. To study the influence of contraction, we introduced the time dependence of the discharge width into our model. The calculations show that contraction significantly influences the intensity of spontaneous emission, but the time behavior of spontaneous emission remains almost the same. To study the influence of contraction in detail, we plan to use a one-dimensional model of a discharge in Ar that is similar to the model used in [14].

4.1. Gas Heating and the Width of the Current Channel

It is clear that, in the zero-dimensional model, the discharge area is an external parameter. This parameter was determined from observations of the discharge glow. However, it is well known [14, 17] that the current channel is somewhat narrower than the glow region. Therefore, it was important to verify the chosen value of the discharge area. To do this, we used the data on the gas temperature (see Section 2). Indeed, the increase in the gas temperature depends of the discharge power and, consequently, on the discharge current density, which, in turn, depends on the discharge area (the length of the discharge is fixed). Note that the discharge voltage is determined by the plasma processes, depends slightly on the discharge current, and increases almost linearly with gas pressure. In calculations with a given discharge width of $w = 0.3$ cm, the gas was heated to the following temperatures: $T = 850$ K for $P = 1$ atm at $U_c = 12$ kV; $T = 820$ and 950 K for $P = 3$ atm at $U_c = 20$ and 28 kV, respectively; and $T = 830$ and 740 K for $P = 6$ atm at $U_c = 30$ and 34 kV, respectively. A comparison of the calculated results with the experimental data on gas heating (see Section 2) shows that, at $P = 3$ and 6 atm, the calculated and measured gas temperatures are close to one another. Note that, at $P = 6$ atm, the higher the charging voltage, the lower the gas temperature. This confirms our conclusion that the capacitor's capacitance depends on the charging voltage. In fact, the higher the voltage, the lower the energy stored in the capacitor. At a pressure of $P = 1$ atm, the calculated gas temperature was somewhat lower than the measured one. As was noted above, the temperature was estimated by using the theoretical dependence of the spectrum width on the temperature, assuming that the populations of the $Ar_2^*(v)$ vibrational levels obey a Boltzmann distribution. This assumption is valid at high pressures; however, at 1 atm, the distribution may deviate from a Boltzmann one. Using the theoretical model described in Section 3, we calculated the distributions for $P = 1$, 3, and 6 atm.

The model included the mixing of the triplet and singlet states of Ar_2^* in collisions with electrons. Indeed, it turned out that, at pressures of $P = 3$ and 6 atm, the distribution over low vibrational levels was close to a Boltzmann one with the corresponding gas temperature, whereas at $P = 1$ atm, the populations of the lower lying levels ($v = 1$–5) were substantially higher than the equilibrium populations; this resulted in the broadening of the Ar_2^* emission spectrum at this pressure. The effective vibrational temperature of the first level Ar_2^* ($v = 1$) was equal to 1000 K for an electron density of $\sim 2 \times 10^{14}$ cm^{-3}. We recall that, in our experiments, we measured the time-integrated spectrum. The main contribution to the discharge glow comes from times larger than ~1100 ns, when the electron density decreases to $\sim 3 \times 10^{14}$ cm^{-3} and lower.

4.2. Spontaneous Radiation

Figure 7 compares the measured and calculated waveforms of the spontaneous emission intensity for different pressures. It can be seen that the calculated waveforms agree well with the measured ones. Note that, in the calculations, short period-oscillations at $P =$ 1 and 3 atm are damped more rapidly than in the experiment. With the equivalent electric circuit used in our model, we could not avoid this discrepancy. It seems that a more complicated equivalent circuit should be used to describe the actual circuit. We also note that the amplitude of the calculated oscillations in the spontaneous emission intensity at $P = 3$ and 6 atm are larger than in the experiment because of an increase in the rates of the processes with the participation of Ar in comparison to those at lower pressures. This discrepancy was avoided by taking into account the instrument function of the photomultiplier ($\Delta t = 20$ ns) used to measure spontaneous emission. For $P = 1$ and 3 atm, this factor is less important. For this reason, Figs. 7a and 7b show the calculated results without smoothing by the instrument function, whereas Fig. 7c ($P = 6$ atm) shows the calculated results with and without smoothing.

5. CONCLUSIONS

The optical and electrical characteristics of a pulsed electric discharge in pure Ar have been studied at pressures of up to 7 atm, at which the discharge becomes unstable. Attempts to achieve generation have been unsuccessful because of the small Q factor of the optical cavity, as is evident from a comparison with the results of calculations. The gas temperature in the discharge has been estimated from measurements of the spectrum width. The pressure dependence of the intensity ratio between the second and the first continua has been used to estimate the constants of the vibrational–translational relaxation of $Ar_2^*(v)$ molecules in their collisions with Ar atoms. The modified zero-dimensional numerical model of a pulsed discharge in Ar is found to satisfactorily describe the experimental results over the entire range of pressures and charging voltages under study and can be used to analyze the possibility of achieving generation.

Preliminary results [18] show that, for the discharge geometry and cavity parameters used in our study, lasing in a uniform discharge is achievable at pressures of ≥10 atm. In this case, the lower the pressure, the narrower the range of the deposited energies at which generation is possible. As the pressure increases, the admissible range of the deposited energies extends and the output energy increases.

The key problem is that of providing the stability of a high-pressure pulsed discharge. Encouraging results were obtained in [4], where a uniform discharge was obtained at pressures of 10–20 atm, but in a device with plasma electrodes. We plan to study the influence of the discharge contraction in detail by using a one-dimensional model of a discharge in Ar, which is similar to [14].

Another important problem is the choice of an efficient system for discharge power supply. The large difference between the voltages that are required to initiate and sustain discharges in noble gases gives no way of achieving an aperiodic regime of pumping the active medium. The energy is deposited during several periods of current oscillations in the electric circuit. However, the discharge usually becomes unstable after the first oscillation; hence, the energy of subsequent oscillations is lost.

ACKNOWLEDGMENTS

We are grateful to. A.P. Napartovich for fruitful discussions of the results obtained. This work was supported in part by the Hong Kong SAR Government RGC (grant no. CUHK 4218/01E) and the Russian Foundation for Basic Research (project no. 02-02-17534).

REFERENCES

1. W. M. Hughes, J. Shannon, and R. Hunter, Appl. Phys. Lett. **24**, 488 (1974).
2. W. G. Wrobel, H. Rohr, and K. H. Steuer, Appl. Phys. Lett. **36**, 113 (1980).
3. H. Ninomiya and K. Nakamura, Opt. Commun. **134**, 521 (1997).
4. K. Nakamura, Y. Ooguchi, N. Umegaki, *et al.*, Proc. SPIE **4747**, 286 (2002).
5. S. Neeser, T. Kunz, and H. Langhoff, J. Phys. D **30**, 1489 (1997).
6. S. Neeser, M. Schumann, and H. Langhoff, Appl. Phys. B **63**, 103 (1996).
7. E. Elson and M. Rokni, J. Phys. D **29**, 716 (1996).
8. K. S. Gochelashvily, A. V. Dem'yanov, I. V. Kochetov, *et al.*, Opt. Commun. **91**, 66 (1992).

9. S. K. Lam, C.-E. Zheng, D. Lo, *et al.*, J. Phys. D **33**, 242 (2000).
10. A. V. Dem'yanov and D. Lo, Fiz. Plazmy **27**, 466 (2001) [Plasma Phys. Rep. **27**, 440 (2001)].
11. S. K. Lam, D. Lo, C.-E. Zheng, *et al.*, Appl. Phys. B **75**, 723 (2002).
12. P. Dube, M. J. Kiik, and B. P. Stoicheff, J. Chem. Phys. **103**, 7708 (1995).
13. E. Morikawa, R. Reininger, P. Gurtler, and V. Saile, J. Chem. Phys. **91**, 1469 (1989).
14. A. V. Dem'yanov, L. Feenstra, P. J. M. Peters, *et al.*, Appl. Phys. B **72**, 823 (2001).
15. P. Millet, A. Birot, H. Brunet, *et al.*, J. Phys. B **15**, 2935 (1982).
16. B. F. Gordiets, A. I. Osipov, and L. A. Shelepin, *Kinetic Processes in Gases and Molecular Lasers* (Nauka, Moscow, 1980).
17. A. V. Dem'yanov, I. V. Kochetov, A. P. Napartovich, *et al.*, Plasma Chem. Plasma Process. **16**, 121 (1996).
18. A. V. Dem'yanov and D. Lo, in *Proceedings of the IV International Conference on Plasma Physics and Plasma Technology, Minsk, 2003*, Vol. 1, p. 191.

Translated by N.F. Larionova

Plasma Physics Reports, Vol. 30, No. 12, 2004, pp. 1061–1070. Translated from Fizika Plazmy, Vol. 30, No. 12, 2004, pp. 1139–1148.

LOW-TEMPERATURE PLASMA

A Self-Consistent Kinetic Model of the Stratification of Plane and Spherical Low-Pressure Discharges in Argon

A. V. Fedoseev and G. I. Sukhinin

Kutateladze Institute of Thermophysics, Siberian Division, Russian Academy of Sciences, pr. Akademika Lavrent'eva 1, Novosibirsk, 630090 Russia

Received November 19, 2003; in final form, March 3, 2004

Abstract—A self-consistent kinetic model is used to describe the effect of stratification of the positive column of a plane and a spherical gas discharge in argon at low pressure. The model is based on solving the Boltzmann kinetic equation for the electron energy distribution function, the time-dependent ion continuity equation, and Poisson's equation for the self-consistent electric field. The spatial distributions of the electron and ion densities and of the electric field in the positive column of a stratified discharge are determined. The kinetic mechanism for discharge stratification in noble gases at low pressures is explained in terms of the proposed model. The model makes it possible to describe the moving strata and to confirm the validity of the experimentally obtained dependence of the radii of the strata on their numbers in a spherical discharge. © *2004 MAIK "Nauka/Interperiodica".*

1. INTRODUCTION

It is well known that, in most cases, the plasma in the positive column (PC) of a gas discharge is unstable [1–4]. Various instabilities lead to stratification of the PC into alternating dark and bright regions (strata). Although discharge stratification has received much experimental and theoretical study, it is not well understood at present and requires further investigation.

Experiments with spherical stratified glow discharges between a small-size central anode and a surrounding large-area spherical cathode were carried out in [5, 6]. Spherical discharges differ from conventional glow discharges in tubes in three important respects: the formation of a spherical electron flow converging toward the central anode, the absence of transverse diffusive fluxes of charged particles, and no loss of charged particles at the walls. Optical measurements showed that a volume discharge initiated by means of a pointlike anode exhibits high spherical symmetry and appears to be a unique object in which all the parameters depend only on the distance from the anode center—a property that renders its modeling in one-dimensional geometry possible.

For many years, the best-developed models of the stratification effect came from the hydrodynamic and kinetic theories of discharge striations (see, e.g., review paper [3]). Not long ago, however, Sigeneger and Winkler [7] advanced a new method for solving the nonlocal Boltzmann kinetic equation for the electron energy distribution function (EEDF). This new method provides fairly reliable calculations of the influence of the electric field nonuniformity on the formation of the electron energy distribution and on its relaxation in the region where the electric field is uniform. Based on Sigeneger and Winkler's method, Golubovskii *et al.* [8, 9] solved the Boltzmann equation for the EEDF for both a prescribed sinusoidal electric field and an experimentally measured electric field. By correctly choosing the spatial period of the prescribed field, they determined the spatial scale on which the electron energy relaxes and described a kinetic mechanism for the formation of periodic distributions of the macroscopic parameters of the plasma electrons. In a recent paper, Golubovskii *et al.* [10] proposed a self-consistent kinetic model in which the distribution function of all the electrons is described with the help of the Boltzmann equation in the two-term approximation and the ions and metastable particles are treated in terms of hydrodynamic balance equations. In [10], a study was made of discharges at moderated pressures under the assumption that the PC is electrically neutral, the electric field being calculated without using Poisson's equation.

In recent years, there has been increased interest in the so-called hybrid models [11, 12], in which high-energy electrons are analyzed by means of the Monte Carlo method while slow electrons, ions, and other heavy particles (metastables) are described by the conventional hydrodynamic equations. This approach makes it possible to increase the reliability of numerical simulations without substantially increasing the amount of computer time. In this way, the electric field in the plasma is determined by the distribution of charges and is self-consistently calculated from Poisson's equation. Hybrid models have been widely used to describe the effects occurring near the cathode and discharges of complex geometric shapes, but never to describe the stratification effect.

1063-780X/04/3012-1061$26.00 © 2004 MAIK "Nauka/Interperiodica"

In this paper, the plasma in the PC of a plane and a spherical glow discharge is studied by simultaneously solving the Boltzmann kinetic equation for the EEDF, the time-dependent ion continuity equation, and Poisson's equation for the self-consistent electric field. We believe that, with this self-consistent kinetic approach, it is possible to give a reliable description of the stratification of low-pressure discharges in noble gases.

2. MODEL

We consider the PC of a plane and a spherical discharge in argon at low pressure ($0.1 < p < 2$ torr). For a plane discharge in a tube, we ignore the influence of the boundary effects and assume that the electric field distribution is axisymmetric. As has already been mentioned, the parameters of a spherical discharge depend only on the radial coordinate r. Hence, the problems for a spherical and a plane discharge are both treated in a one-dimensional formulation. In what follows, all expressions in spherical and plane geometry will be written in the same form, the spatial variable being the coordinate r.

The electron flow entering the region of a spatially periodic self-consistent electric field in the PC, as well as the relaxation of the flow as it converges in this field toward the anode, is described by the Boltzmann kinetic equation for the electron velocity distribution function $f(r, v)$:

$$\mathbf{v}\cdot\nabla_{\mathbf{r}} f - \frac{e}{m}\mathbf{E}\cdot\nabla_{\mathbf{v}} f = S^{\mathrm{el}}(f) + \sum_k S_k^{\mathrm{in}}(f), \qquad (1)$$

where S^{el} is the elastic collision integral, S_k^{in} is the inelastic collision integral, and $-e$ and m are the charge and mass of an electron. Since the characteristic time scale on which the plasma relaxes to a certain state is governed by the velocity of the slow ions, and since this time scale is long enough for the distribution of the electrons (which are faster than the ions) to follow the ion distribution, the Boltzmann equation is taken to be time-independent.

The direction of the electric field is chosen to be such that the electrons are accelerated in the positive direction along the coordinate r. In the expansion of the EEDF in Legendre polynomials, we take into account only the first two terms:

$$f\left(U, \frac{v_r}{v}, r\right) = \frac{1}{2\pi}\frac{1}{(2/m)^{3/2}}\left[f_0(U, r) + f_r(U, r)\frac{v_r}{v}\right], \qquad (2)$$

where $U = mv^2/2$ is the electron kinetic energy and $f_0(U, r)$ and $f_r(U, r)$ are the isotropic and anisotropic parts of the EEDF, respectively.

We substitute expansion (2) into Eq. (1), multiply the resulting equation by unity and by $\mu = v_r/v$, and integrate over $2\pi d\mu$ to arrive at the following set of two equations (for more details, see [7]):

$$\frac{1}{3}\frac{1}{r^n}\frac{\partial}{\partial r}[r^n U f_r] - \frac{eE_r(r)}{3}\frac{\partial}{\partial U}[U f_r]$$

$$-\frac{\partial}{\partial U}\left[2\frac{m}{M}U^2 N_g Q^d(U) f_0\right] + \sum_k U N_g Q_k^{\mathrm{in}}(U) f_0 \qquad (3)$$

$$-\sum_k (U + U_k^{\mathrm{in}}) N_g Q_k^{\mathrm{in}}(U + U_k) f_0(U + U_k^{\mathrm{in}}, r) = 0,$$

$$\frac{\partial}{\partial r} f_0 - eE_r(r)\frac{\partial}{\partial U} f_0 + H(U) f_r = 0, \qquad (4)$$

where $n = 0$ and 2 for plane and spherical geometry, respectively, and N_g is the density of neutral particles of mass M. The third term in Eq. (3) incorporates the energy loss in elastic collisions, which are characterized by the scattering cross sections $Q^d(U)$. The fourth term accounts for the energy loss in inelastic collisions; here, $Q_k^{\mathrm{in}}(U)$ is the cross section for the kth inelastic process. The coefficient in the third term in Eq. (4) is equal to $H(U) = N_g Q^d(U) + \sum_k N_g Q_k^{\mathrm{in}}(U)$. The last (fifth) term in Eq. (3) describes the production of an electron with the kinetic energy U in the kth inelastic collision in which an electron with the initial energy $U + U_k$ loses an amount of energy equal to U_k.

If we switch from the kinetic energy U to the total electron energy $\varepsilon = U - eW(r)$, where $W(r)$ is the radial profile of the electric potential in the PC, then Eqs. (3) and (4) become much simpler. Eliminating the anisotropic part of the EEDF in the set of equations yields the following equation for the isotropic part of the distribution function:

$$\frac{1}{r^n}\frac{\partial}{\partial r}\left[\frac{r^n U}{3H(U)}\frac{\partial}{\partial r} f_0(\varepsilon, r)\right]$$

$$+\frac{\partial}{\partial \varepsilon}\left[2\frac{m}{M}U^2 N_g Q^d(U) f_0(\varepsilon, r)\right]$$

$$-\sum_k U N_g Q_k^{\mathrm{in}}(U) f_0(\varepsilon, r) \qquad (5)$$

$$+\sum_k (U + U_k^{\mathrm{in}}) N_g Q_k^{\mathrm{in}}(U + U_k) f_0(\varepsilon + U_k^{\mathrm{in}}, r) = 0.$$

The anisotropic and isotropic parts of the EEDF are related by the expression

$$f_r = -\frac{1}{H(U)}\frac{\partial}{\partial r} f_0. \qquad (6)$$

Figure 1 shows the computation region, i.e., the region over which Eq. (5) was solved in the (ε, *r*) coordinate plane for an arbitrary periodic electric field. The chosen radial profile of the potential energy, $-eW(r)$, determines the lower boundary of the computation region (curve *C*). The left boundary of the computation region corresponds to the cathode-side boundary of the PC and is denoted by *A*. At the entrance to the PC, the anisotropic part of the EEDF was given by a Gaussian function,

$$\hat{f}_r(U) = cU\exp\left[-\left(\frac{U-U_m}{\Delta U}\right)^2\right], \quad r = 0,$$

which models an electron beam. In simulations, we varied the mean electron energy U_m and the energy spread ΔU of the beam and found that the variations affected the solution only slightly and only in a narrow region near boundary *A*. The maximum total electron energy ε_∞ was chosen in such a way that the distribution function of the electrons with energy ε_∞ vanishes everywhere. Thus, the condition at the upper boundary *B* of the computation region is $f_0(\varepsilon \geq \varepsilon_\infty, r) = 0$. At the lower boundary *C*, the electron kinetic energy is zero; hence, the anisotropic part f_r of the distribution function is also zero. The condition for the isotropic part at this boundary can be obtained from Eq. (6):

$$\left[\frac{\partial}{\partial r'} f_0(\varepsilon = -eW(r), r')\right]_{r'=r} = 0.$$

For a plane discharge, the parameters of the computation region were as follows: $r_c = 0$ is the position of the cathode-side boundary of the PC and $r_a = 20$ cm is the position of the anode-side boundary of the PC. For a spherical discharge, the radius of the cathode-side boundary of the PC is $r_c = 11$ cm, the anode radius being $r_a = 1$ cm. The boundary condition at the anode corresponds to full absorption of the electrons by the anode surface (boundary *D*):

$$f_r(U, r_a) = \gamma f_0(U, r_a), \quad \gamma = \frac{3}{2}.$$

Equation (5) was discretized by a scheme of second-order accuracy similar to the Crank–Nicholson scheme and was solved by a procedure analogous to that described in [7]. In our simulations, in contrast to [7], the points of the numerical mesh were spaced uniformly along the energy axis while the mesh spacing in the radial direction was nonuniform and depended on the potential distribution. Such a mesh made it possible to reduce the error in calculating the balance of particles and energies to several hundredths of a percent, even for highly nonuniform electric fields. It also facilitates the integration of all the macroscopic parameters over energy because there is no need for the computation region in the (ε, *r*) coordinate plane to be additionally readjusted to that in the (*U*, *r*) coordinate plane.

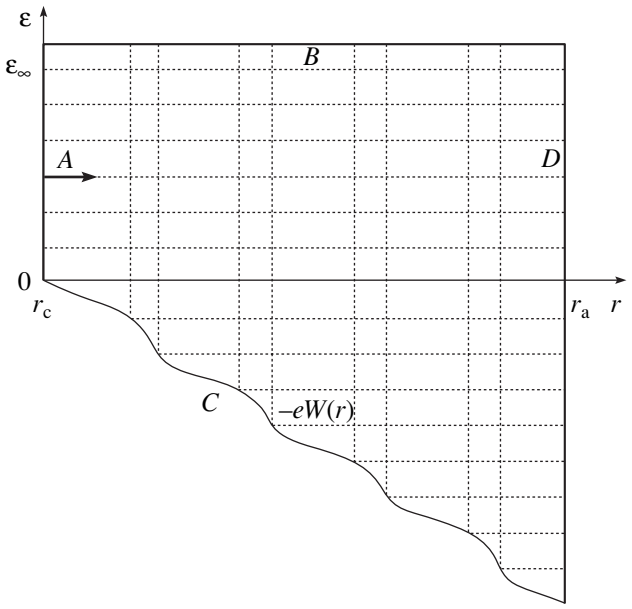

Fig. 1. Computation region and boundary conditions for the Boltzmann equation in the (ε, *r*) coordinate plane.

Parabolic equation (5) in finite differences was solved numerically by the sweep method over the coordinate *r* for each value of the total energy ε, from its highest value to a zero value. In this way, for a given value of the energy ε, the last term in Eq. (5) was calculated from the distribution functions already computed for higher energy values.

The cross sections for electron scattering in argon were taken from the database in [13]. The gas atoms were assumed to be immobile, and collisions of electrons with ions and metastable particles were ignored. All the processes by which the electrons lose energy were divided into four groups, three of which are characterized by different excitation thresholds, 11.3, 11.7, and 12.9 eV, and one includes ionizing collisions, the ionization threshold being 15.7 eV. All ionizing collisions were regarded merely as energy-loss processes, which do not change the number of electrons.

Having found the spatial distribution of the EEDF from Boltzmann equation (5), we can determine some macroscopic parameters of the plasma electrons by integrating the distribution function over energies. We thus obtain the following spatial profiles of the electron density and the electron flux density in the PC:

$$n_e(r) = \int_0^\infty f_0(U, r)U^{1/2}dU, \tag{7}$$

$$j_r(r) = \frac{1}{3}\sqrt{2/m}\int_0^\infty f_r(U, r)UdU. \tag{8}$$

The distributions of the electric field and potential that were used to calculate the total electron energy in Eq. (5) were determined as follows: We consider the nonstationary ion transport equation in the drift approximation:

$$\frac{\partial n_i(r,t)}{\partial t} + \frac{1}{r^n}\frac{\partial}{\partial r}(r^n n_i(r,t)\mu_i E(r,t)) = 0, \quad (9)$$

where μ_i is the ion mobility in argon. The electron density distribution was assumed to be known and was determined from formula (7). The right-hand side of Eq. (9) was assumed to be zero. Preliminary computations showed that, in the parameter range under consideration (for a reduced electric field of about $E/p \sim 1$ V/cm/torr), the number of electrons changes only slightly in the course of impact ionization, which plays an important role only at $E/p > 10$ V/(cm torr).

The electric field E satisfies Poisson's equation

$$\frac{1}{r^n}\frac{\partial r^n E(r,t)}{\partial r} = 4\pi e_0[n_i(r,t) - n_e(r)]. \quad (10)$$

For a plane discharge ($n = 0$), the solutions for the ion density and electric field are sought in the form of running waves, $n_i = n_i(\xi = v_i^0 t + r)$ and $E = E(\xi = v_i^0 t + r)$, where we have introduced the new variable $\xi = v_i^0 t + r$. The constant $v_i^0 = \alpha\mu_i E^0$ is on the order of the ion drift velocity; here, E^0 is the mean electric field in the PC and the absolute value of the parameter $|\alpha|$ is about unity. Inserting these expressions into Eq. (9), we obtain

$$\frac{\partial(n_i(\xi)\alpha)}{\partial\xi} + \frac{\partial}{\partial\xi}\left(n_i(\xi)\frac{E(\xi)}{E^0}\right) = 0. \quad (11)$$

Integration of Eq. (11) over ξ yields

$$n_i(\xi)(\alpha + E(\xi)/E^0) = \text{const}. \quad (12)$$

The constant on the right-hand side of Eq. (12) was chosen to be the value of $n_i(\xi)(\alpha + E(\xi)/E^0)$ at the cathode-side boundary of the PC at $t = 0$: const $= n_i(r_c)(\alpha + 1)$. The ion density at this boundary was assumed to be equal to the electron density. Poisson's equation and Eq. (12) yield the equation

$$E(r) = E^0\left[\frac{n_e(r_c)(\alpha+1)}{n_e(r) + \frac{1}{4\pi e}\frac{\partial E}{\partial r}} - \alpha\right]. \quad (13)$$

Equation (13) was solved by the iterative method. Since the coefficient of the field gradient on the right-hand side of Eq. (13) is small, only a few (about three) iterations were needed.

Similar manipulations can be carried out for a spherical discharge ($n = 2$). We introduce the dimensionless ion density $\bar{n}_i(t, r)$ and dimensionless electric field $\bar{E}(t, r)$ through the relationships

$$n_i(t,r) = n_i^0\left(\frac{r_c}{r}\right)^\beta \bar{n}_i\left(v_i^0 t + \frac{r_c}{(3-\beta)}\left(\frac{r}{r_c}\right)^{3-\beta}\right), \quad (14)$$

$$E(t,r) = E^0\left(\frac{r_c}{r}\right)^{2-\beta} \bar{E}\left(v_i^0 t + \frac{r_c}{(3-\beta)}\left(\frac{r}{r_c}\right)^{3-\beta}\right), \quad (15)$$

where n_i^0 and E^0 are the characteristic values of the ion density and electric field at the cathode-side boundary $r = r_c$ of the PC. The functions $\bar{n}_i(t, r)$ and $\bar{E}(t, r)$ describe spherical waves and depend on a single variable ξ:

$$\xi = v_i^0 t + \varphi(r) = v_i^0 t + \frac{r_c}{(3-\beta)}\left(\frac{r}{r_c}\right)^{3-\beta}, \quad (16)$$

where the function $\varphi(r)$ is chosen so as to reduce the equation of ion motion (9) to an equation in only one variable ξ. Hence, the functions $n_i(t, r)$ and $E(t, r)$ describe waves whose amplitudes vary over time and whose propagation velocity $v_{st} \sim v_i^0 (r_c/r)^{2-\beta}$ depends on r.

Substituting expressions (14) and (15) for the ion density and electric field distributions into Eq. (9), we obtain

$$\frac{\partial(\bar{n}_i(\xi)\alpha)}{\partial\xi} + \frac{\partial}{\partial\xi}(\bar{n}_i(\xi)\bar{E}(\xi)) = 0. \quad (17)$$

Equation (17) for the dimensionless ion density and dimensionless electric field coincides with Eq. (11), which refers to a plane discharge. Integrating Eq. (17) yields the following relationship between the ion density and the electric field:

$$\bar{n}_i(\xi)(\alpha + \bar{E}(\xi)) = \text{const} = (\alpha + 1). \quad (18)$$

Equation (18) and Poisson's equation were solved together by iteration, just as was done for a plane discharge. The calculated electric field profile $E(r, t = 0)$ was substituted into Eq. (5) to compute the electron distribution function and the new values of the electron density distribution in the iterative procedure.

The first approximation to the distribution function $f_0^0(r, U)$ was obtained by solving parabolic equation (5) with the corresponding boundary conditions for an arbitrary electric field $E^0(r)$. The initial electric field distribution was taken to be uniform. At each iteration step, a new electric field distribution $E(r, t)$ was computed from the already calculated electron density distribution (7) by means of the procedure described

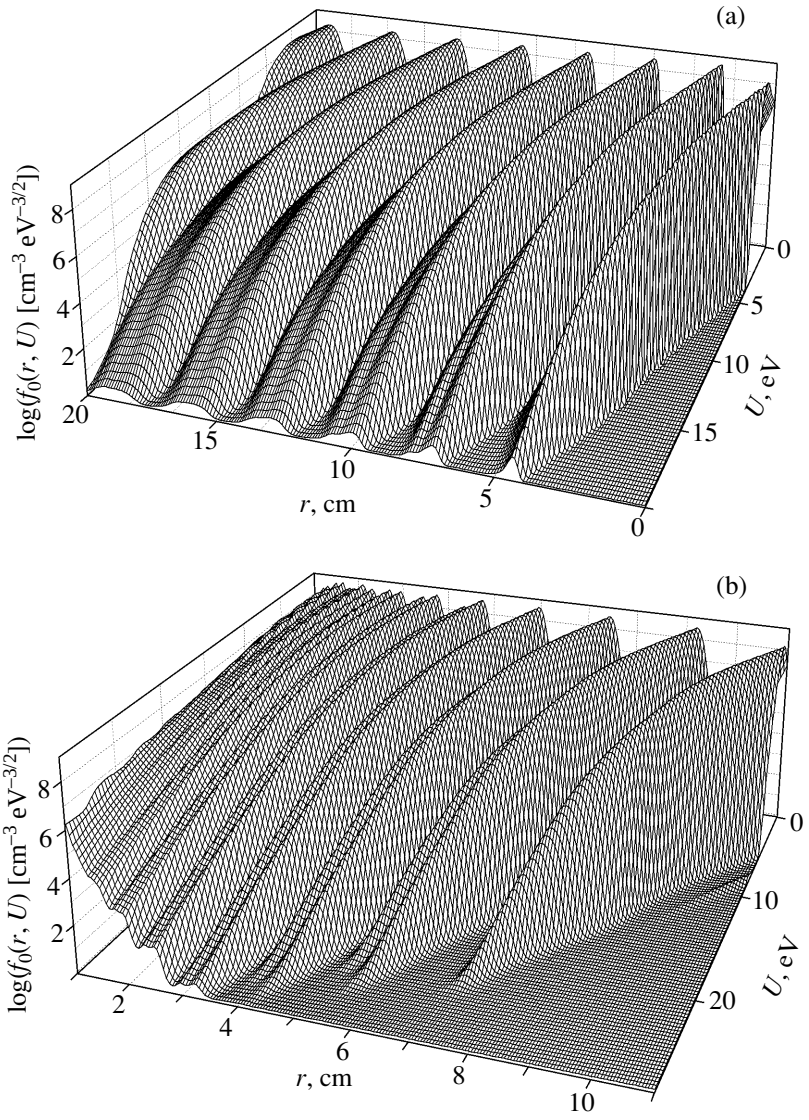

Fig. 2. Distributions of the isotropic part of the EEDF in the (r, U) plane for (a) a plane discharge (the cathode-side boundary of the PC is at r_c = 0 cm, and the anode-side boundary is at r_a = 20 cm) and (b) a spherical discharge for $\beta = 1$ (r_a = 1 cm, r_c = 11 cm).

above. The procedure was repeated until the solutions converged to final distributions satisfying the Boltzmann equation, the equation of ion motion, and Poisson's equation. In general, the number of iterations required to achieve the convergence was about ten. The final distribution of the axial electric field was found to be independent of the choice of the initial electric field distribution $E^0(r)$.

3. RESULTS

The iterative solution described above yielded the spatial evolutions of the EEDF in a plane (Fig. 2a) and a spherical (Fig. 2b) discharge. Figures 2a and 2b show how the logarithm of the isotropic part of the EEDF (plotted on the vertical axis) depends on the U and r coordinates. We can see that, as the distance from the anode decreases, the hump in the EEDF is periodically displaced toward higher kinetic energies. When the hump reaches the threshold for the excitation of the first energy levels, it appears in the low-energy range of the EEDF. Then, this process repeats over and over again.

The model constructed here gives different solutions for different ranges of the parameter α. For $\alpha > 0$, the electric field becomes negative in some regions. The proposed model cannot be applied to this case because of the appearance of regions with potential wells that trap the electrons. Initially, when we did not switch to a moving frame of reference, we found that, in the course of numerical solution, the electric field distribution always lagged behind the electron density distribution in phase. Passing over to a moving reference frame

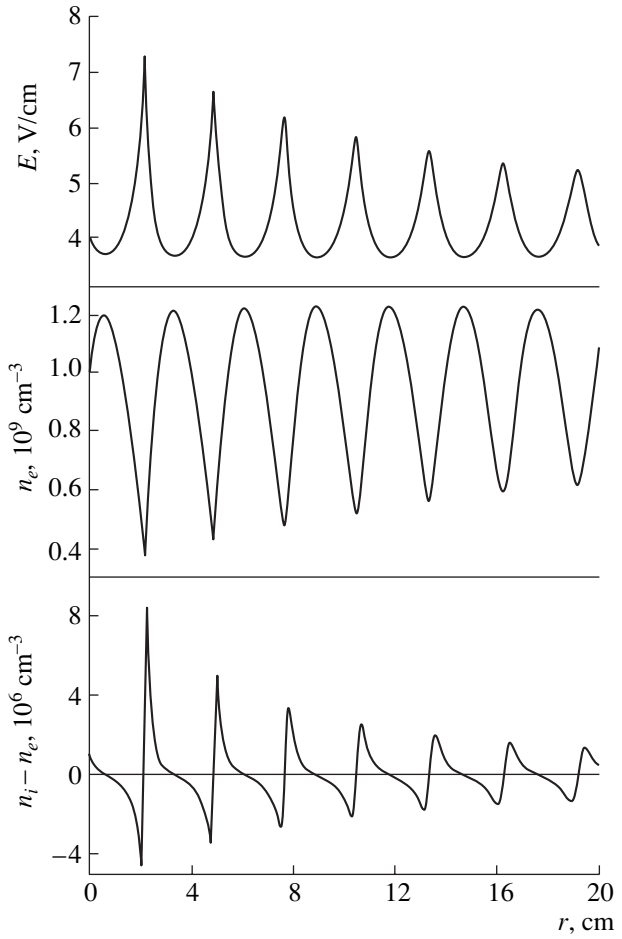

Fig. 3. Distributions of the electric field and electron density and distribution of the difference between the ion and electron densities in a plane stratified discharge in argon at a pressure of $p = 0.5$ torr for $\alpha = -0.5$.

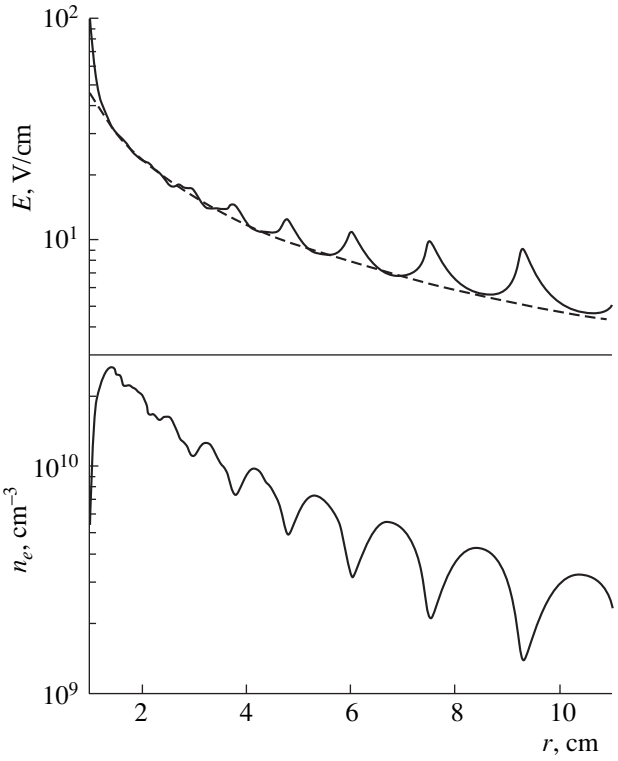

Fig. 4. Distributions of the electric field and electron density in a spherical stratified discharge in argon at a pressure of $p = 0.5$ torr for $\beta = 1$.

allowed us to appropriately adjust the electric field distribution to the electron density distribution: in the range $-1 < \alpha < -0.25$, the iterative process converged and the amplitudes of the final distributions of all the plasma parameters became larger. The strata were observed to move from the cathode toward the anode. In the range $-0.25 < \alpha < 0$ (the value $\alpha = 0$ corresponds to standing strata), the iterative process diverged. For $\alpha < -1$, a region appeared in which the electric field distribution was nonphysical (with wells in place of humps). The solutions that will be presented below were obtained for a definite time and for the value $\alpha = -0.5$, at which the amplitude of all the distributions remained large and the iterative process converged fairly rapidly.

Figure 3 illustrates the distributions of the self-consistent electric field, electron density, and space charge in a plane discharge. We can see that the electric field possesses a nonsinusoidal structure with very pronounced periodic peaks. The electron density is similar in structure to the electric field, but the electron density variations are in antiphase with the electric field variations. In our model, the distribution of the electrons differs from that of the ions. The deviation from the charge neutrality in the PC of a plane discharge is on the order of $|\Delta n|/n_i \sim 10^{-2}$–$10^{-3}$. The distribution of the space charge resembles periodic damped double layers.

In a spherical discharge, the spatial separation between the strata and their velocity depend on the parameter β. Our simulations were carried out for two different β values. For $\beta = 2$, the mean electric field $E(r)$ and the velocity of the strata v_{st} remain constant. The strata are equidistant; their amplitude decreases toward the anode only at the expense of elastic losses. In the radial direction, the electron density $n_e(r)$ changes, on the average, in inverse proportion to the square of the distance from the anode. Analogous radial profiles of the electron density in spherical glow discharges were obtained in the drift-diffusion approximation [14]. For $\beta = 1$, the mean electric field and the ion and electron densities, n_i and n_e, change in inverse proportion to r (see Fig. 4). In this case, the velocity of the strata decreases with distance from the anode and the spatial separation between the peaks in the electric field decreases toward the anode.

Calculation of the radii of the corresponding strata from the position of the peaks in the distribution of

energy loss for the excitation of the first energy state shows that, for $\beta = 1$, they follow a geometric progression $r_n \approx r_0 K^n$. Figure 5 shows the ratio of the radius of the nth stratum, r_n, to the radius of the first stratum, r_0, for different argon pressures. The coefficient K is seen to lie within the range $K \sim 1.31$–1.36. The same result, namely, $K \sim 1.3$–1.5, was obtained in a number of experiments aimed at studying the stratification of spherical discharges in nitrogen with a small acetone admixture [6].

That the height of the peaks in the calculated profiles of the discharge parameters decreases toward the anode is related to the elastic losses and the presence of inelastic energy losses that have thresholds of similar magnitude. When there are no elastic losses and when there is only one energy loss process with the threshold U_1 and with a large cross section (the black wall approximation), the distributions of the macroscopic parameters are undamped and the spatial separation between the strata corresponds to the length $L = U_1/eE^0$, over which the electrons acquire the energy U_1 in the electric field [15]. This loss mechanism operates to produce a periodic resonant electric field in which the hump of the electron distribution function transforms into narrow peaks moving along the resonant trajectories (the so-called bunching effect [16]). As early as 1952, Klyarfel'd [17] pointed out that stratification in the PC can result from an analogous mechanism by which the electrons periodically gain energy in the electric field and lose it in inelastic collisions. In fact, the first thorough analysis of the kinetic mechanism for stratification was made by Tsendin [15].

An important aspect of the analysis of solutions to the Boltzmann equation for the EEDF is to consider the moments of the distribution function. Multiplying Eq. (5) by unity and by U and integrating over the entire energy range under consideration, we arrive, respectively, at the particle and energy balance equations. The electron balance equation has the form

$$\frac{1}{r^n}\frac{d}{dr}(r^n j_r(r)) = 0, \qquad (19)$$

where the integral $j_r(r)$ is given by formula (8). The satisfaction of Eq. (19) served as an additional criterion for the correctness of the simulations based on Eq. (5).

In the plane discharge model, the EEDF is normalized so that the electron density at the entrance to the PC is about $n_e \approx 10^9$ cm^{-3}. In the spherical discharge model, the distribution function is normalized to the magnitude of the discharge current at the cathode,

$$J = 4\pi r_c^2 e j_r(r_c).$$

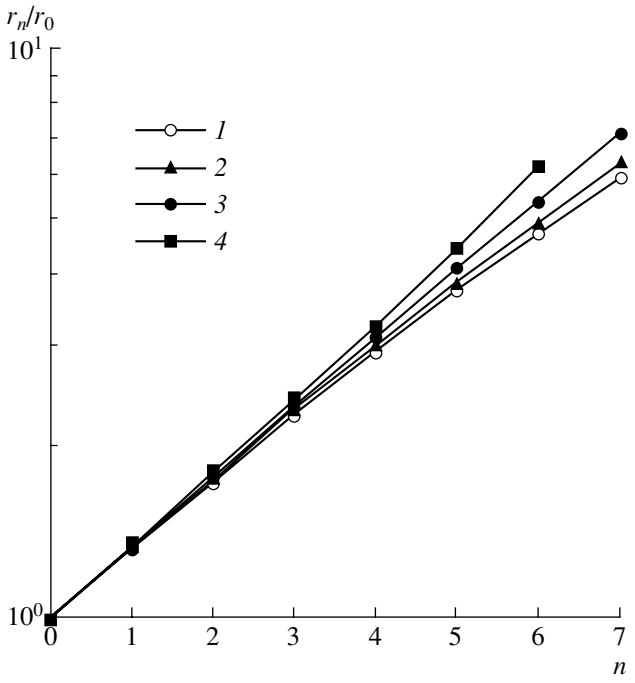

Fig. 5. Ratio of the radius of the nth stratum, r_n, to the radius of the central ($n = 0$) stratum vs. number of the stratum for discharges in argon at pressures of p = (*1*) 0.5, (*2*) 1.0, (*3*) 1.25, and (*4*) 1.5 torr and $\beta = 1$.

The discharge current was chosen to be 10 mA, which corresponds to experimental regimes of the stratification of spherical discharges.

The electron energy balance equation has the form

$$\frac{1}{r^n}\frac{d}{dr}(r^n j_u(r)) = P^f(r) - P^{\rm el}(r) - \sum_k P_k^{\rm in}(r), \qquad (20)$$

where the electron energy flux density $j_u(r)$ is given by the formula

$$j_u(r) = \frac{1}{3}\sqrt{2/m}\int_0^\infty f_r(U, r) U^2 dU. \qquad (21)$$

The gradient of the electron energy flux density is determined by the difference between the energy acquired by the electrons in the electric field,

$$P^f(r) = -j_r(r) eE(r), \qquad (22)$$

and the energy lost by them in elastic collisions,

$$P^{\rm el}(r) = 2\frac{m}{M}\sqrt{2/m}\int_0^\infty U^2 N Q^d(U) f_0(U, r) dU, \qquad (23)$$

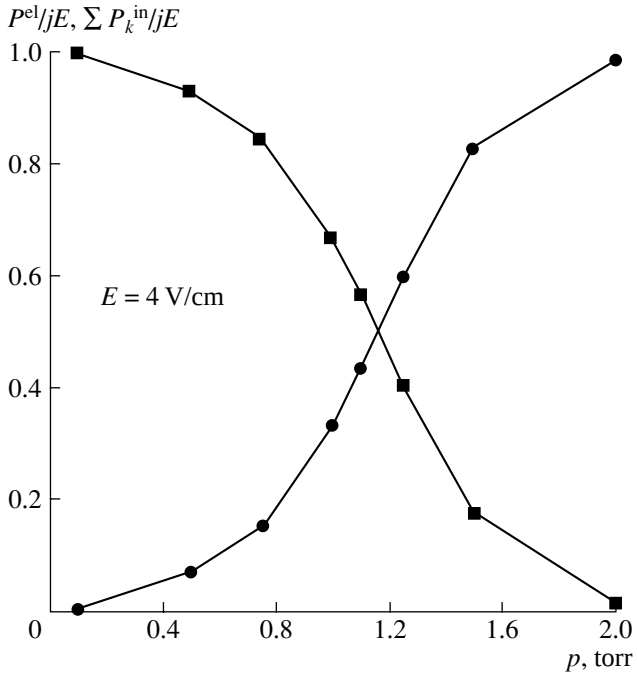

Fig. 6. Relative contributions from elastic energy loss P^{el} (circles) and from energy losses ΣP_k^{in} in all inelastic collisional processes (squares) vs. pressure.

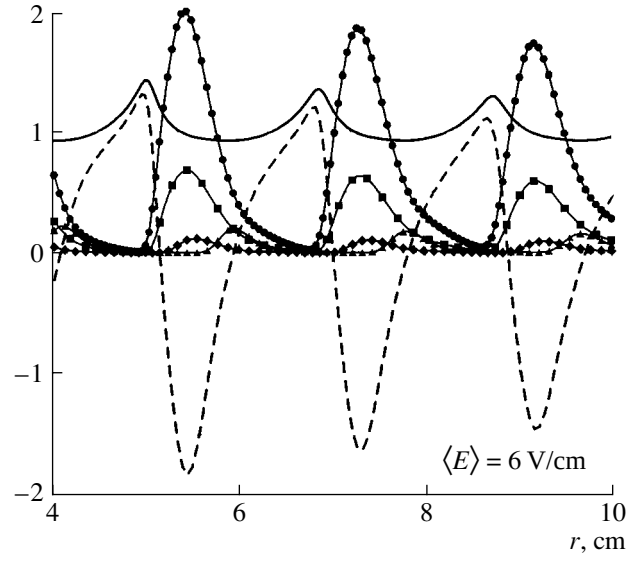

Fig. 7. Radial profile of the absolute value of the energy gain P^f (solid curve) and radial profiles of the energy losses in inelastic collisional processes: P_1 (circles), P_2 (squares), P_3 (diamonds), and P_{ioniz} (triangles), for a discharge in argon at a pressure of p = 0.5 torr. The dashed curve shows the energy flux gradient.

and in different inelastic collisional processes,

$$P_k^{in}(r) = U_k^{in}\sqrt{2/m}\int_0^\infty UNQ_k^{in}(U)f_0(U,r)dU. \quad (24)$$

The discharge plasma can exist either in a state dominated by elastic energy losses (see formula (23)) or in a state dominated by inelastic energy losses (see formula (24)). Figure 6 shows how the relative contributions of elastic and inelastic energy losses to the energy balance depend on argon pressure for a plane discharge in an electric field with the mean strength $\langle E \rangle$ = 4 V/cm. It can be seen that, at high pressures (p > 1.5 torr), the energy losses in elastic collisions predominate over those in inelastic collisions; in this case, the gradient of the electron energy flux density is indeed small in comparison to the remaining terms in the energy balance equation. The plasma state is homogeneous; hence, nonlocal effects can be ignored. We found that, at high argon pressures (p > 1.5 torr), the strata do not arise because much energy is lost in elastic collisions. This case can be described in the so-called local field approximation.

At lower argon pressures, p < 1.5 torr, elastic losses cause the amplitudes of all the distributions to decrease slightly toward the anode; in this case, the lower the argon pressure, the more pronounced the nonlocal effects. Figure 7 shows the radial profile of the absolute value of energy gain (22) and the radial profiles of energy losses (24) (normalized to P^f) in each of the inelastic collisional processes. The simulations were carried out for an argon pressure of p = 0.5 torr and for a mean electric field of $\langle E \rangle$ = 6 V/cm. Under these conditions, the elastic energy loss given by expression (23) is relatively small and the energy density gradient is comparable in magnitude to the terms describing energy losses in inelastic collisions. The energy gained by the electrons in the electric field is displayed by the solid curve. The curves showing the energy losses in inelastic collisions are slightly shifted in phase with respect to the solid curve and are also shifted somewhat toward the anode. The loss term having the maximum amplitude corresponds to energy losses in the process with the lowest energy threshold (11.3 eV). The phase shift between the energy gain profile and the profile of the energy losses in ionization processes with an energy threshold of 15.7 eV is the largest, $\Delta(P^f, P_{ioniz}) \approx \pm\pi$. It is the phase shift between variations in the energy loss by ionization and in the electron density that gives rise to an ionization wave—the strata.

Figure 8 shows how the spatial separation between the strata in a plane discharge depends on the electric field. The points calculated for different argon pressures and different magnitudes of the mean electric field are seen to lie essentially on the same curve. From this figure, we can conclude that, for a given value of

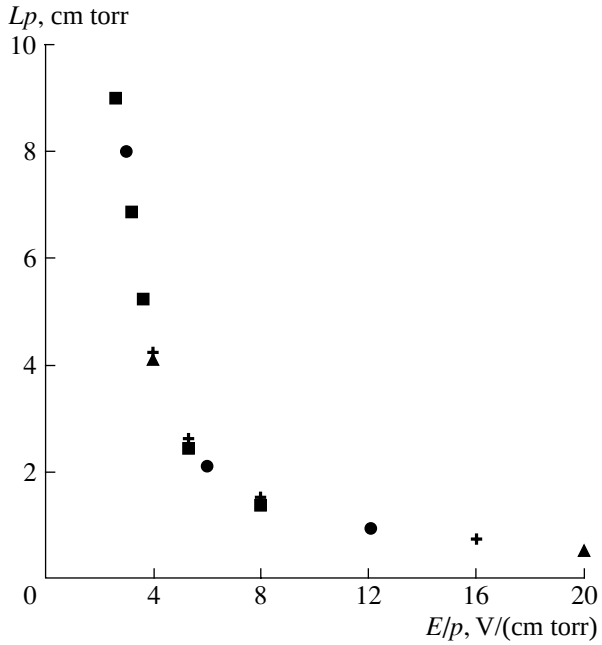

Fig. 8. Length of the strata as a function of the reduced electric field in a plane discharge.

the reduced electric field E/p, the spatial separation between the strata is inversely proportional to the gas pressure, $L \sim 1/p$.

4. CONCLUSIONS

We have developed a one-dimensional self-consistent model of moving strata in a plane and a spherical glow discharge in argon. The model is based on solving the nonlocal Boltzmann equation, the nonstationary ion balance equation, and Poisson's equation by the iterative method. Using this model, we have described the electron and ion plasma components and have determined the distribution of the self-consistent electric field in the PC of a discharge. In the self-consistent model, the spatial period of variation of the macroscopic parameters under consideration is determined automatically, without invoking a prescribed spatial period of the electric field.

The main results obtained with the help of the proposed model are as follows:

(i) In the stratified PC of a plane discharge, the electric field distribution is periodic but possesses a nonsinusoidal structure. The distribution of the electric field is peaked at the positions of the strata, and the electron density distribution lags behind the field distribution in phase by half a period. The degree to which the PC of a plane discharge is nonquasineutral is on the order of $|\Delta n|/n_i \sim 10^{-2}$–$10^{-3}$; in this case, the distribution of the positive space charge resembles double layers.

(ii) The model predicts the existence of moving strata in discharges in argon at low pressures. It is only when the strata move from the cathode toward the anode that the phase shift between the electric field and electron density distributions is adjusted self-consistently and peaks in the distributions of all the parameters grow resonantly.

(iii) At low argon pressures ($p < 1$ torr), when energy loss in elastic collisions is small, the distributions of all macroscopic plasma parameters are spatially periodic. At higher pressures ($p > 1$ torr), the amplitudes of all the distributions decrease strongly toward the anode because of the large energy loss in elastic collisions.

(iv) For a given magnitude of the reduced electric field E/p, the spatial separation between the strata is inversely proportional to the gas pressure, $L \sim 1/p$.

(v) For $\beta = 1$, the proposed model of a spherical discharge makes it possible to confirm the validity of the experimentally obtained dependence of the radii of the strata on their numbers.

It should be noted that the model presented here can be used to describe stratification in discharges in noble gases at low pressures ($p < 1$ torr). The subject of our ongoing studies will be to perform calculations for high-molecular gases and to adequately take into account the phenomena occurring in them. For discharges in gases at higher pressures, it is also necessary to account for metastable particles and stepwise ionization processes. In addition, the right-hand side of the ion balance equation should be supplemented with the terms describing ionization and recombination processes; in simple models (including the model developed here), the contributions from ionization and recombination are assumed to cancel one another out.

ACKNOWLEDGMENTS

This work was supported in part by the RF Presidential Program for State Support of Leading Scientific Schools (project no. NSh-910.2003.1) and the International Science and Technology Center (grant no. 1425).

REFERENCES

1. A. V. Nedospasov, Usp. Fiz. Nauk **94**, 439 (1968) [Sov. Phys. Usp. **11**, 174 (1968)].
2. L. Pekarek, Usp. Fiz. Nauk **94**, 463 (1968) [Sov. Phys. Usp. **11**, 88 (1968)].
3. P. S. Landa, N. A. Miskinova, and Yu. V. Ponomarev, Usp. Fiz. Nauk **132**, 601 (1980) [Sov. Phys. Usp. **23**, 813 (1980)].
4. Yu. P. Raizer, *Gas Discharge Physics* (Nauka, Moscow, 1987; Springer-Verlag, Berlin, 1991).
5. O. A. Nerushev, S. A. Novopashin, V. V. Radchenko, and G. I. Sukhinin, Fiz. Plazmy **26**, 81 (2000) [Plasma Phys. Rep. **26**, 78 (2000)].
6. O. A. Nerushev, S. A. Novopashin, V. V. Radchenko, and G. I. Sukhinin, Phys. Rev. E **58**, 4897 (1998).

7. F. Sigeneger and R. Winkler, Contrib. Plasma Phys. **36**, 551 (1996).
8. Yu. B. Golubovskii, A. Yu. Skoblo, V. A. Maiorov, V. O. Nekutchaev, *et al.*, Plasma Sources Sci. Technol. **11**, 309 (2002).
9. Yu. B. Golubovskii, R. V. Kozakov, V. A. Maiorov, *et al.*, Phys. Rev. E **62**, 2707 (2000).
10. Yu. B. Golubovskii, V. A. Maiorov, V. O. Nekutchaev, *et al.*, Phys. Rev. E **63**, 036409 (2001).
11. A. Bogaerts and R. Gijbels, J. Tech. Phys. (Warsaw) **41**, 183 (2000).
12. Z. Donko, Phys. Rev. E **57**, 7126 (1998).
13. W. L. Morgan, J. P. Boeuf, and L. Pitchford, *Siglo Data Base, CPAT, and Kinema Software*, http://www.csn.net/siglo (1998).
14. G. I. Sukhinin and A. V. Fedoseev, Teplofiz. Aeromekh. **10**, 63 (2003).
15. L. D. Tsendin, Zh. Tekh. Fiz. **52**, 635 (1982) [Sov. Phys. Tech. Phys. **27**, 407 (1982)].
16. Yu. B. Golubovskii, I. A. Porokhova, J. Behnke, *et al.*, J. Phys. D **31**, 2447 (1998).
17. B. N. Klyarfel'd, Zh. Éksp. Teor. Fiz. **22**, 66 (1952).

Translated by O.E. Khadin

Plasma Physics Reports, Vol. 30, No. 12, 2004, pp. 1071–1074. Translated from Fizika Plazmy, Vol. 30, No. 12, 2004, pp. 1149–1152.

BRIEF COMMUNICATIONS

A Nonlinear Single-Mode Structure in a Plasma with Anisotropic Temperature

V. Yu. Bychenkov

Lebedev Physical Institute, Russian Academy of Sciences, Leninskiĭ pr. 53, Moscow, 119991 Russia

Received February 3, 2004

Abstract—An exact solution is derived to the equations of vortex electron anisotropic hydrodynamics for a plasma that is unstable against the Weibel instability driven by the electron temperature anisotropy. This solution describes saturation of the Weibel instability in the single-mode regime with an arbitrary wavelength and corresponds to a standing helical wave of magnetic perturbations in which the amplitude of the generated magnetic field varies periodically over time. The longitudinal and transverse (with respect to the rotating anisotropy axis) plasma temperatures are subject to the same periodic variations. In this case, the maximum magnetic field energy can be on the order of the plasma thermal energy. © *2004 MAIK "Nauka/Interperiodica".*

A plasma with anisotropic electron temperature is unstable against electromagnetic perturbations in which the magnetic field is generated on a characteristic time scale that is much longer than the period of the electron plasma wave [1]. The nonlinear stage of the Weibel instability is, as a rule, studied by means of numerical simulations [2–9]. On the other hand, the so-called vortex electron anisotropic hydrodynamics (VEAH) model, which was proposed at the end of 1980s, provides a fairly efficient tool for developing an analytic theory of the Weibel instability. With this model, for instance, two classes of analytic solutions to the VEAH equations were obtained: self-similar explosive solutions [10–13] and single-mode periodic solutions [14–16]. The present study, whose aim is to extend the second class of solutions, is a continuation of paper [16], in which a long-wavelength single-mode solution was derived that described a standing magnetic structure produced in a plasma without changing its anisotropic pressure. Below, a solution will be obtained that describes the same type of magnetic structure but with an arbitrary wavelength. The single-mode solution that was found in [14] corresponds to the case in which the pressure is constant along the generated magnetic field. The solution obtained in our study corresponds to self-consistent pressure variations along the magnetic field. In addition, this solution provides a physically clear interpretation of the relevant nonlinear plasma state in terms of spatiotemporal variations in the direction of the anisotropy axis and periodic variations in pressure both along and across this direction.

The nonlinear evolution of a plasma with anisotropic electron pressure is described by the following VEAH equations for the magnetic field **B** and pressure tensor $\overleftrightarrow{\mathbb{P}}$ [17]:

$$\frac{\partial}{\partial t}\left(\boldsymbol{\Omega} - \frac{c^2}{\omega_p^2}\Delta\boldsymbol{\Omega}\right)$$

$$= \frac{c^2}{\omega_p^2}\nabla\times\left[(\boldsymbol{\Omega}\cdot\nabla)\boldsymbol{\Omega} - \frac{c^2}{\omega_p^2}((\nabla\times\boldsymbol{\Omega})\cdot\nabla)\nabla\times\boldsymbol{\Omega}\right]$$

$$-\frac{1}{mn}\nabla\times(\nabla\cdot\overleftrightarrow{\mathbb{P}}), \qquad (1)$$

$$\frac{\partial\mathbb{P}}{\partial t} + \frac{c^2}{\omega_p^2}((\nabla\times\boldsymbol{\Omega})\cdot\nabla)\mathbb{P}$$

$$+\frac{c^2}{\omega_p^2}\{(\mathbb{P}\cdot\nabla)\nabla\times\boldsymbol{\Omega}\} = \{\mathbb{P}\times\boldsymbol{\Omega}\}.$$

Here, $\boldsymbol{\Omega} = e\mathbf{B}/mc$ is the electron cyclotron frequency; $\omega_p = (4\pi e^2 n/m)^{1/2}$ is the electron plasma frequency; e and m are the charge and mass of an electron; n is the electron density; and the braces $\{\ldots\}$ indicate symmetrization of the tensor, i.e., $\{A_{ij}\} = A_{ij} + A_{ji}$. Equations (1) describe the vortex motions of the electron plasma component with negligible variations in the electron density n. For a plasma with anisotropic pressure $\overleftrightarrow{\mathbb{P}} = P_\parallel\mathbf{nn} + P_\perp(\overleftrightarrow{I} - \mathbf{nn})$ (where $P_\perp > P_\parallel$, $\mathbf{n}$ is a unit vector, and $\overleftrightarrow{I}$ denotes the unit tensor), the linearized set of Eqs. (1) describes a Weibel instability whose growth

1063-780X/04/3012-1071$26.00

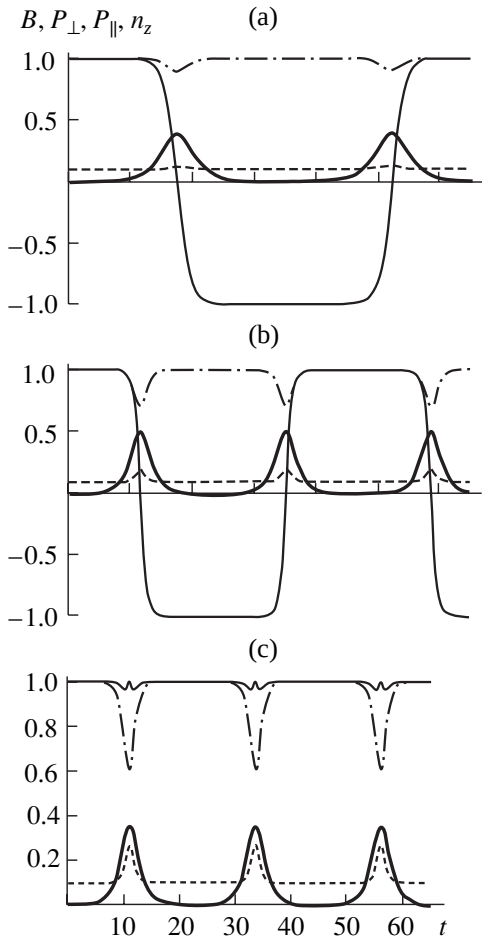

Fig. 1. Evolution of the magnetic field (heavy solid curves), the transverse pressure (dashed-and-dotted curves), the longitudinal pressure (dashed curves), and the z component of the anisotropy vector (light solid curves) for an initial magnetic field strength of $B_0 = 0.01$; a pressure anisotropy of $P_{\perp 0}/P_{\parallel 0} = 10$; and k = (a) 0.5, (b) 1, and (c) 2.

rate is maximum across the direction in which the pressure is higher (i.e., along the unit vector **n**).

In [17], a description of the plasma in terms of the evolution of the anisotropy vector **n** was developed for the case of a uniaxial anisotropy and long-wavelength vortex structures occurring on spatial scales much longer than c/ω_p. The corresponding ($ck \ll \omega_p$) one-dimensional solution for a helical magnetic structure of the form $\mathbf{B} = \{B(t)\sin kz,\ B(t)\cos kz,\ 0\}$ in a plasma with anisotropic pressure ($P_\perp$ = const, $P_\parallel$ = const) was obtained in [16]. Here, that solution is extended to the case of an arbitrary wavenumber, $k \gtrless \omega_p/c$, by introducing the time dependence in the following way: $P_\perp(t)$ with $P_\perp(0) = P_{\perp 0}$, $P_\parallel(t)$ with $P_\parallel(0) = P_{\parallel 0}$, and $\mathbf{n}(t, z) = \{\sin\Phi\cos kz,\ \sin\Phi\sin kz,\ \cos\Phi\}$ with $\mathbf{n}(0, z) = \{0, 0, 1\}$. As a result, Eqs. (1) reduces to the following set of ordinary differential equations:

$$
\begin{aligned}
&(P_\parallel - P_\perp)\frac{d\Phi}{dt} \\
&= \Omega\left[P_\perp\left(1 + \frac{c^2k^2}{\omega_p^2}\sin^2\Phi\right) - P_\parallel\left(1 + \frac{c^2k^2}{\omega_p^2}\cos^2\Phi\right)\right], \\
&\left(1 + \frac{c^2k^2}{\omega_p^2}\right)\frac{d\Omega}{dt} = k^2\frac{P_\parallel - P_\perp}{mn}\cos\Phi\sin\Phi, \qquad (2) \\
&\frac{dP_\perp}{dt} = \Omega\frac{c^2k^2}{\omega_p^2}P_\perp\cos\Phi\sin\Phi, \\
&\frac{dP_\parallel}{dt} = -2\Omega\frac{c^2k^2}{\omega_p^2}P_\parallel\cos\Phi\sin\Phi.
\end{aligned}
$$

In the limit $t \longrightarrow 0$, when $eB/mc = \Omega = \Omega_0$ and $\Phi = 0$, Eqs. (2) describe an exponential increase in the magnetic field at a rate equal to the growth rate of the Weibel instability, $(k/\sqrt{mn})\sqrt{P_{\perp 0}/(1 + c^2k^2/\omega_p^2) - P_{\parallel 0}}$, provided that $P_{\perp 0} > P_\parallel(0)(1 + c^2k^2/\omega_p^2)$. In what follows, it is assumed that the last inequality holds. In the long-wavelength limit, $ck \ll \omega_p$, Eqs. (2) degenerate into a set of two equations for Ω and Φ with constant pressure components $P_\parallel$ and $P_\perp$, yielding the same result as that obtained in [16].

The set of ordinary differential equations (2) has the integrals

$$
\begin{aligned}
&P_\parallel P_\perp^2 = P_{\parallel 0}P_{\perp 0}^2, \\
&\left(1 + \frac{c^2k^2}{\omega_p^2}\right)(\Omega^2 - \Omega_0^2) \qquad (3) \\
&= \frac{\omega_p^2}{mnc^2}(P_{\parallel 0} - P_\parallel - 2P_\perp + 2P_{\perp 0})
\end{aligned}
$$

and thus is rather easy to solve numerically. Here, the solutions to Eqs. (2) are illustrated in terms of dimensionless variables, specifically, the time, the coordinate (the inverse wavenumber), the pressure components, and the magnetic field are expressed in units of $(c/\omega_p)\sqrt{nm/P_{\perp 0}}$, c/ω_p, $P_{\perp 0}$, and $\sqrt{4\pi P_{\perp 0}}$, respectively. Figure 1 shows the solutions for the magnetic field B; the transverse and longitudinal pressure components, $P_\perp$ and $P_\parallel$; and the z coordinate of the anisotropy vector, $n_z = \cos\Phi$. The initial exponential increase in the magnetic field is accompanied by a decrease in the higher (transverse) pressure component and an increase in the lower (longitudinal) pressure component. After the magnetic field saturates, it decreases to its initial value and the plasma pressure components also relax to their initial values. The process then repeats itself periodically. For small wavenumbers, $k \lesssim 1$, the anisotropy

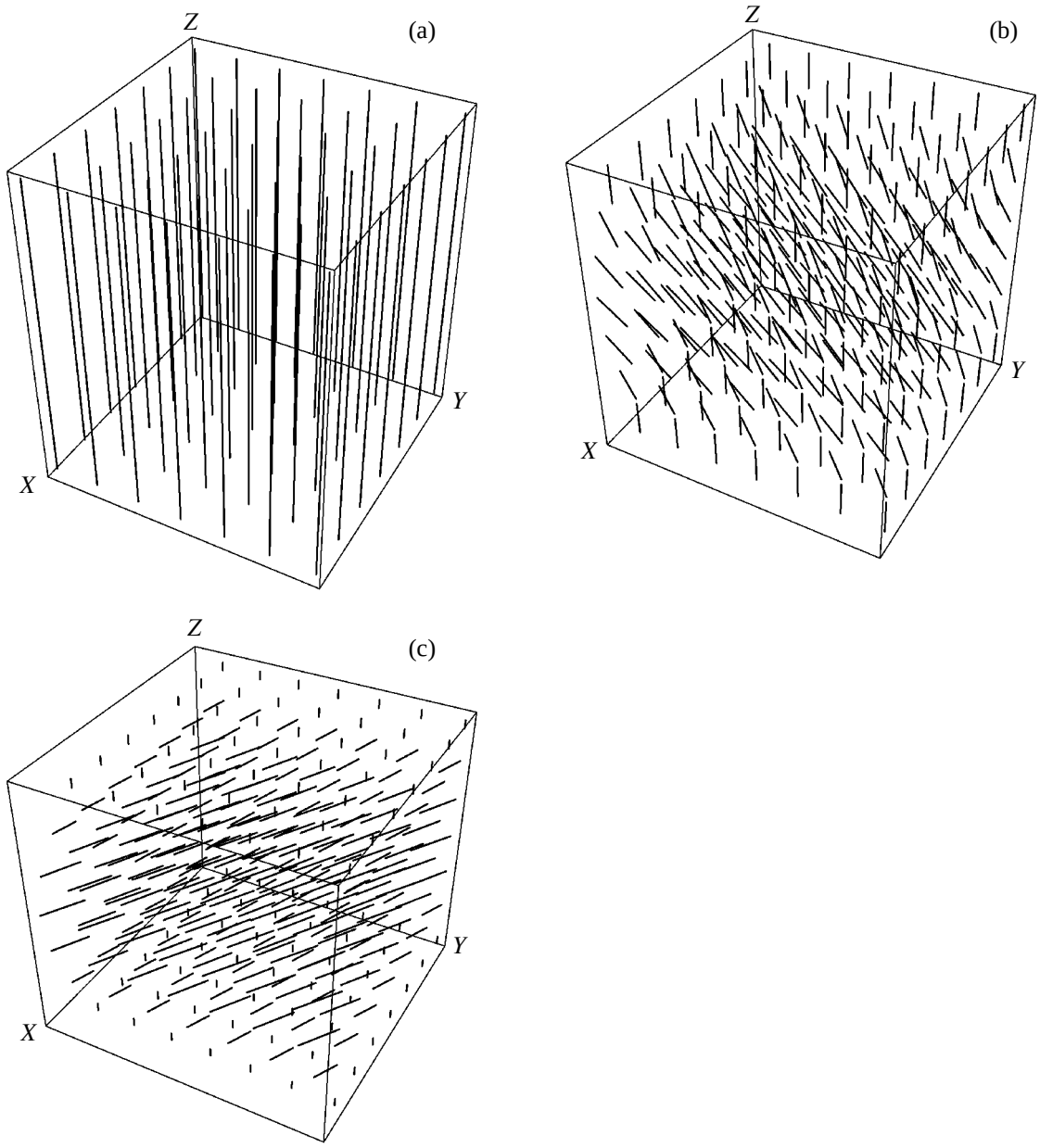

Fig. 2. Field of the anisotropy vector **n** in the region $0 \le z \le \pi/k$ for an initial magnetic field strength of $B_0 = 0.01$, a pressure anisotropy of $P_{\perp 0}/P_{\|0} = 10$, and $k = 1$ at t = (a) 0, (b) 10, and (c) 12.

vector reverses its direction during plasma relaxation (see Figs. 1a, 1b). The reverse occurs at about the same time the magnetic field reaches its maximum value $B_{\max}$. A regime with a flip-over of the anisotropy vector does not arise in the case of large wavenumbers $k > 1$ (see Fig. 1c).

The period T of the nonlinear oscillations depends on the wavenumber and the initial magnetic field B_0. As in the long-wavelength limit [16], this period increases logarithmically with decreasing B_0; i.e., $T \propto \ln B_0$. When the degree of pressure anisotropy is high ($P_\perp/P_\| \gg 1$), the oscillation period is minimal at $k \sim 1$ and can be estimated in order of magnitude by its limiting (at $k \longrightarrow 1$) value in the long-wavelength theory: $T \sim (4/\sqrt{P_{\perp 0}})\ln 4/B_0$. For both long ($k \ll 1$) and short ($k \gg 1$) wavelengths, the maximum magnetic energy is low in comparison to the plasma thermal energy; however, for $k \sim 1$, these energies are comparable: $B_{\max}^2/4\pi P_\perp \simeq 1/4$. The magnetic energy averaged over the period of nonlinear oscillations is always much lower than the plasma thermal energy.

Physically, the Weibel instability is stabilized by the following two effects: a self-consistent decrease in the

degree of plasma anisotropy during the generation of the magnetic field (see Eqs. (1)) and spatial variations in the direction of the anisotropy vector. In the long-wavelength limit ($k \ll 1$), the second effect is insignificant [17] (which is clearly demonstrated in Fig. 1a). In this case, the instability saturation is associated with the rotation of the anisotropy axis [16]. Spatiotemporal variations in the direction of the anisotropy vector are illustrated in Fig. 2.

To conclude, note that the above analytical solution to the VEAH equations describes the relaxation of the Weibel instability in a single-mode regime in which a helical magnetic structure consistent with the formation of helical pressure anisotropy is generated. The solution for periodic time variations in the magnetic field and plasma pressure components is qualitatively similar to that obtained earlier in [14, 15]. The difference lies primarily in the structure of the anisotropic pressure tensor, but there are also slight differences in the shapes and amplitudes of the magnetic pulses. The solution obtained has a physically clear interpretation: the instability saturates because of a decrease in the degree of anisotropy and the rotation of the anisotropy axis. It should be noted that three-dimensional numerical simulations carried out in [9] revealed the formation of a one-dimensional helical magnetic structure. This result allows one to suppose that the solution derived here plays the role of an attractor for a three-dimensional relaxation of the Weibel instability. It is worthwhile to carefully check this supposition (both theoretically and numerically) in view of the opportunity to verify it in the unique experiments that are planned for the near future as part of a project on an ultra-high-brightness free-electron laser [18]. In the interaction of a short high-power X-ray pulse with a gas, the Weibel instability is very likely to occur as a result of photoionization, which leads to anisotropy in the electron velocity distribution.

ACKNOWLEDGMENTS

This work was supported in part by the Russian Foundation for Basic Research, project no. 03-02-16428.

REFERENCES

1. E. S. Weibel, Phys. Rev. Lett. **2**, 83 (1959).
2. R. L. Morse and C. W. Nielson, Phys. Fluids **14**, 830 (1971).
3. J. M. Wallace and E. M. Epperlein, Phys. Fluids B **3**, 1579 (1991).
4. R. C. Davidson, D. A. Hammer, I. Haber, and C. E. Wagner, Phys. Fluids **15**, 317 (1972).
5. V. Yu. Bychenkov, V. N. Novikov, V. P. Silin, and V. T. Tikhonchuk, Fiz. Plazmy **17**, 463 (1991) [Sov. J. Plasma Phys. **17**, 272 (1991)].
6. V. Yu. Bychenkov, V. N. Novikov, and V. P. Silin, Fiz. Plazmy **17**, 830 (1991) [Sov. J. Plasma Phys. **17**, 485 (1991)].
7. V. Yu. Bychenkov and V. N. Novikov, Fiz. Plazmy **23**, 726 (1997) [Plasma Phys. Rep. **23**, 670 (1997)].
8. V. Yu. Bychenkov, A. I. Golubev, N. A. Izmaĭlova, *et al.*, Fiz. Plazmy **26**, 57 (2000) [Plasma Phys. Rep. **26**, 54 (2000)].
9. D. V. Romanov, V. Yu. Bychenkov, W. Rozmus, *et al.*, Bull. Am. Phys. Soc. **47**, 87 (2000).
10. V. Yu. Bychenkov, V. P. Silin, and V. T. Tikhonchuk, Fiz. Plazmy **15**, 706 (1989) [Sov. J. Plasma Phys. **15**, 407 (1989)].
11. V. Yu. Bychenkov, V. P. Silin, and V. T. Tikhonchuk, Phys. Lett. A **138**, 127 (1989).
12. V. Yu. Bychenkov, V. F. Kovalev, and V. V. Pustovalov, Fiz. Plazmy **22**, 1101 (1996) [Plasma Phys. Rep. **22**, 999 (1996)].
13. V. A. Terekhin, E. V. Uvarov, V. Yu. Bychenkov, and V. F. Kovalev, Fiz. Plazmy **25**, 453 (1999) [Plasma Phys. Rep. **25**, 409 (1999)].
14. V. A. Terekhin, V. T. Tikhonchuk, and E. V. Uvarov, Phys. Lett. A **254**, 210 (1999).
15. V. A. Terekhin, V. T. Tikhonchuk, and E. V. Uvarov, Fiz. Plazmy **26**, 334 (2000) [Plasma Phys. Rep. **26**, 308 (2000)].
16. V. Yu. Bysḥenkov, W. Rozmus, and S. E. Capjack, Pis'ma Zh. Éksp. Teor. Fiz. **78**, 150 (2003) [JETP Lett. **78**, 119 (2003)].
17. V. Yu. Bychenkov, V. P. Silin, and V. T. Tikhonchuk, Zh. Éksp. Teor. Fiz. **98**, 1269 (1990) [Sov. Phys. JETP **71**, 709 (1990)].
18. T. Tschentscher, Proc. SPIE **4500**, 1 (2001).

Translated by O.E. Khadin

Plasma Physics Reports, Vol. 30, No. 12, 2004, pp. 983–987. Translated from Fizika Plazmy, Vol. 30, No. 12, 2004, pp. 1059–1063.

TOKAMAKS

Effect of Anomalous Ion Inertia and Oblique Ion Viscosity on the Radial Electric Field in FT-2 Tokamak Experiments

S. I. Lashkul and A. Yu. Popov

Ioffe Institute for Physics and Technology, Russian Academy of Sciences, Politekhnicheskaya ul. 26, St. Petersburg, 194021 Russia

Received April 3, 2003; in final form, November 17, 2003

Abstract—Results are presented from numerical simulations that show that, in a plasma with well-developed turbulence, the radial electric field can be positive in the region where the gradients of the plasma parameters are steep. In a plasma in which the turbulence is suppressed (as is the case with auxiliary lower hybrid heating), the radial electric field is found to exhibit a nearly neoclassical behavior during the formation of a transport barrier and transition to the H-mode. *© 2004 MAIK "Nauka/Interperiodica".*

1. INTRODUCTION

In experiments on the FT-2 tokamak, it was observed that, during the RF heating of the plasma ions by lower hybrid (LH) waves, the plasma evolved into an improved energy and particle confinement regime [1]. During auxiliary plasma heating, steep gradients were found to arise on the electron density and ion temperature profiles in the region $r = 4.5$–6 cm, thus indicating the formation of an internal transport barrier (ITB) there. Additional on-axis heating of the plasma electrons that was observed during RF heating was attributed to a sharp decrease in electron heat transport. Furthermore, after the LH heating pulse had come to an end, an L–H transition was detected. The transition was accompanied by the formation of an external transport barrier (ETB) in the vicinity of the last closed flux surface (LCFS), whose position in the tokamak was controlled by a poloidal limiter of radius $r_L = 7.8$ cm. The fact that the particle and energy confinement times both increase, while the recycling of neutral hydrogen at the plasma edge becomes far slower, is in good agreement with the data from spectral, bolometric, diamagnetic, and other measurements [1]. In a number of papers (see, e.g., [2]), it was suggested that the main mechanism responsible for suppressing anomalous transport in a tokamak plasma is an increase in the shear of the poloidal plasma rotation. In our experiments, the increase in the shear of the poloidal $\mathbf{E} \times \mathbf{B}$ plasma rotation was governed by the steepening of the ion temperature and electron density gradients, ∇T_i and ∇n_e, in the region $r = 4.5$–6 cm. The hypothesis that was proposed to explain these experimental data implied that the shear of the poloidal rotation frequency $\omega_{\mathbf{E}\times\mathbf{B}}$ increases because of the efficient ion heating, which results in a steepening of the ion temperature gradient in the region $r = 4.5$–6 cm. This hypothesis was confirmed by numerical simulations carried out with the BATRAC transport code [3]. The fact that a considerable increase in the radial electric field amplitude $|E_r|$ is governed by the steepening of the ion temperature and electron density gradients, ∇T_i and ∇n_e, was also supported by computations with the ASCOT code [4], in which the distribution function of the plasma ions was simulated by the Monte Carlo method. The experimental verification of the above hypothesis was based on direct spectral and probe measurements of the radial electric field E_r [5]. The measurement results are as follows:

(i) The negative radial electric field E_r does indeed increase in absolute value within the gradient region. In [5], it was shown that, in the region where the ITB forms, the radial electric field E_r increased from –10 to –23 kV/m. These values are somewhat higher than the neoclassical ones [6, 7] and agree better with those computed by the ASCOT code, in which the radial ambipolar electric fields are modeled with allowance for nonambipolar ion fluxes.

(ii) In different stages of the discharge, the radial electric field near the LCFS (at the plasma edge) can become positive, which contradicts the generally accepted neoclassical theory [6] and requires a special explanation. It should be noted that similar experimental results (i.e., showing that the field E_r becomes positive at the discharge periphery) were reported in several other papers (see, e.g., [8]). Such behavior of E_r in the edge plasma indicates that the longitudinal force balance in this region is more complicated than that considered in the generally accepted neoclassical theory [6] and should thus be further refined in order to provide a correct description of the observed phenomena. The objective of the present paper is to resolve the existing contradiction between the experimental data and the views based on the standard neoclassical theory.

It is well known that, during an L–H transition, the parameters of the wall plasma can change substantially

1063-780X/04/3012-0983$26.00 © 2004 MAIK "Nauka/Interperiodica"

on spatial scales comparable to the poloidal ion gyroradius. Under these conditions, the profile of the radial electric field can be affected not only by the longitudinal ion viscosity [9, 10] but also by the anomalous ion inertia and oblique ion viscosity. The effect of the latter two factors is important only when the gradients of the plasma parameters are sufficiently steep. Analytic expressions for the anomalous ion inertia and oblique ion viscosity were first derived by Rozhansky and Tendler [9]. Here, we suppose that the observed profile of the radial electric field E_r in FT-2 tokamak experiments can be explained by taking into account anomalous inertia and oblique viscosity, which play a significant role at the discharge periphery.

Our paper is organized as follows: In Section 2, we describe a theoretical model constructed with allowance for the anomalous effects associated with the plasma microturbulence. In Section 3, we analyze the results of numerical simulations carried out on the basis of the model proposed. In the Conclusion, we present the main results of our study and compare them to the experimental data.

2. PHYSICAL MODEL

We consider a hydrodynamically equilibrium toroidal plasma column in the ideal MHD approximation. Taking into account the geometric parameters of the FT-2 tokamak (R = 0.55 m, r_L = 0.079 m, I_{pl} = 22 kA, and B_t = 2.2 T), we consider a magnetic field model corresponding to the case of small toroidal nonuniformities and circular flux surfaces:

$$\mathbf{B} = B_0\frac{\theta(r)\mathbf{e}_\vartheta + \mathbf{e}_z}{1+\varepsilon(r)\cos\vartheta}, \tag{1}$$

where $\varepsilon(r) = r/R_0 \ll 1$ is the inverse aspect ratio, $\theta(r) = \varepsilon(r)/q(r)$, $q(r)$ is the safety factor, and R_0 is the tokamak major radius. Representation (1) is written in a curvilinear coordinate system in which the element of length is defined by

$$dl^2 = g_{11}dr^2 + g_{22}d\vartheta^2 + g_{33}dz^2, \tag{2}$$

where $g_{11} = 1$, $g_{22} = r^2$, and $g_{33} = (1+\varepsilon\cos\vartheta)^2$ are the metric tensor components and $\mathbf{e}_r$, $\mathbf{e}_\vartheta$, and $\mathbf{e}_z$ are unit vectors corresponding to the radial, poloidal, and toroidal directions in a quasi-toroidal coordinate system, respectively.

In order to obtain an expression for the radial component of the electric field, we consider the longitudinal force balance equation

$$\langle \mathbf{B}\cdot(\nabla\cdot\overleftrightarrow{\pi}_i)\rangle = -\langle \mathbf{F}\cdot\mathbf{B}\rangle. \tag{3}$$

Here, $\overleftrightarrow{\pi}_i$ is the ion viscosity; $\mathbf{F}$ is the inertial force; and the angle brackets denote averaging over the flux surface,

$$\langle\ldots\rangle = \frac{1}{2\pi}\int_0^{2\pi}\ldots\sqrt{g_{33}}d\vartheta.$$

Following [9, 11], we represent the ion viscosity as the sum of neoclassical and anomalous viscosities: $\overleftrightarrow{\pi}_i = \overleftrightarrow{\pi}_i^{(\mathrm{NEO})} + \overleftrightarrow{\pi}_i^{(\mathrm{AN})}$. We also assume that $\mathbf{F}\equiv\mathbf{F}^{(\mathrm{AN})}$. In terms of the averaged longitudinal ion velocity $u_{\parallel,i} = \langle\mathbf{u}_i\cdot\mathbf{B}\rangle/|B|$, the anomalous viscosity and inertial force can be written as

$$\begin{aligned} F^{(\mathrm{AN})} &= m_i n_e u_r\frac{\partial u_{\parallel,i}}{\partial r},\\ \frac{\mathbf{B}}{|\mathbf{B}|}(\nabla\cdot\overleftrightarrow{\pi}_i)^{(\mathrm{AN})} &= -\frac{1}{r}\frac{\partial}{\partial r}\left(r\eta\frac{\partial u_{\parallel,i}}{\partial r}\right),\end{aligned} \tag{4}$$

where n_e is the electron density, m_i is the mass of an ion, η is the anomalous viscosity coefficient, $u_{\parallel,i}$ is the longitudinal ion velocity, and u_r is the radial plasma drift velocity in the ambipolar electric field. In our simulations, u_r is given by the expression

$$u_r = -\frac{D}{n}\frac{dn}{dr}, \tag{5}$$

where D is the anomalous diffusion coefficient. The anomalous viscosity coefficient η can be estimated by

$$\eta \sim Dm_i n_e. \tag{6}$$

The longitudinal plasma velocity can be represented as

$$u_{\parallel,i} \simeq \bar{u}_z + \theta V_\vartheta/(1+\varepsilon\cos\vartheta), \tag{7}$$

where $\bar{u}_z = \langle u_z/(1+\varepsilon\cos\vartheta)\rangle$. We have no direct experimental data on the toroidal rotation velocity $\bar{u}_z$ in the plasma of the FT-2 tokamak. However, if there are no external factors (such as, for example, auxiliary NBI heating), we can assume that $\bar{u}_z \simeq 0$. Substituting expressions (4) and (5) into Eq. (3) and using representation (7), we obtain the following second-order differential equation for the poloidal rotation velocity:

$$\begin{aligned}\frac{\langle\mathbf{B}\cdot(\nabla\overleftrightarrow{\pi}_i)\rangle^{(\mathrm{NEO})}}{\theta B_0} &- (1+2q^2)n_e m_i u_r\frac{\partial V_\vartheta}{\partial r}\\ &+ (1+2q^2)\frac{1}{r}\frac{\partial}{\partial r}\left(r\eta\frac{\partial V_\vartheta}{\partial r}\right) = 0.\end{aligned} \tag{8}$$

The neoclassical ion viscosity $\langle\mathbf{B}\cdot(\nabla\cdot\overleftrightarrow{\pi}_i)\rangle^{(\mathrm{NEO})}$ is described by the expression $\langle\mathbf{B}\cdot(\nabla\cdot\overleftrightarrow{\pi}_i)\rangle^{(\mathrm{NEO})} = n_e m_i\mu(V_\vartheta - V_\vartheta^{(\mathrm{NEO})})$, where the coefficient μ depends on the collisionality regime. When the ion inertia can be ignored, the right-hand side of Eq. (8) vanishes and the plasma rotation velocity is given by the neoclassical

formula $V_\vartheta \equiv V_\vartheta^{(\mathrm{NEO})} = (1 - k_T)c/(eB_0)\partial T_i/\partial r$, where the coefficient k_T is equal to 2.69 in the Pfirsch–Schlüter regime, to 1.5 in the plateau regime, and to –0.17 in the banana regime [7]. Depending on the experimental conditions, the plasma in the FT-2 tokamak is in one of the two collisionality regimes: the plasma at half the minor radius is in the plateau regime, while the edge plasma is in the Pfirsch–Schlüter regime. In order to describe all collisionality regimes, we represent μ in the form

$$\mu = \frac{\mu^{\mathrm{pl}}}{1 + \mu^{\mathrm{pl}}/\mu^{\mathrm{ps}}}, \qquad (9)$$

where μ^{pl} and μ^{ps} are the values of μ in the plateau and Pfirsch–Schlüter regimes, respectively. Using explicit expressions for the neoclassical ion viscosity [6, 7], we rewrite representation (9) as

$$\mu = \frac{1}{2}\sqrt{\frac{\pi}{2}}\frac{q^2\nu_i^*}{1 + 0.87\nu_i/\nu_i^*}B_0, \qquad (9a)$$

where ν_i is the ion collision frequency and $\nu_i^* = \dfrac{v_{ti}}{qR_0}$ is the threshold frequency between the plateau and Pfirsch–Schlüter regimes. Representation (9) provides an asymptotically correct description of the coefficient μ for both of these regimes. For $\varepsilon^{3/2}\nu_i^* \ll \nu_i \ll \nu_i^*$, we have $\mu \simeq \mu^{\mathrm{pl}} \equiv \dfrac{1}{2}\sqrt{\dfrac{\pi}{2}}\dfrac{qv_{ti}}{R_0}B_0$, and, for $\nu_i^* \ll \nu_i$, we have $\mu \simeq \mu^{\mathrm{ps}} \equiv 0.96\dfrac{3}{4}\dfrac{v_{ti}^2}{\nu_i R_0^2}B_0$. Taking into account the parameters of the FT-2 tokamak discharges ($q \sim 5$–7 at the plasma boundary) and assuming that estimate (6) is an exact equality, we reduce Eq. (8) to a form that is more convenient for examination and numerical computation:

$$\frac{d^2V_\vartheta}{dr^2} + \xi(r)\frac{1}{r}\frac{dV_\vartheta}{dr} + q^2(r)(V_\vartheta - V_\vartheta^{(\mathrm{NEO})}) = 0, \qquad (8a)$$

where $q^2(r) = \dfrac{1}{\theta D(r)}\dfrac{1}{4}\sqrt{\dfrac{\pi}{2}}\dfrac{\nu_i^*}{1 + 0.87\nu_i/\nu_i^*}$ and $\xi(r) = \dfrac{d\ln n_e}{d\ln r} + \dfrac{d\ln D}{d\ln r} + 1$. Equation (8a) can be analyzed as follows. Let the plasma rotation velocity V_ϑ vary on the scale l_V. Under the conditions $q \gg 1/l_V$, $\sqrt{1/(al_V)}$ (where a is the tokamak minor radius), the poloidal rotation velocity and the radial electric field are close to their neoclassical values [7], $V_\vartheta \simeq V_\vartheta^{(\mathrm{NEO})}$ and $E_r \simeq E_r^{(\mathrm{NEO})} \equiv (T_i/e)(d\ln n_e/dr + k_T d\ln T_i/dr)$. Accordingly, for $q \sim 1/l_V$, $\sqrt{1/(al_V)}$, the terms with spatial derivatives in Eq. (8a) are important. In this case, the radial electric field differs from its neoclassical value. For arbitrary radial profiles $D(r)$, $n_e(r)$, and $T_i(r)$, Eq. (8a) can be solved only numerically. In the next section, we will exemplify this solution.

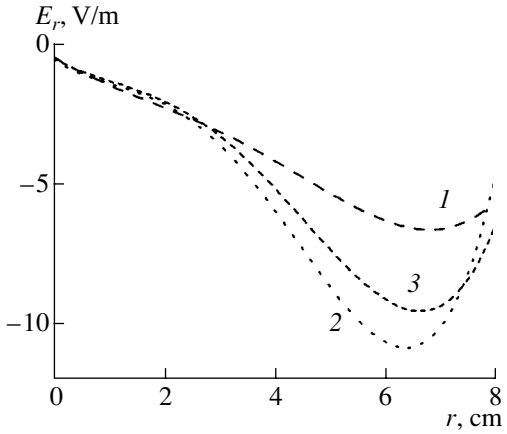

Fig. 1. Profiles of the neoclassical radial electric field calculated without allowance for anomalous viscosity and inertia for three different times during a typical FT-2 discharge with auxiliary LH heating: (*1*) in the ohmic heating phase, (*2*) in the LH heating phase, and (*3*) in the post-heating phase.

3. NUMERICAL SIMULATIONS

To calculate the radial electric field profile by means of Eq. (8a), we took the experimental data on the ion temperature $T_i(r)$ and electron density $n_e(r)$ from [1]. Using the data published in [1, 3], we approximated the profile of the anomalous diffusion coefficient by $D(r) = D_0[1.2 + 3.5(r/a)^2]$, where $D_0 = 4 \times 10^3$ cm^2/s. In calculating the radial electric field, the numerical coefficient k_T, which depends on the collisionality regime, was described by the approximate expression proposed in [6]. Having specified the diffusion coefficient $D(r)$ and having chosen typical experimental data on the ion temperature $T_i(r)$ and electron density $n_e(r)$ [1], we can calculate the coefficients of differential equation (8a). We note that, at the center of the plasma column, anomalous effects play a negligible role in the formation of the profile of the poloidal rotation velocity. In the axial region, the radial electric field is, with good accuracy, close to its neoclassical value, and it is only in the region of steep gradients at the discharge periphery that the radial electric field is far from being neoclassical. This enables us to impose the boundary conditions $V_\vartheta|_{r=0} = V_\vartheta^{(\mathrm{NEO})}$ and $\left.\dfrac{dV_\vartheta}{dr}\right|_{r=0} = \dfrac{dV_\vartheta^{(\mathrm{NEO})}}{dr}$. Hence, by solving Eq. (8a) with the prescribed boundary conditions by the Runge–Kutta method, we can obtain the

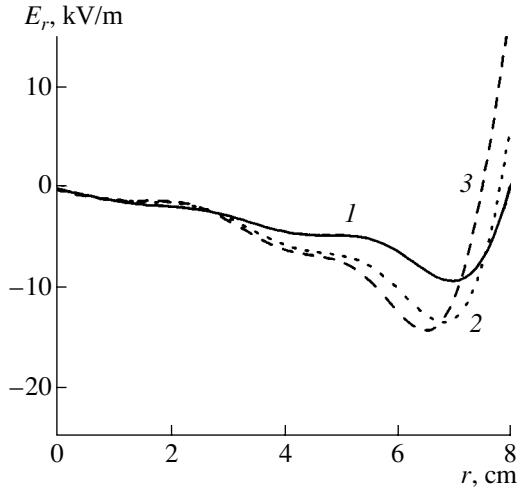

Fig. 2. Radial electric field calculated by using Eq. (8a) for the same times as in Fig. 1.

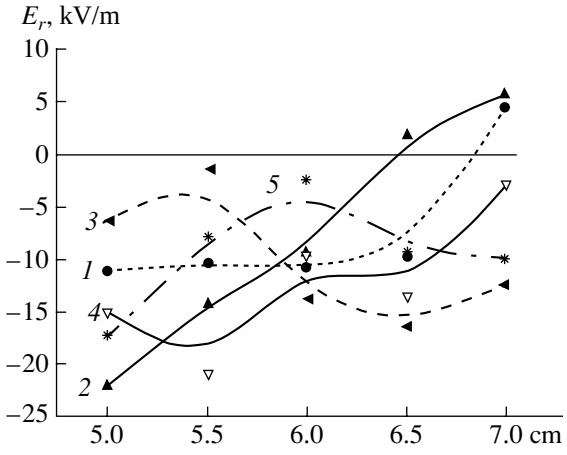

Fig. 3. Measured profiles of the radial electric field [5]: profile *1* refers to the beginning of the RF pulse (30 ms), profiles *2* and *3* refer to the LH heating phase (31 and 34 ms, respectively), and profiles *4* and *5* refer to the H-mode in the post-heating phase of the discharge (38 and 40 ms, respectively).

profile of the neoclassical radial electric field. Figure 1 shows the neoclassical radial field profiles calculated without allowance for the effects of anomalous viscosity and inertia and by using the above experimental data on the ion temperature and electron density profiles [1] for three different times during a typical discharge. Figure 2 presents the results from solving Eq. (8a) numerically. A comparison of Figs. 1 and 2 shows that the main difference between the radial electric field calculated from Eq. (8a) and the neoclassical radial electric field lies in the fact that the former can become positive at the plasma edge. This agrees with the experimental data from spectral and probe measurements at r = 5–7 cm [5]. The results of these simulations allow us to draw the following conclusions:

(i) At the center of the plasma column, the radial electric field is close to its neoclassical value.

(ii) Near the wall, the neoclassical field is seen to differ appreciably from that calculated with allowance for inertia and anomalous viscosity. For the chosen values of the anomalous electron diffusion coefficient, the calculated results are seen to correlate with the experimental data before and during the LH heating phase (Figs. 1, 2; curves *1*, *2*). In the post-heating phase, the measured radial electric field is negative, $E_r < 0$ (Fig. 3; curves *3*, *4*), while the calculated values of E_r at the plasma periphery are positive (Fig. 2, curve *3*). This is likely related to the suppression of turbulence in the post-heating phase [12].

Hence, one of the possible mechanisms by which the radial electric field E_r can become positive near the separatrix is associated with the effect of inertia and anomalous viscosity, which in turn have their origin in well-developed plasma turbulence.

4. CONCLUSIONS

Our simulations have shown that, in a plasma with well-developed turbulence, the radial ambipolar electric field can be positive in the region of steep gradients of the plasma parameters. One of the possible mechanisms that cause the radial electric field to deviate strongly from its neoclassical values is associated with the inertia and anomalous viscosity of the plasma. In our simulations, these two plasma parameters were introduced empirically. In a plasma in which the turbulence is suppressed (as is the case with auxiliary LH heating), the radial electric field exhibits a nearly neoclassical behavior during the formation of a transport barrier and transition to the H-mode. According to our numerical analysis, this neoclassical behavior results from a reduction in transport coefficients at the discharge periphery and from a decrease in the level of anomalous viscosity. Such behavior of the radial electric field E_r is confirmed by the experimentally obtained profiles *4* and *5* in Fig. 3 (which reproduces Fig. 6 from [5]): these profiles show the radial electric field in the H-mode and differ from profiles *1* and *2* (which correspond to the ohmic heating phase and the initial phase of LH heating) in that the radial electric field is everywhere negative.

ACKNOWLEDGMENTS

This work was supported in part by the Russian Foundation for Basic Research (project no. 02-02-17684) and INTAS (grant no. 2001-2056).

REFERENCES

1. S. I. Lashkul, V. N. Budnikov, E. O. Vekshina, *et al.*, Fiz. Plazmy **27**, 1059 (2001) [Plasma Phys. Rep. **27**, 1001 (2001)].
2. Y. Kamada, Plasma Phys. Controlled Fusion **A65**, 42 (1999).
3. S. P. Voskoboynikov, S. I. Lashkul, A. Yu. Popov, and V. A. Rozhanskii, in *Proceedings of the 27th EPS Conference on Controlled Fusion and Plasma Physics, Budapesht, 2000*; ECA **24B**, 288 (2000).
4. T. Kurki-Suonio, S. I. Lashkul, and J. A. Heikkinen, Plasma Phys. Controlled Fusion **44**, 331 (2002).
5. S. I. Lashkul, V. N. Budnikov, A. D. Gurchenko, *et al.*, Proc. Czechoslovak J. Phys. **52**, 1149 (2002).
6. F. L. Hinton and R. D. Hazeltine, Rev. Mod. Phys. **48**, 290 (1976).
7. S. P. Hirshman, Phys. Fluids **21**, 224 (1978).
8. R. J. Groebner, Phys. Fluids B **5**, 2343 (1993).
9. V. Rozhansky and M. Tendler, Phys. Fluids B **4**, 1877 (1992).
10. V. Rozhansky and M. Tendler, in *Reviews of Plasma Physics*, Ed. by B. B. Kadomtsev (Consultants Bureau, New York, 1996), Vol. 19, p. 147.
11. S. I. Lashkul and A. Yu. Popov, Contrib. Plasma Phys. **42**, 253 (2002).
12. V. N. Budnikov, V. V. D'yachenko, L. A. Esipov, *et al.*, Fiz. Plazmy **21**, 865 (1995) [Plasma Phys. Rep. **21**, 817 (1995)].

Translated by I.A. Kalabalyk

Plasma Physics Reports, Vol. 30, No. 12, 2004, pp. 988–994. Translated from Fizika Plazmy, Vol. 30, No. 12, 2004, pp. 1064–1070.

MAGNETIC CONFINEMENT SYSTEMS

Bifurcation of the Equilibrium of a Current-Carrying Plasma Column

V. I. Ilgisonis and Yu. I. Pozdnyakov

Nuclear Fusion Institute, Russian Research Centre Kurchatov Institute, pl. Kurchatova 1, Moscow, 123182 Russia

Received April 22, 2004

Abstract—The classical (for the Grad–Shafranov equation) formulation of the equilibrium problem for a cylindrical current-carrying plasma column is shown to admit multiple solutions. The multiple solutions are bifurcational in character and appear due to the nonlinearity of the equilibrium equation. This was demonstrated analytically using a stepped current profile as an example. Bifurcational solutions found for the cylindrical case survive in toroidal geometry too. © *2004 MAIK "Nauka/Interperiodica".*

1. INTRODUCTION

The theory of plasma equilibrium is one the most extensively developed branches of plasma physics. In the case of axial symmetry, which is typical for both astrophysical objects (stars) and fusion devices (like tokamaks or pinches), static plasma equilibrium equations can be reduced to a two-dimensional elliptical (generally, nonlinear) partial differential equation [1] supplemented with standard boundary conditions. The nonlinearity results from the nonlinear dependence of the current density on the magnetic flux. As a rule, in the equilibrium problem, this dependence is prescribed a priori. The solution to such a boundary problem turns out to be rather sensitive to the values of the input parameters that determine the geometry of the plasma boundary, the magnitudes and profiles of the plasma current and pressure, etc. Solutions corresponding to a set of nested magnetic surfaces are usually of practical interest.

For simple profiles, few exact or approximate solutions are known that correspond well to real experiments, the problem formulation often being mathematically correct. Note that there is no general claim of how to correctly formulate the equilibrium problem—only a few particular cases of the correct problem formulation are known (see, e.g., [2]). Nevertheless, the viewpoint exists that, within a wide range of parameters corresponding to appropriate experimental conditions, the solution describing a set of nested magnetic surfaces is unique and is a continuous function of the parameters of the problem. This opinion is mainly based on the well developed methods of finding such solutions numerically.

At the same time, spontaneous transitions from one steady state to another (such as the so-called L–H transition [3] and the internal transport barrier formation [4]) are often observed in tokamaks. These transitions demonstrate typical bifurcational features, such as fast changes in the equilibrium parameters (in particular, the average plasma pressure), hysteresis, etc. There have been attempts to explain this phenomenon by the bifurcation of the transport coefficients (as a rule, anomalous ones [5]), although, as was shown in [6] long before the discovery of transport barriers, the neoclassical transport coefficients also may, in principle, demonstrate bifurcational behavior. However, changes in the macroscopic plasma state that result from changes in transport processes would occur on time scales comparable to the plasma lifetime and/or the dissipation time (or to the source/sink time), whereas in real experiments, they occur much faster.

A fast change in the macroscopic state means that the plasma leaves its initial equilibrium state, giving rise to hydrodynamic plasma motion that can, in particular, have the form of developed plasma turbulence. The plasma can then relax into some new equilibrium state or be maintained by means of instabilities in a state that can be called equilibrium only on average. This and other similar considerations were discussed in detail in [7], where the appearance of a transport barrier was interpreted as a bifurcation of equilibrium. It is well known that bifurcational transitions occur when the number of the degrees of freedom of a system is restricted. The analysis of these restrictions is important for determining both the possibility of transition itself and the admissible changes in the parameters of the system. In [8], which followed [7] and detailed it, the conservation of the cross helicity was considered to be such an additional restriction.

The bifurcational mechanism itself was discussed neither in [7] nor in [8]. Changes in the equilibrium state were assumed to be localized in a rather narrow barrier zone. For example, the assumption regarding a spontaneous change of the magnetic surface structure (a transition from an equilibrium with magnetic islands to nested magnetic surfaces and vice versa) seems to be physically reasonable. Zakharov, Smolyakov, and Subbotin were the first to consider this opportunity [9]. The

1063-780X/04/3012-0988$26.00 © 2004 MAIK "Nauka/Interperiodica"

idea that the bifurcation of an equilibrium state can occur without breaking the nested structure of the magnetic surfaces has been recently proposed by Solano [10]. However, there are no accurate calculations (including numerical) that could explicitly demonstrate bifurcational transitions in the framework of the above two hypotheses. It should also be noted that the theory of bifurcations for boundary problems is still poorly developed. Catastrophe theory usually deals with the asymptotic behavior of dynamic systems; this behavior is determined by the peculiarities of the vector field on the phase portraits of the systems [11].

In the present paper, we demonstrate the possibility of the existence of multiple solutions to the classical problem of the equilibrium of a current-carrying plasma column. A simple current profile that admits analytical solutions is considered. The chosen parametrization of the problem allows us to reveal bifurcational transitions between these solutions without breaking the structure of the toroidally nested magnetic surfaces. It should be noted that multiple solutions are related to the nonlinearity of the equilibrium equation, rather than to toroidal effects (the main result is obtained for a cylindrical plasma column).

The paper is organized as follows: In Section 2, we present the mathematical formulation of the problem. In Section 3, the solutions obtained are described and their bifurcational character is demonstrated. In Section 4, the results obtained are generalized to the case of toroidal geometry.

2. FORMULATION OF THE PROBLEM

The equilibrium of an axisymmetric plasma is described in cylindrical coordinates r, φ, and z by the well-known Grad–Shafranov equation [1],

$$\left[r\frac{\partial}{\partial r}\left(\frac{1}{r}\frac{\partial}{\partial r}\right)+\frac{\partial^2}{\partial z^2}\right]\psi = -r^2p' - FF'. \quad (1)$$

This equation is the projection of the force balance equation

$$\nabla p = (\nabla\times\mathbf{B})\times\mathbf{B} \quad (2)$$

onto the direction of the gradient of the poloidal flux ψ of the magnetic field $\mathbf{B}$, which can be written in a general form as $\mathbf{B} = \nabla\psi\times\nabla\varphi + F\nabla\varphi$. The two remaining components of Eq. (2) determine the functional dependences of the plasma pressure p and the poloidal current F, which, in an axisymmetric case ($\partial/\partial\varphi \longrightarrow 0$), are surface functions:

$$p = p(\psi), \quad F = F(\psi). \quad (3)$$

Since 1957, Eq. (1) has been a subject of serious attention of physicists and mathematicians. Traditionally, dependences (3) are a priori prescribed in a certain region $r, z \in \Omega$ in which Eq. (1) is to be solved. The boundary conditions result from the physical formulation of the problem. An example of bifurcation with a free boundary is described in [12], where a possible transition from a toroidal equilibrium to a helical one is discussed. In the present paper, we consider a fixed-boundary problem: $\psi|_{r,z\in\partial\Omega} = \psi_b$, which corresponds, e.g., to an experimental situation in which the plasma boundary is determined by a well-conducting wall. The quantity ψ is equal to the poloidal magnetic flux to within an arbitrary constant; therefore, the value of ψ at the boundary can be set at zero, $\psi_b = 0$.

There are several known examples [13–17] of analytical solutions to Eq. (1) in which the functions $p'(\psi)$ and $FF'(\psi)$ are chosen to be linear. Another well-known analytical method of solving the equilibrium problem is the method of moments [18]. In this method, the structure of the magnetic surfaces is a priori assumed to have the form

$$\begin{cases}\psi = \psi(a)\\ r \approx R + \Delta(a) - (a - \epsilon(a)\cos 2\theta - \ldots)\cos\theta\\ z \approx (a - \epsilon(a)\cos 2\theta - \ldots)\sin\theta,\end{cases} \quad (4)$$

where the quantities Δ, ϵ, etc., determine the displacement, ellipticity, and other moments of a magnetic surface with a characteristic radius a (a = const on the magnetic surface ψ = const), respectively. The following ordering is assumed for the nesting of the surfaces: $\Delta(a) \sim a/R$, $\epsilon(a) \sim a(a/R)^2$, etc. Here, R is the major radius of the torus (it is assumed that $a/R \ll 1$, so we can use expansion in the inverse aspect ratio a/R). Substituting expressions (4) into Eq. (1) and setting the coefficients by different harmonics of θ to be zero, we obtain equations for $\psi(a)$, $\Delta(a)$, $\epsilon(a)$, etc. In particular, the equation for ψ in the leading order in a/R can be written in the form

$$\frac{1}{R}\frac{d}{da}(a\psi'(a)) = -a\left(\frac{FF'_\psi}{R} + Rp'_\psi\right), \quad (5)$$

which is equivalent to a cylindrical approximation to within normalizing coefficients. The prime denotes the derivative over the argument. On the right-hand side of Eq. (5), the expression in brackets,

$$j(\psi) = \frac{FF'_\psi}{R} + Rp'_\psi \quad (6)$$

is the toroidal current density, which is independent of r in a cylindrical approximation.

We normalize the argument a to the plasma column radius a_b, the current density $j(\psi)$ to the characteristic value j_0, and the flux ψ to $j_0a_b^2R$ and use the same notation for the dimensionless quantities:

$$\frac{\psi}{j_0a_b^2R} \longrightarrow \psi, \quad \frac{j}{j_0} \longrightarrow j, \quad \frac{a}{a_b} \longrightarrow a \in [0,1]. \quad (7)$$

In dimensionless variables, Eq. (5) takes the form

$$\frac{d}{da}(a\psi'(a)) = -aj(\psi). \quad (8)$$

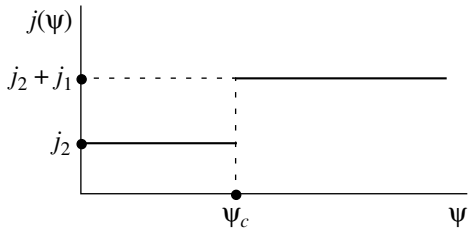

Fig. 1. Stepped current profile.

As was mentioned above, when solving a problem with a fixed plasma boundary, we can choose $\psi(1) = 0$. The second boundary condition, $\psi'(0) = 0$, ensures the regular behavior of the current density at the column axis. Thus, we have a *boundary* problem for the second-order differential equation. In general, this equation is nonlinear since the density profile depends on the unknown function ψ and this dependence is not necessarily linear.

We consider a stepped current density profile (Fig. 1)

$$j = j_2 + j_1\Theta(\psi - \psi_c), \tag{9}$$

where $j_2 > 0$, $j_1 \geq 0$, and Θ is the Heavyside function,

$$\Theta(x) = \begin{cases} 1, & x \geq 0 \\ 0, & x < 0. \end{cases} \tag{10}$$

This choice is justified by the fact that over each segment with a constant value of j, Eq. (8) can easily be integrated. On the other hand, for a finite value of j_1, the dependence $j(\psi)$ is substantially nonlinear. Therefore, using this profile as an example, we can reveal the properties of Eq. (8) that are of interest to us. Moreover, by increasing the number of steps on the $j(\psi)$ profile, it is possible to model almost every current profile (in this case, the procedure of solving the problem is only technically more complicated).

Finally, for $j(\psi)$ given by expression (9), the boundary problem in a cylindrical approximation takes the form

$$\frac{d}{da}(a\psi'(a)) = -a(j_2 + j_1\Theta(\psi - \psi_c)), \quad \psi(1) = 0, \quad \psi'(0) = 0. \tag{11}$$

In this problem, j_1, j_2, and ψ_c are parameters. In fact, the set j_1 and j_2 contains only one independent parameter because the initial current density is normalized to a certain characteristic value j_0 and any of the two values j_1 and j_2 can be chosen as j_0 (provided that it is nonzero); hence, j is equal to unity on the corresponding segment.

3. BIFURCATIONAL PROPERTIES OF THE GRAD–SHAFRANOV EQUATION IN A CYLINDRICAL APPROXIMATION

In the absence of a current jump ($j_1 = 0$), the solution to boundary problem (11) is well known and has the form of a parabola:

$$\psi(a) = j_2\frac{1 - a^2}{4}. \tag{12}$$

If the current jump is positive ($j_1 > 0$) and if $\psi_c > j_2/4$, then additional solutions appear:

$$\psi(a) = \begin{cases} \psi_c + j_2\left(\dfrac{\psi_0 - \psi_c}{j_1 + j_2} - \dfrac{a^2}{4}\right) + j_1\dfrac{\psi_0 - \psi_c}{j_1 + j_2}\ln\dfrac{4(\psi_0 - \psi_c)}{a^2(j_1 + j_2)}, \\ a \in (a_c, 1] \\ \psi_0 - (j_1 + j_2)\dfrac{a^2}{4}, \quad a \in [0, a_c], \end{cases} \tag{13}$$

where a_c is the argument value corresponding to $\psi_c = \psi(a_c)$:

$$\frac{\psi_0 - \psi_c}{j_1 + j_2} = \frac{a_c^2}{4}. \tag{14}$$

Note that solution (13) is smooth at a_c.

The value of ψ at the plasma column axis ($\psi_0 = \psi(0) \geq \psi_c$) is determined by the algebraic equation

$$\psi_c + j_2\left(\frac{\psi_0 - \psi_c}{j_1 + j_2} - \frac{1}{4}\right) + j_1\frac{\psi_0 - \psi_c}{j_1 + j_2}\ln\frac{4(\psi_0 - \psi_c)}{(j_1 + j_2)} = 0. \tag{15}$$

If $\psi_c \leq j_2/4$, then the parabolic solution vanishes, the remaining solutions being those described by formulas (13) and (15). The number of solutions to problem (11) is determined by the number of roots, ψ_0, of algebraic equation (15). This number depends on the values of the parameters entering into this equation.

To investigate how the number of solutions to boundary problem (11) depends on the parameters j_1, j_2, and ψ_c, we consider the *Cauchy problem* for the same equation,

$$\frac{d}{da}\left(\frac{a}{R}\psi'(a)\right) = -a(j_2 + j_1\Theta(\psi - \psi_c)), \quad \psi(0) = \psi_0, \quad \psi'(0) = 0, \tag{16}$$

where the value ψ_0 of the function $\psi(a)$ at the column axis ($a = 0$) is as yet arbitrary. Let us investigate how the boundary value $\psi(1)$ depends on ψ_0. We trace the solution to Eq. (16), which is equal to ψ_0 at the column axis, and find the corresponding value of ψ at the boundary.

Introducing the notation $\psi(1) \equiv \psi_f$, we obtain the dependence $\psi_f(\psi_0)$. The value of ψ_0 at which $\psi_f(\psi_0) = 0$ corresponds to the solution to Cauchy problem (16) that coincides with the solution to initial boundary problem (11). Therefore, the number of the roots to the equation $\psi_f(\psi_0) = 0$ is equal to the number of solutions to the boundary problem in a cylindrical approximation. In order to find the dependence $\psi_f(\psi_0)$, we solve problem (16) and substitute the boundary value of the argument $a = 1$ into the solution obtained. As a result, we arrive at

$$\psi_f(x) = \psi_c + \frac{j_2}{4}(x-1) + \frac{j_1}{4}x\left(1 + \Theta(x)\ln\left(\frac{x}{e}\right)\right), \quad (17)$$

where Θ is the Heavyside function and e is the natural logarithmic base. It can be seen that ψ_0 enters into Eq. (17) only through the quantity

$$x = 4\frac{\psi_0 - \psi_c}{j_1 + j_2}. \quad (18)$$

The dependence $\psi_f(x)$ is schematically shown in Figs. 2 and 3. The function $\psi_f(x)$ is linear at $x \le 0$ and reaches its maximum at $x = 0$. At $x > 0$, $\psi_f(x)$ has a minimum at $x = x^* = \exp(-1 - j_2/j_1)$. The values of $\psi_f(x)$ at the extremum points are

$$\psi_f^0 \equiv \psi_f(x = 0) = \psi_c - \frac{j_2}{4}, \quad (19)$$

$$\psi_f^* \equiv \psi_f(x = x^*) = \psi_c - \frac{j_1}{4}\exp\left(-\frac{j_2 + j_1}{j_1}\right) - \frac{j_2}{4}. \quad (20)$$

Depending on its extremal values ψ_f^0 and ψ_f^*, the function $\psi_f(x)$ (and, therefore, $\psi_f(\psi_0)$) can have different number of zeros. Let us consider three situations:

1. If $\psi_f^0 > 0$ (i.e., $\psi_c > j_2/4$), then the function $\psi_f(x)$ always has at least one zero at $x < 0$: $x = x_* = -\dfrac{4\psi_c - j_2}{j_1 + j_2}$. In addition, at $x > 0$, the function $\psi_f(x)$ has two zeros, one zero, or no zeros, depending on the sign of ψ_f^* (Fig. 2):

(a) if $\psi_f^* > 0$, there are no zeros at $x > 0$;

(b) if $\psi_f^* = 0$, then, at $x > 0$, the function $\psi_f(x)$ has one zero, $x = x^*$; and

(c) if $\psi_f^* < 0$, the function $\psi_f(x)$ has two zeros at $x > 0$: $x = x_1^*$ and $x = x_2^*$.

As was mentioned above, each zero of $\psi_f(x)$ corresponds to a solution to problem (11). Figure 4 shows such solutions calculated for case 1c at $\psi_c = 0.28$, $j_2 = 1$, and $j_1 = 1$.

2. If $\psi_f^0 = 0$ ($\psi_c = j_2/4$), the dependence $\psi_f(x)$ has exactly two zeros (Fig. 3, curve *a*); this corresponds to

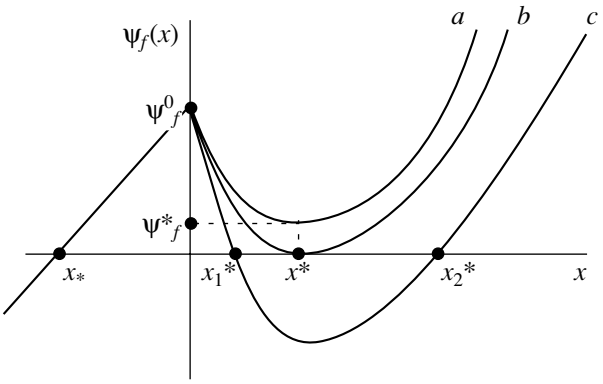

Fig. 2. Schematic profiles of $\psi_f(x)$ at $\psi_f^0 > 0$: (*a*) $\psi_f^* > 0$, (*b*) $\psi_f^* = 0$, and (*c*) $\psi_f^* < 0$.

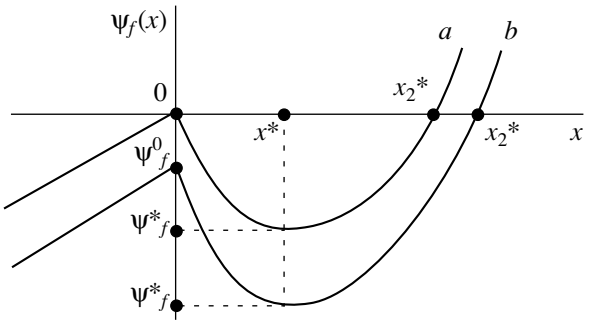

Fig. 3. Schematic profiles of $\psi_f(x)$ at (*a*) $\psi_f^0 = 0$ and (*b*) $\psi_f^0 < 0$.

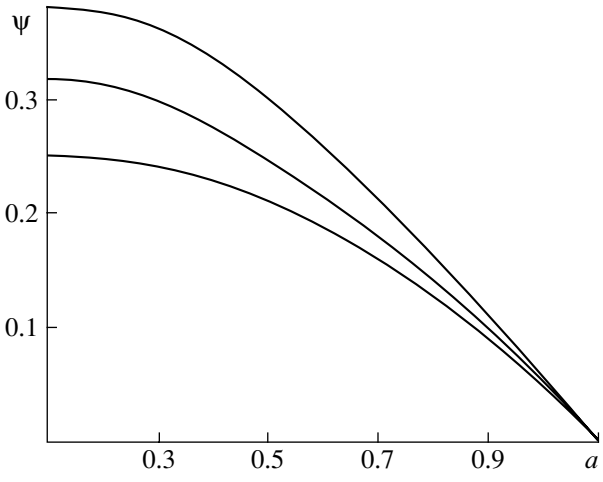

Fig. 4. Solutions to boundary problem (11) at $\psi_f^* < 0$ (see Fig. 2, curve *c*) for $\psi_c = 0.28$, $j_2 = 1$, and $j_1 = 1$.

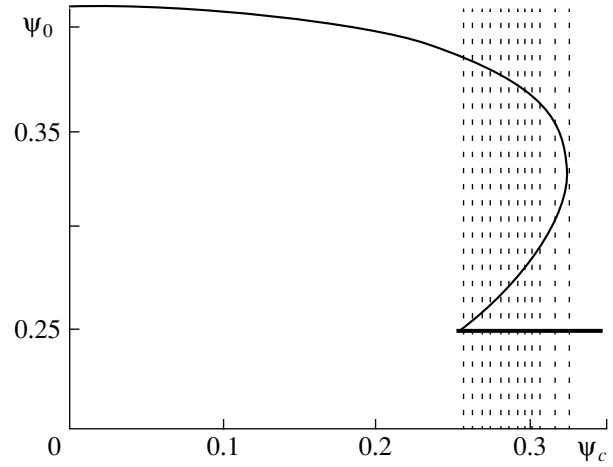

Fig. 5. Dependence $\psi_0(\psi_c)$ at j_1 =1.2. The domain corresponding to multiple solutions is marked by dots.

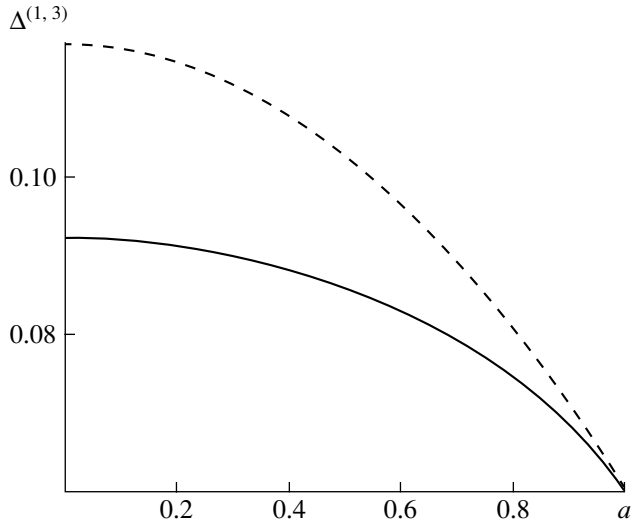

Fig. 6. Profiles $\Delta^{(1,3)}(a)$. The dashed and solid lines correspond to $\Delta^{(1)}(r, z)$ and $\Delta^{(3)}(r, z)$, respectively.

the existence of two solutions to boundary problem (11).

3. If $\psi_f^0 < 0$ ($\psi_c < j_2/4$), there is only one zero (Fig. 3, curve *b*) and boundary problem (11) has a unique solution.

It follows from the above considerations that solutions to the equilibrium problem for a cylindrical current-carrying plasma column are bifurcational in character. By bifurcation, we mean a situation in which gradual variations in the parameters of the problem (in our case, j_1, j_2, and ψ_c) result in a stepwise change in the number of solutions. As was shown above, the number of solutions is equal to the number of zeros of the function $\psi_f(x)$. The dependence of the number of solutions on these parameters can also be graphically interpreted as follows: As was pointed out in the beginning of this section, the solutions to boundary problem (11) depend on the parameter ψ_0, which can be found from transcendental algebraic equation (15). The number of roots of this equation and the possibility of the existence of parabolic solution (12) determine the number of solutions to initial boundary problem (11). Let us assume that $j_2 \neq 0$ (the peripheral current density is nonzero) and choose the normalizing value j_0 to provide $j_2 = 1$. For any nonnegative j_1, Eq. (15) at $\psi_0 > \psi_c$ implicitly determines the curve $\psi_0(\psi_c)$, which at $\psi_0 \leq \psi_c$ transforms into the straight line $\psi_0 = 1/4$. Such a curve is depicted in Fig. 5 for $j_1 = 1.5$. In the hatched area, each ψ_c value corresponds to three roots of ψ_0; outside this area, it corresponds to one root; and, at the boundary, it corresponds to two roots.

4. ACCOUNTING FOR TOROIDICITY

Multiple solutions to the equilibrium problem in a cylindrical approximation obviously have their analogues in toroidal geometry. This can easily be proved using moment representation (4) for the magnetic surfaces. For nearly circular magnetic surfaces with a large (but finite) aspect ratio $\lambda = R/a_b \gg 1$, the main toroidal effect is the Shafranov shift $\Delta(a)$. The equation for the shift can be integrated in the leading order of the expansion in $1/\lambda$. It is important that the multiple solutions found above do not break the adopted estimate $\Delta/a_b \sim 1/\lambda \ll 1$; conserve the nested structure of the magnetic surfaces; and, therefore, correspond to different equilibrium states in toroidal geometry too. We present an example of calculation of $\Delta(a)$ for a linear dependence $p(\psi)$: $p'(\psi) = 0.1$ (the pressure is normalized to $j_0^2 R^2$). We choose the current profile in form (9) taking $j_2 = 1$, $j_1 = 1.5$, and $\psi_c = 0.255$. Boundary problem (11) with these parameters has three solutions $\psi(a)$ with the following values of ψ_0: $\psi_0^{(1)} = 0.25$, $\psi_0^{(2)} \simeq 0.26$, and $\psi_0^{(3)} \simeq 0.57$. It is known [18] that the Δ value is determined by the relation

$$\Delta(a) = (1/\lambda)\int_a^1 t[l_i(t)/2 + \beta_J(t)]dt, \qquad (21)$$

where the internal inductance l_i and the parameter β_J for our solutions can be calculated analytically:

$$l_i^{(1)}(a) = 1/2, \qquad (22)$$

$$\beta_J^{(1)}(a) = 0.1a^2\lambda, \qquad (23)$$

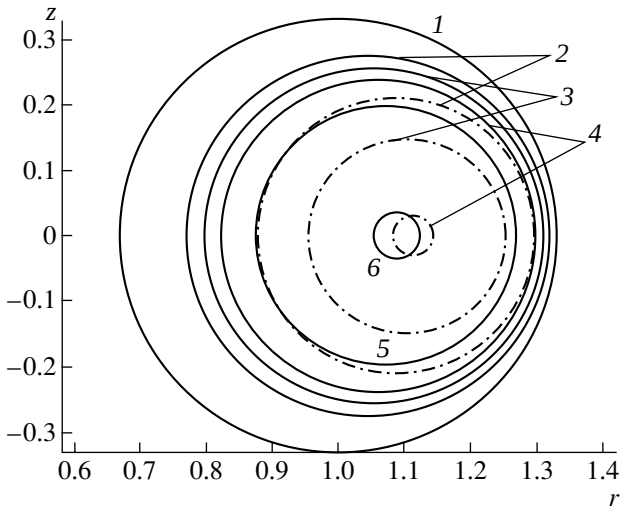

Fig. 7. Cross sections of the magnetic surfaces $\psi^{(1,3)}$ = const in the (r, z) plane for ψ = (*1*) 0, (*2*) 0.15, (*3*) 0.2, (*4*) 0.248, (*5*) 0.35, and (*6*) 0.563. The dashed-and-dotted and solid lines correspond to $\psi^{(1)}(r, z)$ and $\psi^{(3)}(r, z)$, respectively.

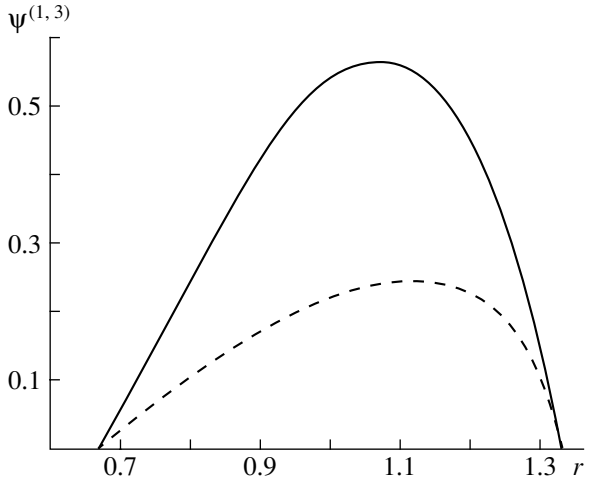

Fig. 8. Profiles $\psi^{(1,3)}(r)$ at $z = 0$. The dashed and solid lines correspond to $\psi^{(1)}(r, z)$ and $\psi^{(3)}(r, z)$, respectively.

$$l_i^{(3)}(a) = \begin{cases} 2(0.04 + a^4/16 + 0.19a^2 + 0.14\ln a), \\ a \in [0.71, 1] \\ 0.5, \quad a \in [0, 0.71), \end{cases} \tag{24}$$

$$\beta_J^{(3)}(a) = 0.2\lambda^2 \begin{cases} \dfrac{0.02 + \dfrac{a^4}{8} + 0.19a^2}{\dfrac{a^2}{4} + 0.38 + \dfrac{0.14}{a^2}}, \quad a \in [0.71, 1] \\ 0.2a^2, \quad a \in [0, 0.71). \end{cases} \tag{25}$$

Shift profiles (21) for these values of $l_i(a)$ and $\beta_J(a)$ are shown in Fig. 7. To give an idea of how our solutions behave in coordinate space, Fig. 7 shows cross sections of two families of the magnetic surfaces $\psi^{(1)}$ = const and $\psi^{(3)}$ = const (the dashed and solid lines, respectively) in the (r, z) plane for $R = 1$ and $\lambda = 3$. It can be seen that there are contours of both families that correspond to the same values ψ. Figure 8 shows the profiles $\psi^{(1,3)}(r)$ at $z = 0$; these curves (with allowance for the relationship $p \sim \psi$) illustrate the pressure profiles along the major radius.

5. CONCLUSIONS

It is well known from the course of differential equations that the solution to a nonlinear boundary problem is not necessarily unique: the problem can also have multiple solutions or no solutions at all. In this paper, we have shown that the Grad–Shafranov equation *in its classical formulation*, i.e., for given dependences $p(\psi)$ and $F(\psi)$, can have several different solutions satisfying *the same* boundary conditions. This result was obtained analytically in a cylindrical approximation using a stepped current profile as an example. Solutions to the equilibrium equation are shown to be bifurcational in character: gradual variations in the parameters determining the current density profile (in our case, these parameters are the magnitude and location of the jump in the current density) result in a stepwise change in the number of solutions. On the plane of these parameters, the bifurcational curve has the fold shape that is typical of catastrophe theory [11]. The simplicity of the model and the standard formulation of the boundary problem allow us to suppose that such behavior of the solutions is most likely general rather than exceptional. In contrast, the prevailing degenerate problem with a current density depending linearly on the magnetic flux should be considered an exception (although this formulation of the problem is widely popular because it allows one to obtain relatively simple analytical solutions).

It should be noted that the bifurcational properties of the Grad–Shafranov equation have already been pointed out in the literature. For example, similar multiple solutions have recently been obtained numerically for an exponentially decreasing pressure profile [19]. An advantage of our approach is not only that our multiple solutions were obtained analytically for a current density profile with which one can model any profile of

the current density but also that these solutions satisfy *precisely the same* boundary conditions, whereas the boundary value of ψ in [19] is a bifurcational parameter itself. Moreover, the solutions $\psi(a)$ (and, accordingly, $p(a)$) obtained in [19] can occur nonmonotonic, whereas our solutions are free of this drawback.

It seems rather surprising that there are no indications of such bifurcations in numerical simulations. It is well known that numerical calculations of the plasma equilibrium from solving the Grad–Shafranov equation accompany any modern tokamak experiment; however, no multiple solutions have been found. In our opinion, this is due to the currently accepted computational procedure in which the range of variations in the dimensionless poloidal magnetic flux ψ is fixed (e.g., by the segment $\psi \in [0, 1]$). At each iteration, the departure of ψ out of this range is compensated for by adjusting the extra scale factor inserted into Eq. (1) in front of the current density. Such a method regularizes the procedure and ensures the convergence of the iteration process (see, e.g., [20]). Note that the solution obtained by means of this procedure does not correspond precisely to the a priori given dependence $j(\psi)$. In contrast, the multiple solutions obtained in our study correspond to the same dependence $j(\psi)$ but to different ranges of ψ. The fixing of the total current (the dimensional physical quantity), which is important for a comparison between the computational and experimental results, does not imply significant restrictions on the selection of solutions, since, in both cases, a comparison is performed by choosing the scale factor j_0 [20]. It cannot be excluded that instabilities of difference schemes revealed in the early stage of numerical simulations of plasma equilibrium in tokamaks (1960s), when the above regularization procedure was not applied, were due to the presence of multiple solutions, rather than to numerical errors.

ACKNOWLEDGMENTS

We are grateful to É.I. Yurchenko, whose useful comments helped to improve the graphical representation of the results obtained. We are also grateful to V.D. Pustovitov, who brought [19] to our attention. This work was supported in part by the Russian Foundation for Basic Research (project no. 02-02-16089) and the RF Presidential Program for Support of Leading Scientific Schools (grant no. NSh-2024.2003.2).

REFERENCES

1. V. D. Shafranov, Zh. Éksp. Teor. Fiz. **33**, 710 (1957) [Sov. Phys. JETP **6**, 545 (1958)].
2. A. S. Demidov, V. V. Petrova, and V. M. Silantiev, Compt. Rend. Ser. Mat. **323**, 353 (1996).
3. F. Wagner, G. Becker, K. Behringer, *et al.*, Phys. Rev. Lett. **49**, 1408 (1982).
4. K. Tobita and JT-60 Team, Plasma Phys. Controlled Fusion **41**, A333 (1999).
5. S.-I. Itoh and K. Itoh, Nucl. Fusion **29**, 1031 (1989).
6. L. M. Kovrizhnykh, Zh. Éksp. Teor. Fiz. **56**, 877 (1969) [Sov. Phys. JETP **29**, 475 (1969)].
7. V. I. Ilgisonis and Yu. I. Pozdnyakov, Fiz. Plazmy **28**, 99 (2002) [Plasma Phys. Rep. **28**, 83 (2002)].
8. V. I. Ilgisonis and Yu. I. Pozdnyakov, in *Theory of Fusion Plasmas (Proceedings of the 20th International School of Plasma Physics, Varena, 2002)*, Ed. by J. W. Connor, O. Sauter, and E. Sindoni (SIF, Bologna, 2002), p. 183.
9. L. E. Zakharov, A. I. Smolyakov, and A. A. Subbotin, Fiz. Plazmy **16**, 779 (1990) [Sov. J. Plasma Phys. **16**, 451 (1990)].
10. E. R. Solano, Plasma Phys. Controlled Fusion **46**, L47 (2004).
11. T. Poston and I. Stewart, *Catastrophe Theory and Its Applications* (Pitman, London, 1978; Mir, Moscow, 1980).
12. Yu. N. Dnestrovskij, D. P. Kostomarov, A. V. Pedorenko, and A. V. Popov, Fiz. Plazmy **13**, 1186 (1987) [Sov. J. Plasma Phys. **13**, 683 (1987)].
13. L. S. Solov'ev, Zh. Éksp. Teor. Fiz. **53**, 626 (1967) [Sov. Phys. JETP **26**, 400 (1968)].
14. E. K. Maschke, Plasma Phys. **15**, 535 (1973).
15. V. A. Overovich, Sol. Phys. **77**, 63 (1982).
16. P. J. McCarthy, Phys. Plasmas **6**, 9 (1999).
17. O. I. Bogoyavlenskiĭ, Usp. Mat. Nauk **55**, 63 (2000).
18. L. E. Zakharov and V. D. Shafranov, in *Reviews of Plasma Physics*, Ed. by M. A. Leontovich and B. B. Kadomtsev (Énergoatomizdat, Moscow, 1982; Consultants Bureau, New York, 1986), Vol. 11.
19. K. V. Brushlinskiĭ, N. M. Zueva, M. S. Mikhaĭlova, and S. V. Sin'ko, Fiz. Plazmy **24**, 973 (1998) [Plasma Phys. Rep. **24**, 907 (1998)].
20. T. Takeda and S. Tokuda, J. Comp. Physiol. **93**, 1 (1991).

Translated by the authors

Plasma Physics Reports, Vol. 30, No. 12, 2004, pp. 995–1005. Translated from Fizika Plazmy, Vol. 30, No. 12, 2004, pp. 1071–1081.

IONOSPHERIC PLASMA

Langmuir Turbulence in Ionospheric Plasma

A. V. Gurevich, H. C. Carlson, Yu. V. Medvedev, and K. P. Zybin

Lebedev Physical Institute, Russian Academy of Sciences, Leninskiĭ pr. 53, Moscow, 119991 Russia

Received December 25, 2003

Abstract—A kinetic theory is developed for strong Langmuir turbulence in the region of the reflection of a high-power ordinary radiowave in ionospheric plasma. The structure and quantity of the cavitons that form in the stage of well-developed turbulence are determined. The acceleration of electrons is investigated, and it is found that the electron distribution function acquires a significant tail with an effective temperature T_{eff} of 50 to 100 times the plasma temperature. The region occupied by fast electrons is hundreds of times thicker than the layer of Langmuir turbulence. The theoretical results are shown to correlate well with the observational data on the electron acceleration and plasma emission in ionospheric experiments. *© 2004 MAIK "Nauka/Interperiodica".*

1. INTRODUCTION

Langmuir turbulence (LT) in the ionosphere can be generated by a vertically directed beam of high-power radiowaves as a result of resonant interaction of an ordinary high-power radiowave with the eigenwaves of the ionospheric plasma in the region where the radiowave is reflected. The extraordinary radiowaves do not reach the region of resonant interaction [1].

In ionospheric experiments, LT is investigated by means of incoherent scatter radars emitting radiowaves at the ion-acoustic and plasma frequencies. LT is responsible for the electron acceleration and for the intense optical emission from the perturbed region of the ionosphere [2–5].

The mechanism for the onset of LT is associated with the parametric instability of the plasma in an alternating electric field [6]. It is this instability that gives rise to plasma waves and ion-acoustic waves. In the nonlinear stage of instability, an important role is played by the cavitons—the wells in the plasma density within which the oscillations of the plasma electrons are trapped. The cavitons govern the acceleration of electrons [7, 8].

A distinctive feature of LT is that it occurs in a narrow ionospheric layer with a thickness of about 100 to 200 m in altitude z, the characteristic vertical scale lengths of the plasma density and plasma temperature being tens of kilometers. The electron mean free path usually exceeds the length of the LT layer. Consequently, LT develops in an essentially collisionless plasma. The nonlinear stage of LT is dominated by the modulational instability [9, 10] and is described by the Zakharov hydrodynamic equations [11, 12]. Numerous analytical studies and numerical simulations based on these equations have made it possible to determine the intensity and spectrum of the established ion-acoustic and plasma oscillations and the number and structure of the generated cavitons, as well as to investigate the nonlinear stage of the collapse of these cavitons [11–16]. However, the electron acceleration cannot be described by the hydrodynamic theory, in which neither the amount of the accelerated electrons nor their inverse effect on the spectrum of the established plasma oscillations can be determined.

The electron acceleration can be described only in terms of kinetic theory. The moving electrons are accelerated when they cross the cavitons; hence, the acceleration process is of a local nature. Moreover, the only electrons that are subject to acceleration are fast electrons in the tail of the electron distributionfunction (EDF). As for the slow (thermal) electrons, they adiabatically oscillate inside the cavitons and do not absorb the field energy. The boundary between the fast and slow electrons is determined by the effective width of the caviton [8].

Under the ionospheric plasma conditions, however, this acceleration process is not finished when an electron leaves the accelerating LT layer. As was mentioned above, the length of the LT layer is much less than the electron mean free path. Consequently, after being accelerated inside the layer, the electron outside the layer can be scattered by collisions in such a way that it returns to the layer and crosses it again, thereby acquiring additional energy. This process may repeat itself many times. Fast electrons are accelerated until the energy that they acquire in the LT layer becomes equal to the energy that they lose in collisions. Because of the repeated crossings of the LT layer, fast electrons are accelerated far more efficiently; as a result, the region occupied by them increases many times, becoming as large as tens of kilometers in size [17]. These theoretical predictions were fully confirmed by experimental observations of the electron acceleration and optical emission in the ionosphere [18–26].

At the same time, a theory of repeated acceleration has been developed based on a rigorous kinetic description of the electrons only outside the accelerating layer [17]. The layer parameters (in particular, the sizes and

1063-780X/04/3012-0995$26.00 © 2004 MAIK "Nauka/Interperiodica"

number of the cavitons, which govern the acceleration process) are described *phenomenologically*. The goal of the present study is to overcome this drawback of the theory and to construct a systematic kinetic solution to the problem not only outside but also inside the accelerating layer.

Our paper is organized as follows: In Section 2, we formulate the kinetic problem in general terms. We focus on the accelerating layer, in which the electric field of the radiowave is strong and the resonance conditions that give rise to intense plasma oscillations are satisfied. Above the layer, the radiowave is absent; below the layer, its effect is unimportant. We derive the general kinetic equation and impose conditions on the electric field at the boundaries of the accelerating layer. In Section 3, we construct a general solution to the kinetic equation outside the layer. In doing so, elastic and inelastic collisions of electrons with both the charged and neutral particles of the ionospheric plasma are fully taken into account. Based on the solution to the kinetic equation outside the layer, closed boundary conditions for the EDF inside the layer are formulated. In Section 4, we use these boundary conditions to obtain a complete solution to the kinetic problem for an accelerating layer with strong LT. Such a problem can only be solved by applying efficient numerical methods. In our simulations, we used the standard particle-in-cell (PIC) technique that was developed to model collisionless plasmas [27]. However, since the electric oscillations excited in the layer are very strong, the collisional absorption plays an important role even in the case of rare collisions. In calculations, these collisions were taken into account by a specially devised numerical method, one which is described in the Appendix. In Section 5, we investigate the electron acceleration.

Our simulations allowed us to examine the cavitons that form in an accelerating layer with strong LT and to determine how the shape and number of the cavitons depend on the strength of the radiowave electric field and on the frequency detuning. We show that the EDF acquires a significant tail of fast electrons and that the tail extends over a spatial region hundreds of times thicker than the accelerating layer because of the coupling of the layer to the surrounding space. We determine how the shape of the tail depends on the parameters of the problem. We demonstrate that fast electrons play an important (and even dominant) role in stabilizing the cavitons. Note that the electron acceleration and the resulting caviton stabilization cannot be described in terms of the previously accepted hydrodynamic model even if some additional parameters are introduced. We also show that an appreciable amount of the field energy is absorbed in rare electron collisions. We determine how the theory developed here is related to the phenomenological theory of electron acceleration [17] and find the main phenomenological parameters. Finally, in Section 6, we summarize the main results of our study and briefly discuss applications of the theory constructed here to ionospheric experiments. It is shown that the theory provides a good description of the optical emission and electron acceleration observed in a vast ionospheric plasma region (extending over tens of kilometers).

2. GENERAL FORMULATION OF THE KINETIC PROBLEM

Let us consider a weakly inhomogeneous (in the z direction) plasma and an electromagnetic wave propagating in it. The kinetic equations describing the motion of the plasma electrons and ions have the form

$$\frac{\partial f_e}{\partial t} + \mathbf{v}\cdot\frac{\partial f_e}{\partial \mathbf{r}} - \frac{e}{m}\left\{\mathbf{E}\cdot\frac{\partial f_e}{\partial \mathbf{v}} + \frac{1}{c}(\mathbf{v}\times\mathbf{B})\cdot\frac{\partial f_e}{\partial \mathbf{v}}\right\} = S_e(f_e),$$

$$\frac{\partial f_i}{\partial t} + \mathbf{v}\cdot\frac{\partial f_i}{\partial \mathbf{r}} + \frac{e}{M}\left\{\mathbf{E}\cdot\frac{\partial f_i}{\partial \mathbf{v}} + \frac{1}{c}(\mathbf{v}\times\mathbf{B})\cdot\frac{\partial f_i}{\partial \mathbf{v}}\right\} = S_i(f_i), \quad (1)$$

$$\mathbf{E} = \mathbf{E}_1 + \mathbf{E}_0(z)\sin\omega t, \quad \nabla\cdot\mathbf{E}_1 = 4\pi e(N_e - N_i).$$

Here, $f_e(\mathbf{v}, \mathbf{r}, t)$ and $f_i(\mathbf{v}, \mathbf{r}, t)$ are the electron and ion distribution functions, respectively; $S_e(f_e)$ and $S_i(f_i)$ are the collision integrals; $N_e(\mathbf{r})$ and $N_i(\mathbf{r})$ are the electron and ion densities; e and m are the charge and mass of an electron; M is the mass of an ion; $\mathbf{E}_1$ is the plasma electric field; $\mathbf{B}$ is the magnetic field; and $E_0(z)$ is the amplitude of the incident ordinary electromagnetic wave of frequency ω. At point z_l, where the radiowave is reflected, its frequency ω coincides with the eigenfrequency ω_l of plasma oscillations; in other words, the following resonance condition is satisfied:

$$\omega = \omega_{pe}(z_l) \equiv \sqrt{\frac{4\pi e^2 N(z_l)}{m}}.$$

In the vicinity of this point, strong LT develops, a large number of cavitons are generated, and the electrons are accelerated. We assume that the wave electric field satisfies the condition $E_0 \gg E_{\text{th}}$, where E_{th} is the threshold for the onset of parametric instability [6].[1]

The scale length of the LT layer is small in comparison to the electron mean free path, and the wave electric field in the resonance region points in the z direction. Consequently, to a first approximation, the collisions in the layer can be ignored and the kinetic equations describing the dynamics of electrons and ions can be written in a simple form as:

$$\frac{\partial f_e}{\partial t} + v_{ez}\frac{\partial f_e}{\partial z} - \frac{e}{m}E\frac{\partial f_e}{\partial v_{ez}} = 0,$$

[1] In ionospheric experiments, this condition is usually satisfied well. In the region where the ordinary wave is reflected, its electric field is polarized parallel to the Earth's magnetic field, which is assumed, for simplicity, to be directed nearly along the vertical z axis.

$$\frac{\partial f_i}{\partial t} + v_{iz}\frac{\partial f_i}{\partial z} + \frac{e}{M}E\frac{\partial f_i}{\partial v_{iz}} = 0, \quad (2)$$

$$E = -\frac{\partial \phi}{\partial z} + E_0(z)\sin(\omega t), \quad \frac{\partial^2 \phi}{\partial z^2} = 4\pi e(N_e - N_i).$$

Of course, these equations are valid only inside the accelerating layer. In order to solve them, we must formulate the conditions on the electric field and on the EDF at the layer boundaries.

The boundary conditions on the electric field and on the wavelength of the incident wave can naturally be chosen as follows:

$$k = \frac{2\pi}{L}, \quad \phi|_{z=0,\, z=L} = 0,$$

where L is the length of the LT layer. The question about the boundary conditions on the EDF is more complicated. In order for the conditions on the EDF at the boundaries of the collisionless LT layer to be correct, it is necessary to consider the kinetic equation for the electrons outside the layer.

3. KINETIC EQUATION OUTSIDE THE LT LAYER

Above the LT layer, there is no radiowave; below the layer, its effect is unimportant. Since the length of the region outside the layer is substantially greater than the electron mean free path, elastic and inelastic collisions play an important role there. The kinetic equation for the electrons outside the layer has the form

$$\frac{\partial f_e}{\partial t} + v\mu\frac{\partial f_e}{\partial z} = S(f_e), \quad (3)$$

where μ is the cosine of the angle between the z axis and the electron velocity. It is important that, in collisions, the direction of the electron velocity changes at a much faster rate than does the electron energy:

$$\delta = \frac{\nu_0}{\nu_1} \ll 1, \quad (4)$$

where ν_1 and ν_0 are the elastic and inelastic electron collision frequencies, respectively. It is well known [1] that, under condition (4), the EDF is symmetrized; therefore, it is natural to expand it in Legendre polynomials:

$$f(t, z, \mu, v) = \sum_{n=0}^{\infty} f_n(t, z, v)P_n(\mu)$$

In this case, kinetic equation (3) splits into a sequence of coupled equations for the functions f_n [1]. Taking into account the smallness of parameter (4), we write out the main equations of the sequence:

$$\frac{\partial f_0}{\partial t} + \frac{v}{3}\frac{\partial f_1}{\partial z} = S_0, \quad S_0 = \frac{1}{2}\int_{-1}^{1} S d\mu = \nu_0 f_0,$$
$$v\frac{\partial f_0}{\partial z} = -\nu_1 f_1, \quad \nu_1 f_1 = \frac{3}{2}\int_{-1}^{1} \mu S d\mu. \quad (5)$$

In writing Eqs. (5), we chose the following form of the collision integral for the fast electrons [16]:

$$S_0(f_0) = \nu_0(\varepsilon)f_0, \quad \nu_0 = v\sigma_0 N_m,$$
$$S_1 = \nu_1(\varepsilon)f_1, \quad \nu_1 = v\sigma_t N_m,$$

where σ_0 is the cross section for inelastic processes, σ_t is the transport cross section, and N_m is the total density of the neutral particles. Finally, Eqs. (5) are reduced to

$$\frac{\partial f_0}{\partial t} = \frac{v^2}{3\nu_1}\frac{\partial^2 f_0}{\partial z^2} - \nu_0 f_0, \quad f_1 = -\frac{v}{\nu_1}\frac{\partial f_0}{\partial z}. \quad (6)$$

Let us consider the problem in a quasi-steady-state formulation ($\partial f_0/\partial t = 0$). The solution to kinetic equations (6) outside the LT layer has the form

$$f(z, v) = F(0, v)e^{-\sqrt{3\delta}\frac{|z|}{l_1}}(1 - \sqrt{3\delta}\mu), \quad l_1 = \frac{v}{\nu_1} \quad (7)$$

where $l_1 = v/\nu_1$ is the electron mean free path. We can see that the distribution function of fast electrons in the collisional region varies on a characteristic spatial scale on the order of $l_1/\sqrt{\delta}$, which is much greater than the mean free path l_1. On the other hand, taking into account that the length of the accelerating layer is much less than the electron mean free path, we can assume it to be zero (as compared to the scales on which the parameters of the problem vary in the z direction). At the upper boundary of the accelerating layer, the electrons in the angular interval $0 < \mu < 1$ flow out of the layer, while the electrons in the interval $-1 < \mu < 0$ flow into it (and vice versa at the lower boundary). Hence, by integrating the distribution function $f_s(v, \mu)$ of the electrons inside the accelerating layer over μ from 0 to 1, we find the total flux of the electrons that flow upward out of the layer:

$$\int_0^1 f_{s_+}(v, \mu)d\mu = F_{s_+}(v).$$

Obviously, this flux is equal to the total electron flux at the boundary $z = 0$ outside the layer (see solution (7)):

$$F_{s_+} = \int_0^1 f_s(v, \mu)d\mu$$
$$= \int_0^1 F(0, v)(1 - \sqrt{3\delta}\mu)d\mu = F(0, v)\left(1 - \frac{1}{2}\sqrt{3\delta}\right). \quad (8)$$

Consequently, the distribution function f_{s_-} of the electrons that return to the layer has the form

$$f_{s_-}(v) = \int_0^1 f_{s_+}(v, \mu)d\mu\left(\frac{1 - \sqrt{3\delta}\mu}{1 - \frac{1}{2}\sqrt{3\delta}}\right), \quad -1 < \mu < 0. \quad (9)$$

In this expression, we eliminated the distribution function $F(0, v)$ outside the layer by means of formula (8). Formula (9) is the sought condition on the EDF at the boundary of the layer: it relates the distribution function of the fast electrons flowing out of the layer to the distribution function of the electrons flowing into the layer. As will be seen below, this condition is sufficient to describe electron acceleration in the LT layer with allowance for its coupling to the surrounding space.

It follows from formulas (8) and (9) that the total electron influx is not the same as the total outflux: a small fraction (about $\sqrt{3\delta}$) of the fast electrons that escape from the layer do not return to it. These losses are compensated for by the diffusion and thermal diffusion of the thermal electrons. In our simulations, these diffusion processes were ignored. It can be shown, that, in a purely kinetic approach, they can be taken into account (with the desired accuracy) by artificially turning this fraction of electrons back into the LT layer. It is this compensation procedure that was implemented in our numerical simulations.

4. KINETIC THEORY OF TURBULENCE IN THE RESONANCE LAYER

Recall that we are interested here in the conditions under which the field of the electromagnetic pump wave is far above the threshold for the onset of parametric instability, $E_0 \gg E_{\text{th}}$. Such conditions are favorable for the efficient generation of strong LT in the resonant layer.

Near the point of a radiowave's reflection, the electric field in the vicinity of its maximum can be represented in the form of a standing wave:

$$E = E_0(z)\cos\omega t, \quad \omega = \omega_{p_e} + \delta\omega,$$

where $\omega_{p_e} = \sqrt{\frac{4\pi e^2 N}{m}}$ is the electron plasma frequency and $\delta\omega$ is the frequency shift with respect to the resonant frequency. The field distribution $E_0(z)$ is described by the Airy function and the electron and ion distributions are described by the kinetic equations.

In kinetic theory, strong LT can be described only numerically. In an actual ionospheric plasma, the electron mean free path is substantially greater than the length of the resonance layer. Consequently, to a first approximation, the plasma can be treated as collisionless. Accordingly, our simulations are based on the PIC method developed to model the processes occurring in collisionless plasmas [27].

Both ions and electrons are modeled as charged particles moving in a superposition of their own electric fields and the electric field produced by an external source. The ratio of the mass M of a model ion to the mass m of a model electron was varied over a broad range. Most of the results that will be presented here were obtained for $M/m = 100$. In simulations, the maximum number of model electrons, as well as of model ions, was 4×10^6.

The accelerating layer can be assumed to be one-dimensional. The length of the layer was varied within wide limits; optimally, it was taken to be equal to 2000 Debye lengths. At the boundaries of the layer, the electric field was set equal to zero and the conditions for the particles were imposed in accordance with formula (9). At the initial instant ($t = 0$), the plasma was assumed to be distributed uniformly over the entire computation region and the ions and electrons were assumed to obey Maxwellian distributions with the same temperatures. The external electric field at $t = 0$ was set at zero, and, at later times, it was assumed to increase gradually according to a certain law. The formulation of the problem must imply a gradual increase in the external electric field from zero. If the initial external electric field were nonzero over the entire layer, then the layer would immediately become subject to strong Langmuir oscillations, which contradicts the actual situation.

An important aspect of the problem in question is associated with the "natural" noise of the system of model particles. In testing the code, we thoroughly investigated this noise and also examined its sensitivity to the computation parameters. We chose the optimal values of the computation parameters in such a way that an increase or a decrease in the computation parameters from these optimal values by a factor of 2 to 3 did not affect the noise level. The only computation parameter to which the noise level was certainly sensitive was the number N_M of the model particles: the noise level turned out to be proportional to N_M^{-1}.

In the stage of well-developed LT, the mean amplitude of the oscillations that are efficiently generated in the plasma is so large that the absorption of the field energy in rare electron collisions can become substantial. In simulations, this absorption was taken into account by a specially devised numerical method (see the Appendix), which supplements the standard PIC

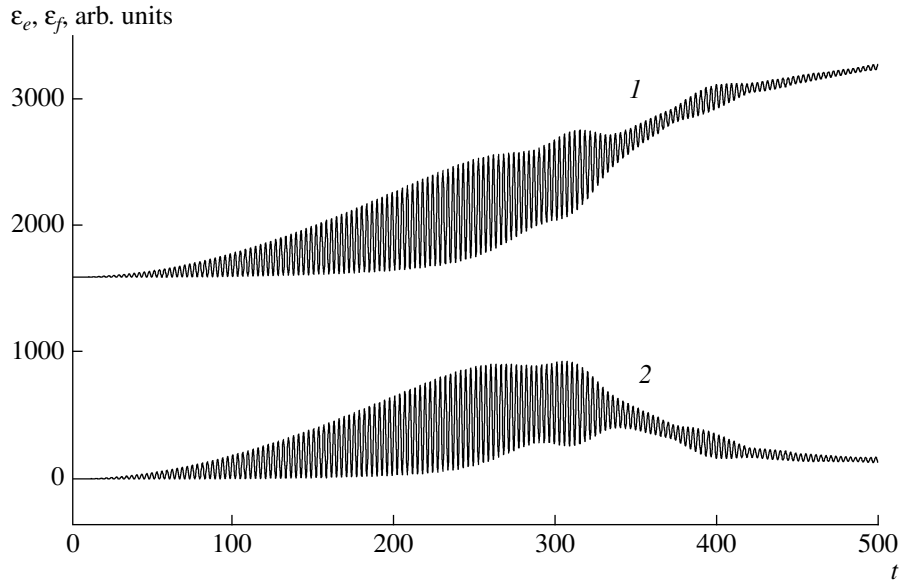

Fig. 1. Time evolution of (*1*) the electron energy density ε_e and (*2*) the electric field ε_f.

method when rare electron collisions begin to play an important role.

For convenience in numerical calculations, we reduced the problem to a dimensionless form. As the units of time, length, and velocity, we adopted the inverse plasma electron frequency $\omega_{p_e}^{-1}$, the electron Debye length $\lambda_{De} = \sqrt{T_{e0}/(4\pi e^2 n_{e0})}$, and the electron thermal velocity $\sqrt{T_{e0}/m_e}$, respectively, and as the units of potential, electric field strength, density, and energy, we adopted the quantities T_{e0}/e, $\sqrt{4\pi n_{e0} T_{e0}}$, n_{e0}, and $T_{e0}/2$, respectively. Here, n_{e0} and T_{e0} are the initial electron density and the initial electron temperature.

Our simulations show that electron oscillations in the system grow very rapidly. In the example illustrated in Fig. 1, we can see that an exponential increase in the energy of the electric-field oscillations is accompanied by a substantial increase in the electron oscillatory energy. At a time of $t \approx 200$–300, the electron oscillatory energy becomes as great as 50% (or even more) of the electron thermal energy. In this case, the energy density of the electric field, ε_f, and the electron kinetic energy, ε_e, oscillate in antiphase at the doubled electron plasma frequency.

Starting from $t_m \approx 250$–300, the energy density stops increasing monotonically because of the strongly nonlinear processes accompanying the development of LT. For $M/m = 100$, the time t_m is just the characteristic time of ion oscillations and thus corresponds to the growth rate of the modulational instability in a strong field [11]. It can be seen that this instability suppresses the rapid growth of the field and electron energies. The simultaneous oscillations of the electrons and ions give rise to wells in the plasma density (cavitons). The cavitons are shown in Fig. 2, which refers to the time $t = 350$. One can see well developed depressions in the plasma density with a depth of up to $(0.2$–$0.4)n_{e0}$. The electron and ion densities are perturbed in essentially the same manner, i.e., the cavitons are quasineutral. The width of the cavitons is $a \approx 15$–$20\lambda_{De}$, the characteristic distance between them being $d \approx 50\lambda_{De}$. The positions of the most strongly excited cavitons coincide naturally with the maxima in the amplitude $E_0(z)$ of the pump wave. The caviton depth correlates closely with the mean energy of the plasma oscillations trapped within

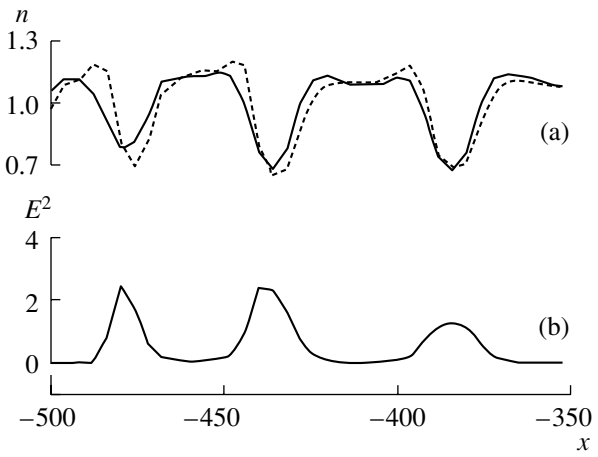

Fig. 2. Profiles of (a) the ion density n_i (solid curve) and the electron density n_e (dashed curve) and (b) the squared electric field at the time $t = 350$.

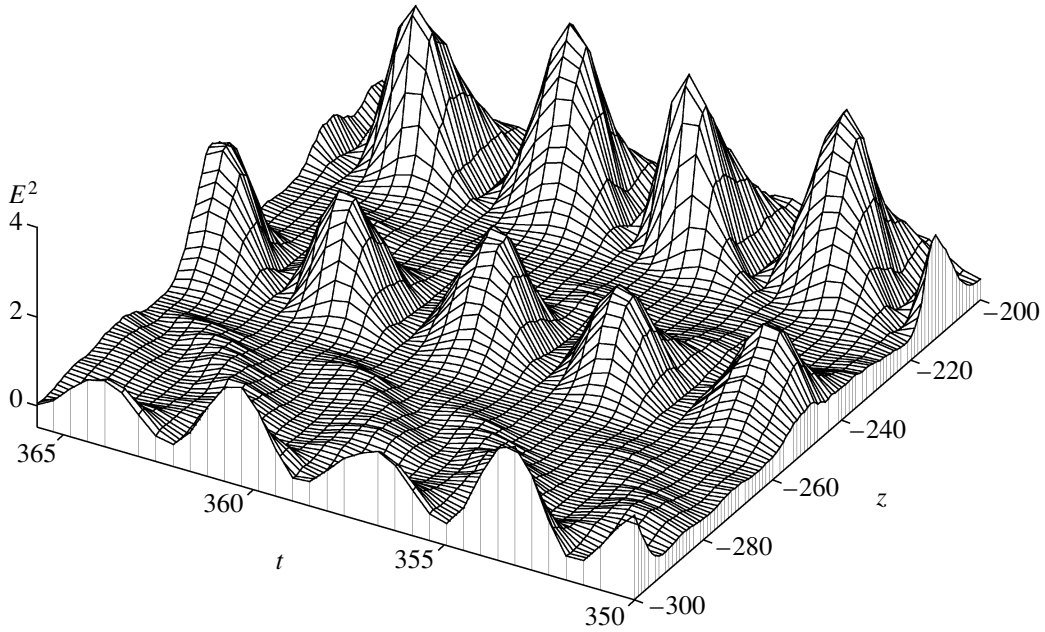

Fig. 3. Spatiotemporal evolution of the squared electric field over the spatial interval $-300 \le z \le -200$ and the time interval $350 \le t \le 366$.

the caviton (Fig. 2). One can see from Fig. 3 that the trapped wave is a standing one. The phases of the oscillations are seen to be different even in two neighboring cavitons. During the initial period (up to $t = 400$–500), the cavitons increase abruptly in depth. The caviton depth then increases at a progressively slower rate, and, on time scales of $t > (1\text{–}2) \times 10^3$, an ion-acoustic wave of amplitude 0.2–0.3 is established. The electron oscillations trapped by this wave have a relatively low intensity (see Fig. 4). Hence, in the problem in question, the cavitons are stabilized (rather than collapse) because the energy of the plasma oscillations excited by the pump wave in the density wells is absorbed by the accelerated electrons. A detailed description of the acceleration of electrons in the course of their interaction with cavitons is given in the next section.

Note that some simulations were carried out with allowance for collisions of thermal electrons in the LT layer. The results of these simulations show that these collisions lead to electron heating and weaken plasma oscillations (or, equivalently, lower the caviton amplitude). The fraction of the pump wave energy that is spent on electron heating is fairly large: under ionospheric conditions, it can be as large as 30%.

5. ELECTRON ACCELERATION

We now consider electron acceleration in the LT layer. The kinetic equation for fast electrons has the form

$$\frac{\partial f}{\partial t} + v_z \frac{\partial f}{\partial z} + \frac{e}{m} E \frac{\partial f}{\partial v_z} = 0. \qquad (10)$$

Here, $E_0(r, t)$ is the electric field of the plasma oscillations; as was shown above, this field is sharply amplified in each caviton (see Figs. 2, 3). Across a caviton, the EDF changes only slightly. This is why Eq. (10) should be averaged over an ensemble of realizations of the electric field values over the entire layer:

$$\frac{\partial \langle f \rangle}{\partial t} + v_z \frac{\partial \langle f \rangle}{\partial z} + \frac{e}{m} \underset{f_1(z,t)}{\left\langle E(z,t) \frac{\partial f_1}{\partial v_z} \right\rangle} = 0$$
$$= -\int_{-\infty}^{+\infty} dz_1 \int_{-\infty}^{t} dt_1 \frac{e}{m} E(z_1, t_1) \delta[z - z_1 v_z (t - t_1)] \frac{\partial \langle f \rangle}{\partial v_z}. \qquad (11)$$

Hence, basic kinetic equation (10) reduces to the diffusion equation in velocity space:

$$\frac{\partial f}{\partial t} + v_z \frac{\partial f}{\partial z} = \frac{e^2}{m^2} \frac{\partial}{\partial v_z} \left(D(v_z, z, t) \frac{\partial f}{\partial v_z} \right), \qquad (12)$$

where the electric field correlator

$$D(v_z, z, t) = \int_{-\infty}^{t} dt_1 \langle E(z, t) E[z - v_z (t - t_1), t_1] \rangle$$

is calculated along the trajectory of an electron.

In order to solve Eq. (12), it is necessary to take into account conditions (8) and (9) at the boundaries of the LT layer. Integrating Eq. (12) over the layer length L,

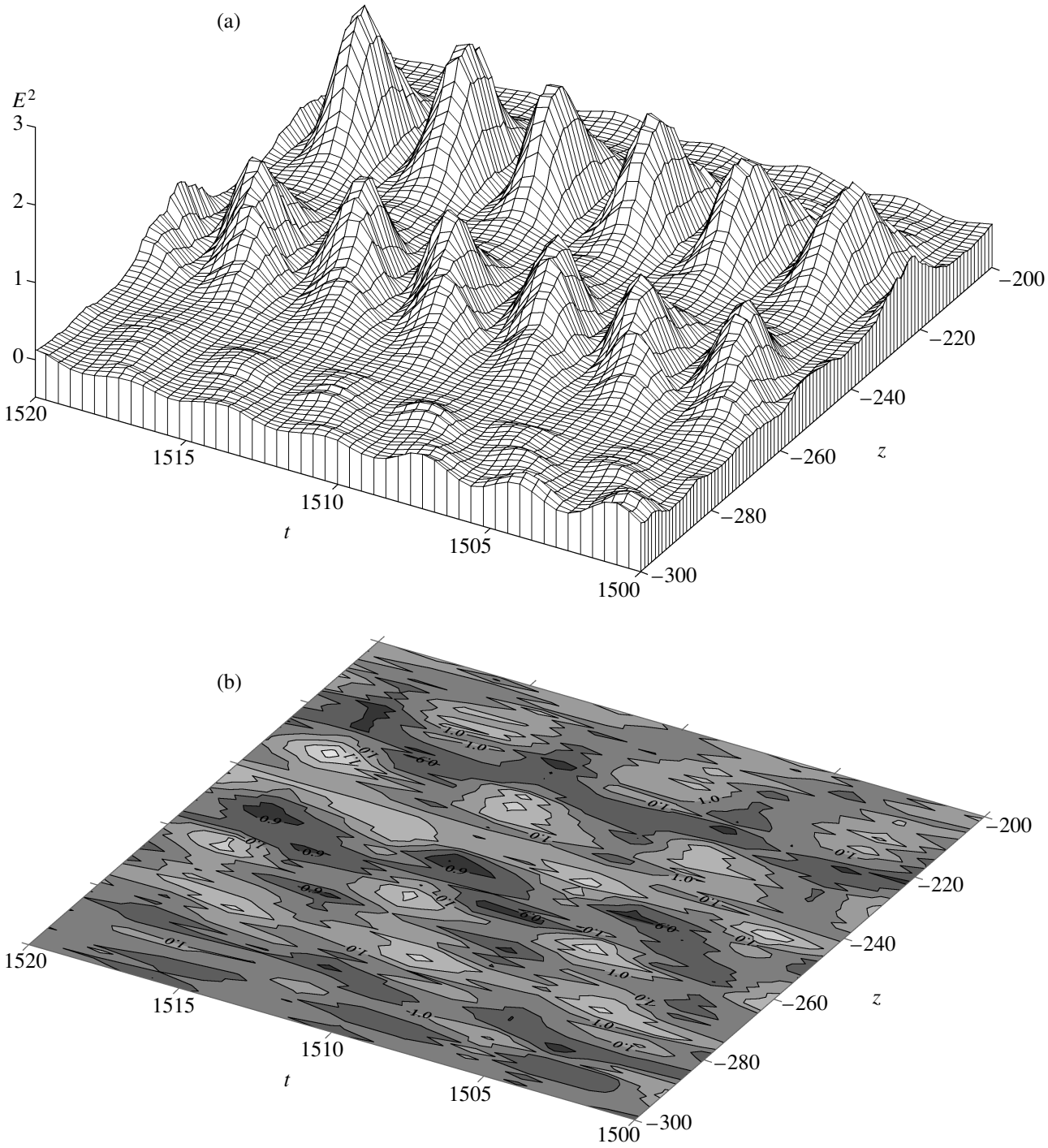

Fig. 4. (a) Spatiotemporal evolution of the squared electric field and (b) the contour plot of the electron density over the spatial interval $-300 \le z \le -200$ and the time interval $1500 \le t \le 1520$.

we obtain the following expression for the change $\Delta f = f(v_z, L, t) - f(v_z, 0, t)$ in the EDF inside the layer:

$$v_z \Delta f = -L\frac{\partial f}{\partial t} + \frac{e^2}{m^2}\frac{\partial}{\partial v_z}\left(\int_0^L D(v_z, z, t)dz\frac{\partial f}{\partial v_z}\right). \quad (13)$$

Using boundary conditions (8) and (9), we can determine how much the EDF changes outside the layer:

$$\Delta f = 2\sqrt{3\delta}f.$$

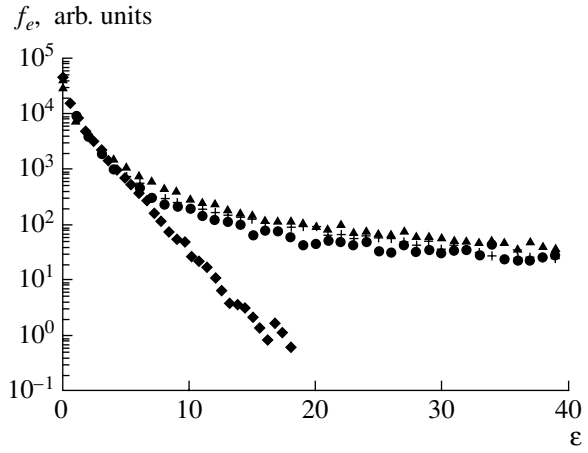

Fig. 5. EDF at the times $t = 0$ (diamonds), 300 (circles), 1000 (crosses), and 3000 (triangles).

We thus arrive at the following final form of the kinetic equation:

$$\frac{\partial f}{\partial t} = \frac{e^2}{m^2}\frac{\partial}{\partial v_z}\left(\frac{1}{L}\int_0^L D(v_z, z, t)dz\frac{\partial f}{\partial v_z}\right) - 2\frac{v_z}{L}\sqrt{3\delta}f. \quad (14)$$

The results of solving Eq. (14) numerically for $\delta = 0.1$ are illustrated in Fig. 5. We can see that the initial Maxwellian distribution is rapidly distorted and the EDF acquires a tail of fast electrons. This tail can be characterized by the effective temperature T_{eff}, which is 50–100 times higher than the initial electron temperature: $T_{\text{eff}} = 5$–10 eV at $T_{e0} = 0.1$ eV. However, only a small fraction (less than 1%) of all the electrons are accelerated to such high temperatures.

Under steady-state conditions, kinetic equation (14) has the form

$$\frac{\partial}{\partial\varepsilon}\left(T_{\text{eff}}^2\frac{\partial f}{\partial\varepsilon}\right) = f, \quad \varepsilon = \frac{mv^2}{2}. \quad (15)$$

Here, according to Eq. (14), the effective temperature T_{eff} is equal to

$$T_{\text{eff}}^2 = e^2\delta^{-1/2}v_z\int_0^L dz\int_{-\infty}^t \langle E(z, t)E[z - v_z(t - t_1)]\rangle dt_1. \quad (16)$$

The correlation function $C(z, z_1) = \langle E(z)E(z_1)\rangle$ of the electric field is shown in Fig. 6. The function is seen to be strongly localized in the vicinities of the cavitons. Therefore, the total integral over z in expression (16) can be approximately replaced by the sum of integrals over the vicinities of the maxima in the correlation function:

$$T_{\text{eff}}^2 = e^2\delta^{-1/2}v_z\sum_{n=1}^N\int_0^\infty \langle E_n(z)E_n(z - v_z\tau)\rangle d\tau,$$

where N is the total number of cavitons in the LT layer. We introduce an average statistical caviton characterized by the root-mean-square electric field $\langle E_c^2\rangle$ and by the mean scale length a to obtain

$$T_{\text{eff}} = \delta^{-1/4}\langle\Delta\varepsilon_c\rangle\sqrt{N}, \quad (17)$$

where $\Delta\varepsilon_c = ea\sqrt{\langle E_c^2\rangle}$ is the mean increment in the energy of an electron in a caviton. Expression (17) for the effective temperature of the electrons that are subject to repeated acceleration in a thin LT layer agrees with the corresponding expression derived earlier in [17]. Relationships (16) and (17) provide a kinetic definition of the phenomenological parameters $\langle E_c^2\rangle$ and a used in the theory [17].

The temperature T_{eff} given by expression (17) correlates well with that obtained from the exact solution of Eq. (14) (see Fig. 5). Note that numerical kinetic calculations of strong parametric instability in a resonance LT layer were carried out earlier in [28]. In that paper, however, no account was taken of the external collisional plasma, the presence of which is implied by correct boundary conditions (9). As a result, the conservation laws were not satisfied: the EDF decreased with energy according to a power law; as a result, the energy flux carried away by the accelerated electrons was several times more intense than the net energy flux of the pump wave. Some possible simplifications in the formulation of the problem in question were also discussed in [28, 29].

6. CONCLUSIONS

In this paper, we have constructed a theory of strong LT that develops in a resonance layer of a weakly inhomogeneous plasma. The three main results of our work are as follows.

(i) We have determined exactly the correlation function of the plasma oscillations trapped within the cavitons and have created a model of a high-energy tail that arises in the electron distribution due not only to electron acceleration in a resonance layer but also to electron collisions in a weakly inhomogeneous unperturbed plasma.

(ii) We have established that fast electrons can have a stabilizing effect on the cavitons. In this case, the cavitons do not collapse but instead evolve gradually into a quasi-steady finite-amplitude ion-acoustic wave in which the enhancement of the plasma oscillations under the action of a high-power radiowave is balanced by their absorption by fast electrons.

(iii) The spatial dimension of the region occupied by the fast electrons is governed by the plasma inhomogeneity. Under ionospheric conditions, this dimension exceeds the spatial scale of the LT layer by two orders of magnitude or more.

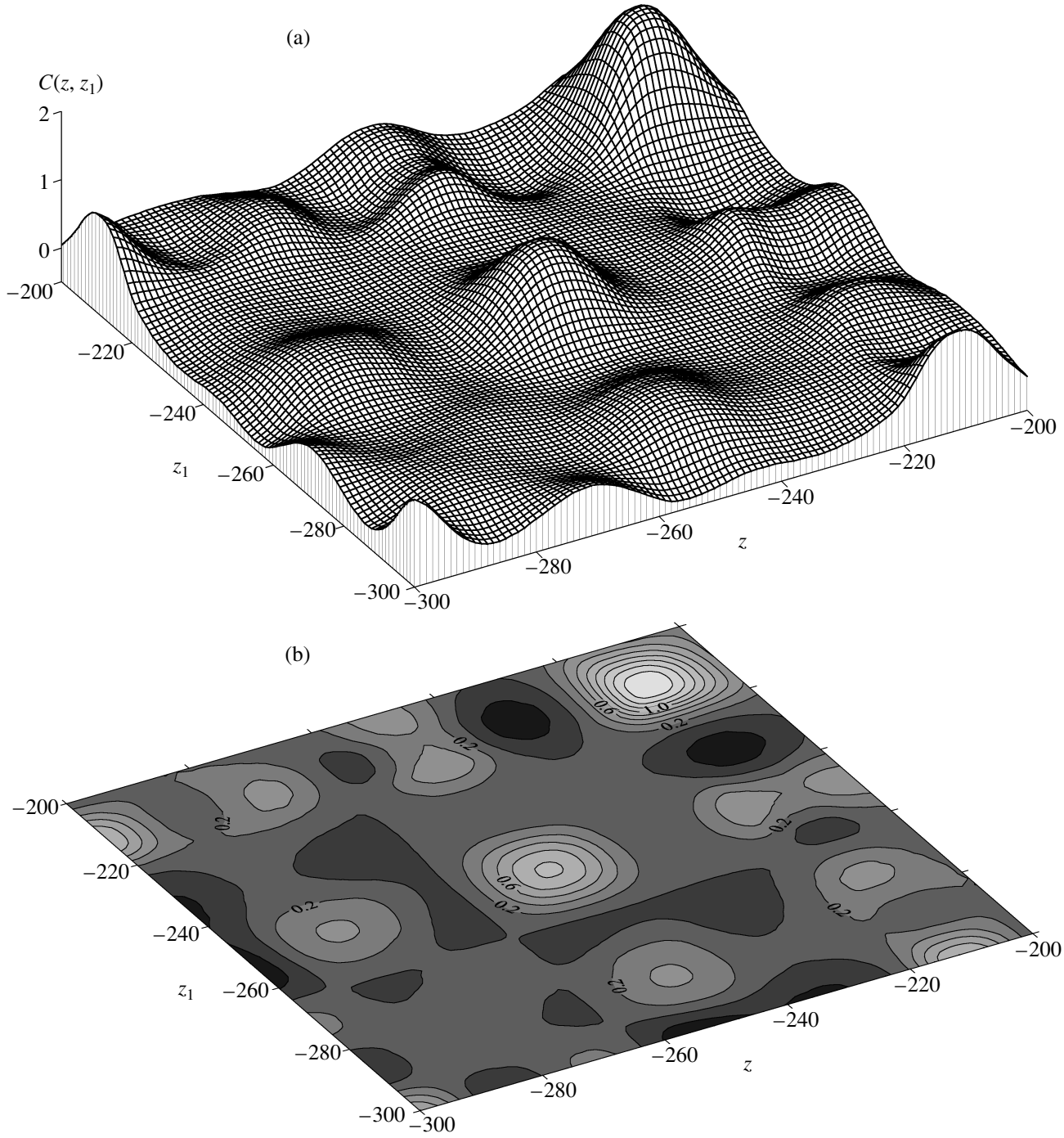

Fig. 6. (a) Correlation function $C(z, z_1)$ and (b) its contours plot.

The theory developed here is fully confirmed by experiments aimed at investigating the influence of high-power radiowaves on the ionospheric plasma. Near the point of its reflection in the resonance layer, an ordinary radiowave gives rise to strong LT. Fast electrons generated in this process are observed to have energies of up to $\varepsilon \approx 20$ eV, which are 100–200 times higher than the temperature of the unperturbed ionospheric plasma, $T_{e0} \approx 0.1$ eV. The shape of the EDF presented in Fig. 5 agrees well with that determined experimentally (see [22]).

The region of artificially produced plasma luminosity is tens of kilometers in size, the length of the resonance LT layer being only 100–300 m [24, 25]. Optical emission from the plasma is observed at the wavelengths of $\lambda_1 = 6300$ Å (the red line), $\lambda_2 = 5577$ Å (the

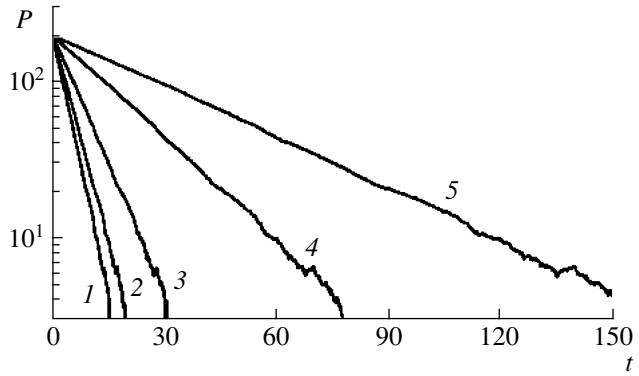

Fig. 7. Time evolution of the momentum of the system for different numbers of the model collisions: (*1*) 10^5, (*2*) 8×10^4, (*3*) 5×10^4, (*4*) 2×10^4, and (*5*) 10^4.

green line), and $\lambda_3 = 8446$ Å (the IR line), which correspond to the excitation potentials of $I_1 = 1.98$ eV, $I_2 = 4.17$ eV, and $I_3 = 10.74$ eV, respectively. Since the deexcitation time of the red line is quite long ($\Delta t \approx 150$ s), the red line emission is especially sensitive to electron collisions with neutral molecules. Consequently, at altitudes of $z \approx 200$–400 km, where the atmospheric density is very low, the red line emission is most intense [17–21], while, at lower altitudes ($z \approx 110$–130 km), the green line emission dominates [30]. The results of the theory constructed here are in good agreement with the observational data.

ACKNOWLEDGMENTS

This work was supported in part by the EOARD–ISTC (grant no. 2236), the Russian Academy of Sciences (under the Mathematical Methods of Nonlinear Dynamics Program), and the RF Program for State Support of Leading Scientific Schools (project no. NSh-1603.2003.2), and INTAS (grant no. 03-51-4286).

APPENDIX

Effect of Rare Electron Collisions

In spite of the fact that, under actual ionospheric conditions, the electron mean free path is much longer than the spatial scale of the accelerating layer, elastic collisions of thermal electrons can play an important role within the layer during the excitation of strong plasma oscillations. With this circumstance in mind, we devised a special modification of a PIC method that makes it possible to take into account the electron scattering process.

The scattering is assumed to be elastic because, at thermal electron energies, the cross section for elastic collisions is much larger than the cross sections for the remaining processes (see [1]). In elastic collisions, the velocity of the model electrons changes its direction but its absolute value remains unchanged. This is why it is necessary to follow all three velocity components of the model electrons. In other words, electron collisions should generally be treated in three-dimensional velocity space. Note that our problem assumes axial symmetry around the z axis, thereby reducing the amount of computation.

The method for modeling collisions consists in the following: In a unit time interval Δt, the direction of the velocity component v_z is randomly changed for a certain number S_M of electrons chosen at random from their total number N_M. The transverse velocity components are changed so that the absolute value of the electron velocity $|v|$ (or the electron energy) remains the same. This scheme of collisions between particles models binary collisions by allowing instantaneous changes in the particle velocity components. An analysis shows that such a scheme is equally applicable to Coulomb interactions, in which the main role is played by long-range collisions accompanied by small changes in the direction of particle motion. Based on the theory of binary collisions, it is an easy matter to find the relationship between the number of "model collisions" S_M at each time step and their effective frequency ν_M in the plasma. To do this, it is natural to introduce the dimensionless collision frequency through the formula

$$S_M = N_M \Delta t \nu_M, \tag{A1}$$

where Δt is the time step in units of ω_{pe}^{-1} and the collision frequency ν_M is in units of ω_{pe}.

We carried out a series of numerical experiments aimed at checking relationship (A1) and determining the collision frequency in a model plasma. The calculations were performed for a system in which all model electrons were assigned a moderate initial velocity V_0 in the same direction, so the entire system possessed a nonzero net initial momentum P_0. We considered how the system comes to equilibrium at the expense of the collisions introduced above. An example of this is illustrated in Fig. 7. We can see that the momentum P of the system decreases according to the law

$$P = P_0 \exp(-\nu_p t). \tag{A2}$$

It turns out that the quantity ν_p is proportional to the value of ν_M determined for a given number S_M of model collisions from formula (A1). This permits relationship (A1) to be used to model processes with a prescribed collision frequency ν_p.

In our investigations, it was also established that, during the damping in elastic collisions, the excess energy of the system, which is determined by the initial velocity V_0, is uniformly distributed over the x, y, and z velocity components. Hence, elastic collisions reduce the excess momentum of the system to zero; moreover, this process is correct from the energy standpoint: the energy ε is exactly conserved, and there is no preferential direction of motion.

Inelastic collisions accompanied by an energy loss $\delta\varepsilon$ are considered by introducing the parameter $\delta(\varepsilon)$, which characterizes the effective (averaged) electron energy losses:

$$\delta(\varepsilon) = \left\langle \frac{\delta\varepsilon}{\varepsilon} \right\rangle.$$

Here, the angle brackets denote averaging over both inelastic and elastic collisions.

REFERENCES

1. A. V. Gurevich, *Nonlinear Phenomena in the Ionosphere* (Springer-Verlag, New York, 1978).
2. W. E. Gordon and H. C. Carlson, Radio Sci. **9**, 1525 (1974).
3. P. A. Bernhardt, C. A. Tepley, and L. M. Duncan, J. Geophys. Res. **95**, 907 (1989).
4. V. L. Frolov, G. P. Komrakov, E. N. Sergeev, *et al.*, Izv. Vyssh. Uchebn. Zaved., Radiofiz. **40**, 1091 (1997).
5. P. Y. Cheung, M. P. Sulzer, D. F. DuBois, and D. A. Russel, Phys. Plasmas **8**, 802 (2001).
6. V. P. Silin, *Parametric Action of High-Power Radiation on Plasma* (Nauka, Moscow, 1973).
7. G. J. Morales and Y. C. Lee, Phys. Rev. Lett. **33**, 1534 (1974).
8. L. M. Kovrizhnykh and A. S. Sakharov, in *Interaction of Strong Electromagnetic Waves with Collisionless Plasma* (IPFAN, Gorki, 1980), p. 117.
9. A. S. Vedenov and L. N. Rudakov, Dokl. Akad. Nauk SSSR **159**, 767 (1964) [Sov. Phys. Dokl. **9**, 1073 (1965)].
10. A. G. Litvak and G. M. Fraĭman, in *Interaction of Strong Electromagnetic Waves with Collisionless Plasma* (IPFAN, Gorki, 1980), p. 50.
11. V. E. Zakharov, Zh. Éksp. Teor. Fiz. **62**, 1745 (1972) [Sov. Phys. JETP **35**, 908 (1972)].
12. A. S. Kingsep, Itogi Nauki Tekh. Ser. Fiz. Plazmy **4**, 48 (1983).
13. D. F. Dubois, A. Hanssen, H. A. Rose, and D. Russel, J. Geophys. Res. **98**, 17543 (1993).
14. P. Stubbe, H. Kohl, and M. T. Rietveld, J. Geophys. Res. **97**, 6285 (1992).
15. R. A. Sprague and J. Fejer, J. Geophys. Res. **100**, 23959 (1995).
16. E. Mjolhus, E. Helmersen, and D. F. DuBois, Nonlin. Processes Geophys. **10**, 151 (2003).
17. V. V. Vas'kov, A. V. Gurevich, and Ya. S. Dimant, Zh. Éksp. Teor. Fiz. **84**, 536 (1983) [Sov. Phys. JETP **57**, 310 (1983)].
18. H. C. Carlson, W. B. Wickwar, and G. P. Mantas, J. Atmos. Terr. Phys. **44**, 1089 (1982).
19. P. A. Bernhardt, W. A. Scales, S. M. Grach, *et al.*, Geophys. Res. Lett. **18**, 1477 (1991).
20. L. M. Duncan, J. B. Sheerin, and R. A. Behnke, Phys. Rev. Lett. **61**, 239 (1988).
21. T. Sergienko, I. Kornilov, E. Belova, *et al.*, J. Atmos. Sol.-Terr. Phys. **59**, 2401 (1997).
22. P. A. Bernhardt, M. Wong, J. D. Huba, *et al.*, J. Geophys. Res. **105**, 10657 (2000).
23. A. V. Gurevich, H. C. Carlson, G. M. Milikh, *et al.*, Geophys. Res. Lett. **27**, 2461 (2000).
24. T. R. Pedersen and H. C. Carlson, Radio Sci. **36**, 609 (2001).
25. B. U. E. Brandstrom, T. B. Leyser, A. Steen, *et al.*, Geophys. Res. Lett. **26**, 2561 (1999).
26. T. B. Leyser, B. Gustavson, B. U. E. Brandstorm, *et al.*, Radio Sci. **36**, 962 (2001).
27. A. Sestero, Nuovo Cimento **98**, 222 (1972).
28. J. G. Wang, D. L. Newman, and M. V. Goldman, Sol. Terr. Phys. **50**, 2461 (1997).
29. K. Y. Sanhonmatsu, H. X. Vu. Bezzerides, and D. F. DuBois, Phys. Plasmas **7**, 2 (2000).
30. F. T. Djuth, P. A. Bernhardt, C. A. Tepley, *et al.*, Geophys. Res. Lett. **26**, 1557 (1999).

Translated by O.E. Khadin